HIGH FREQUENCY WAVE PROPAGATION IN THE EARTH: THEORY AND OBSERVATION

Thesis by

David Paul Hill

In Partial Fulfillment of the Requirements

For the Degree of

Doctor of Philosophy

California Institute of Technology

Pasadena, California

1971

(Submitted May 18, 1971)

ACKNOWLEDGMENTS

The author gratefully acknowledges the advice and encouragement given by Dr. C. B. Archambeau throughout the development of this study. In addition, the author is indebted to the staff of the Seismological Laboratory for many stimulating and useful discussions, and in particular to Drs. D. L. Anderson, D. L. Helmberger, and D. Harkrider. Dr. Paul Richards (now at the University of California at San Diego) provided invaluable assistance in the early stages of the mathematical development of this study. Mr. Thomas Hanks read most of the manuscript and supplied many helpful comments.

The author is especially grateful to Mr.Laszlo Lenches for preparation of the figures and to Mrs. Barbara Sloan for the difficult task of typing the manuscript.

During the period of this research the author was supported by the U. S. Geological Survey through the Government Training Act. This research was also supported by the Advanced Research Projects Agency of the Department of Defense and was monitored by the Air Force Office of Scientific Research under Contract No. F44620-69-C-0067.

ABSTRACT

The wave-theoretical analysis of acoustic and elastic waves refracted by a spherical boundary across which both velocity and density increase abruptly and thence either increase or decrease continuously with depth is formulated in terms of the general problem of waves generated at a steady point source and scattered by a radially heterogeneous spherical body. A displacement potential representation is used for the elastic problem that results in high frequency decoupling of P-SV motion in a spherically symmetric, radially heterogeneous medium. Through the application of an earth-flattening transformation on the radial solution and the Watson transform on the sum over eigenfunctions, the solution to the spherical problem for high frequencies is expressed as a Weyl integral for the corresponding half-space problem in which the effect of boundary curvature maps into an effective positive velocity gradient. The results of both analytical and numerical evaluation of this integral can be summarized as follows for body waves in the crust and upper mantle:

1) In the special case of a critical velocity gradient (a gradient equal and opposite to the effective curvature gradient), the critically refracted wave reduces to the classical head wave for flat, homogeneous layers.

2) For gradients more negative than critical, the amplitude of the critically refracted wave decays more rapidly with distance than the classical head wave.

3) For positive, null, and gradients less negative than critical, the amplitude of the critically refracted wave decays less rapidly with distance than the classical head wave, and at sufficiently large distances, the refracted wave can be adequately described in terms of ray-theoretical diving waves. At intermediate distances from the critical point, the spectral amplitude of the refracted wave is scalloped due to multiple diving wave interference.

These theoretical results applied to published amplitude data for P-waves refracted by the major crustal and upper mantle horizons (the Pg, P*, and Pn travel-time branches) suggest that the 'granitic' upper crust, the 'basaltic' lower crust, and the mantle lid all have negative or near-critical velocity gradients in the tectonically active western United States. On the other hand, the corresponding horizons in the stable eastern United States appear to have null or slightly positive velocity gradients. The distribution of negative and positive velocity gradients correlates closely with high heat flow in tectonic regions and normal heat flow in stable regions. The velocity gradients inferred from the amplitude data are generally consistent with those inferred from ultrasonic

measurements of the effects of temperature and pressure on crustal and mantle rocks and probable geothermal gradients. A notable exception is the strong positive velocity gradient in the mantle lid beneath the eastern United States (2×10^{-3} sec^{-1}), which appears to require a compositional gradient to counter the effect of even a small geothermal gradient.

New seismic-refraction data were recorded along a 800 km profile extending due south from the Canadian border across the Columbia Plateau into eastern Oregon. The source for the seismic waves was a series of 20 high-energy chemical explosions detonated by the Canadian government in Greenbush Lake, British Columbia. The first arrivals recorded along this profile are on the Pn travel-time branch. In northern Washington and central Oregon their travel time is described by $T = \Delta/8.0 + 7.7$ sec, but in the Columbia Plateau the Pn arrivals are as much as 0.9 sec early with respect to this line. An interpretation of these Pn arrivals together with later crustal arrivals suggest that the crust under the Columbia Plateau is thinner by about 10 km and has a higher average P-wave velocity than the 35-km-thick, 62-km/sec crust under the granitic-metamorphic terrain of northern Washington. A tentative interpretation of later arrivals recorded beyond 500 km from the shots suggests that a thin 8.4-km/sec horizon may be present in the upper mantle beneath

the Columbia Plateau and that this horizon may form the lid to a pronounced low-velocity zone extending to a depth of about 140 km.

TABLE OF CONTENTS

GENERAL INTRODUCTION

During the last decade considerable advances were made in the definition of the velocity structure of the crust and upper mantle based on studies of elastic body wave propagation through the earth. To a large extent, these advances were made possible through the advent of both large stationary arrays and mobile recording units with broad band instrumentation and uniform recording characteristics together with improved methods of data processing by digital computers. These body wave studies have primarily centered around two approaches. One involves the accurate determination of phase velocities with which different arrivals sweep across a large, fixed array from sources at varying distances and azimuths ($dT/d\Delta$ methods). The second, and much more common approach, is based on the standard seismic refraction and reflection techniques of recording waves from a fixed source with a number of recording units at varying distances.

The majority of the published studies taking either of the above approaches use ray-theoretical methods to invert the data for velocity structure, and their success attests to the wide validity of geometrical ray theory in describing body wave propagation in the earth. However, inspite of the great success of ray-theoretical methods, a large part of the radiation field can only be explained in part, or not at all by ray theory. Some well known

examples of such events include surface waves, diffracted waves (e.g. P-waves diffracted by the core-mantle boundary), and critically refracted energy, or head waves. Furthermore, ray theory will not in general give a valid description of waves propagating through media with continuously varying properties or transition zones (although for arbitrarily high frequencies, the ray-theoretical description will become arbitrarily good). Thus, if we are to make maximum use of the information contained on a seismogram in attempting to interpret the fine structure of the earth it is necessary to supplement the ray-theoretical methods with more complete wave-theoretical solutions.

In this thesis we are primarily concerned with the wave-theoretical nature of energy that is critically refracted or nearly critically refracted by an abrupt increase in velocity. Waves associated with such energy are commonly the first arrivals recorded on seismograms out to distances of 1000 km or more from the source. They form the well known Pg and Pn branches on local travel-time curves and represent the primary data of classical seismic-refraction studies. Nearly all that is known about the best established and most widely recognized structures in the outer 200 km of the earth (e.g. the 'granitic layer' in the continental crust or the Mohorovichic discontinuity, which defines the top of the mantle

lid) is derived from ray-theoretical studies of the travel times of these phases. Clearly a thorough understanding of the effects of boundary curvature, velocity gradients, transition zones, and anelasticity on the waveform or spectrum of these phases is crucial in further attempts to refine our understanding of the major structural units of the crust and upper mantle. Equally important is the ability to account for these propagation effects in studies of body wave spectra aimed at determining source parameters.

A principle contribution of this thesis is the extension of wave-theoretical solutions for critically refracted and nearly critically refracted waves (hereafter collectively referred to as near-critical waves) to include the effects of boundary curvature and continuous velocity gradients in the medium beneath the boundary.

The theoretical treatment presented here differs from the earlier works on the effects of small gradients on near-critical waves by Chekin (1964, 1965) in the following respects; 1) we include the effects of boundary curvature, which is of the same order as the effects of small velocity gradients, 2) we use a potential representation introduced by Richards (1970) that results in true high-frequency decoupling of P-SV motion in a heterogeneous elastic medium, 3) we obtain a complete solution for the turning point problem in the case of a positive velocity gradient in the refractor, and 4) we evaluate

the basic integral exactly by numerical integration, which serves as a check on the asymptotic solutions and extends the results to include lower frequencies and more complicated interference phenomena.

In Chapter 1 the basic problem is formulated in terms of waves generated by a point source and scattered by a spherical body within which the material properties may be radially heterogeneous. Through the devices of an exact earth-flattening transformation and the Watson transform, the spherical solution is converted from an infinite sum over spherical eigenfunctions to an integral over continuous wave numbers. For high-frequency waves, this integral reduces to the form of the Weyl integral associated with plane-boundary problems. This integral is then evaluated both analytically and numerically to obtain expressions and curves for the spectral amplitudes of waves reflected and refracted by a spherical horizon within which the wave velocity may either increase or decrease with depth.

The results of the theoretical work in Chapter 1 are applied to published amplitude data for waves refracted by the major boundaries in the crust and upper mantle (the Pg, P*, and Pn waves) in Chapter 2 in a first attempt to determine velocity gradients within these major structural units. Knowledge of the distribution and size of

velocity gradients in the crust and mantle provides an important constraint on the compositional and geothermal regimes in the earth. On the basis of this preliminary study, we find negative velocity gradients in the crust and mantle lid in the western United States which correlate with high heat flow and high geothermal gradients and positive velocity gradients in the eastern United States which correlate with lower heat flow and lower geothermal gradients. An important conclusion reached in this chapter is that a compositional gradient appears to be required in the mantle lid beneath the stable eastern United States to explain the inferred positive velocity gradients in terms of available geothermal data and laboratory measurement of physical properties for mantle material.

In Chapters 1 and 2 the earth is regarded as being radially heterogeneous but laterally homogeneous. However, we can expect the assumption of lateral homogeneity to be only approximately true even in under the 'simplest' and most uniform geologic provinces. In Chapter 3 we consider new seismic data over an area previously unexplored by deep seismic-refraction methods and find evidence for strong lateral variations. The area is the Columbia Plateau flood basalt province in eastern Washington and Oregon, and the data were obtained by recordings of large chemical explosions detonated in southern British Columbia along a 800-km profile from the Canadian border into central Oregon. Because of the obvious lateral variations

along this profile, we have not attempted an analysis of the amplitude data using the wave-theoretical results obtained in Chapter 1. Instead we concentrated on a ray-theoretical analysis of the travel-time data in an attempt to define the gross radial and lateral velocity variations in the crust and upper mantle under the Columbia Plateau.

CHAPTER I

Introduction:

The general problem of waves from a concentrated source reflected by a layered velocity structure is of considerable interest to seismologists, and a wealth of solutions for a variety of structures can be found in the literature. These solutions can be broadly divided into two groups; (1) time-domain solutions of progressive waves based on an initial-boundary-value formulation, and (2) frequency-domain solutions of steady waves based solely on a boundary value formulation. A concise review of the basic methods involved is given in Chapter 6 of Grant and West (1965).

Time-domain solutions formulated as initial-value problems have an inherent advantage in seismological applications since nearly all wave phenomena in the earth of seismological interest, and body waves in particular, involve the propagation of transient effects. The technique introduced by Cagniard (1939) and its modification by de Hoop (1960) have been particularly successful for obtaining exact, whole-wave solutions for pulses reflected from a plane boundary between two homogeneous media. Helmberger (1968) has recently extended this approach to successfully generate synthetic seismograms for pulses reflected from an arbitrary number of homogeneous layers. A principle limitation of the Cagniard

method is that the technique depends on having a frequency-independent reflection coefficient. Thus problems involving media with velocity gradients or curved boundaries (both of which result in a frequency-dependent reflection coefficient) are not particularly well-suited to this approach, although approximate solutions for the vicinity of a wave front have been obtained for some problems of this sort (Knopoff and Gilbert, 1959, and Gilbert and Helmberger, 1971).

In this study of waves reflected by curved boundaries and heterogeneous layers, we will take the second approach and work for solutions in the frequency domain based on a steady-state boundary-value formulation of the problem. This approach has the advantage that solutions in the frequency domain are readily interpretable in terms of seismological data; in fact, it is common to find seismological data presented in terms of spectral amplitudes and phases. Thus, it is generally not necessary to do the final integration over frequency (the inverse Fourier transform) to obtain a considerable amount of useful information about the problem. This is clearly a significant advantage in doing problems that yield a complicated, frequency-dependent reflection coefficient. Of course it is always possible, in principle at least, to do the final integration over frequency either numerically or by approximate analytical methods to express the solution in the time domain.

However, the integral is not necessarily convergent, and considerable care must be exercised if the integration is attempted. In this study we will leave the solutions in the frequency domain and not attempt to do the final inverse Fourier transform.

Because the basic problem we are considering involves waves from a point source scattered by a finite, heterogeneous body embedded in an infinite homogeneous space, we avoid a fundamental difficulty associated with the steady-state approach to wave propagation problems of choosing the proper radiation conditions at infinity. The well-known Sommerfeld condition, which in essence requires that the wave at infinity from a point source in a homogeneous medium be outgoing (Stoker, 1957), applies in this case. However, it is not at all clear that analogous conditions can be applied when one or more boundaries or a material heterogeneity extends to infinity (Dix, 1952; Stoker, 1957). When working with the flat earth analog of the spherical problem obtained by an earth-flattening transformation in Section 3 of this Chapter (a case in which the boundary as well as the heterogeneity of the lower half space extends to infinity) we can appeal to the Rainbow expansion (Bremmer, 1949) for waves in a closed spherical body to obtain the approximate radiation conditions. In addition, we present some plausibility arguments for the proper radiation condition in the heterogeneous half-space as such.

A considerable body of literature exists on wave propagation

problems in the frequency domain formulated as steady-state boundary-value problems. Many of the solutions and mathematical techniques for treating heterogeneous media and spherical geometry that were developed in the study of radio wave propagation in the ionosphere and in acoustics have only recently been applied to wave problems in solid earth geophysics. Fairly complete reviews of these methods and solutions can be found in books by Brekhovskikh (1960), Budden (1960, 1961), and Bremmer (1949).

The basic problem of steady-state spherical waves reflected by a plane boundary between two homogeneous half-spaces has been thoroughly studied. Brekhovskikh (1948) first formulated the problem with a steady point source and evaluated the branch cut in a Weyl integral to obtain an expression for the head wave, and later Heelan (1953) obtained analogous expressions for head waves in two elastic half spaces with a finite cylindrical source. Cerveny (1965) has treated this problem in considerable detail with particular emphasis given to evaluating the wave field in the immediate vicinity of the critical point, which is complicated by the close proximity of the 'head wave' branch cut and the reflected wave saddle point. A review of this problem with references to additional literature is given by Onda (1968). Berry and West (1966) extended this basic solution to obtain solutions of both reflected and head waves from several homogeneous layers in terms of generalized rays.

Some of the effects of small velocity gradients in the refracting medium on reflected and head waves have been investigated by Chekin (1964, 1965). He considered the effects of negative gradients on elastic P-SV waves and positive gradients on acoustic waves. However, as pointed out by Richards (1971), Chekin did not choose the proper potential representation for P-SV motion in a heterogeneous medium. His formulation of the positive gradient problem for acoustic waves is incomplete in the sense that this reflection coefficient does not contain both up-going and down-going waves between the turning point and the reflecting boundary. The effects of positive gradients on acoustic 'head waves' have also been investigated by Cerveny and Jansky (1967) and Cerveny (1966). Their conclusions are primarily based on Chekin's (1965) results and ray-theoretical solutions. The effects of transition zones on reflected wave amplitudes have been studied by a number of authors, including Nakamura (1964), Fuchs (1968), and most recently by Hirasawa and Berry (1971).

Most of the work mentioned above is based on a Weyl or Sommerfeld integral formulation of a steady spherical wave (see Chapter 6 in Grant and West, 1965). This work is wave-theoretical in the sense that the reflection coefficient in the integral is usually obtained from exact solutions to Helmholtz equation. A somewhat different approach, generally referred to as asymptotic ray theory, is beginning to find its way into the geophysical literature. This approach is based on an expansion of the field

quantities in a powers series of inverse frequency ($1/\omega$) introduced by Kline (1951) and Karal and Keller (1959). Hron and Kanasewich (1971) have used this approach from a generalized ray point of view to obtain synthetic seismograms for waves from a point source reflected and refracted by an arbitrary number of plane, homogeneous layers. Their work is essentially the high frequency analog of Helmberger's (1968) work based on the Cagniard-de Hoop method.

The first seismological application of the Watson transform for studying waves reflected from a spherical body was made by Scholte (1956). Since then a number of authors (Knopoff and Gilbert, 1961; Phinney and Alexander, 1966; Sato, 1968; Phinney and Cathles, 1969; Teng and Richards, 1969; Richards, 1970; Chapman, 1969) have applied this approach to the study of waves diffracted by the earth's core. Gilbert and Helmberger (1971) have recently applied the Watson transform to formulate a generalized ray theory for a layered sphere for pulse problems in the time domain. To take advantage of the Cagniard-de Hoop technique, they expand the spherical reflection coefficient in an asymptotic, frequency-independent form.

In this study of waves reflected by spherical boundaries and heterogeneous media, we will rely on techniques developed for both the Watson transform and the Weyl integral solution. Our approach will be to model the earth as a spherically symmetric, radially heterogeneous body in a homogeneous space. We will take

the material velocity at the surface of the body to be greater than in the surrounding homogeneous space and consider the wave field scattered by the body from a steady point source located in the homogeneous space (see Figure 1). This corresponds to the geophysical problem of a source in a homogeneous layer over a first order discontinuity in velocity below which the velocity may vary smoothly with depth, however in this treatment we neglect the effects of layering and the free surface above the source.

In formulating the elastic problem, we use the displacement potential representation introduced by Richards (1971) which results in the approximate decoupling of the equations of motion for P and SV waves at high frequencies in an isotropic spherically symmetric, radially heterogeneous body. By using this representation the equations of motion for P, SV, SH, as well as acoustic waves can be expressed as separate canonical wave equations.

The wave equations are operated on by a Fourier transform with respect to time to reduce them to Helmholtz equations in the frequency domain, where we have used the following convention for the Fourier transform pair:

$$f(\omega) = \int_{-\infty}^{\infty} F(t)\, e^{i\omega t}\, dt$$

$$F(t) = \frac{1}{2\pi} \int_{-\infty}^{\infty} f(\omega)\, e^{-i\omega t}\, d\omega$$

The general solution to the Helmholtz equations and boundary conditions for the wave field scattered by the spherical body can then be expressed in terms of an infinite sum over discrete wave numbers. In Section 2 we develop an expression for this general solution, and then, by applying an earth-flattening transformation to the radial part of the solution and the Watson transform to the angular part of the solution, we convert the solution from a sum over discrete wave numbers (or order numbers) to an integral over a continuum of wave numbers in a flat earth. The earth-flattening transformation is exact for the homogeneous Helmholtz equation and spherical boundary conditions, but when the point source is included, the transformation is valid only for sources not too far from the boundary compared with the radius of the boundary and for wave lengths significantly less than the radius of the boundary. This integral expression is in the form of a Weyl integral, and we can take advantage of many of the techniques developed for its analytical evaluation. Because the reflection coefficient in the integral, in principle at least, contains the exact spherical eigenfunctions for the radially heterogenous body, its evaluation will give a valid approximation for the wave field reflected at an arbitrary depth within the spherical body by an arbitrary heterogeneity. For example, it appears that this integral representation when coupled with the Epstein method for evaluating

flat problems with continuous velocity variations (Epstein, 1930; also see Phinney, 1970, for a discussion of geophysical applications of this method) provides a promising approach for studying waves reflected from a variety of interesting transition zones in a spherical earth.

Here we are primarily interested in the effects of curvature and velocity gradients in the immediate vicinity of the boundary on waves near the critical angle of incidence. To simplify the analysis, we will use a linear approximation to the earth-flattening transformation which is valid in the vicinity of the boundary. The principle effect of the linear transformation is to superimpose a linear velocity gradient on the physical velocity in the flat problem. High frequency asymptotic solutions to the Helmholtz equations of the type described by Langer (1949) can then be used to describe the wave field in the heterogeneous medium with the curvature-mapping gradient included. However, in carrying out the actual analysis, we will choose the form of the velocity variations so that the solutions to the Helmholtz equations are exactly Airy functions. In Section 3 we carry out this program in detail for acoustic waves in fluid media for both negative and positive velocity gradients. Using the acoustic case as a guide, we then do the complete elastic case for SH and decoupled P-SV motion. Finally, in Section 4, we consider the implications of

our results for a number of geophysically interesting situations and compare the asymptotic analytical solutions with exact solutions obtained by numerical integration of the Weyl integral.

Through this chapter we will use the word heterogeneous to refer to continuous variations in the physical properties of a medium and reserve the word inhomogeneous for describing differential equations with a source term on the right.

1. Equations of motion and potential representations

We will restrict our considerations to plane-layered and spherically-layered heterogeneous, isotropic media. Specifically, we will consider acoustic and elastic isotropic media in which the scalar material parameters vary smoothly as a function of either depth or radius alone and in which there is a single surface (z = const or r = const) across which the parameters change discontinuously. Furthermore, we will consider a single, isotropic point source so that the resulting field depends only on two coordinates (z and r in a cylindrical system and r and θ in a spherical system).

In an inviscid fluid media the acoustic approximation to the equations of motion are

$$\begin{aligned} \frac{\partial P}{\partial t} + \rho c^2 \nabla \cdot \underline{V} &= 0 \\ \frac{\partial \underline{V}}{\partial t} + \rho^{-1} \nabla P &= 0 \end{aligned} \tag{1.1}$$

where $\underline{V}$ is the particle velocity (assumed to be infinitesimal), P is the deviation from the static ambient pressure, ρ is the density and c is the acoustic velocity (both considered to be a function of depth or radius only). The following assumptions are made in obtaining (1.1)

$$|\rho\nabla\cdot\underline{V}| >> |\underline{V}\cdot\nabla\rho|$$

$$\left|\frac{\partial \underline{V}}{\partial t}\right| >> |(\underline{V}\cdot\nabla)\underline{V}| \qquad (1.2)$$

The first inequality limits considerations to small density gradients such that the term on the right is the product of two small quantities. The second inequality is a statement of the usual linearity approximation in hydrodynamics.

Taking the Fourier transform of (1.1) and eliminating $\underline{V}$ gives

$$\nabla^2\overline{P} + k^2\overline{P} - \rho^{-1}\nabla\overline{P}\cdot\nabla\rho = 0 \qquad (1.3)$$

where $\overline{P}$ is the Fourier transform of P, $k = \omega/c$ is a wave number and ω is the angular frequency. Following Brekhovskikh (1960) we introduce the pressure potential

$$\Phi = \overline{P}\ \rho^{-\frac{1}{2}} \quad , \qquad (1.4)$$

which reduces (1.3) to the form of a Helmholtz equation

$$\nabla^2\Phi + k^2\Phi = 0 \qquad (1.5)$$

In obtaining (1.5) we have made the assumption that

$$|k^2| >> \left|\frac{1}{2\rho}\nabla^2\rho - \frac{3}{4\rho^2}(\nabla\rho)^2\right| \quad , \qquad (1.6)$$

i.e. that density gradients are small with respect to the wave number. In this system a steady point pressure source, P is represented by the potential

$$D = P\,\rho^{-\frac{1}{2}} = \begin{cases} \dfrac{\delta(r-r_o)\,\delta(\theta-0_+)\,e^{-i\omega t}}{2\pi r^2 \sin\theta} \\ \dfrac{\delta(z-z_o)\,\delta(r-0_+)\,e^{-i\omega t}}{2\pi r} \end{cases}$$

in a spherical or cylindrical system respectively.

Richards (1970) has developed potential representations for the vector wave equation in radially heterogeneous and vertically heterogeneous (in spherical and Cartesian systems, respectively) isotropic, elastic media. From his formulation he is able to show that 1) coupled P and SV solutions exist for all possible displacement solutions, 2) SH solutions are decoupled from the P-SV solutions, and 3) at sufficiently high frequencies P-SV solutions tend to decouple into forms that can be identified with the standard irrotational P-wave and solenoidal SV-wave solutions in homogeneous media. The last two results are of particular interest here because they permit formulation of the radially or vertically inhomogeneous elastic wave propagation problems in terms of three uncoupled Helmholtz equations for frequencies commonly encountered in crustal and upper mantle seismic-refraction studies.

In a spherically symmetric system, Richard's displacement potentials for P, SV, and SH motion (P,S, and T, respectively) have the following relation to the displacement vector, $\underline{U}(\underline{r})$, at $\underline{r} = (r,\theta,\phi)$

$$\underline{U}(r) = \left[f(r)\right]^{-1} \left\{ \text{grad}\left(\frac{f(r)}{[\rho(r)]^{\frac{1}{2}}} P(\underline{r}) \right) + \text{curl curl}\left(\frac{rf(r)}{[\rho(r)]^{\frac{1}{2}}} S(\underline{r}),0,0 \right) \right\}$$

$$+ \text{curl}\left(\frac{r}{[\mu(r)]^{\frac{1}{2}}} T(\underline{r}),0,0 \right) \tag{1.7}$$

where $\rho(r)$ and $\mu(r)$, the density and shear modulus, are functions of radius and where the scale factor, $f(r)$, is any sufficiently smooth, bounded function of radius. The associated source potentials are related to the applied force per unit mass, $\mathfrak{L}$, by

$$\mathfrak{L} = f^{-1} \left\{ \text{grad}\left(\frac{f}{\rho^{\frac{1}{2}}} D \right) + \text{curl curl}\left(\frac{rf}{\rho^{\frac{1}{2}}} F,0,0 \right) \right\}$$

$$+ \text{curl}\left(\frac{r}{\mu^{\frac{1}{2}}} E,0,0 \right) \tag{1.8}$$

The spheroidal (P-SV) equations of motion can be written in terms of $P(\underline{r})$ and $S(\underline{r})$ as a fourth and fifth order pair of coupled

equations. Richards (1971) shows that if the scaling factor, f(r), is chosen such that

$$\left(\frac{\lambda + \mu}{\lambda + 2\mu}\right) \frac{f'}{f} = \frac{\rho'}{\rho} + \frac{2\mu'}{\lambda + 2\mu} \quad ,$$

where λ and μ are Lame parameters and the prime indicates differentiation with respect to radius, and if the source potential is of the form

$$D = \frac{\delta(r-r_o)\ \delta(\theta-0_+)\ e^{-i\omega t}}{2\pi r^2 \sin\theta} \quad , \quad F = 0 \quad , \quad E = 0$$

then the following relations between P and S are both sufficient and necessary for high frequency decoupling of the P and S potentials in the spheroidal equations of motion:

$$\frac{\rho D}{\lambda + 2\mu} + \nabla^2 P + \frac{\rho\omega^2}{\lambda + 2\mu} P = 0(1)\cdot P \qquad (1.9a)$$

and

$$S = 0(\omega^{-2})\cdot P \qquad (1.9b)$$

Richards shows that as a consequence of (1.9b)

$$\nabla^2 S + \frac{\rho\omega^2}{\mu} S = 0 \tag{1.10}$$

Noting that $\nabla^2 P = 0(\omega^2)P$, we see that the right hand side of (1.9a) is two orders down in frequency with respect to the left hand side. Thus for sufficiently high frequencies, (1.9a) can be written

$$\nabla^2 P + \frac{\rho\omega^2}{\lambda + 2\mu} P \simeq - \frac{\rho D}{\lambda + 2\mu} \tag{1.11}$$

where, by (1.9b), the S coupled potential is two orders down in frequency with respect to P. In other words, for an appropriate source of compressional energy and for sufficiently high frequencies, the P and S displacement potentials approximately satisfy the separate Helmholtz equations (1.10) and (1.11).

The toroidal, or SH, equation of motion is simply

$$\nabla^2 T + \frac{\rho\omega^2}{\mu} T + \varepsilon_T(r)\, T = - \frac{\rho}{\mu} E$$

for a steady source of the form

$$E = \frac{\delta(r-r_o)\ \delta(\theta)}{2\pi r^2 \sin\theta} e^{i\omega t} \quad , D = 0, \quad F = 0$$

where

$$\varepsilon_T = \frac{1}{4}\left(\frac{\mu'}{\mu}\right)^2 + \frac{1}{2}\frac{\mu''}{\mu} - \frac{2\mu'}{r\mu}$$

(Richards, 1971). If we assume that shear modulus gradients are small with respect to the SH wave number so that

$$|\varepsilon_T| << \left|\frac{\rho\omega^2}{\mu}\right|$$

then the torsional potential satisfies a Helmholtz equation as well

$$\nabla^2 T + \frac{\rho\omega^2}{\mu} T = -\frac{\rho}{\mu} E \qquad (1.12)$$

Note that the assumption of small shear modulus gradients is analogous to the assumption of small density gradients made in obtaining the Helmholtz representation for acoustic motion (1.5).

The displacement potential representation for a vertically heterogeneous Cartesian system are similar to those for a spherical system. In particular, the displacement and source vectors are represented at the point $\underline{r} = (x,y,z)$ by

$$\underline{U}(\underline{r}) = \left[f \quad (z)\right]^{-1} \left\{ \text{grad} \left(\frac{f(z)}{[\rho(z)]^{\frac{1}{2}}} P(\underline{r}) \right) + \text{curl curl} \left(0,0, \frac{f(z)}{[\rho(z)]^{\frac{1}{2}}} S(\underline{r}) \right) \right\}$$

$$+ \text{curl} \left(0,0, [\ \mu(z)\ ]^{-\frac{1}{2}} T(\underline{r}) \right) \tag{1.13}$$

and

$$\underline{\mathcal{E}} = f^{-1} \left\{ \text{grad} \left(\frac{f}{\rho^{\frac{1}{2}}} D \right) + \text{curl curl} \left(0,0, \frac{f}{\rho^{\frac{1}{2}}} F \right) \right\}$$

$$+ \text{curl} \left(0,0,\mu^{-\frac{1}{2}} E \right) \tag{1.14}$$

These potentials decouple at high frequencies in the same manner as those in the spherical system. Equations (1.9a,b) and (1.10) apply to both systems.

Richards (1971) points out that the commonly chosen potential representation for P-SV motion

$$\underline{U} = \text{grad } \Phi + \text{curl curl } (0,0,X) \tag{1.15}$$

where Φ and X are assumed to satisfy

$$\nabla^2\Phi + \frac{\rho(z)\ \omega^2}{\lambda(z) + 2\mu(z)} \Phi = 0 \ , \quad \nabla^2 X + \frac{\rho(z)\ \omega^2}{\mu(z)} X = 0 \tag{1.16}$$

does not lead to decoupled equations in Φ and X at high frequencies except in the special case of constant density. Thus, if we are to allow for the effects of a variable density, the potential representations (1.7) or (1.13) must be used.

2. Earth-flattening transformation for the Helmholtz equation and a point source

Earth-flattening approximations have been used for some time in making corrections for the earth's curvature in radio-wave propagation problems (see Budden, 1960). More recently, Kovach and Anderson (1962) and Anderson and Toksoz (1963) have introduced an earth-flattening transformation for Love waves that involves transforming radially symmetric, isotropic shells into flat, vertically inhomogeneous, anisotropic layers. Biswas and Knopoff (1970) have modified this transformation such that SH wave motion in a flat, vertically inhomogeneous isotropic problem can be transformed exactly to SH motion in a spherical radially inhomogeneous, isotropic earth. Somewhat earlier, Sato (1968) independently developed an exact earth-flattening transformation for SH motion. These exact earth-flattening transformations apply only to homogeneous equations (no source), and are thus most useful for surface wave and normal mode problems. Analogous exact transformations for Rayleigh waves (P-SV motion) have not been considered. One might expect that such a transformation cannot be made exactly since the velocity gradients that serve to map spherical to plane geometries would introduce spurious P-SV coupling.

In this section an earth-flattening transformation is introduced that will allow body wave solutions from a point source in a spherical

earth to be expressed in terms of solutions to analogous point source problems in a flat geometry. This transformation will be developed for the inhomogeneous Helmholtz equation to take advantage of the potential representations presented in the preceding section. The transformation involving the point source (and a spherical wave front) will be approximate; however, in the process of its derivation we will obtain an exact earth-flattening transformation for the homogeneous (no source) Helmholtz equation. This in turn, will be an exact transformation for acoustic and SH motion in homogeneous spherical media (although it will be approximate if the media properties vary with radius in accordance with the small density- and shear modulus-gradient assumption made in obtaining (1.5) and (1.10)). It will also, of course, be an approximate transformation for P and SV motion because of the decoupling assumption made in obtaining (1.9).

Consider a spherically symmetric medium that is homogeneous for $r > a$ and radially heterogeneous for $r < a$ and in which the scalar field, ψ, satisfies the Helmholtz equation. If a point source is located in the homogeneous medium at $r = r_o$ ($r_o > a$) and $\theta = 0_+$, the field, ψ, will be given by

$$\nabla^2\psi + \begin{pmatrix} k_o^2 \\ \\ k^2 \end{pmatrix} \psi = \begin{pmatrix} \dfrac{-\delta(r-r_o)\quad \delta(\theta-0_+)}{2\pi r^2 \sin\theta} \\ \\ 0 \end{pmatrix} \begin{matrix} r > a \\ \\ r < a \end{matrix} \qquad (2.1)$$

where k_o = const and $k = k(r)$ (see Figure 1). The general solution to (2.1) in $r > a$ will be

$$\psi = \psi_o + \psi_p \tag{2.2}$$

where ψ_o is the solution to the homogeneous equation, which includes the effects of both a boundary at $r = a$ and the underlying heterogeneous medium in a reflection coefficient, and ψ_p is a particular solution to the inhomogeneous equation.

An appropriate solution to (2.1) is the infinite space Green's function, or

$$\psi_p = \frac{e^{ikR}}{R} \tag{2.3}$$

where R is the straight line distance between the source at $\underline{r} = (r_o, 0_+)$ and any point $\underline{r} = (r,\theta)$. Using equations (10.1.45) and (10.1.46) in Abramowitz and Stegun (1964), the particular solution can be represented as

$$\psi_p = ik_o \sum_{\ell=0}^{\infty}{}' (2\ell + 1) \begin{bmatrix} j_\ell(kr)\, h_\ell^{(1)}(kr_o) \\ j_\ell(kr_o)\, h_\ell^{(1)}(kr) \end{bmatrix} P_\ell(\cos\theta); \quad \begin{matrix} r \leq r_o \\ r > r_o \end{matrix} \tag{2.4}$$

where j_ℓ and $h_\ell^{(1)}$ are spherical Bessel and Hankel functions and P_ℓ is a Legendre polynomial.

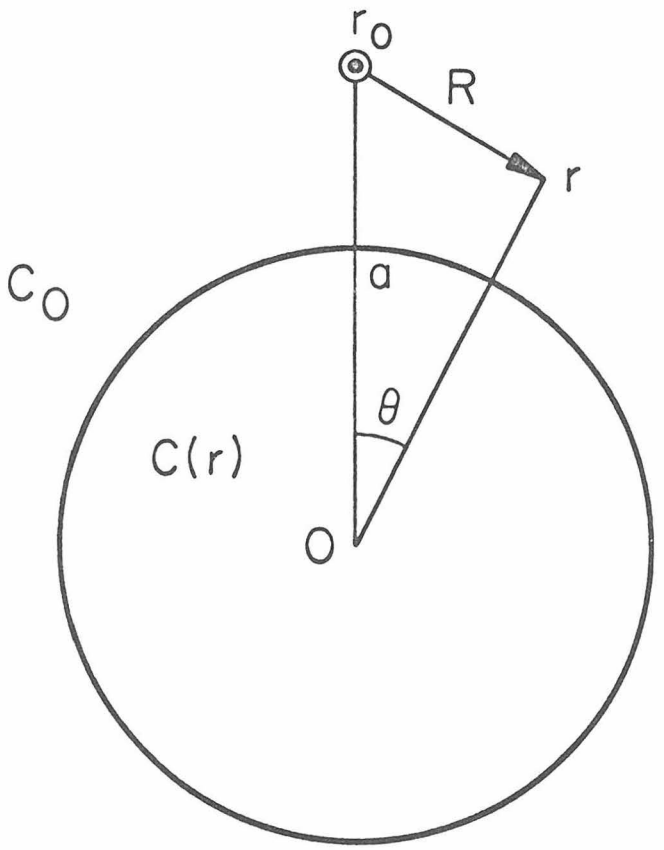

Figure 1

We apply a Legendre transform to (2.1), where the Legendre transform pair is defined by

$$\hat{\psi}_\ell = \int_0^\pi \psi P_\ell(\cos\theta)\,\sin\theta\,d\theta$$

$$\psi = \sum_{\ell=0}^{\infty} \left(\ell + \frac{1}{2}\right) \hat{\psi}_\ell P_\ell(\cos\theta), \tag{2.5}$$

and obtain

$$\frac{d^2\hat{\psi}_\ell}{dr^2} + \frac{2}{r}\frac{d\hat{\psi}_\ell}{dr} + \left(k^2 - \frac{\ell(\ell+1)}{r^2}\right)\hat{\psi}_\ell = \begin{pmatrix} \dfrac{-\delta(r-r_o)}{2\pi r^2} \\ \\ 0 \end{pmatrix} \tag{2.6}$$

Our aim is to rearrange the homogeneous part of (2.6) into a form that can be identified with the analogous differential equation in z for a cylindrical system $\underline{r} = (\rho,\theta,z)$

$$\frac{d^2\phi}{dz^2} + \left(k_f^2 - \kappa^2\right)\phi = 0 \tag{2.7}$$

To accomplish this we first transform the independent variable in (2.6) according to

$$-z = a\,\ln(a/r), \tag{2.8}$$

which gives

$$\frac{d^2\hat{\psi}_\ell}{dz^2} + \frac{r}{a}\frac{d\hat{\psi}_\ell}{dz} + \left(k^2 \left(\frac{r}{a}\right)^2 - \frac{\ell(\ell+1)}{a^2} \right) \hat{\psi}_\ell = 0 \qquad (2.9)$$

and then transform the dependent variable according to

$$\hat{\psi}_\ell = \phi_\ell \left(\frac{a}{r}\right)^{1/2} = \phi_\ell \cdot e^{-z/2a} \qquad (2.10)$$

to get

$$\frac{d^2\phi_\ell}{dz^2} + \left[k^2 \left(\frac{r}{a}\right)^2 - \frac{\ell(\ell+1) + 1/4}{a^2} \right] \phi_\ell = 0 \qquad (2.11)$$

which is the desired result.

A direct comparison between (2.11) and (2.7) yields the following exact earth-flattening transformation for the homogeneous Helmholtz equation:

$$k_f = k\left(\frac{r}{a}\right)$$

$$\kappa^2 = \frac{\ell(\ell+1) + 1/4}{a^2} \qquad (2.12)$$

with

$$r = a\, e^{z/a}$$

$$\phi = \sqrt{\frac{r}{a}}\, \psi$$

where k_f and k are the flat and spherical wave numbers respectively. Note in particular that the expression in the brackets multiplying ϕ_ℓ in (2.11) is the radial (vertical) wave number in the spherical case. Thus we identify κ in (2.12) as the angular (horizontal) wave number, and from this we obtain the well known relation

$$\kappa a = \ell + 1/2.$$

The propagation velocity in the medium is given by $c = \omega/k$, thus

$$c_f = c_s e^{-z/a} \tag{2.13}$$

where c_f and c_s refer to the velocities in the flat and spherical systems respectively. If we are interested in the field in the vicinity of $r = a$, the transformation can be approximated by

$$\begin{aligned} c_f &\simeq c_s(1-z/a) \\ & \left| \frac{z}{a} \right| << 1 \\ r &\simeq a(1+z/a) \end{aligned} \tag{2.14}$$

These represent the earth-flattening approximations used by earlier workers (Budden, 1960).

The above development is similar to that of Biswas and Knopoff (1970) or Sato (1968) for their exact transformation of the homogeneous equation for SH motion, although the particular potential representation used results in minor differences in the transformation.

In making the above transformation, we have implicitly assumed that the properties of the medium vary smoothly with radius. If we allow a discontinuous jump in properties at some level, say r=a, it is necessary to consider how the continuity (boundary) conditions for this jump transform. To illustrate this we will compare the spherical and flat boundary conditions for SH waves under the above transformation.

Continuity of both displacement and stress are required across a welded boundary. For SH (or torsional) motion across a spherical boundary these conditions are

$$[U_\phi]_{a+} = [U_\phi]_{a-}$$

for displacement and

$$[\mu\ \varepsilon_{r\phi}]_{a+} = [\mu\ \varepsilon_{r\phi}]_{a-}$$

or

$$\left[\mu\left(\frac{\partial U_\phi}{\partial r} - \frac{U_\phi}{r}\right)\right]_{a+} = \left[\mu\left(\frac{\partial U_\phi}{\partial r} - \frac{U_\phi}{r}\right)\right]_{a-}$$

for stress. Using the displacement potential representation for SH motion in a spherical system given by the last term in (1.7) or

$$|\underline{U}| = U_\phi = -\frac{1}{r}\frac{\partial}{\partial\theta}\left(\frac{r}{\mu^{\frac{1}{2}}}T\right) \quad ,$$

the continuity conditions become

$$\frac{\partial}{\partial\theta}\left[\frac{T}{\mu^{\frac{1}{2}}}\right]_{a+} = \frac{\partial}{\partial\theta}\left[\frac{T}{\mu^{\frac{1}{2}}}\right]_{a-} \tag{2.15}$$

and

$$\left\{\mu\,\frac{\partial}{\partial\theta}\left[\frac{\partial}{\partial r}\left(\frac{T}{\mu^{\frac{1}{2}}}\right)-\frac{1}{r}\left(\frac{T}{\mu^{\frac{1}{2}}}\right)\right]\right\}_{a+} = \left\{\mu\,\frac{\partial}{\partial\theta}\left[\frac{\partial}{\partial r}\left(\frac{T}{\mu^{\frac{1}{2}}}\right)-\frac{1}{r}\left(\frac{T}{\mu^{\frac{1}{2}}}\right)\right]\right\}_{a-}$$

respectively. The potential, T, satisfies the Helmholtz equation (1.10), and its eigenfunctions in a spherical system are of the form

$$T_{\ell}(r,\theta) = \left(\ell+\frac{1}{2}\right)\hat{T}_{\ell}(r)\;P_{\ell}(\cos\theta)$$

where $\hat{T}_{\ell}(r)$ is the radial variable-separable solution. Putting this into the continuity conditions (3.15) we obtain

$$\left[\hat{T}/\mu^{\frac{1}{2}}\right]_{a+} = \left[\hat{T}/\mu^{\frac{1}{2}}\right]_{a-}$$

$$\left\{\mu\left[\frac{d}{dr}\left(\frac{\hat{T}}{\mu^{\frac{1}{2}}}\right)-\frac{1}{a}\left(\frac{\hat{T}}{\mu^{\frac{1}{2}}}\right)\right]\right\}_{a+} = \left\{\mu\left[\frac{d}{dr}\left(\frac{\hat{T}}{\mu^{\frac{1}{2}}}\right)-\frac{1}{a}\left(\frac{\hat{T}}{\mu^{\frac{1}{2}}}\right)\right]\right\}_{a+} \tag{2.16}$$

By (2.12), the mapping of $\hat{T}(r)$ into the flat potential, $\hat{T}_f(z)$, is given by

$$\hat{T}(r) = \left(\frac{a}{r}\right)^{1/2} \hat{T}_f(z)$$

$$\left(\frac{a}{r}\right)^{1/2} = e^{-z/2a}$$

and the derivative terms in the stress boundary condition assume the form

$$\frac{d}{dz}\left[\mu^{-1/2}\,\hat{T}_f(z)\,e^{-z/2a}\right]\frac{dz}{dr} = \left[\frac{\mu'}{\mu^{3/2}} + \mu^{-1/2}\left(\hat{T}_f' - \frac{\hat{T}_f}{2a}\right)\right]\left(\frac{a}{r}\right)^{3/2}$$

where the primes indicate differentiation with respect to z. Accordingly, the exact boundary conditions in a spherical system map into

$$\left[\mu^{-1/2}\,\hat{T}_f\right]_{0+} = \left[\mu^{-1/2}\,\hat{T}_f\right]_{0-} \tag{2.17}$$

$$\left[\frac{\mu'}{\mu^{1/2}} - \mu^{1/2}\left(\hat{T}_f' - \frac{3T_f}{2a}\right)\right]_{0+} = \left[\frac{\mu'}{\mu^{1/2}} - \mu^{1/2}\left(\hat{T}_f' - \frac{3T_f}{2a}\right)\right]_{0-}$$

On the other hand, the analogous continuity conditions for a flat boundary are

$$[U_\phi]_{0+} = [U_\phi]_{0-}$$

for displacement (ϕ represents the angular coordinate in a cylindrical

system or the x coordinate in a Cartesian system), and

$$\left\{ \mu \left[\frac{\partial}{\partial \rho} \left(\frac{\partial}{\partial z} U_\phi \right) \right] \right\}_{0+} = \left\{ \mu \left[\frac{\partial}{\partial \rho} \left(\frac{\partial}{\partial z} U_\phi \right) \right] \right\}_{0-}$$

for stress (ρ represents the radial or x coordinate in cylindrical and Cartesian systems respectively). In this case, T_p, is the displacement potential for a plane system given by the last term in (1.11), or

$$|\underline{U}| = U_\phi = - \frac{\partial}{\partial \rho} \frac{T_p}{\mu^{\frac{1}{2}}}$$

and the boundary conditions become

$$\frac{\partial}{\partial \rho} \left(\frac{T_p}{\mu^{\frac{1}{2}}} \right)_{0+} = \frac{\partial}{\partial \rho} \left(\frac{T_p}{\mu^{\frac{1}{2}}} \right)_{0-}$$

$$\left\{ \mu \frac{\partial}{\partial \rho} \left[\frac{\partial}{\partial z} \left(\frac{T_p}{\mu^{\frac{1}{2}}} \right) \right] \right\}_{0+} = \left\{ \mu \frac{\partial}{\partial \rho} \left[\frac{\partial}{\partial z} \left(\frac{T_p}{\mu^{\frac{1}{2}}} \right) \right] \right\}_{0-}$$

Again, the potential, T_p, satisfies the Helmholtz equation, and its eigenfunctions in a cylindrical system, for example, are

$$T_p = \hat{T}_p(z) \; J_o(\kappa \rho)$$

Thus, the above continuity conditions become

$$\left[\mu^{-\frac{1}{2}} \hat{T}_p \right]_{0+} = \left[\mu^{-\frac{1}{2}} \hat{T}_p \right]$$

and

$$\left\{ \mu \frac{d}{dz} \left(\frac{\hat{T}_p}{\mu^{\frac{1}{2}}} \right) \right\}_{0+} = \left\{ \mu \frac{d}{dz} \left(\frac{\hat{T}_p}{\mu^{\frac{1}{2}}} \right) \right\}$$

or, expressed in a form similar to (2.17)

$$\left[\mu^{-\frac{1}{2}} \hat{T}_p \right]_{0+} = \left[\mu^{-\frac{1}{2}} \hat{T}_p \right]_{0-}$$

$$\left[\frac{\mu'}{\mu^{\frac{1}{2}}} - \mu^{\frac{1}{2}} \hat{T}_p' \right]_{0+} = \left[\frac{\mu'}{\mu^{\frac{1}{2}}} - \mu^{\frac{1}{2}} \hat{T}_p' \right]_{0-} \qquad (2.18)$$

where, again, the primes indicate differentiation with respect to z. Comparing (2.18) with (2.17), we see that the boundary conditions for the spherical boundary expressed in terms of the earth-flattening transformation are identical to the boundary conditions for the plane boundary except for the term of order $(\hat{T}_f/a)$ subtracted from $\hat{T}_f'$ in the stress condition in the spherical case. Because the two potentials $\hat{T}_p$ and $\hat{T}_f$ enter the boundary conditions in the same way, it is possible to use the plane boundary formulation and potential representation to obtain solutions for the spherical boundary problem, although for an exact spherical solution, conditions (2.17) must be used rather than the natural conditions for a plane boundary, (2.18).

However, we note that

$$\hat{T}'_f = 0\left(\frac{1}{\eta}\,\hat{T}_f\right)$$

where η is a vertical wave number. Thus the additional term in the spherical stress boundary condition (2.17) is of order $(\eta a)^{-1}$ with respect to $\hat{T}'_f$. In most crustal and upper mantle body wave problems $|(\eta a)^{-1}|$ will be small (provided we avoid grazing angles of incidence), and the natural plane boundary conditions (2.18) can be used with little loss in accuracy. Similar remarks hold for the transformation of boundary conditions for the decoupled P-SV system and for acoustic motion.

We now turn to the development of an approximate earth-flattening transformation when the point source of spherical waves is inlcuded. To keep the algebra to a minimum, we will use the

acoustic case as an example; the elastic SH and P-SV cases follow in a parallel manner.

The model is shown in Figure 1 and the Legendre transformed field equations are given by (2.6). Here we take ψ to be the pressure potential defined by (1.4). By comparing the form of the sum in the inverse Legendre transform with the series representation of the particular solution (2.4), we see that

$$\hat{\psi}_{p\ell} = 2ik_o \begin{cases} j_\ell(k_o r)\, h_\ell^{(1)}(k_o r_o) & r \leq r_o \\ j_\ell(k_o r_o)\, h_\ell^{(1)}(k_o r) & r > r_o \end{cases} \tag{2.19}$$

Accordingly, the general form of the solution can be written as

$$\hat{\psi}_{o\ell} = 2ik_o\, h_\ell^{(1)}(k_o r_o)\, j_\ell(k_o r) + A\, h_\ell^{(1)}(k_o r), \quad a < r \leq r_o$$

$$\psi_{1\ell} = B\left(\frac{a}{r}\right)^{1/2} \Phi_\ell \quad , \qquad r < a \tag{2.20}$$

The first term in the solution for $r > a$ is the source field (2.19), and the second term is the field scattered by the sphere. In the second term, A is a constant determined by the boundary conditions and $h_\ell^{(1)}(k_o r)$ is a solution to (2.6) representing outward traveling waves for $r >> 1$. We represent the solution to the field inside the sphere, which may be radially heterogeneous, in terms of the exact earth-flattening transformation (2.11) and (2.12).

The boundary conditions at the surface of the sphere, r = a, require continuity of pressure and the normal component of particle velocity for an acoustic field, or

$$\left[\rho_o^{\frac{1}{2}}\,\hat{\psi}_{0\ell}\right]_{a+} = \left[\rho_1^{\frac{1}{2}}\,\hat{\psi}_{1\ell}\right]_{a-}$$

$$\left[\rho_o^{-1}\,\frac{d}{dr}\left(\rho_o^{\frac{1}{2}}\,\hat{\psi}_{0\ell}\right)\right]_{a+} = \left[\rho_1^{-1}\,\frac{d}{dr}\left(\rho_1^{\frac{1}{2}}\,\hat{\psi}_{1\ell}\right)\right]_{a-} \tag{2.21}$$

Putting (2.20) into these boundary conditions gives

$$\begin{bmatrix} \rho_o^{\frac{1}{2}}\,h_\ell^{(1)}(k_o r) & -\rho_1^{\frac{1}{2}}\left(\frac{a}{r}\right)^{\frac{1}{2}}\,\Phi_\ell \\ \rho_o^{-\frac{1}{2}}\,\frac{d}{dr}\,h_\ell^{(1)}(k_o r) & -\rho_1^{-1}\,\frac{d}{dr}\left[\rho_1^{\frac{1}{2}}\left(\frac{a}{r}\right)^{\frac{1}{2}}\,\Phi_\ell\right] \end{bmatrix} \begin{bmatrix} A \\ B \end{bmatrix} = -S \begin{bmatrix} \rho_o^{\frac{1}{2}}\,j_\ell(k_o r) \\ \rho_o^{-\frac{1}{2}}\,\frac{d}{dr}\,j_\ell(k_o r) \end{bmatrix}$$

where $S = 2ik_o\,h_\ell^{(1)}(k_o r_o)$. Solving this system for A we obtain

$$A = ik_o h_\ell^{(1)}(k_o r_o)\;\frac{j_\ell(k_o a)}{h_\ell^{(1)}(k_o a)}\;V\,, \tag{2.22}$$

where V can be regarded as a generalized spherical reflection coefficient given by

$$V = \left[\frac{\rho_o^{\frac{1}{2}} \rho_1^{-1} \frac{d}{dr}\left[\left(\rho_1 \frac{a}{r}\right)^{\frac{1}{2}} \Phi_\ell \right] - \left(\frac{\rho_\perp}{\rho_o}\right)^{\frac{1}{2}} \Phi_\ell k_o \frac{j_\ell'(k_o r)}{j_\ell(k_o r)}}{\rho_o^{\frac{1}{2}} \rho_1^{-1} \frac{d}{dr}\left[\left(\rho_1 \frac{a}{r}\right)^{\frac{1}{2}} \Phi_\ell \right] + \left(\frac{\rho_\perp}{\rho_o}\right)^{\frac{1}{2}} \Phi_\ell k_o \frac{h_\ell^{(1)'}(k_o r)}{h_\ell^{(1)}(k_o r)}} \right]_{r=a}$$

The expression for the spectral amplitude and phase of the external field can now be obtained by applying the inverse Legendre transform (2.5) to $\hat{\psi}_{0\ell}$ in (2.20) with A given by (2.22). Thus it is necessary to sum the series

$$\psi_o = \frac{1}{2} \sum_{\ell=0}^{\infty} (2\ell+1)\, \hat{\psi}_{0\ell}\, P_\ell(\cos\theta)$$

This series is known to converge slowly for large $\ell = ka^{-\frac{1}{2}}$, which is just the range of interest for body wave studies. The standard way around this problem is to convert the sum into an integral using the Watson transform (see, for example, Bremmer, 1949; Scholte, 1956; Chapman, 1969; or Gilbert and Helmberger, 1971). Accordingly, we obtain

$$\psi_o = \frac{1}{2i} \int_c \frac{\nu d\nu}{\cos(\nu\pi)}\, \hat{\psi}_o(\nu)\, P_{\nu-\frac{1}{2}}\left[\cos(\pi-\theta)\right] \qquad (2.23)$$

where $\nu = ka = \ell + 1/2$, $\hat{\psi}_o(\nu) = \hat{\psi}_{0\ell}$, and the contour, c, is shown in Figure 2. The integrand in (2.23) is odd since $\hat{\psi}_o(\nu) = \hat{\psi}_o(-\nu)$

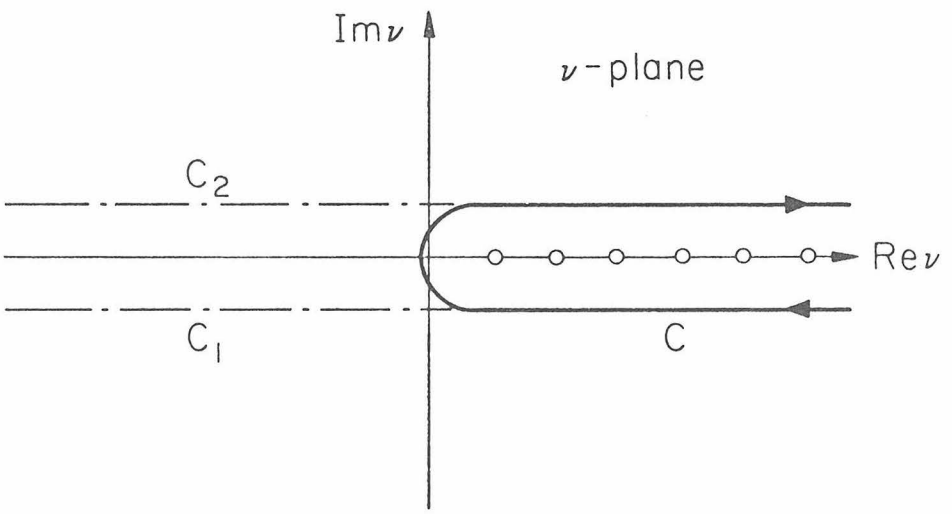

Figure 2

and $P_{\nu-\frac{1}{2}}(\mu) = P_{-\nu-\frac{1}{2}}(\mu)$ so that the path, c, can be transformed into c_1 or c_2 as shown in Figure 2.

At this stage we decompose the integrand in (2.23) into terms that can more readily be given a physical interpretation. Using the identity

$$j_\ell(k_o r) = \frac{1}{2}\left[h_\ell^{(1)}(k_o r) + h_\ell^{(2)}(k_o r)\right] , \tag{2.24}$$

the spherical Bessel function in the source term can be separated into spherical Hankel functions representing outgoing and ingoing traveling waves. Physically, of course, we are only interested in the incoming waves from the source. Introducing this separation into $\hat{\psi}_o(\nu)$ as it appears in (2.23), we obtain

$$\psi_o(\nu) = ik_o h^{(1)}_{\nu-\frac{1}{2}}(k_o r_o)\left[h^{(1)}_{\nu-\frac{1}{2}}(k_o r) + h^{(2)}_{\nu-\frac{1}{2}}(k_o r)\right] + \left(A_1 + A_2\right) h^{(1)}_{\nu-\frac{1}{2}}(k_o r)$$

where A_1 and A_2 are the parts of A associated with the outgoing and ingoing waves from the source. A little algebra shows that

$$\begin{aligned} A_1 &= - ik_o\, h^{(1)}_{\nu-\frac{1}{2}}(k_o r) \\ A_2 &= - ik_o\, h^{(1)}_{\nu-\frac{1}{2}}(k_o r_o)\ \frac{h^{(2)}_{\nu-\frac{1}{2}}(k_o a)}{h^{(1)}_{\nu-\frac{1}{2}}(k_o a)}\ V \end{aligned} \tag{2.25}$$

where

$$V = \frac{\rho_o^{\frac{1}{2}} \rho_1^{-1} \frac{d}{dr}\left[\left(\rho_1 \frac{a}{r}\right)^{\frac{1}{2}} \phi(\nu)\right]_{r=a} - \left(\rho_1/\rho_o\right)^{\frac{1}{2}} \phi(\nu)\, k_o\, h_2}{-\rho_o^{\frac{1}{2}} \rho_1^{-1} \frac{d}{dr}\left[\left(\rho_1 \frac{a}{r}\right)^{\frac{1}{2}} \phi(\nu)\right]_{r=a} + \left(\rho_1/\rho_o\right)^{\frac{1}{2}} \phi(\nu)\, k_o\, h_1} \qquad (2.26)$$

with

$$h_1 = \left[h^{(1)'}_{\nu-\frac{1}{2}}(k_o r) \Big/ h^{(1)}_{\nu-\frac{1}{2}}(k_o r) \right]_{r=a}$$

and

$$h_2 = \left[h^{(2)'}_{\nu-\frac{1}{2}}(k_o r) \Big/ h^{(2)}_{\nu-\frac{1}{2}}(k_o r) \right] .$$

Thus we see that the scattered field associated with the outgoing source field exactly cancels the outgoing source field (Phinney and Alexander, 1966), and we are left with

$$\psi_o(\nu) = ik_o\, h^{(1)}_{\nu-\frac{1}{2}}(k_o r_o) \left[h^{(2)}_{\nu-\frac{1}{2}}(k_o r) + \frac{h^{(2)}_{\nu-\frac{1}{2}}(k_o a)}{h^{(1)}_{\nu-\frac{1}{2}}(k_o a)}\, V\, h^{(1)}_{\nu-\frac{1}{2}}(k_o r) \right] \qquad (2.27)$$

in the integral (2.23).

Following Chapman (1969), we now introduce the representation for Legendre functions given by

$$P_{\nu-\frac{1}{2}}\left[\cos\ (\pi-\theta)\right] = -\ i\ e^{i\pi\nu}\ Q^{(1)}_{\nu-\frac{1}{2}}\ (\cos\ \theta) + i\ e^{-i\pi\nu}\ Q^{(2)}_{\nu-\frac{1}{2}}\ (\cos\ \theta) \tag{2.28}$$

where asymptotically

$$Q^{(1,2)}_{\nu-\frac{1}{2}}\ (\cos\ \theta) \sim \frac{e^{\mp i(\nu\theta-\pi/4)}}{(2\pi\nu\ \sin\ \theta)^{\frac{1}{2}}} \tag{2.29}$$

for $\varepsilon \leq \theta \leq \pi - \varepsilon$, $|\nu| >> 1$, and $|\nu|\ \varepsilon >> 1$ (Nussenzveig, 1965). Substituting (2.28) together with the expansion

$$\left[\cos\ (\nu\pi)\right]^{-1} = 2e^{\pm i\nu\pi} \sum_{h=0}^{\infty} (-1)^n\ e^{\pm 2i\pi\nu n}$$

into the integral (2.23), we obtain

$$\psi_o(\nu) = \sum_{n=0}^{\infty}\left[\int_{c_2}(-1)^n\hat{\psi}_o(\nu)\ Q^{(1)}_{\nu-\frac{1}{2}}\ (\cos\ \theta)\ e^{i2\pi\nu n}\ \nu d\nu\right.$$

$$\left. -\int_{c_1}(-1)^n\ \hat{\psi}_o(\nu)\ Q^{(1)}_{\nu-\frac{1}{2}}\ (\cos\ \theta)\ e^{-i2\pi\nu n}\ \nu d\nu\ \right]$$

From the asymptotic representation of $Q^{(1,2)}_{\nu-\frac{1}{2}}$ it is evident that the nth term in the first integral represents waves having traveled around the earth n times in the $+\theta$ direction, while the corresponding, term in the second series represents waves having made n circuits in the $-\theta$ direction. Thus direct body waves propagating in the $+\theta$ direction are represented by the first integral with n = 0, or

$$\psi_o(\nu) = \int_{C_2} \hat{\psi}_o(\nu)\, Q^{(2)}_{\nu-\frac{1}{2}}(\cos\theta)\, \nu d\nu \qquad (2.30)$$

It now remains to be shown that this direct body wave integral reduces to the form of a Weyl integral for a point source and flat geometry for the case of body waves in the crust and upper mantle. To show this we introduce the asymptotic forms for spherical Hankel functions given by Nussenzeig (1965).

$$h^{(1)}_\ell(\rho) \sim \rho^{-\frac{1}{2}} (\rho^2-\nu^2)^{-\frac{1}{4}} e^{i\chi(\rho)}$$
$$h^{(2)}_\ell(\rho) \sim \rho^{-\frac{1}{2}} (\rho^2-\nu^2)^{-\frac{1}{4}} e^{-i\chi(\rho)} \qquad (2.31)$$

where

$$\chi(\rho) = (\rho^2-\nu^2)^{\frac{1}{2}} - \nu \cos^{-1}(\nu/\rho) - \pi/4$$

$$\nu = \ell + \frac{1}{2} \qquad \nu < \rho$$

The corresponding asymptotic forms of the derivatives are

$$h^{(1)'}_\ell(\rho) \sim i\left(1 - \frac{\nu^2}{\rho^2}\right)^{\frac{1}{2}} h^{(1)}_\ell(\rho)$$
$$h^{(2)'}_\ell(\rho) \sim -i\left(1 - \frac{\nu^2}{\rho^2}\right)^{\frac{1}{2}} h^{(2)}_\ell(\rho) \qquad (2.32)$$

Thus the terms in h_1 and h_2 (2.26) become

$$\left[\frac{h^{(2)'}_{\nu-\frac{1}{2}}(k_o r)}{h^{(2)}_{\nu-\frac{1}{2}}(k_o r)} \right]_{r=a} \sim -i \left[1 - \frac{\kappa^2}{k_o^2} \right]^{\frac{1}{2}} = \frac{-i}{k_o} \left(k_o^2 - \kappa^2 \right)^{\frac{1}{2}}$$

and

$$\left[\frac{h^{(1)'}_{\nu-\frac{1}{2}}(k_o r)}{h^{(1)}_{\nu-\frac{1}{2}}(k_o r)} \right]_{r=a} \sim \frac{i}{k_o} \left(k_o^2 - \kappa_o^2 \right)^{\frac{1}{2}}$$

so that V becomes

$$V \sim \frac{\phi(\nu) \left[im\eta + \frac{\rho_1'}{2\rho_1} - \frac{1}{2a} \right] + \phi'(\nu)}{\phi(\nu) \left[im\eta - \frac{\rho_1'}{2\rho_1} + \frac{1}{2a} \right] - \phi'(\nu)} \qquad (2.33)$$

where the implicit differentiation with respect to r has been carried out, and the primes here indicate differentiation with respect to z; $m = \rho_1/\rho$, and $\eta = (k_o^2 - \kappa^2)^{\frac{1}{2}}$. This is precisely the form of the reflection coefficient obtained for plane waves incident on a plane boundary when the transformed spherical boundary conditions are used and $\phi(\nu)$ is a solution to (2.11) in the lower medium. If the natural boundary conditions for a plane boundary are used, the term (1/2a) will be absent, and V will be the true plane wave-plane boundary reflection coefficient (see 3.22, 3.23, 3.24). As indicated above, $\left| \frac{1}{2a} \right| << |\eta m|$ for crustal and upper mantle body waves, and the true plane wave reflection coefficient

can be used in (2.30) with no significant loss in accuracy.

Substituting the asymptotic forms (2.31) and (2.32) into the remaining terms in $\psi_o(\nu)$ (2.27) and using the linear approximation to the earth-flattening transformation (2.14), we obtain

$$\hat{\psi}_o(\nu) \sim \frac{1}{a^2} \left\{ \frac{e^{-i\eta(z-z_o)}}{i\eta} + i \frac{e^{i\eta(z+z_o)}}{\eta} \; V \right\} \tag{2.34}$$

which is the form of the source and reflected solutions for the flat problem (see (3.18) and (3.24)). Finally, substituting the asymptotic form for $Q^{(2)}_{\nu-\frac{1}{2}}$ (2.29) into the integral (2.30), we have

$$\psi_o \sim e^{-i\frac{\pi}{4}} \int_{C_1} \frac{\hat{\psi}_o(\eta)\, e^{i(\eta\varepsilon)}}{(2\pi\nu \sin\theta)^{\frac{1}{2}}} \nu d\nu \tag{2.35}$$

If we consider only the reflected field (the second term in (2.34)), then

$$\psi_r \sim e^{i\frac{\pi}{4}} \frac{k_o^{\frac{1}{2}}}{(2\pi a \sin\theta)^{\frac{1}{2}}} \int_{C_1} e^{ik_o[a\theta p + q(z+z_o)]} \; V \frac{p^{\frac{1}{2}}}{q} \; dP \tag{2.36}$$

where the variable of integration has been changed to sine of the angle of incidence, p, ($\kappa = k_o p$), and $q - \eta/k_o = (1 - p^2)^{\frac{1}{2}}$. If we restrict our considerations to relatively small angular distances, θ, such that

$$a\theta \sim \rho \;, \qquad a \sin\theta \sim \rho$$

where ρ is arc distance, then

$$\psi_r \sim e^{i\frac{\pi}{4}} \left(\frac{k_o}{2\pi\rho} \right)^{\frac{1}{2}} \int_{C_1} e^{ik_o[\rho P+(z+z_o)q]} V \frac{P^{\frac{1}{2}}}{q} \, dP \qquad (2.37)$$

This integral is identical with the asymptotic form of the Weyl integral for the reflected field from a point source over a plane boundary (see (3.28)).

Thus we can obtain approximate solutions for crustal and upper mantle point source body wave problems in a spherically symmetric earth by solving the analogous flat problem using 1) the velocity modified by (2.14), and 2) the modified Weyl integral (2.36) with angular distance replacing horizontal distance. The resulting approximate solutions will be valid under the conditions:

1) $|z/a| << 1$; the source and receiver distances from the boundary at r = a are small with respect to a.

2) $|\kappa a| << 1$ and $|\eta a| >> 1$; the wave length is much less than the radius, a, and both near normal and near grazing angles of incidence are avoided.

3) $\theta \geq \varepsilon$, where $|\kappa a| \varepsilon >> 1$; near normal angles of incidence are avoided. This is consistent with (2) above as well as the assumption made in taking the asymptotic form of the Bessel function for the flat case to obtain (3.28).

Note that this approximate solution can be extended to fairly

large angular distances (provided we don't approach grazing angles of incidence) if (2.36) is used. However, even if the tangent distance is used in (2.37), the solution will be valid up to angular distances of 10° for a 1% error in amplitude (i.e. for $\sin\theta \sim \theta$). Note also that, other than the assumptions made in section 1 to put the equations of motion in canonical form, there are no restrictions made on the velocity variation below the boundary at a. Thus, since the functions $[(a/r)^{\frac{1}{2}}\ \Phi(\nu)]$ in the reflection coefficient, V, are the exact spherical eigenfunctions for $r > a$, the integral (2.36) will give a valid approximation to the reflected field for $r < a$ with an arbitrary velocity variation for $r < a$. In practice, of course, we are limited by the number of velocity variations for which we can obtain exact solutions to (2.11) and (2.12).

3. Acoustic formulation.

In this section we will develop in detail asymptotic expressions for acoustic waves from a point source reflected at a plane boundary below which the acoustic velocity and density may either decrease or increase continuously with depth. Having obtained the solutions for the plane boundary, we will then apply the earth-flattening transformation presented in the last section to obtain analogous expressions for acoustic waves reflected from a spherical boundary. Finally, we will compare the asymptotic analytic solutions with those obtained by direct numerical integration of the inverse Hankel transform.

Reflection coefficient for a point source and plane boundary.-

Consider two fluid, inviscid half-spaces joined at $z = 0$ in a cylindrical coordinate system $\underline{r} = (\rho, \phi, z)$. Let the upper half-space ($z > 0$) be homogeneous in density and acoustic velocity, and in the lower half-space ($z < 0$) let both density and velocity vary in the z direction only. Our goal is to determine the acoustic field in the upper, homogeneous half-space due to a steady, isotropic point source of acoustic energy at $\underline{r} = (0, z_o)$. In this formulation the field is symmetric about the z axis and independent of the angular coordinate, ϕ.

The total acoustic field in the upper half space is a combination of direct energy from the source and energy reflected from the lower, heterogeneous half-space. We are interested in the latter portion of the field for the case in which both the velocity and density of the heterogeneous half-space are greater than in the homogeneous half-space at z = 0 and either decrease or increase smoothly away from the boundary in the negative z direction. The relation between the source and receiver to the boundary between the two half spaces is illustrated in Figure 3a.

For the problem described above, and illustrated in Figure 3a, the acoustic pressure potential field is described by

$$\nabla^2\Phi_1 + k_o^2\,\Phi_1 = -\frac{\delta(\rho)\,\delta(z-z_o)}{2\pi\rho} \qquad z > 0$$

$$\nabla^2\Phi_2 + k^2(z)\,\Phi_2 = 0 \qquad z < 0 \tag{3.1}$$

with the boundary conditions at z = 0

$$\rho_o^{\frac{1}{2}}\,\Phi_1 = \rho(z)^{\frac{1}{2}}\,\Phi_2; \quad \text{(continuity of pressure)} \tag{3.2}$$

$$\rho_o^{-1}\frac{\partial}{\partial z}\left(\rho_o^{\frac{1}{2}}\,\Phi_1\right) = \rho^{-1}(z)\,\frac{\partial}{\partial z}\left(\rho(z)^{\frac{1}{2}}\,\Phi_2\right); \quad \text{(continuity of vertical component of particle velocity)} \tag{3.3}$$

together with the appropriate radiation conditions.

The general solution to (3.1) for z > 0 is of the form

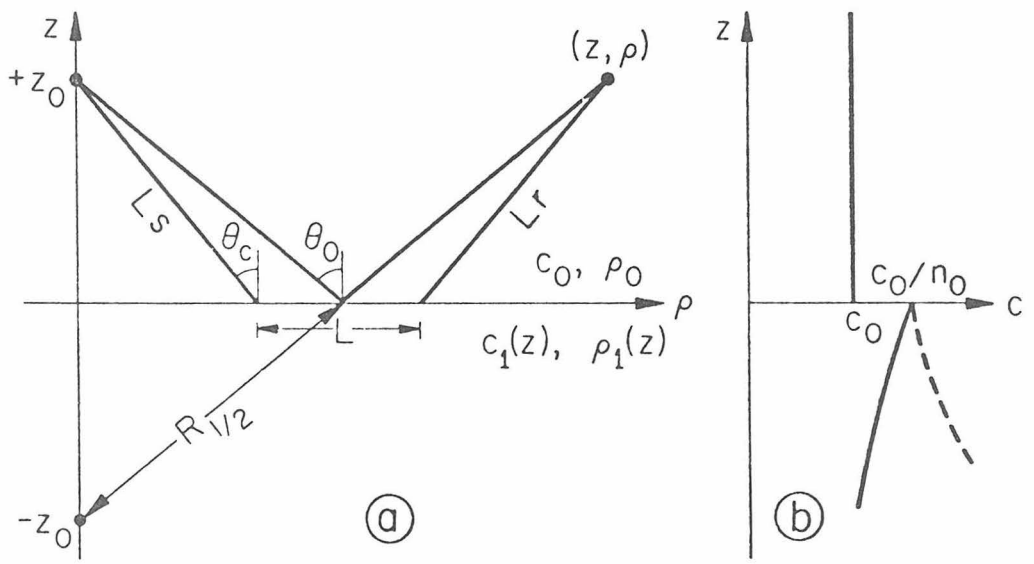

Figure 3

$$\Phi_1 = \Phi_p + \Phi_o$$

where Φ_p is the particular solution and Φ_o is the homogeneous solution. As was indicated in section 1, the particular solution for a spherically symmetric point source in a homogeneous medium is

$$\Phi_p = \frac{e^{ik_o R}}{R} \tag{3.4}$$

where $R = \left[\rho^2 + (z-z_o)^2 \right]^{\frac{1}{2}}$.

To obtain the solutions for Φ_o and Φ_2 we operate on the homogeneous form of (3.1) with a Hankel transform defined by

$$\hat{\Phi}(z,\kappa,\omega) = \int_0^\infty J_o(\kappa\rho)\ \Phi(z,\rho,\omega)\ \rho d\rho$$
$$\Phi(z,\rho,\omega) = \int_0^\infty J_o(\kappa\rho)\ \hat{\Phi}(z,\kappa,\omega)\ \kappa d\kappa. \tag{3.5}$$

to get

$$\frac{d^2\hat{\Phi}_o}{dz^2} + \left(k_o^2 - \kappa^2 \right) \hat{\Phi}_o = 0 \tag{3.6}$$

$$\frac{d^2\hat{\Phi}_2}{dz^2} + \left(k^2(z) - \kappa^2 \right) \hat{\Phi}_2 = 0. \tag{3.7}$$

Performing the same operation on the particular solution (3.4) gives

$$\hat{\Phi}_p = \frac{i}{\eta} \begin{cases} e^{i\eta(z-z_o)} & z > z_o \\ e^{i\eta(z_o-z)} & ; \quad 0 \geq z \leq z_o \end{cases} \tag{3.8}$$

where $\eta = (k_o^2 - \kappa^2)^{\frac{1}{2}}$ (Ewing et al., 1957).

Here we note that k_o is the magnitude of the wave number vector, $\underline{k}$, in the homogeneous medium and that κ and η are the ρ and z components of this vector, respectively. Thus $\kappa = k_o \sin\theta$ and $\eta = k_o \cos\theta$, where θ is the angle of incidence. We introduce the notation

$$\begin{aligned} p &= \sin\theta \\ q &= \cos\theta = [1-p^2]^{\frac{1}{2}} \end{aligned} \tag{3.9}$$

so that $\kappa = k_o p$ and $\eta = k_o q$, and we take the root of q defined by $\mathrm{Re}(q) > 0$ in the complex p-plane.

The solutions to (3.6) are familiar and can be written down immediately. They are

$$\hat{\Phi}_o = V e^{i\eta z} + U e^{-i\eta z} \tag{3.10}$$

where V and U are arbitrary functions of κ.

Exact solutions to (3.7) can be obtained only for a few specific functional variations of the wave number, k(z), or acoustic

velocity $c(z) = \omega/k(z)$. In general, these solutions will be rather complicated hypergeometric functions. However, even for some of the simplest velocity variations, the solutions will be expressed in terms of Bessel functions whose order is some function of the parameters defining the velocity variation. (See Bhattacharyo (1971) for a summary of solutions to equation (3.7) for a number of specific velocity laws.) As an example, solutions to (3.7) for a linear velocity gradient

$$c(z) = c_o\left(n_o^{-1} - \gamma z\right)$$

are of the form

$$\Phi \propto v^{\frac{1}{2}} \begin{cases} I_{\pm\nu}(v) \\ K_\nu(v) \end{cases}$$

where I_ν and K_ν are modified Bessel functions and

$$\nu = i\left(\varepsilon^2 - 1/4\right)^{\frac{1}{2}}$$

$$v = \varepsilon^{-1}\, p\left(n_o^{-1} - \gamma z\right)$$

$$\varepsilon = \gamma/k_o$$

(see Nakamura, 1964). Although the properties of these Bessel functions, as well as some of the more general hypergeometric functions, are well known, they are often inconvenient to work with in carrying out the analysis required to invert the Hankel transform.

Approximate solutions to (3.7) can be obtained by applying the classical WKB method (see Brekhovskikh (1960) for a detailed discussion of the WKB method applied to vertically heterogeneous wave propagation problems). WKB approximations corresond to ray-theoretical solutions, and they break down when the vertical wave number, $(k^2(z) - \kappa^2)$, approaches zero (e.g. in the vicinity of a turning point). Furthermore, special care must be taken to insure that the WKB solutions on either side of a turning point are properly matched. Because the dynamic properties of waves are often strongly influenced by velocity variations in the immediate vicinity of a turning point, WKB solutions have limited application in theoretical studies of wave amplitudes.

An approach intermediate to obtaining exact solutions or approximate WKB ray-theoretical solutions is described by Langer (1949). He has shown that solutions to linear, second-order differential equations of the form

$$\frac{d^2\omega}{dz^2} + \left[\lambda^2 p(z) + q(z,\lambda) \right] \omega = 0 \qquad (3.11)$$

can be represented in terms of one-third order Hankel functions (or Airy functions) plus terms of order $|\lambda^{-1}|$ provided that

1) $p(z)$ is analytic in a region R with a zero at $z = z_o$, and

2) $q(z,\lambda)$ is analytic in z for $z \supset R$.

(Here p and q are not related to the definition (3.9).) This approach has the double advantage that the resulting solutions are valid at the turning point and that Airy functions are particularly convenient to work in the analysis of wave propagation problems. A concise summary of the principal results obtained by Langer for complex values of λ is given in section 10.4 of Abramowitz and Stegun (1964).

For most cases of interest, $k^2(z)$ in (3.7) can be put in the form $k_o^2 p(z)$, where k_o represents the magnitude of the wave number at some reference point in the medium (at the boundary $z = 0$, for example). Accordingly, (3.7) has the form of (3.11) with λ (or k_o) real and positive in the case of a losless medium. Following the outline in Abramowitz and Stegun (1964), we introduce the transformation

$$\xi = \xi(z) \quad , \quad u = \left[p(z)/\xi(z) \right]^{1/4} \omega(z)$$

where ξ is defined by

$$\xi^{3/2} = \frac{3}{2} \int_{z_o}^{z} p^{1/2}(\zeta) \, d\zeta \quad ; \quad p(z_o) = 0.$$

This puts the original differential equation (3.11) into the form

$$\frac{d^2u}{d\xi^2} + \left[\lambda^2\xi + f(\xi,\lambda) \right] u = 0.$$

Solutions to this equation are such that

$$u = \begin{cases} Ai\left(-\lambda^{2/3}\xi\right)\left[1 + O(\lambda^{-1}) \right] \\ Bi\left(-\lambda^{2/3}\xi\right)\left[1 + O(\lambda^{-1}) \right] \end{cases}$$

uniformly on the bounded interval $a \leq \xi \leq b$ which includes the origin (ξ=0). Thus solutions to the original differential equation (3.11) are

$$\omega = \left[p(z)/\xi(z) \right]^{-\frac{1}{4}} \begin{cases} Ai\left(-\lambda^{2/3}\xi\right)\left[1 + O(\lambda^{-1}) \right] \\ Bi\left(-\lambda^{2/3}\right)\left[1 + O(\lambda^{-1}) \right] \end{cases}$$

where Ai and Bi are Airy functions.

Using this approach, it is possible to obtain high frequency ($k_o >> 1$) asymptotic solutions to (3.7) for velocity variations that either increase of decrease in a monotonic, but otherwise artibrary, way. (The monotonic requirement is imposed by the restriction that there be a single zero of p(z) in R.) Chekin (1964, 1965) used asymptotic solutions of this form (but expressed in terms of one-third order Hankel functions) in his analysis of the effects of

small velocity gradients on reflected waves.

In the present case, we will take the following specific form for the variation of acoustic velocity, c_1, and density, ρ_1, in the lower, heterogeneous half space:

$$\left.\begin{aligned} c_1(z) &= c_o\left(n_o^2 \pm \gamma z\right)^{-\frac{1}{2}} \\ \rho_1(z) &= \rho_o\left(n_o^2 \pm \gamma z\right)^{-\frac{1}{2}} \end{aligned}\right\} \qquad z \leq 0 \tag{3.12}$$

where c_o and ρ_o are the velocity and density in the upper, homogeneous half-space, $n_o = c_o/c_1(0)$ is the index of refraction at the boundary $z = 0$, and $\pm\gamma$ is a gradient parameter defining increasing (+) and decreasing (-) velocities with depth. These functions are illustrated in Figure 3b. This particular form for the velocity variation has the following advantages:

1) It results in exact solutions to the differential equation (3.7), and thus allows us to put off the need to work with asymptotic form until later stages in the analysis.

2) The exact solutions are Airy functions which are convenient to use in wave propagation problems, and as indicated above, they form the leading term in the high-frequency asymptotic solutions to (3.7) for more general velocity laws.

In other words, we are interested in the effects of small velocity gradients, and detailed differences in the exact form

of the velocity laws for small gradients will not change things significantly. Thus for convenience, we choose to use the velocity law that gives the leading term in the more general asymptotic solution as the exact solution. Finally, a third advantage is that the above velocity law is physically well suited to half-space problems; in particular, it does not result in negative acoustic velocities in the negative gradient case. The density was chosen to parallel the velocity law on the basis that this is a commonly observed relation in geophysical materials.

Note that the gradient parameter, γ, in (3.12) is essentially an index of refraction gradient with dimensions of km^{-1}. The corresponding velocity gradient for $|\gamma| << 1$ is given by

$$\gamma_c = \frac{c_o}{2\, n_o^3}\, \gamma \tag{3.12a}$$

where γ_c has dimensions km/sec/km, or sec^{-1}.

To obtain solutions to (3.7) for the velocity law given by (3.12), we note that the square of the wave number, k(z), is

$$k^2(z) = \begin{cases} k_o^2 = (\omega/c_o)^2 & z > 0 \\ k_o^2(n_o^2 \pm \gamma z) & z < 0 \end{cases} \tag{3.13}$$

So that (3.7) becomes

$$\frac{d^2\hat{\Phi}_2}{dz^2} + k_o^2 \left(n_o^2 - p^2 \pm \gamma z \right) \hat{\Phi}_2 = 0.$$

Transforming the independent variable by introducing

$$\zeta(z) = \varepsilon^{-2} \left(n_o^2 - p^2 \pm \gamma z \right); \quad \varepsilon = (\gamma/k_o)^{1/3} \tag{3.14}$$

then gives

$$\frac{d^2\hat{\Phi}_2}{d\zeta^2} + \zeta\hat{\Phi}_2 = 0 \tag{3.15}$$

This is Stokes' differential equation, and its solutions are Airy functions. Some of the properties of Airy functions useful for our purposes are described in Appendix I. Although numerically it is immaterial which independent pair of Airy functions are taken for solutions to (3.15), we will choose the following two sets for physical reasons

$$\hat{\Phi}_2 = T_- \, Ai\left(- \zeta e^{i\frac{2\pi}{3}} \right) + S_- \, Ai\left(- \zeta e^{-i\frac{2\pi}{3}} \right) \quad ; \quad \gamma < 0 \tag{3.16}$$

$$\hat{\Phi}_2 = T_+ \, Ai\,(-\zeta) + S_+ \, Bi\,(-\zeta) \quad ; \quad \gamma > 0 \tag{3.17}$$

In (3.16) the Airy functions associated with T and S represent down-going and up-going traveling waves, respectively, for large argument, while those in (3.17) represent standing waves when $\zeta > 0$

and exponentially decaying and growing waves when $\zeta < 0$ (see Appendix I). These asymptotic properties are obviously useful in choosing solutions that will satisfy the radiation conditions for the respective problems.

We now proceed with the evaluation of the arbitrary functions of κ in the solutions for $\hat{\Phi}_o$ (3.10) and $\hat{\Phi}_2$ (3.16) and (3.17) by first applying the appropriate radiation conditions at infinity and then the continuity conditions at the boundary z = 0.

In taking the Hankel transform of Φ_o and Φ_2, we implicitly made an assumption about the condition at infinity in the ρ direction. That is, if the integral in (3.5) is to be convergent, we must have

$$\rho^{\frac{1}{2}} \Phi(z,\rho,\omega) \to 0 \quad \text{as} \quad \rho \to \infty$$

Next, to preclude waves propagating downward from $z = +\infty$ (i.e. from above the source) we must set U = 0 in (3.10). This is an application of the Sommerfeld radiation condition, which in essence states that the wave at infinity from a point source in a homogeneous medium behaves like an outgoing spherical wave (Stoker, pg. 175,1957). The corresponding radiation condition at $z = -\infty$ in the heterogeneous medium is not so obvious. The difficulty arises because waves propagating in a heterogeneous medium are continually back-scattered by the local heterogeneities along the way.

In the case of the negative gradient ($\gamma < 0$ in (3.12)), the velocity gradient $dc(z)/dz \to 0$ as $z \to -\infty$, and we will assume that the analogous conditions applies. In particular, we assume that in the neighborhood of $z = -\infty$ the wave is downgoing, and we set $S_- = 0$ in (3.16). This assumption is justified by two arguments presented in Appendix II. Briefly stated, these arguments are:

1) The back-scattering due to the inhomogeneity becomes negligibly small as $z \to -\infty$ for the velocity variation (3.12) with $\gamma < 0$, and

2) The reflection coefficient obtained using this assumption is the leading term in the generalized ray expansion of the reflection coefficient for the case in which the inhomogeneous medium is bounded below by a second homogeneous medium, which in turn, extends to $-\infty$ (i.e. a case in which the radiation condition can be properly applied).

In the case of the positive gradient ($\gamma > 0$ in (3.1)) all of the waves entering the lower medium are turned around at a finite depth. Above the turning point depth there will be a system of down-going and upgoing traveling waves, which combine to form a standing wave in a steady state. Below the turning point depth the waves

behave exponentially. Thus, to insure a bounded solution as $z \to -\infty$, we assume exponentially decaying waves with depth and set $S_+ = 0$ in (3.17).

The loci of turning points for the negative and positive gradients can be determined by noting that the vertical wave number is zero at a turning point. Thus from (3.14) the loci of turning points in the p-z plane are given by

$$n_o^2 - p^2 \pm \gamma z = 0$$

This function is plotted in Figure 4 illustrating the effect of negative, positive, and zero gradients on the locus of turning points as a function of angle of incidence and depth. Also shown is the nature of the vertical wave field with respect to the locus of turning points and the boundary at $z = 0$ as defined by the radiation conditions assumed above.

Having applied the radiation conditions, the complete solutions are now in the form

$$\hat{\Phi}_1 = -\frac{e^{-i\eta(z-z_o)}}{i\eta} + v_{\mp} e^{i\eta z} \qquad z > 0 \qquad (3.18)$$

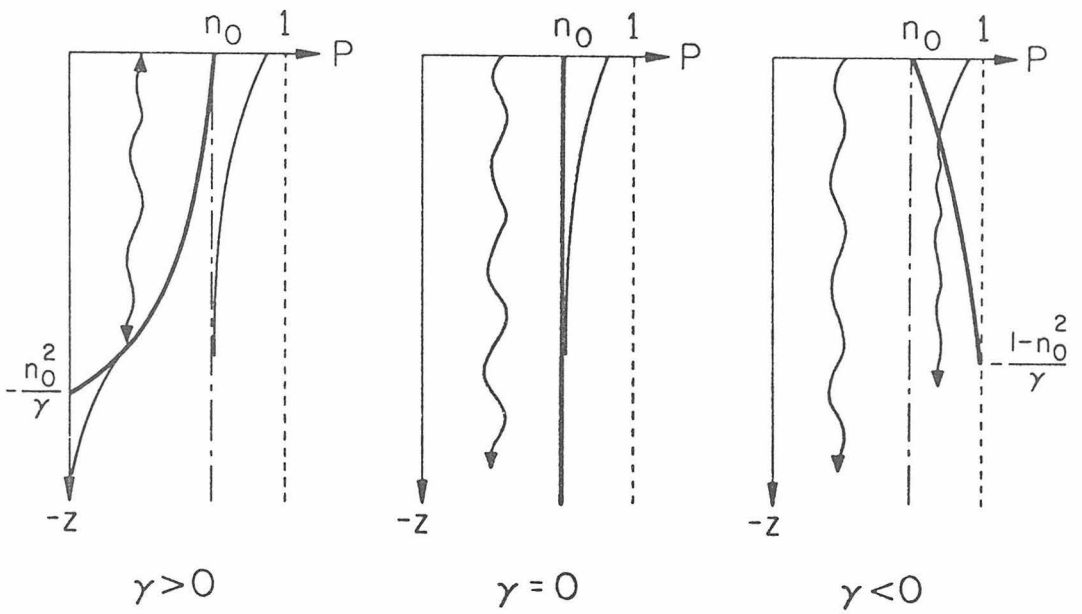
n_0
1
P
$-\frac{n_0^2}{\gamma}$
-z
$\gamma > 0$
n_0
1
P
-z
$\gamma = 0$
n_0
1
P
$-\frac{1-n_0^2}{\gamma}$
-z
$\gamma < 0$

Figure 4

$$\hat{\Phi}_2 = T_{\mp} \begin{pmatrix} A_i\left(-\zeta\, e^{i\frac{2\pi}{3}}\right) \\ A_i(-\zeta) \end{pmatrix} \quad ; \begin{pmatrix} \gamma < 0 \\ \gamma > 0 \end{pmatrix} z < 0 \tag{3.19}$$

when these equations are substituted into the Hankel transformed boundary conditions (3.2) and (3.3), the following systems are obtained for $\gamma < 0$

$$\begin{pmatrix} 1 & -m^{\frac{1}{2}} A_i^{(1)}(-\zeta_o) \\ i\eta & -m^{-\frac{1}{2}}\left[A_i^{(1)}(-\zeta_o)\,\frac{\gamma}{4n_o^3 m} + A_i^{(1)'}(-\zeta_o)\varepsilon^{-2\gamma}\, e^{i\frac{2\pi}{3}}\right] \end{pmatrix} \begin{pmatrix} v_- \\ T_- \end{pmatrix} = \begin{pmatrix} \frac{e^{i\eta z_o}}{i\eta} \\ -e^{i\eta z_o} \end{pmatrix} \tag{3.20}$$

and for $\gamma > 0$

$$\begin{pmatrix} 1 & -m^{\frac{1}{2}} A_i(-\zeta_o) \\ i\eta & m^{\frac{1}{2}}\left[A_i(-\zeta_o)\,\frac{\gamma}{4n_o^3 m} + A_i'(-\zeta_o)\,\varepsilon^{-2\gamma}\right] \end{pmatrix} \begin{pmatrix} v_+ \\ T_+ \end{pmatrix} = \begin{pmatrix} \frac{e^{i\eta z_o}}{i\eta} \\ -e^{i\eta z_o} \end{pmatrix} \tag{3.21}$$

where $m = \rho(0_-)/\rho_o$ (the density ratio at the boundary), and

$$\zeta_o = \varepsilon^{-2} (n_o^2 - p^2)$$

$$A_i^{(1)}(-\zeta_o) \equiv A_i\left(-\zeta_o\, e^{i\frac{2\pi}{3}}\right)$$

$$A_i^{(1)'}(-\zeta_o) \equiv A_i'\left(-\zeta_o\, e^{i\frac{2\pi}{3}}\right)$$

for brevity. Solving these systems for the reflection coefficients, $v_{\pm}$, gives for $\gamma < 0$

$$v_- = \frac{A_i^{(1)}(-\zeta_o)\left[iqm + \frac{\varepsilon^3}{4n_o^3 m} \right] + e^{i\frac{2\pi}{3}}\, \varepsilon\, A_i^{(1)'}(-\zeta_o)}{A_i^{(1)}(-\zeta_o)\left[iqm - \frac{\varepsilon^3}{4n_o^3 m} \right] - e^{i\frac{2\pi}{3}}\, \varepsilon\, A_i^{(1)'}(-\zeta_o)} \left[i\, \frac{e^{i\eta z_o}}{\eta} \right] \tag{3.22}$$

and for $\gamma > 0$

$$v_+ = \frac{A_i(-\zeta_o)\left[iqm - \frac{\varepsilon^3}{4n_o^3 m} \right] - \varepsilon\, A_i'(-\zeta_o)}{A_i(-\zeta_o)\left[iqm + \frac{\varepsilon^3}{4n_o^3 m} \right] + \varepsilon\, A_i'(-\zeta_o)} \left[i\, \frac{e^{i\eta z_o}}{\eta} \right] \tag{3.23}$$

where v_- and v_+ are the spherical wave reflection coefficients for the negative and positive velocity and density gradients defined by (3.12) and with a point source at $\underline{r} = (0, z_o)$. The corresponding

plane wave reflection coefficients are identical to the above but without the factor $(e^{i\eta z_o}/i\eta)$. Thus

$$v_{\mp} = v_{p_{\mp}} \left[i \frac{e^{i\eta z_o}}{\eta} \right] \tag{3.24}$$

where $v_{p_{\mp}}$ are the plane-wave reflection coefficient for the negative and positive gradients, respectively.

The modulus and phase of the plane-wave reflection coefficient for the negative gradient case (v_{p_-}) are plotted in Figure 5 with $\varepsilon = (\gamma/k_o)^{1/3}$ as a parameter. Note that as ε becomes very small, the modulus and phase approach the limiting values for two homogeneous media. This can also be seen analytically by substituting the asymptotic forms of the Airy functions (Appendix I) into v_{p_-}. The result is

$$v_o = \frac{mq - \sqrt{n_o^2 - p^2}}{mq + \sqrt{n_o^2 - p^2}} \tag{3.25}$$

which is just the plane-wave reflection coefficient for two homogeneous media (Brekhovskikh, 1960).

The modulus of the plane-wave reflection coefficient for the positive gradient case (v_{p_+}) is unity. In other words, all of the energy entering the lower medium is eventually reflected into the upper, homogeneous half space, and the reflection coefficient can be expressed as

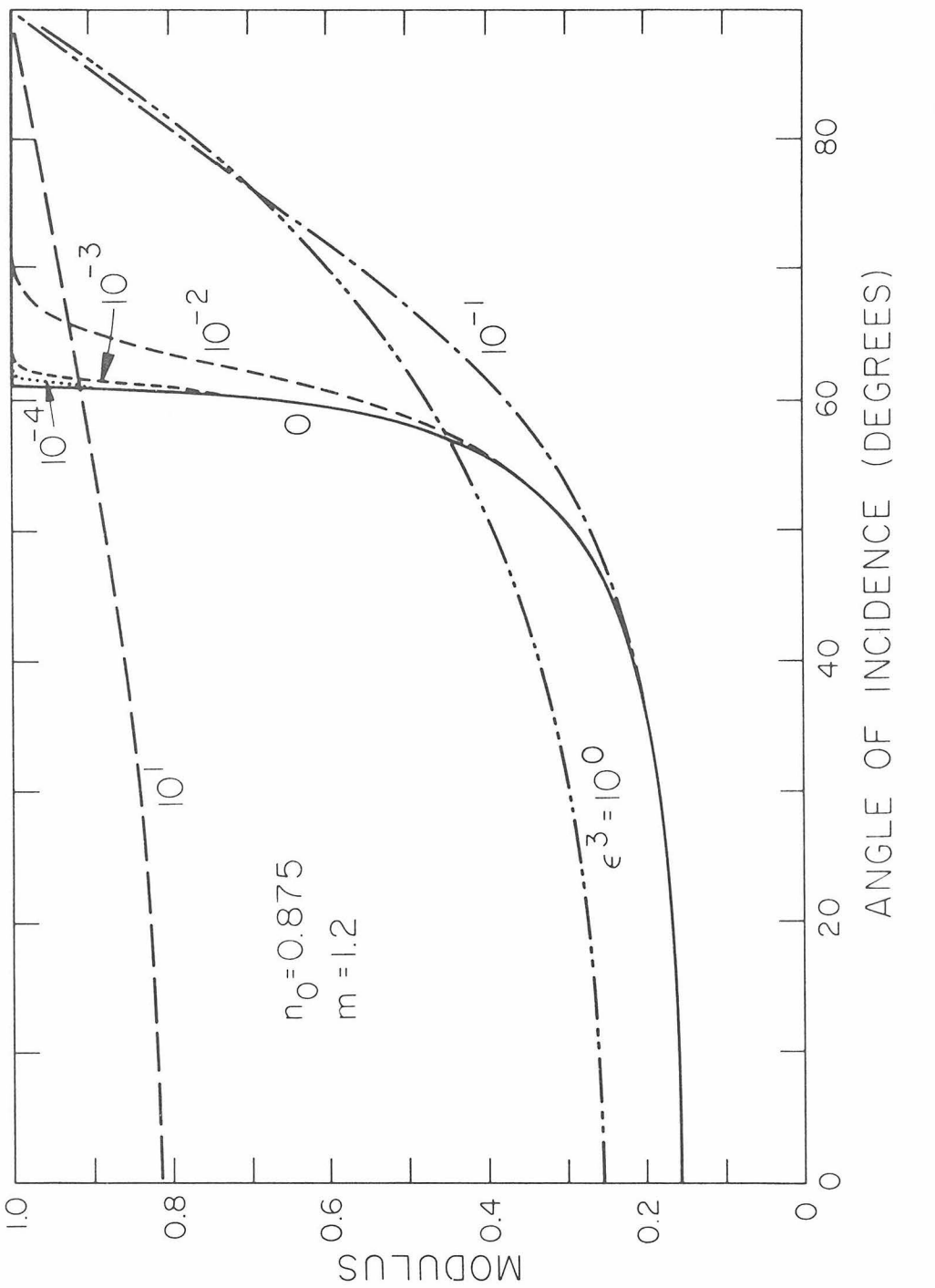
MODULUS
ANGLE OF INCIDENCE (DEGREES)
1.0
0.8
0.6
0.4
0.2
0
0
20
40
60
80
10^{-4}
10^{-3}
10^{-2}
10^{-1}
0
10^{1}
n_0=0.875
m = 1.2
$\epsilon^3 = 10^0$

Figure 5a

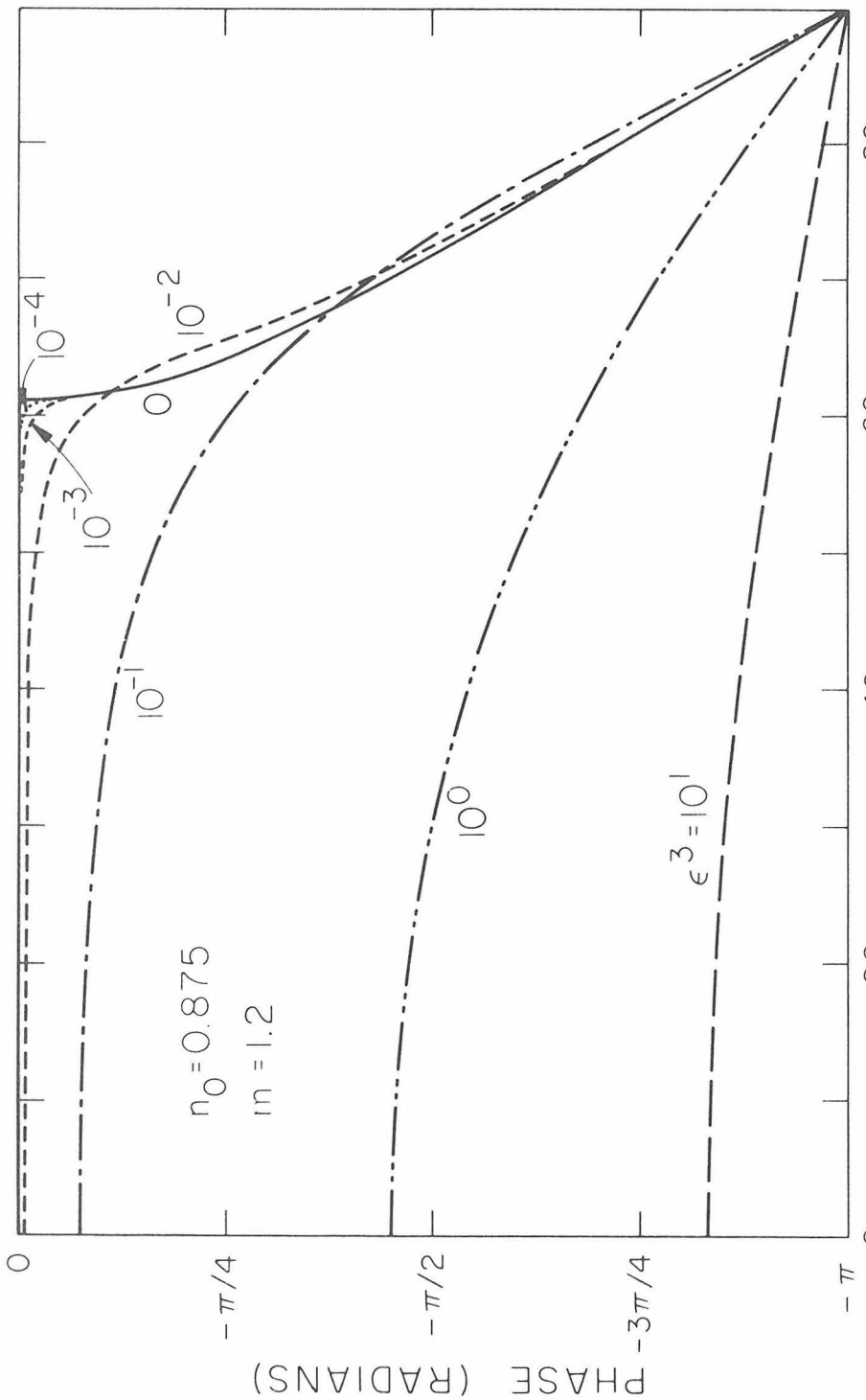
PHASE (RADIANS)
0
-π/4
-π/2
-3π/4
-π
ANGLE OF INCIDENCE (DEGREES)
0
20
40
60
80
10^{-4}
0
10^{-2}
10^{-3}
10^{-1}
10^{0}
$\epsilon^3=10^1$
$n_0=0.875$
$m = 1.2$

Figure 5b

$$v_{p_+} = \exp\left[i2 \tan^{-1}\left(\frac{\varepsilon}{\eta m} \frac{A_i'(-\zeta_o)}{A_i(-\zeta_o)} \right) \right]. \tag{3.26}$$

For $p > n_o$ (i.e. angle of incidence greater than critical), (2.23) also goes to the homogeneous reflection coefficient (3.25) when the asymptotic forms of the Airy functions are substituted. For $p < n_o$ the analogous limiting process is complicated by the diving wave phenomenon. We will consider this later.

The effect of the density gradient in the lower medium enters the reflection coefficients through the second term in the brackets multiplying $A_i^{(1)}(-\zeta_o)$ and $A_i(-\zeta_o)$ in (3.22) and (3.23) respectively. Under the assumption of small density gradients made in obtaining (1.5), we have

$$|mq| >> \varepsilon^3/4n_o^3 m$$

except when $q \sim 0$. Thus since $q = \cos\theta$, the density gradient in the lower medium has a negligible effect on the reflected wave except near grazing angles of incidence. We will neglect the effect of the density gradient in most of what follows.

Integral representation for the reflected field.-An expression describing the spectral amplitude and phase of the acoustic field in the homogeneous medium can now be obtained by taking the inverse Hankel transform of (3.18). Thus

$$\Phi_1 (\rho, z, \omega) = \frac{e^{ik_o R}}{R} + \int_0^\infty J_o(\kappa\rho)\, v_{\mp}(\kappa)\, e^{i\eta z}\, \kappa d\kappa$$

where $v_{\mp}(\kappa)$ is given by (3.22) or (3.23) for the negative and positive gradient cases, respectively. As indicated earlier, the first term on the right gives the direct field from the source, and the second term gives the field reflected from the lower inhomogeneous medium. We are primarily interested in the latter, which on changing the variable of integration to p (3.9), can be written as

$$\Phi_{\mp}(\rho, z, \omega) = i\, k_o \int_0^\infty J_o(k_o \rho p)\, v_{p_{\mp}}(p)\, e^{i\eta(z+z_o)}\, \frac{p}{q}\, dp$$

where we have introduced the plane wave reflection coefficients according to (3.24). Using the identities

$$J_o(u) = \frac{1}{2}\left[H_o^{(1)}(u) + H_o^{(2)}(u) \right]$$

and

$$H_o^{(2)}(u\, e^{-i\pi}) = H_o^{(2)}(-u) = - H_o^{(1)}(u)$$

(section 9.1, Abramowitz and Stegun, 1964) together with the fact that $v_{p_{\mp}}(-p) = v_{p_{\mp}}(p)$, the above integral can be rewritten as

$$\Phi_{\mp}(\rho, z, \omega) = \frac{ik_o}{2} \int_{-\infty}^{\infty} H_o^{(1)}(k_o \rho p)\, v_{p_{\mp}}(p)\, e^{i\eta(z+z_o)}\, \frac{pdp}{q} \qquad (3.27)$$

which is the desired integral representation for the reflected field.

The form of (3.27) is identical to equation (19.6) in Brekhovskikh (1960) for the field from a point source reflected at a plane boundary except that here the variable of integration is $p = \sin\theta$ instead of the angle of incidence, θ. This is a form of the Weyl integral representation, and as such, can be interpreted as a means of summing up plane waves to generate a spherical wave front (see Chapter 6 in Grant and West (1965)). Formally, the integral can be considered as an operator on the plane wave reflection coefficients, $v_p(p)$, for an arbitrary layered inhomogeneous half space to yield the reflected field in the overlying homogeneous half space containing a point source.

We are mainly interested in the reflected field from incident waves near the critical angle and beyond. These are the waves that are 'critically' refracted and give rise to the head wave. For most geophysical applications the product $(k_o \rho p)$ will be large for critical waves, and we can rewrite the Weyl integral (3.27) in an approximate form using the asymptotic form for large argument of $H_o^{(1)}(u)$, where

$$H_o^{(1)}(u) \sim \sqrt{\frac{2}{\pi u}}\, e^{i(u - \frac{\pi}{4})} \quad ; \quad |u| >> 1 \quad .$$

Thus

$$\Phi_{\mp}(\rho, z,\omega) \sim e^{i\frac{\pi}{4}} \left(\frac{k_o}{2\pi\rho} \right)^{\frac{1}{2}} \int_{-\infty}^{\infty} e^{ik_o [\rho p + q(z+z_o)]} v_{p_{\mp}}(p) \frac{p^{\frac{1}{2}}}{q} dp ,$$

or, since from Figure 1, $(z+z_o) = R_1 q_o$ and $\rho = R_1 p_o$

$$\Phi_{\mp}(\rho, z,\omega) \sim e^{i\frac{\pi}{4}} \sqrt{\frac{k}{2\pi\rho}} \int_{-\infty}^{\infty} e^{ik_o R_1 (qq_o + pp_o)} v_{p_{\mp}}(p) \frac{\sqrt{p}}{q} dp \qquad (3.28)$$

where $p_o = \sin \theta_o$, θ_o is then an angle of incidence for a wave reflected at the boundary and recorded at $\underline{r} = (\rho,z)$, and $q_o = \sqrt{1-p_o^2}$. The integral is now in a form that can be evaluated by saddle point methods for $(k_o R_1)$ large and real. We will consider the asymptotic evaluation of the integral (3.28) for the negative and positive velocity gradients separately.

Asymptotic evaluation of Weyl integral-negative gradient.-We consider the approximate integral (3.28) with the plane wave reflection coefficient v_{p-} given by (3.22) and (3.24). The integrand has branch points at $p = \pm 1$ associated with $q = \sqrt{1-p^2}$ and at $p = 0$ associated with $p^{\frac{1}{2}}$. We choose the branch cuts such that

$$-\frac{\pi}{2} < \arg(q) \leq \frac{\pi}{2}$$

$$-\frac{\pi}{2} < \arg(p^{\frac{1}{2}}) \leq \frac{\pi}{2}$$

on the upper Reimann sheet. The location of the branch cuts in the p-plane and the sign of the real and imaginary parts of the radical q on the upper sheet are shown in Figure (6a) together with the integration path. Note that the Airy functions in $v_{p-}(p)$ are entire functions in the finite complex p-plane.

The integral we are considering (3.28) is of the form

$$I = \int_{-\infty}^{\infty} e^{bf(p)} F(p)\, dp \tag{3.29}$$

where $b = k_o R_1$, $f(p) = i(qq_o + pp_o)$, and $F(p) = v_{p_-}(p) \frac{\sqrt{p}}{q}$. The saddle point for the integrand is determined by

$$\frac{df(p)}{dp} = p_o - \frac{pq_o}{q} = 0$$

or

$$p = p_o$$

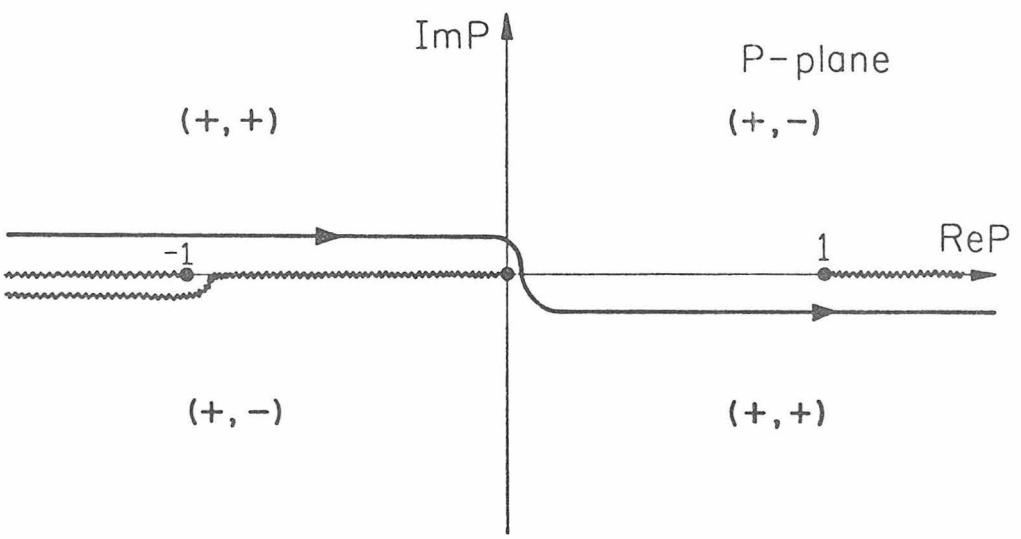

Figure 6a

In other words, the saddle point is on the real p axis and is equal to the sine of the angle of incidence, θ_o.

To determine the steepest descents path across the saddle point we put

$$f(p) = f(p_o) - s^2$$

where s is real and varies between $-\infty$ and ∞. This insures that $f(p)$ remains real and that the exponential term decreases rapidly along the integration path on either side of the saddle point. The appropriate path, Γ, is found to be given by

$$\mathrm{Re}\left\{ qq_o + pp_o \right\} = 1$$

As shown in Figure (6b), Γ approaches the saddle point along a path from the second quadrant in the p plane (asymptotic to a line at an angle of $(\pi - \tan\theta_o)$ from the origin as $s \to -\infty$) and crosses the saddle point at an angle of $3\pi/4$. Beyond $p = 1/p_o$, we can let the deformed path, Γ, coincide with the original path just below the cut along the positive real p axis since here $\mathrm{Im}(f(p)) > 0$ and $\exp\left[k_o R\, \acute{o}(p) \right]$ is decreasing exponentially.

According to the theory of the saddle point method, the only significant contributions to the integral come from the immediate vicinity of the saddle point plus any singularities passed over in deforming the integration path. As indicated in Figure (6b), the deformed contour, Γ, does not cross any of the branch cuts in

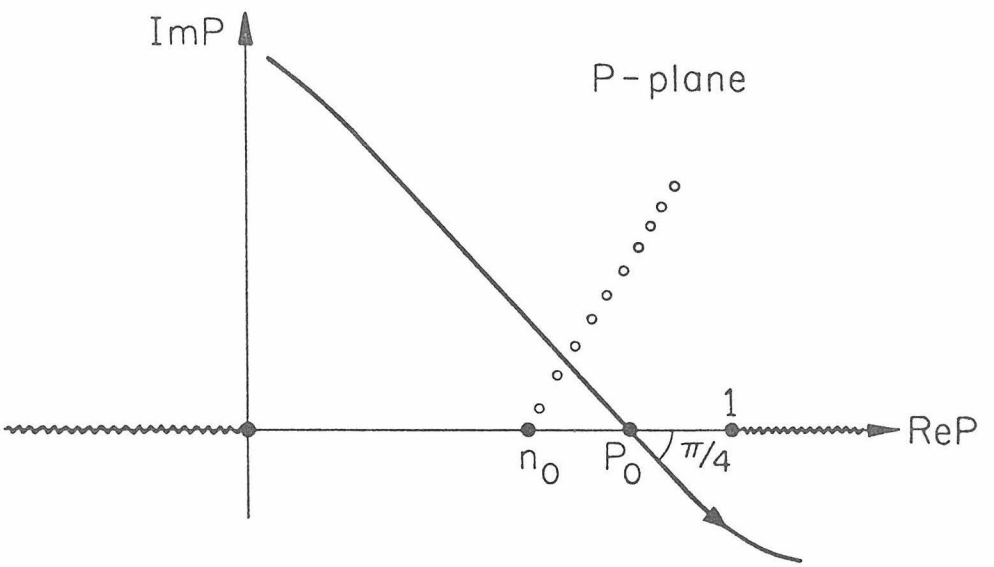

Figure 6b

the p-plane, but as will be shown below, it does cross a line of poles associated with the reflection coefficient $v_{p_-}(p)$ when $p_o > n_o$ (i.e. when the angle of incidence, θ_o, is greater than the critical angle θ_o). It will turn out that these poles give rise to the head wave while the saddle point gives rise to the wave reflected at the boundary z = 0. We will represent these "separate" contributions from the integral for the total reflected field, Φ_-, using the following notation

$$\Phi_- = \begin{cases} \Phi_{r_-} & p_o < n_o \\ \Phi_{r_-} + \Phi_{n_-} & p_o > n_o \end{cases} \qquad (3.30)$$

where Φ_{r-} is the saddle-point contribution giving the reflected wave and Φ_{n-} is the contribution from the poles giving the head wave. For near-critical angles of incidence ($p_o \sim n_o$) the phase difference between these "separate" contributions is small, and it is no longer meaningful to make a distinction between the two.

Having deformed the original integration path into the steepest descents path, (3.29) becomes

$$I = \int_{\Gamma} e^{bf(p)} F(p)\, dp$$

plus the sum of residues of any poles crossed. Methods for approximately evaluating the above integral over the steepest descents path are well known (see Brekhovskikh (1960) or Ewing et al. (1957)).

The result as given in Brekhovskikh (1960) is

$$I \simeq e^{bf(p)} \sqrt{\frac{\pi}{b}} \left[\psi(0) + \frac{1}{4b} \psi''(0) + \ldots \right] \tag{3.31}$$

where

$$\psi(0) = \left[- \frac{2}{f''} \right] F$$

$$\psi''(o) = \psi(0) \left[\frac{f'''}{(f'')} \quad \frac{F'}{F} + \frac{1}{4} \frac{f}{(f'')^2} - \frac{5}{12} \frac{(f''')^2}{(f'')^3} - \frac{F''}{Ff''} \right]$$

Substituting the appropriate variables into the above formula and multiplying by the leading factor in (3.28) thus gives

$$\Phi_{r-}(n,z,\omega) \simeq \frac{e^{ik_o R_1}}{R_1} \; v_{p_-}(p_o) \tag{3.32}$$

to first order. This expression is the geometrical ray theory approximation to the field reflected from the boundary at z = 0 for waves at an angle of incidence θ_o. It is valid as long as the source and receiver are not too close to the reflecting boundary, or as long as the angle of incidence is not near grazing. For these cases additional terms must be retained in (3.31). Equation (3.32) also breaks down near the critical angle, θ_c; here the saddle point and "head wave" poles interfere and require a more elaborate analysis.

We now turn to the problem of determining the singularities in the reflection coefficient, $v_{p_-}(p)$, and evaluating their contribution

to the integral expression for the reflected field. In what follows it will be convenient to introduce the notation

$$v_{p_-}(p) = N(p)/D(p)$$

where N(p) and D(p) are the numerator and denominator of the plane wave reflection coefficient (v_{p_-}).

As remarked above, the Airy functions in the reflection coefficient have no singularities in the p plane, and the branch cuts associated with $q = (1-p^2)^{\frac{1}{2}}$ have already been accounted for. Thus any singularities of $v_{p_-}(v)$ must be due to zeros of D(p). On purely physical grounds we would expect to find one or more zeros of D(p) in the vicinity of $p = n_o$, where n_o is the index of refraction ($c_o/c(o)$) at the boundary and is equal to the sine of the critical angle, θ_c. In other words, we expect the head wave to have a horizontal phase velocity close to $c_r = \omega/(k_o \sin \theta_c)$. Thus we begin by considering the properties of D(p) for small arguments of its Airy functions. For convenience in what follows we will refer to the region $|p-n_o| << 1$ as $\mathcal{R}$.

Expanding $\zeta_o(p)$ about $p = n_o$ gives

$$\zeta_o(p) = \varepsilon^{-2}\,(n_o^2-p^2) = \varepsilon^{-2}\left\{ - 2n_o(p-n_o) + 0\left[(p-n_o)^2\right]\right\} \quad ,$$

so that the arguments of the Airy functions are approximately given by

$$-\zeta_o e^{i\frac{2\pi}{3}} \simeq -2n_o \varepsilon^{-2}(n_o-p) e^{i\frac{2\pi}{3}} = -\tau$$

for $|n_o-p| << 1$. It is known that both $Ai(-\tau)$ and $Ai'(-\tau)$ have zeros on the positive real τ axis only (Abramowitz and Stegun, p. 450, 1964). Thus since

$$p \simeq n_o + \frac{\varepsilon^2\tau}{2n_o} e^{i\pi/3} \tag{3.33}$$

both $Ai(-\tau)$ and $Ai'(-\tau)$ will have their zeros along a line extending from $p = n_o$ at an angle of $\pi/3$ with the positive p axis in R.

Now from (3.22), we see that in R, D(p) has the form

$$D(p) = Ai(-\tau)\ O\left(\sqrt{1-n_o^2}\right) - Ai'(-\tau)\ O(\varepsilon).$$

Thus under the condition that

$$\left|Ai(-\tau)\ O\left(\sqrt{1-n_o^2}\right)\right|_{max} >> \left|Ai'(-\tau)\ O(\varepsilon)\right|_{max}$$

the zeros of D(p) will be given by the zeros of $Ai(-\tau)$ plus a small correction. The above condition will be maintained as long as

$$\left|\tau\right| >> \left|\frac{1-n_o^2}{\varepsilon^2}\right|. \tag{3.34}$$

An approximate analytic expression for the zeros of D(p) in

R can be obtained using the Newton-Raphson root-finding algorithm. Let a_j be the jth zero of $Ai(-\tau)$. Then the jth zero of $D(\tau)$, where $\tau = \tau(p)$, will approximately be given by

$$\tau_j \simeq a_j - \left[D(p)/D'(p) \right]_{\tau=a_j}$$

or, after performing the indicated differentiation,

$$\tau_j \simeq a_j + \frac{\varepsilon e^{i(2\pi/3)}}{imq_j} \tag{3.35}$$

where

$$q_j \simeq \left(1 - n_o^2 - \varepsilon^2 a_j e^{i(2\pi/3)} \right)^{\frac{1}{2}} \simeq (1-n_o^2)^{\frac{1}{2}}.$$

Putting (3.35) into (3.33), the location of the zeros of $D(p)$ is approximately given by

$$p_j \simeq n_o + \frac{\varepsilon^2 a_j}{2n_o} e^{i(\pi/3)}$$

Thus the poles of $v_{p_-}(p)$ lie approximately along a line extending from $p = n_o$ into the first quadrant of the p-plane at an angle of $\pi/3$ (see Figure 6a and 6b).

It now remains to evaluate the residues of the integrand for the poles of $D(p)$ crossed over in deforming the path of integration to the steepest descents path when the saddle point, p_o, is beyond

n_o (see Figure 6b). By the residue theorem

$$\Phi_{n-} = i\, e^{i(\pi/4)} \sqrt{\frac{2\pi k_o}{\rho}} \sum_{j=1}^{N} \text{Res}\left[F(\tau_j)\right]$$

where N is the number of poles crossed, $p(\tau)$ is given by (3.33) and

$$\text{Res}\left[F(\tau_j)\right] = \left\{ \frac{p^{\frac{1}{2}}}{q} \frac{N(\tau)}{D'(\tau)\frac{d\tau}{dp}} e^{ik_o R_1 (qq_o + pp_o)} \right\}_{\tau = \tau_j} \tag{3.36}$$

$$q(\tau) = \sqrt{1-n_o^2} - \frac{\varepsilon^2 \tau\, e^{i(\pi/3)}}{2\sqrt{1-n_o^2}}$$

$$D'(\tau) = Ai(-\tau)\left[imq'(\tau) - \tau\varepsilon e^{i(2\pi/3)} \right] - Ai'(-\tau)\left[imq(\tau) - \frac{\varepsilon^3}{4n_o^3 m} \right]$$

$$\frac{d\tau}{dp} = \frac{2n_o\, e^{-i(\pi/3)}}{\varepsilon^2} \tag{3.37}$$

Expanding $Ai(-\tau)$ about $\tau = a_j$, we have

$$Ai(-\tau) = Ai(-a_j) - Ai'(-a_j)(\tau - a_j) + \cdots$$

$$Ai(-\tau) \simeq Ai'(-a_j) \frac{\varepsilon e^{i(2\pi/3)}}{imq}$$

which together with the above gives

$$\left\{ \frac{p^{\frac{1}{2}}}{q} \frac{N(\tau)}{D'(\tau)\,\frac{d\tau}{dp}} \right\}_{\tau=\tau_j} \simeq \frac{-i\,\varepsilon^3}{\sqrt{n_o q_c^2 m}}$$

for $\varepsilon^2 a_j << |m^2 q^2|$. Putting (3.33) and (3.37) into the exponential term in (3.36) we have

$$\begin{aligned} k_o R_1 (pp_o + qq_o) &= k_o R_1 \left[p_o \left(n_o + \frac{\varepsilon^2 \tau\, e^{i\pi/3}}{2n_o} \right) \right. \\ &\quad \left. + q_o \left(\sqrt{1-n_o^2} - \frac{\varepsilon^2 \tau\, e^{i\pi/3}}{2\sqrt{1-n_o^2}} \right) + O(\varepsilon^4) \right] \\ &\simeq k_o R_1 \cos(\theta_c - \theta_o) \\ &\quad + k_o R_1 \frac{\varepsilon^2 \tau\, e^{i\pi/3}}{2n_o} - \left(\sin\theta_o - \tan\theta_c \cos\theta_o \right) \end{aligned}$$

or using the geometric relations shown in Figure (1),

$$k_o R_1 (pp_o + qq_o) \simeq \left[k_o (L_s + L_r) + k_1 L \right] + \frac{k_o L\, \varepsilon^2}{2n_o} \tau e^{i\frac{\pi}{3}} \qquad (3.38)$$

where L_s and L_r are the source-refractor and refractor-receiver

'ray' path lengths, L is the path length along the refractor, and k_1 is the wave number just below the boundary in the lower medium ($k_1 = n_o k_o$). Here we recognize the first term on the right as being the ray-theoretical phase of the head wave, ϕ_o, and the second term as a complex correction factor due to the velocity gradient.

Substituting for the remaining terms in (3.36) we obtain

$$\text{Res}\left[F(\tau_j)\right] \simeq -i\,\frac{\varepsilon^3}{m n_o^{\frac{1}{2}}(1-n_o^2)}\,\exp\left[i\left(\phi_o + k_o L\varepsilon^2\tau_j\, e^{i\frac{\pi}{3}}/(2n_o)\right)\right]$$

Thus

$$\Phi_{n-}(r,z,\omega) \simeq +\sqrt{\frac{2\pi k_o}{n_o \rho}}\,\frac{\varepsilon^3\, e^{i(\phi_o + \pi/4)}}{m(1-n_o^2)} \qquad (3.39)$$

$$\times \sum_{j=1}^{N} \exp\left[i\,\frac{k_o L\varepsilon^2\tau_j\, e^{i\frac{\pi}{3}}}{2n_o}\right]$$

which is an expression for the head wave spectral amplitude and phase for the model shown in Figure (1).

This expression can be recast into a simpler and more useful form for two limiting cases. We define the parameter, σ_-, to be

$$\sigma_{-} = - i\left(\frac{3\pi}{8}\right)^{2/3} \frac{k_o L\varepsilon^2}{2n_o} e^{i\pi/3} \tag{3.40}$$

and consider the cases for which $|\sigma|<<1$ and $|\sigma_{-}|>>1$.

In the first case ($|\sigma_{-}|<<1$) we attempt to sum the series in (3.30). Thus consider

$$S_N = \sum_{j=1}^{N} e^{-\sigma_{-}\tau_j} \quad . \tag{3.41}$$

To first order, the zeros of $Ai(-\tau)$, and thus the approximate zeros of $D(\tau)$, are given by

$$a_j \simeq \left[\frac{3\pi}{8} (4j - 1) \right]^{2/3}$$

(Abramowitz and Stegun, p. 450, 1964). Accordingly, we let $\tau_j = (4j - 1)^{2/3}$ in (3.41) where the factor $(3\pi/8)^{2/3}$ has been included in the definition of σ_{-}. Using the Euler-Maclaurin summation formula (Abramowitz and Stegun, p. 16, 1964),(3.41) can be rewritten as

$$S_N = \int_0^{N+1} e^{-\sigma_{-}\tau(x)} dx - \frac{1}{2}\left[f(0) + f(N) \right] + \frac{1}{12}\left[f'(N) + f'(0) \right] + \cdots \tag{3.42}$$

where j has been replaced by the continuous variable, x, in the integral and $f(x) = e^{-\sigma_- \tau(x)}$. To evaluate the integral in S_N we consider the limit as $N \to \infty$, in other words

$$I = \lim_{N\to\infty} \int_0^{N+1} e^{-\sigma_- \tau(x)} dx = \int_0^{\infty} e^{-\sigma_- \tau(x)} dx \tag{3.43}$$

Note that by (3.34), we must have

$$\lim_{N\to\infty} \left| \frac{1 - n_o^2}{(4N - 1)^{2/3}} \right| >> \varepsilon^2. \tag{3.44}$$

In other words, ε^2 must approach zero more rapidly than τ_N approaches infinity as $N \to \infty$.

Changing the variable of integration in (3.43) to

$$U = (4X - 1)^{2/3}$$

gives

$$I = \frac{3}{8} \int_1^{\infty} e^{-\sigma_- U} U^{1/2} dU$$

The integral is now in a form of the integral representation of an incomplete Gamma function (Abramowitz and Stegun, 6.5.10,

p. 262, 1964). Thus

$$I = \frac{3}{8}\,\sigma_-^{-3/2}\,\Gamma(3/2,\sigma_-) = \frac{3}{8}\,\sigma_-^{-3/2}\,\Gamma(3/2)\left[1 - \sigma_-^{3/2}\,\gamma^*(3/2,\sigma_-)\right]$$

where $\Gamma(3/2) = \frac{1}{2}\,\pi^{1/2}$ and

$$\gamma^*(3/2,\sigma_-) = e^{-\sigma_-}\sum_{n=0}^{\infty}\frac{\sigma_-^n}{\Gamma(3/2 + 1 + n)}\,, \qquad -\,|\sigma_-| < \infty$$

Recalling that $f(x) = e^{-\sigma\tau(x)}$ and $\tau(x) = (4x - 1)^{2/3}$, we have $f(o) = e^{-\sigma_-}$, $f'(o) = i\ 8/3\ e^{-\sigma}$, $\lim_{N\to\infty} f(N) = 0$, $\lim_{N\to\infty} f'(N) = 0$, etc., and (3.42) becomes

$$\lim_{N\to\infty} S_N = \sqrt{\frac{-2}{\pi k_o}}\,\frac{n_o^{3/2}\,e^{i\frac{\pi}{4}}}{L^{3/2}\gamma}$$

$$\times \left\{1 - \sigma_-^{3/2}\,e^{-\sigma_-}\left[\sum_{n=0}^{\infty}\frac{\sigma_-^n}{\Gamma(5/2 + n)} - g_-^{-1}\left(\frac{1}{2} - \frac{1}{6}\,\sigma_- + \cdots\right)\right]\right\}$$

where

$$g_- = \sqrt{\frac{2}{\pi k_o}} \left(\frac{n_o \sigma}{L} \right)^{3/2} \gamma^{-1} e^{i\pi/4}$$

Thus, in the limit as $\varepsilon^2 \to 0$, we can rewrite (3.39) in the form

$$\Phi_{n-} \simeq \left[\frac{+ 2in_o e^{i\phi_o}}{km(1-n_o^2)\, r^{1/2} L^{3/2}} \right] \times \left\{ 1 - \sigma_-^{3/2} e^{-\sigma_-} \left[\sum_{n=0}^{\infty} \frac{\sigma_-^n}{\Gamma(n/2 + n)} - g_-^{-1} \left(\frac{1}{2} + \frac{1}{6} \sigma_- + \cdots \right) \right] \right\} \tag{3.45}$$

Note that the leading term in the brackets is just the head wave potential for the case in which the lower medium is homogeneous (see Brekhoviskikh, 1960). This expression is valid in the limit of small ε, but at large distances from the critical point, many terms in the series must be included. At relatively small distance from the critical point, such that $|\sigma| << 1$, we have

$$\Phi_{n-} \approx \frac{2in_o e^{i\phi_o}}{km(1-n_o^2)\, \rho^{1/2} L^{3/2}} \left[1 - \sigma_-^{3/2} \right] \tag{3.46}$$

In the immediate vicinity of the critical point itself, (3.45) and (3.46) are invalid because of the interaction of the saddle point and head wave poles. However, because $L \ll 1$ and $|\sigma_-|$ becomes negligibly small as the critical point is approached, we expect that the theory previously worked out for waves reflected and refracted from a homogeneous medium in the vicinity of the critical point by Cerveny (1965) will be a good approximation to the inhomogeneous case as well.

To obtain an expression for (3.39) in the case $|\sigma_-| \gg 1$, it is convenient to separate the argument of the exponential terms under the summation sign into real and imaginary parts, where by (3.33) and (3.40)

$$\arg\left[\exp\right] = -\left(\frac{3\pi}{8}\right)^{-3/2} \sigma_-\left(a_j + i\,\frac{\varepsilon}{mq_i}\, e^{i\frac{2\pi}{3}}\right)$$

and where the first few a_j (zeros of $Ai(-\tau)$) are given on pg. 478 of Abramowitz and Stegun (1964) to be $a_1 = 2.338$, $a_2 = 4.008$, $a_3 = 5.521$, etc. Thus

$$\begin{pmatrix} \mathrm{Re} \\ \mathrm{Im} \end{pmatrix} \arg\left[\exp\right] = \begin{pmatrix} -\frac{\sqrt{3}}{4}\,\frac{k_o L\,\varepsilon^2}{n_o}\left[a_j - \varepsilon/(\sqrt{3}m\,\sqrt{1-n_o^2})\right] \\ \frac{k_o L\,\varepsilon^2}{4n_o}\left(a_j - \frac{\sqrt{3}}{4}\,\frac{\varepsilon}{m\sqrt{1-n_o^2}}\right) \end{pmatrix} \qquad (3.47)$$

Now because the real part of the exponential term is negative, the pole nearest the real p-axis (or the first term in the series in (3.39)) gives the largest contribution, and for $|\sigma_-| >> 1$, the contributions from the remaining poles will be negligible. Hence,

$$\Phi_{n-} \approx - \sqrt{\frac{2\pi k_o}{\rho}} \; \frac{\varepsilon^3 \, e^{i(\phi_o + \frac{\pi}{4})}}{m(1 - n_o^2)} \; \exp\left(i \, \frac{k_o L \, \varepsilon^2 \tau_i \, e^{i\pi/3}}{2n_o} \right) \tag{3.48}$$

for $|\sigma_-| >> |, \quad \sigma$

$$\Phi_{n-} \simeq - \sqrt{\frac{2\pi k_o}{\rho}} \; \frac{\varepsilon^3 \, e^{i(\phi_o + \delta_- + \pi/4)}}{m(1 - n_o^2)} \; \exp\left[- \frac{\sqrt{3}}{4} \, \frac{k_o L \varepsilon^2}{n_o} \left(a_1 \, \frac{\varepsilon}{\sqrt{3} m \sqrt{1-q^2}} \right) \right] \tag{3.49}$$

where $\delta_- = \mathrm{Im}\left[\arg\ (\exp)\right]$ in (3.47)

From the last expression, we see that at large distances from the critical point ($L >> 1$), the head wave spectral amplitude decays exponentially as $(\varepsilon^2 L)$. We also see that because of δ_-, there is an additional phase shift; furthermore, since δ_- is a function of the wave number k_o, the head wave is slightly dispersed by the negative velocity gradient. In particular, at large distance, the horizontal phase velocity of the head wave is approximately given by

$$c_{n-} \simeq c_o / \left[\sin(n_o + \delta_-) \right] .$$

Asymptotic evaluation of Weyl integral-positive gradient.-We now turn to the evaluation of (3.28) with the plane wave reflection coefficient for the positive gradient, v_{p+}, given by (3.23) and (3.24). The branch cuts for q and $p^{\frac{1}{2}}$ will be taken as defined for the negative gradient case (see Figure 6a). Evaluation of the saddle point and steepest descents contour for the reflected wave remains the same as in the negative gradient case. However, as we will see, poles of the reflection coefficient now lie just above the real p-axis in the interval $0 < p < n_o$ (see Figure 7). This simple change in the position of the poles results in a marked difference in both analyses and the nature of the reflected field. For angles of incidence greater than critical ($p_o > n_o$) we can make a distinction between 'separate' contributions to the total reflected field similar to (3.30) in the negative gradient case. That is

$$\Phi_+ = \Phi_{r+} + \Phi_{n+} \quad ; \quad p_o > n_o$$

where, as before, Φ_{r+} is the saddle point contribution giving the reflected wave and Φ_{n+} is the contribution from the poles giving the "refracted" waves. By the same argument leading to (3.31), the first-order saddle-point contribution yields the geometrical ray theory approximation for waves reflected at the boundary $z = 0$

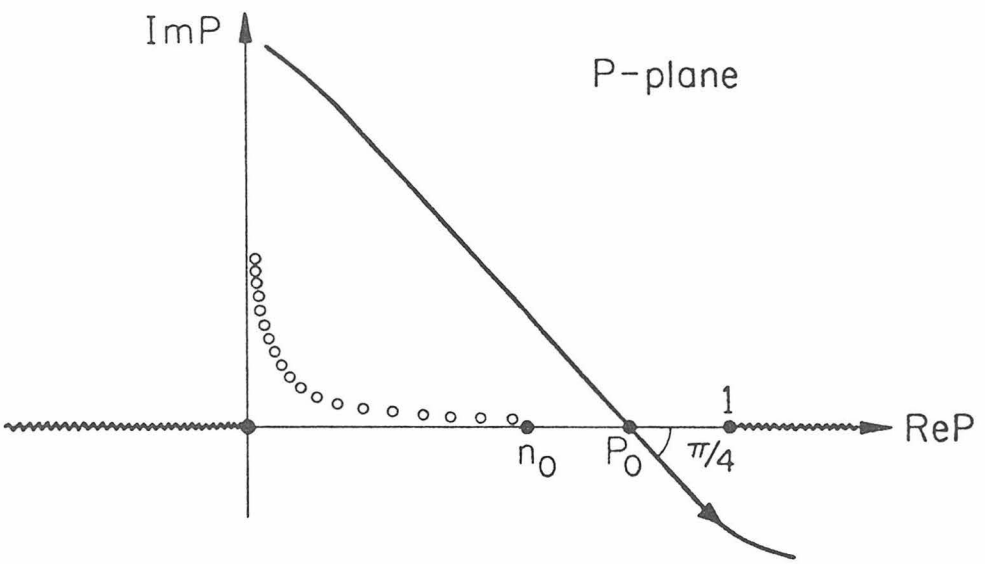

Figure 7

$$\Phi_{r+} \simeq \frac{e^{ik_o R_1}}{R_1} \; v_{p+}(p_o) \qquad ; \qquad p_o > n_o$$

For angles of incidence less that critical ($p_o < n_o$) the saddle point lies near the line of poles. To handle this case, we will modify our approach by expanding the reflection coefficient. In doing so, we will find that a similar separation of contributions can be made, i.e.

$$\Phi_+ = \Phi_{r+} + \Phi_d \qquad ; \quad p_o < n_o$$

where Φ_{r+} is again the saddle-point contribution giving the reflected wave, but where Φ_d is now a series of saddle points giving the diving wave contributions.

To determine the position of the poles of $v_{p+}(p)$, we proceed as before and define

$$v_{P+}(p) = \frac{N_+(p)}{D_+(p)}$$

By the same argument used in the negative gradient case, we expect the zeros of $D_+(p)$ to be near the zeros of $Ai(-\zeta_o)$ for $|p^2 - n_o^2| << 1$. Hence in this region, the zeros of $D_+(p)$ will be given by

$$\zeta_{o_j} \simeq a_j - \left[D(\zeta_o)/D'(\zeta_o) \right]_{\zeta_o = a_j}$$

where

$$D'(\zeta_o) = Ai(-\zeta_o)\left[iq'm + \varepsilon\zeta_o \right] + Ai'(-\zeta_o)\left[iqm + \frac{\varepsilon^3}{4n_o^2 m} \right] \qquad (3.50)$$

Accordingly, we find that

$$\zeta_{o_j} \simeq a_j - \left[\frac{\varepsilon Ai'(-\zeta_{o_j})}{-Ai(-\zeta_{o_j})\left[iqm + \frac{\varepsilon^3}{4n_o^2 m} \right]} \right]$$

or

$$\zeta_{o_j} \simeq a_j - \frac{i\varepsilon}{qm} \qquad (3.51)$$

Expanding p about $\zeta = 0$, we get

$$p = n_o - \frac{\varepsilon^2 \zeta_o}{2n_o} - \frac{\varepsilon^4 \zeta_o^2}{8n_o^3} + O(\varepsilon^6 \zeta_o^3) \qquad (3.52)$$

Recalling that $q = \sqrt{1 - p^2}$, we also get

$$q = q_c + \frac{\varepsilon^2 \zeta_o}{2q_c} - \frac{\varepsilon^4 \zeta_o^2}{8q_c^3} + O(\varepsilon^6 \zeta_o^3) \qquad (3.53)$$

where, as before $q_c = \sqrt{1 - n_o^2}$. (In the negative gradient case only the first two terms in the expansions for p and q were kept, however in this case, it is necessary to carry the next term in the expansions to insure the convergence when we attempt to sum the residues of the poles.) Putting (3.50) into (3.51), gives for the location of the poles in the p-plane as

$$p_j \simeq \left[n_o - \frac{\varepsilon^2}{2n_o} a_j \right] + i \frac{\varepsilon}{q_m} \left[1 + \frac{\varepsilon^4 a_j}{8n_o^3} \right] .$$

Thus, as indicated above, the poles lie just above the real p axis for $p < n_o$. Furthermore, they move gradually away from the real axis (in a positive imaginary direction) as a_j gets larger and $p \to 0$. This is just the behavior required for convergence indicated above. It turns out that for $|p^2 - n_o^2| > 1$, the position of the poles is dominated by the $Ai'(-\zeta_o)$ term in $D_+(\zeta_o)$, and the poles move up the positive imaginary axis.

The contribution to the integral by the poles crossed in deforming the original contour along the real p axis into the steepest descents path is given by

$$\Phi_{n+} = i\, e^{i\frac{\pi}{4}} \sqrt{\frac{2\pi k_o}{\rho}} \sum_{j=0}^{N} \operatorname{Res}\left[F(\zeta_{o_j}) \right] \qquad (3.54)$$

where

$$\text{Res}\left[F(\zeta_{o_j})\right] = \left\{ \frac{p^{\frac{1}{2}}}{q} \quad \frac{N_+(\zeta_o)}{D'_+(\zeta_o)\,\frac{d\zeta_o}{dp}} \quad e^{\psi} \right\}_{\zeta_o=\zeta_{o_j}} \tag{3.55}$$

and

$$\psi = ik_o R_1 (pp_o + qq_o)$$

Note that when the angle of incidence is greater than critical so that the saddle point, p_o, is greater than n_o, all of the poles in the interval $0 < p < n_o$ will have been crossed as shown in Figure 7. Expanding $Ai(-\zeta_o)$ about ζ_{o_j} and using relations (3.50) through (3.53) gives

$$\left\{ \frac{p^{\frac{1}{2}}}{q} \quad \frac{N_+(\zeta_o)}{D'_+(\zeta_o)\,\frac{d\zeta_o}{dp}} \right\}_{\zeta_o=\zeta_{o_j}} \simeq \frac{i\,\varepsilon^3}{\sqrt{r_o q_o^2 m}} \tag{3.56}$$

for $\varepsilon << q$ and $|n_o^2 - p^2| << |q^2 m^2|$. Substituting (3.52) and (3.53) into the expression for ψ gives

$$\psi \simeq i\,\phi_o - \frac{k_o L\varepsilon^3}{2n_o q_c m} - i\,\frac{k_o\varepsilon^2}{2n_o}\left[\left(L - \frac{i\,\ell\varepsilon^3}{n_o^2 q_o m}\right)a_j + \frac{\varepsilon^2\ell}{2n_o^2}\,a_j\right] \qquad (3.57)$$

where

$$\phi_o = k_o R_1(q_o q_c + p_o n_o) = k_o(L_s + L_r) + k_1 L$$

(the ray-theoretical head-wave phase)

$$\ell = \left(L + \frac{\rho_c}{q_c^3}\right)$$

and

ρ_c = critical distance.

(See the geometric relations illustrated in Figure 4.) Thus (3.54) becomes

$$\Phi_{n+} \simeq -\,e^{i\frac{\pi}{4}}\sqrt{\frac{2\pi k_o}{\rho n_o}}\;\frac{\varepsilon^3 e^{\,i\phi_o - \frac{k_o L\varepsilon^3}{2n_o q_r m}}}{q_c^2 m}$$

$$\times \sum_{j=1}^{N} \exp\left\{-i\,\frac{k_o\varepsilon^2}{2n_o}\left[\left(L - \frac{i\,\ell\varepsilon^3}{n_o^2 q_c m}\right)a_j + \frac{\varepsilon^2\ell a_j^2}{2n_o^2}\right]\right\} \qquad (3.58)$$

This expression is comparable with (3.39) for the negative gradient case. It can be regarded as a sum over normal modes leaking into the overlying homogeneous half space from the "wave guide" formed by the first order discontinuity in velocity at z = 0 above and the continuous increase in velocity below.

To identify a head wave-like contribution, from the poles, we want to sum the series (3.58) as was done for (3.39) in the negative - gradient case. Thus consider

$$S_N = \sum_{j=1}^{N} \exp\left\{ - i \sigma_+ \left[(1 - i\Lambda_1)\, a_j + \Lambda_2 a_j^2 \right] \right\} \tag{3.59}$$

where we define

$$\sigma_+ = \frac{k_o L \varepsilon^2}{2n_o}$$

$$\Lambda_1 = \frac{\varepsilon^3 d}{n_o^2 q_c^m} \tag{3.60}$$

$$\Lambda_2 = \frac{\varepsilon^2 d}{2n_o^2}$$

$$d = \left(1 + \frac{\rho_c}{L q_o^3} \right) \quad .$$

Recall that for $j >> 1$; $a_j \simeq \left[\frac{3\pi}{8} (4j-1) \right]^{2/3}$, where a_j is the jth zero of Ai(-a). To allow for this approximate expression for a_j, we rewrite (3.59) as

$$S_N = \sum_{j=1}^{N} \exp \left\{ - i \sigma_+ \left[(1-i\Lambda_1) \tau_j + \Lambda_2 \tau_j \right] \right\} + \Delta_M \qquad (3.61)$$

where

$$\tau_j \equiv \left[\frac{3\pi}{8} (4j-1) \right]^{2/3} \text{ for all j and}$$

$$\Delta_m = \sum_{j=1}^{M} \exp \left\{ -i \sigma_+ \left[(1-i\Lambda_1) a_j + \Lambda_2 a_j^2 \right] \right\}$$

$$- \sum_{j=1}^{M} \exp \left\{ - i\sigma_+ \left[(1-i\Lambda_1) \tau_j + \Lambda_2 \tau_j^2 \right] \right\}$$

For $j = 3$, a_j and τ_j differ by only 0.2%, thus in practice $M = 3$ is probably sufficient for computing the correction term, Δ_M. As before, we apply the Euler-Maclaurin summation formula to the first term in S_N (3.61)

$$S_N = \int_0^{N+1} e^{-i\sigma_+ g(x)}\, dx - \frac{1}{2}\left[f(0) + f(N)\right] + \frac{1}{12}\left[f'(N) - f'(0)\right] + \cdots \tag{3.62}$$

where

$$g(x) = (1 - i\Lambda_1)\,\tau(x) + \Lambda_2\tau^2(x)$$

$$\tau(x) = \left[\frac{3}{8}\pi(4x - 1)\right]^{2/3}$$

$$f(x) = e^{-i\sigma_+ g(x)}$$

and consider the limit of S_N and $N \to \infty$. The remainder terms in S_N (3.62) have the form

$$f(0) = e^{-i\sigma_+(\lambda_1 + \lambda_2)}$$

$$f'(0) = i\frac{8\sigma_+}{3}\left[\lambda_1 + 2\lambda_2\right] e^{-i\sigma_+(\lambda_1 + \lambda_2)}$$

$$f(N) = e^{-i\sigma_+ g(N)}$$

$$f'(N) = -i\sigma_+ \frac{8}{3}\left[\lambda_1(4N - 1)^{-1/3} + 2\lambda_2\,(4N - 1)^{1/3}\right] e^{-i\sigma_+ g(N)}$$

where

$$g(N) = \left[\lambda_1 (4N - 1)^{2/3} + \lambda_2 (4N - 1)^{1/3} \right]$$

$$\lambda_1 = b(1 - i\Lambda_1), \quad \lambda_2 = b^2 \Lambda_2$$

$$b = \left(\frac{3\pi}{8}\right)^{2/3}$$

Because g(N) has a negative imaginary part, the exponential terms in f(N) and f'(N) result in

$$\lim_{N\to\infty} \begin{pmatrix} f(N) \\ f'(N) \end{pmatrix} = 0 \ .$$

Now consider the integral in (3.62), which has the form

$$I = \int_0^{N+1} e^{-i\sigma_+ \left[(1-i\Lambda_1)\, \tau(x) + \Lambda_2 \tau^2(x) \right]} dx$$

Let $u = (4x - 1)^{2/3}$, $du = \frac{4}{3} (4x - 1)^{-1/3} dx$, so that we can consider,

$$I_\infty = \lim_{N\to\infty} \int_1^{\left[4(N+1) - 1\right]^{2/3}} e^{-i\sigma_+ (\lambda_1 u + \lambda_2 u^2)} u^{\frac{1}{2}} du \qquad (3.63)$$

where λ_1 and λ_2 are defined above. Note that

$$\lambda_1 = |\lambda_1|\, e^{i\delta}$$

$$\delta = \tan^{-1}\left(\frac{-d\varepsilon^3}{n_o^2 q_c m}\right) \ .$$

The integral in (3.63) has a form similar to that of the integral representation of a parabolic cylinder function of three-halves order ((3), 8.3, Erdelyi, et al., vol. 2, 1953).

$$D_{-3/2}(\zeta) = \frac{e^{-\zeta^2/4}}{\Gamma(3/2)} \int_0^\infty e^{-\zeta t - \frac{1}{2} t} t^{\frac{1}{2}} dt \qquad (3.64)$$

To identify (3.68) with (3.64), we define

$$t = \sqrt{2\sigma_+\lambda_2}\ u\ e^{i\pi/4}$$

$$\zeta = \frac{\sqrt{\sigma_+\lambda_1}}{\sqrt{2\lambda_2}}\ e^{i\pi/4}$$

so that

$$u = \frac{e^{i\pi/4}}{\sqrt{2\sigma_+\lambda_2}}\ t \quad , \quad du = \frac{e^{-i\pi/4}}{\sqrt{2\sigma_+\lambda_2}}$$

Thus (3.63) can be written as

$$I_\infty = \frac{3}{8} \frac{e^{-i3\pi/8}}{(2\sigma_+\lambda_2)^{3/4}} \int_0^{\infty e^{i\pi/4}} e^{-\zeta t - \frac{1}{2} t^2} t^{\frac{1}{2}} dt - I_o \qquad (3.65)$$

where

$$I_o = \frac{3}{8} \int_0^1 e^{-i\sigma_+(\lambda_1 u + \lambda_2 u^2)} \, u^{\frac{1}{2}} du \tag{3.66}$$

The first integral on the right is now identical to that of (3.64) except that the integration path is along a line inclined at $\pi/4$ instead of along the real t axis. In Appendix III we show that in this case the two paths are equivalent, and we can write

$$I_\infty = \frac{3}{8} \frac{e^{-i\frac{3\pi}{8}}}{(2\sigma_+\lambda_2)^{3/4}} \Gamma\left(\frac{3}{2}\right) e^{\zeta^2/4} D_{-3/2}(z) = I_o$$

The asymptotic form of $D_{-3/2}(z)$ for $|z| >> 1$ can be written as

$$D_{-3/2}(\zeta) = \zeta^{-3/2} e^{-\zeta^2/4} \left[1 + \sum_{n=1}^{N} \frac{(3/4)_n (5/4_n}{n!\left(-\frac{1}{2}\zeta^2\right)_n} + 0|\zeta^2|^{-N-1} \right]$$

where the notation $(x)_n$ is defined as

$$(x)_n = x(x+1) \cdots (x+n-1)$$

(Erdelyi, et al., 1953). Substituting this asymptotic form into the above expression for I_∞ together with the definitions of λ_1 and λ_2 gives

$$I_\infty = \sqrt{\frac{2}{\pi}}\ \frac{n_o^{3/2}\ e^{-i3\pi/4}}{k_o^{3/2}\ L^{3/2}\varepsilon^3}\left(1 + i\,\frac{3}{2}\,\frac{d\varepsilon^3}{n_o^2 q_c m}\right)\left[1 + \sum_{n=1}^{N}\frac{(3/4)_n\ (5/4)_n}{n!\left(-\frac{1}{2}\mathfrak{z}^2\right)^n}\right] - I_o$$

where

$$\mathfrak{z} = \sqrt{\frac{k_o L}{2dn_o^3}}\left(-\,i\,\frac{d\varepsilon^3}{n_o^2 q_c m}\right)e^{i\pi/4}$$

When $|\sigma| << 1$, we can obtain an approximate expression for I_o (3.66) by expanding the exponential and integrating term by term. Thus

$$I_o = \frac{3}{8}\int_0^1\left[1 - i\sigma_+(\lambda_1 u + \lambda_2 u^2) - \frac{\sigma^2}{2}\,(\lambda_1^2 u^2 + 2\lambda_1\lambda_2 u^3 + \lambda_2^2 u^4) + \cdots\right]u^{\frac{1}{2}}\,du$$

$$= \frac{3}{4}\left[\frac{1}{3} - \sigma_+\left(\frac{i\lambda_1^2}{5} + \frac{i\lambda_2}{7}\right) + O(\sigma_+^2)\right]$$

or

$$I_o = \frac{1}{4} - i\,\frac{3}{5}\left(\frac{3\pi}{8}\right)^{4/3}\ \frac{k_o L\varepsilon^2}{2n_o} + O(\varepsilon^4) \qquad (3.67)$$

Combining the above results and substituting into (3.58) gives

$$\psi_{on} \simeq \left[\frac{2in_o e^{i\phi_o}}{km(1 - n_o^2)\, \rho^{1/2} L^{3/2}} \right]$$

$$\times \left\{ 1 + \varepsilon\sigma_+ \left[\left(\frac{\pi k_o L}{2n_o} \right)^{1/2} e^{-i\pi/4} \left(\frac{1}{2} + e^{-i\sigma_+(\lambda_1 + \lambda_2)} \right) - (q_c m)^{-1} \right] \right.$$

$$\left. + e^{-\frac{k_o L \varepsilon^3}{2n_o q_c m}} \sum_{n=1}^{M} \frac{(3/4)_n \, (5/4)_n}{n! \left(-\frac{1}{2} \zeta^2 \right)^n} + O(\varepsilon\sigma^2) \right\}$$

(3.68)

where the leading term in the brackets is the head-wave potential for a zero gradient in the lower medium and

$$\zeta \simeq \sqrt{\frac{k_o L}{2dn_o^3}}\, e^{i\pi/4} \quad ; \quad |\zeta| >> 1$$

$$\sigma_+(\lambda_1 + \lambda_2) \simeq \sigma_+ \left(\frac{3\pi}{8} \right)^{2/3}.$$

This expression is analogous to (3.45) in the negative-gradient case. It expresses the result that for $|\sigma| << 1$ and $|\zeta| >> 1$, the "critically refracted" field from a medium with a positive velocity gradient looks like the head-wave potential from a homogeneous medium plus a connection series. Keeping only the

first term in (3.68), we have

$$\psi_{n+} \simeq \frac{2in_o e^{i\phi_o}}{km(1-n_o^2)\ \rho^{\frac{1}{2}}\ L^{3/2}} \left[\ 1 + \varepsilon\sigma_+ g\ \right] \tag{3.69}$$

where

$$g = \left[\left(\frac{\pi k_o L}{2n_o}\right)^{\frac{1}{2}} e^{-i\pi/4} \left(\frac{1}{2} + e^{-i\sigma_+ \left(\frac{3\pi}{8}\right)^{2/3}} \right) - \frac{1}{q_c m} \right] .$$

This expression is analogous to (3.46) for negative gradients. As the distance, L, increases for a given gradient and frequency, the magnitude of σ_+ increases, and it is necessary to include terms of increasing order in σ_+ in (3.68). At sufficiently large distances (L) this becomes impractical, and another approach is required.

As indicated earlier the approach we take is to expand the plane-wave reflection coefficient, v_{p+}. We will do so using the asymptotic forms for the Airy functions given in Appendix I. The result will be an expression for the refracted field at large L in terms of diving waves, which at sufficiently high frequencies represent rays turned around by the increasing gradient. Some aspects of geometrical ray theory for the positive-gradient case are summarized in Appendix IV.

Substitution of the asymptotic form for $Ai(-\zeta_o)$ and $Ai'(-\zeta_o)$ into v_{p+} ((3.23) and (3.24)) gives

$$v_{p+} \simeq \frac{iqm \sin \beta + \sqrt{n_o^2 - p^2} \cos \beta}{iqm \sin \beta - \sqrt{n_o^2 - p^2} \cos \beta} \tag{3.70}$$

for $|\zeta_o| >> 1$ and where

$$\beta = w_o + \pi/4$$

$$w_o = \frac{2}{3} \varepsilon^{-3} (n_o^2 - p^2)^{3/2} .$$

Using the exponential representation for circular functions, (3.70) can be rewritten as

$$v_{p+} \simeq \frac{\left(q_m + \sqrt{n_o^2 - p^2}\right) e^{i2\beta} - \left(qm - \sqrt{n_o^2 - p^2}\right)}{\left(q_m - \sqrt{n_o^2 - p^2}\right) e^{i2\beta} - \left(qm + \sqrt{n_o^2 - p^2}\right)}$$

or

$$v_{p+} \simeq \frac{v_o - e^{i2\beta}}{1 - v_o e^{i2\beta}} \tag{3.71}$$

where

$$v_o = \frac{q_m - \sqrt{n_o^2 - p^2}}{q_m + \sqrt{n_o^2 - p^2}}$$

This expression for v_o is the same as (3.25); it is the plane wave reflection coefficient for the case in which both the upper and lower half-spaces are homogeneous. For $p < n_o$, $|v_o| < 1$, and we expand (3.71) to obtain

$$v_{p+} \simeq \left[v_o - e^{i2\beta} \right] \left[1 + v_o\, e^{i2\beta} + v_o^2\, e^{i4\beta} + \cdots + v_o^m\, e^{i2m\beta} + \cdots \right],$$

which can be rewitten as

$$v_{p+} \simeq v_o - \left[(1 - v_o^2)\, e^{i2\beta} + v(1 - v_o^2)\, e^{i4\beta} + \cdots + v^n(1 - v_o^2)\, e^{i2(n+1)\beta} + \cdots \right].$$

Putting this into the asymptotic form of the Weyl integral (3.28), gives

$$\psi_+ \simeq e^{i\frac{\pi}{4}} \sqrt{\frac{k_o}{2\pi\rho}} \int_{-\infty}^{\infty} dp\, \frac{\sqrt{p}}{q} \times \left[v_o - \sum_{n=0}^{\infty} v_o^n\, (1 - v_o^2)\, e^{i2(n+1)\beta} \right] e^{ik_o(rp + q(z + z_o))} \tag{3.72}$$

Equation (3.71) is a valid approximation to v_{p+} for $0 \leq p < n_o$. Thus the above integral will only give a valid approximation to that part of the reflected field arising from contributions to the original integral (3.28) along the interval $0 \leq p < n_o$.

The above integral has branch points at $p = \pm n_o$ associated with the radical $(n_o^2 - p^2)^{3/2}$ in β (see equation 3.70) in addition to those already discussed. We choose this branch cut such that $\text{Re}\left[(n_o^2 - p^2)^{\frac{1}{2}}\right] < 0$ (see Figure 8). This insures that $\text{Im}\left[(n_o^2 - p^2)^{3/2}\right] > 0$ along the original integration path for $|p| > 1$. It also insures that we stay slightly below the real p axis over the interval $n_o \geq p \geq 1$, along which our expansion of (3.71) might not converge.

We rewrite (3.72) in the following form

$$\Phi_+ \simeq \Phi_{r+} + \Phi_d \tag{3.73}$$

where

$$\Phi_{r+} \simeq e^{i\frac{\pi}{4}} \sqrt{\frac{k_o}{2\pi\rho}} \int_{-\infty}^{\infty} e^{ik_o(r\rho + q(z + z_o)} v_o \frac{\sqrt{p}}{q} \, dp \tag{3.74}$$

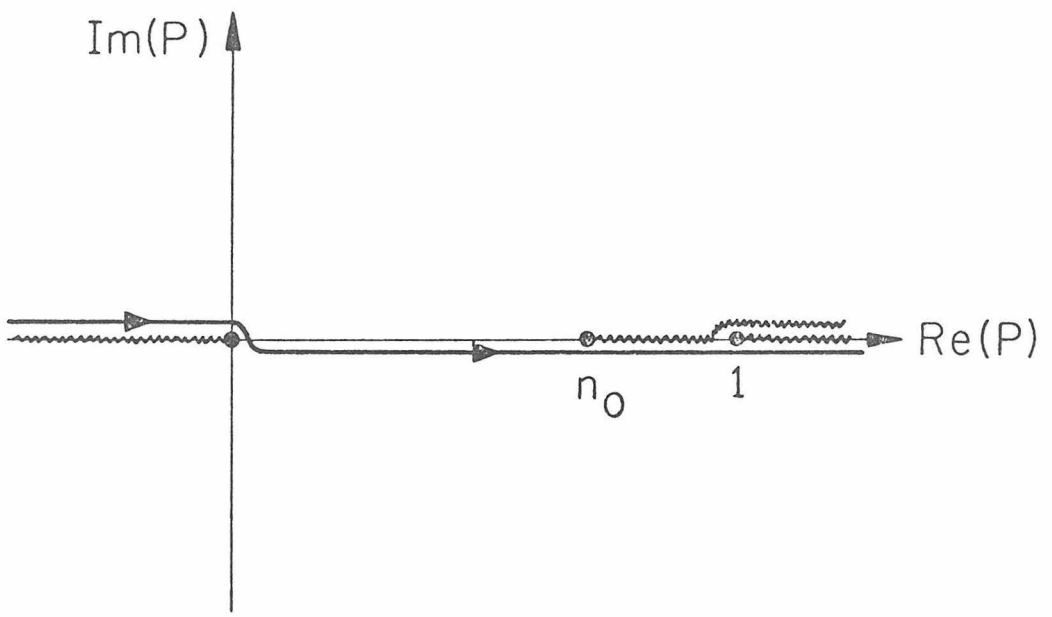

Figure 8a

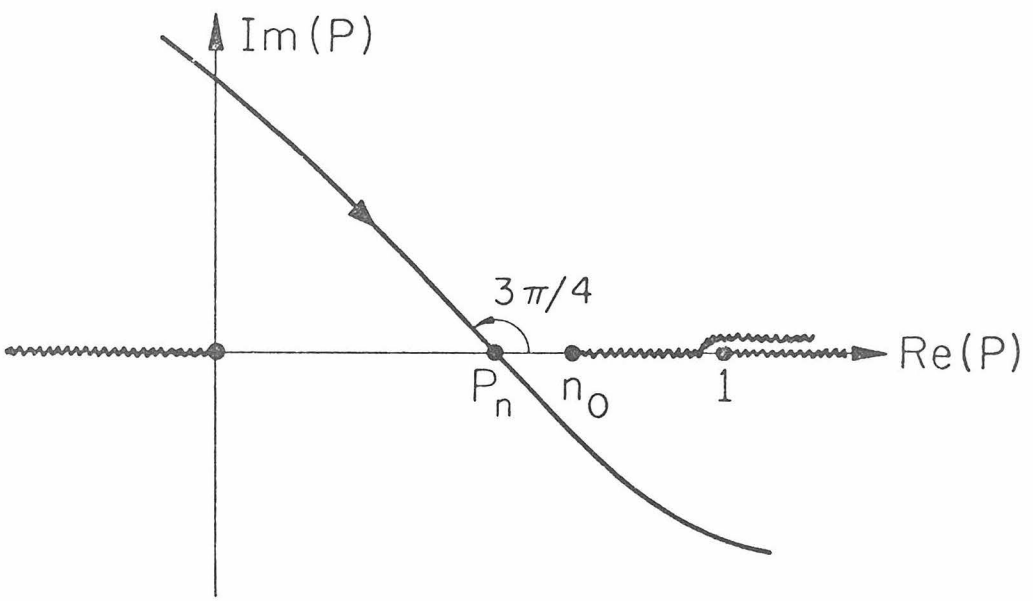

Figure 8b

and

$$\Phi_d \simeq - e^{i\frac{\pi}{4}} \sqrt{\frac{k_o}{2\pi\rho}} \int_{-\infty}^{\infty} \frac{\sqrt{p}}{q} \; e^{ik_o(r\rho + q(z + z_o))} \tag{3.75}$$

$$\times \sum_{n=0}^{\infty} v_o^n \, (1 - v_o^2) \; e^{i2(n+1)\beta} \, dp$$

Thus we identify the 'separate' contributions to the total reflected field for angles of incidence less than critical ($p < n_o$) as indicated at the beginning of this section.

The saddle-point evaluation of Φ_{r+} (3.74) goes exactly as before, and we obtain the geometrical ray-theory result for waves reflected at the boundary $z = 0$ for angles of incidence less than critical, i.e.

$$\Phi_{r+} \simeq \frac{e^{ik_o R_1}}{R_1} \; v_o(p_o) \quad ; \quad p < n_o \tag{3.76}$$

Turning to the evaluation of Φ_d (3.75), we interchange the order of integration and summation and consider the saddle point approximation to the nth term

$$\Phi_d^{(n)} \simeq - e^{i\frac{\pi}{4}} \sqrt{\frac{k_o}{2\pi\rho}} \int_{-\infty}^{\infty} e^{k_o f_n(p) + i\frac{(n+1)\pi}{2}} v_o^n \, (1 - v_o^2) \, \frac{\sqrt{p}}{q} \, dp \tag{3.77}$$

where

$$f_n(p) = i\left[\rho p + (z + z_o)\, q + \frac{4(n+1)}{3\gamma}\,(n_o^2 - p^2)^{3/2}\right]. \qquad (3.78)$$

The saddle point is given by

$$\frac{d\, f_n(p)}{dp} = 0$$

or

$$\left[\rho - \frac{p}{\sqrt{1-p^2}}\,(z + z_o) - \frac{4(n+1)}{\gamma}\, p\,(n_o^2 - p^2)^{\frac{1}{2}}\right] = 0 \qquad (3.79)$$

From the geometrical ray relationships outlined in Appendix IV we have the following expression for the horizontal distance covered by a diving wave entering the lower medium at an angle of incidence, Θ_n, and reflecting n times at the boundary $z = 0$ before arriving at the point $\underline{r} = (\rho, z)$:

$$\rho = \frac{p_n}{\sqrt{1-p_n^2}}\,(z + z_o) + \frac{4(n+1)}{\gamma}\, p_n (n_o^2 - p_n^2)^{\frac{1}{2}}$$

(see Figure A4-1). Comparing this with (3.79), we see that

$$p = p_n = \sin \Theta_n \qquad (3.80)$$

is the saddle point for the nth term in the series. The steepest descents path for this integrand approaches the saddle point at an angle of $3\pi/4$ as illustrated in Figure 8b. No singularities are crossed in deforming the contour, so that the entire contribution for each term in the series comes from the immediate vicinity of the respective saddle points. Note that $p_n < n_o$ for all n, and the integral (3.45) thus will give a valid approximation to the field in the upper medium from the waves reflected by the positive gradient in the lower medium (the so-called diving waves).

Using the formulae presented earlier for the saddle point method (3.31), and noting that

$$f_n''(p_n) = - i \left[\frac{(z + z_o)}{(1 - p_n^2)^{3/2}} + \frac{4(n+1)}{\gamma} \frac{(n_o^2 - 2p_n^2)}{(n_o^2 - p_n^2)^{1/2}} \right]$$

we obtain to first order

$$\phi_d^{(n)} \simeq - e^{i \frac{(n+1)}{2}} \sqrt{\frac{\gamma}{\rho}} \times \left[\frac{p_n (1-p_n)^{3/2} (n_o^2-p_n^2)^{1/2}}{4(n+1)\, q_n^3 (n_o^2-2p_n^2) + \gamma (n_o^2-p_n^2)^{1/2} (z+z_o)} \right] v_o^n (1-v_o^2)\, e^{k_o f_n(p_n)}$$

(3.81)

where $f_n(p_n)$ is given by (3.78) and $v_o(p_n)$ is given by (3.25). This result expresses the geometrical ray-theory phase and amplitude for the diving wave reflected n times at the boundary z = 0 (although it does include a $-\pi/2$ phase shift acquired by a wave each time it passes through a turning point, which is not predicted by geometrical ray theory). In particular, we note the following aspects of the above result:

1) The argument of the exponent, $f_n(p_n)$, is the phase of the nth diving wave derived using Snell's law in Appendix IV.

2) The factor $(1 - v_o^2(p_n))$ is the product of the homogeneous, plane-wave transmission coefficients for energy entering and leaving the lower half space at an incident angle of Θ_n (i.e. $m^{-1}(1 + v_o(p_n))$ and $m(1 - v_o(p_n))$, respectively.

3) The factor $v_o^n(p_n)$ is the product of n reflection coefficients for the n reflections at the boundary z = 0. The reflection coefficient for waves reflecting at z = 0 from below, v_1, is the negative of v_o. Thus the strict representation for this product of reflection coefficients is $(- v_o(p_n))^n$. In (3.81) this sign is carried in the leading exponential.

4) The leading exponential, $- \exp [i(n+1) \pi/2]$, contains the $-\pi/2$ phase shift acquired by the wave when passing through each of the (n+1) turning points, as well as the $(-1)^n$ sign required for the factor v_o^n mentioned above.

5) The remaining radical gives the spreading factor for a tube of rays leaving the point source $(0, z_o)$ and arriving at (ρ, z).

The range of validity of the diving wave result (3.81) is limited by two approximations. The first is the assumption that $|\zeta_o| >> 1$ made in obtaining the asymptotic form of the reflection coefficient (3.70). For most purposes, it will be adequate to take

$$|\zeta_o| = \left| \left(\frac{k_o}{\gamma} \right)^{2/3} \left(n_o^2 - p_n^2 \right) \right| > 3$$

This restriction can be translated into limitations on the minimum depth of penetration by the diving wave below the boundary, $z = 0$, and the minimum horizontal distance traveled by the diving wave in the lower medium using the geometrical ray theory results presented in Appendix IV. The maximum depth of penetration in the lower medium for a ray incident on the boundary at an angle θ_n is

$$z_m = - \frac{n_o^2 - p_n^2}{\gamma}$$

by (A4-5), where p_n and sin θ_n. Thus by the above restriction the diving wave result will be valid for waves that bottom at depths greater than z_{min} where

$$z_{min} \sim 3(\gamma\ k_o^2)^{-1/3} \qquad (3.82)$$

By (A4-9), the corresponding horizontal distance covered by the ray bottoming at z_m is

$$\rho_m = \frac{p_n}{\left(1 - p_n^2\right)^{\frac{1}{2}}} (z + z_o) + \frac{4(n+1)}{\gamma} p_n \left(n_o^2 - p_n^2\right)^{\frac{1}{2}}$$

and the diving wave result will be valid for waves at distances greater than

$$\rho_{min} \sim \frac{p_n}{\left(1 - p_n^2\right)^{\frac{1}{2}}} (z + z_o) + \frac{4\sqrt{3}\,(n+1)}{\left(k_o \gamma^2\right)^{1/3}} \left(\gamma z_{min} + n_o^2\right) \tag{3.83}$$

The second approximation comes from retaining only the first term in the steepest descents evaluation of the integral (3.77); this is the geometrical ray-theory approximation. To obtain a frequency-dependent connection to the geometrical ray-theory approximation, it is necessary to include the next term in the steepest-descent result. Referring to (3.31), we see that if the second term is included, the diving wave expression will be of the form

$$\Phi_{d_2}^{(n)} = \Phi_{d_1}^{(n)} \left[1 + \frac{1}{4k_o} G_n\right]$$

where $\Phi_{d_1}^{(n)}$ is given by (3.77),

$$G_n = \left[\frac{f_n'''}{(f_n'')^2} \frac{F_n'}{F_n} + \frac{1}{4} \frac{f_n^{IV}}{(f_n'')^2} - \frac{5}{12} \frac{(f_n''')^2}{(f_n'')^3} - \frac{F_n''}{f'' F_n}\right],$$

$$F_n = V_o^n(p) \left(1 - V_o^2(p)\right) \frac{\sqrt{p}}{q},$$

and f_n is given by (3.78). (Here the primes indicate differentiation with respect to p.) Obviously, the form of the correction term is cumbersome, and in practice, it will be expedient to proceed directly with an "exact" numerical saddle point integration of (3.77) rather than to work with this analytic form. Here we only need note that $G = 0(\gamma)$ so that

$$\Phi_{d_2}^{(n)} = \Phi_{d_1}^{(n)} \left[1 + 0\left(\frac{\gamma}{k_o} \right) \right]$$

We can summarize our results for the effect of a positive gradient on refracted waves as follows:

1) At relatively short distances beyond the critical distance, such that $|\sigma_+| >> 1$ or

$$L << \frac{2n_o}{\left(k_o \gamma^2 \right)^{1/3}}$$

(see (3.60)), the head wave can be represented by (3.68) or (3.69) as a sum of "normal modes" propagating between the discontinuous boundary and the underlying positive gradient and leaking into the overlying half space.

2) At sufficiently large distances beyond the critical distance, such that

$$L_d > \frac{4\sqrt{3}\, p_o}{\left(k_o \gamma^2 \right)^{1/3}} ,$$

the refracted field can be described as a sum of diving waves

$$\Phi_d = \sum_{n=0}^{\infty} \Phi_d^{(n)}$$

where $\Phi_d^{(n)}$ is given by (3.81) in the ray-theoretical limit ($|\gamma/k_o| << 1$); and L_d is the horizontal distance covered by the direct diving wave (see (3.83) or (A4-9)). By (3.82), the expression for any given diving wave, $\Phi_d^{(n)}$, will be valid as long as the wave bottoms at a depth greater than at least $z_m \sim (\lambda^2/\gamma)^{1/3}$ beneath the boundary $z = 0$.

At this point we can infer some simple time-domain properties of waves refracted by a positive gradient from the phase and spectral variations obtained above. The ray-theoretical expression for diving wave travel times (A4-17) shows that at sufficiently large distances the direct diving wave will arrive first and will be followed at successively later times by waves reflecting an increasing number of times beneath the boundary $z = 0$. The last group of waves to arrive will be those that are very close to critical incidence and propagate just below the boundary making a great many reflections; their travel time will essentially be that of the true head wave in the case of a zero gradient. However, because these waves are confined to a thin zone just below the boundary, the ray-theoretical expression for their amplitudes (3.81) will not be valid except at very high frequencies by (3.82).

We can obtain an expression for the combined effect of these boundary-layer waves by referring to the normal mode equation (3.58). For $|\sigma_+| >> 1$, the phases of the modes are well separated (i.e. the poles are spread out in the p-plane), and the phase of the first mode (j = 1) is nearest to that of a head wave for zero gradient. Thus we can expect that this first mode represents the combined effects of the boundary-layer diving waves and corresponds most closely to what might be considered a true head wave at large distances in the presence of a positive gradient. From (3.58), the expression for this boundary-layer wave (or head wave) is

$$\phi_n^* \simeq - e^{i\frac{\pi}{4}} \sqrt{\frac{2\pi k_o}{\rho n_o}} \frac{\varepsilon^3}{q_c^2 m} \exp\left\{ i(\phi_o - \delta_+) - \frac{\varepsilon^3}{n_o q_c^m} \left(\frac{k_o L}{2} + \frac{\ell}{n_o} \right) \right\} \tag{3.84}$$

where $|\sigma_+| = \left| \frac{k_o L \varepsilon^2}{2 n_o} \right| >> 1$, and $\delta_+ = (\sigma_+ a_1)$.

This expression is similar to that for the head wave at large distances, $|\sigma_-| >> 1$, in the negative-gradient case (3.49). The primary difference is that in the positive-gradient case, the exponential decay of the amplitude goes as ε^3 compared with ε^2 in the negative gradient case. In other words, the high-frequency components of the 'head wave' die off less rapidly with distance for a positive gradient than for a negative gradient when the magnitudes of the gradients are comparable. A second difference

is that the factor δ_+ is subtracted from the homogeneous head wave phase, ϕ_o, so that the head wave for the positive gradient is also slightly dispersed, but in the opposite sense from the negative gradient case. The horizontal phase velocity for the positive gradient 'head wave' is given by

$$c_{n+1} \simeq c_o/[\sin (n_o - \delta_+)] \quad .$$

Thus, in view of the above remarks, we can expect that a seismogram of the refracted waves in the case of a positive gradient would be spread in time between the first arrival of the direct diving wave and the last arrival of the boundary layer, or 'head wave'. This spread in time will increase with increasing distance. At short distances everything will arrive at nearly the same time, and the combined effect will give an arrival very much like the classical head wave in character as indicated by (3.69). In the time domain, this arrival will look like the time integral of the direct arrival. At larger distances the character of the refracted wave group will be dominated by the large amplitudes of the first few diving waves (P, PP, etc.), and, in practice, the true head wave would probably be difficult to identify. In the time domain, the individual diving waves will have the same wave form as the direct wave.

Results for a spherical boundary-We now wish to extend the above results for a plane boundary to obtain expressions for waves reflected from a spherical boundary. Taking advantage of the earth-flattening transformation with a point source presented in Section 2, we assume that both source and receivers are such that $|z/a| << 1$ and that $|k_o a| >> 1$. Furthermore, we are primarily concerned with waves near critical angles of incidence, which for most crustal and upper mantle problems are neither near-normal nor near-grazing angles. Thus, according to the results in Section 2, all that is necessary is to put the plane-wave reflection coefficient for the velocity distribution modified according to the earth-flattening transformation (2.13) or (2.14) into the Weyl integral (2.36) or (2.37).

To introduce the approximate linear velocity earth-flattening transformation (2.37) into the form of the velocity variation (3.1), we expand (3.1) and match coefficients of like powers of z. The result gives the following correspondence between the flat velocity gradient, γ, and the curvature mapping gradient (1/a).

$$\frac{1}{a} \leftrightarrow \frac{\gamma}{2n_o^2}$$

for $|1/a| << 1$ and $|\gamma| << 1$. Thus the appropriate earth-flattening velocity transformation is

$$c_s \simeq c_o \left[n_o^2 + \left(\frac{2n_o^2}{a} \pm \gamma \right) z \right]^{-1/2} . \qquad (3.85)$$

We introduce a new gradient parameter, γ_s, by defining

$$\gamma_s = \frac{2n_o^2}{a} \pm \gamma \qquad (3.86)$$

where the first term on the right is the modified curvature-mapping gradient and the second term is the velocity gradient in (3.1) describing the physical velocity variation, so that (3.85) becomes

$$c_s = c_o \left(n_o^2 + \gamma_s z \right)^{-1/2} \qquad (3.87)$$

This is the same form as (3.1) and the solution to (3.9) will still be the Airy functions given by (3.19) but with γ_s in place of γ.

The form of the integrand of the Weyl integral remains unchanged by the earth-flattening transformation under our approximations (the changes introduced in the exponential term inside the integral (2.36) by replacing 'ρ' by '$a\theta$' are of order (z/a) and can be neglected), and the rest of the analysis proceeds as before. Thus the asymptotic expressions for waves reflected from a spherical boundary are obtained simply by replacing γ by γ_s in the flat expression, and for distances greater than about 10 degrees replacing $\rho^{-\frac{1}{2}}$ by $(a \sin \theta)^{-\frac{1}{2}}$.

An obvious consequence of the velocity transformation (3.87) and the definition of γ_s is that an effective null gradient corresponds

to a physical gradient $\gamma = -2n_o^2/a$, and thus that the negative and positive asymptotic solutions for the flat case correspond to physical velocity gradients more negative and less negative than $(-2n_o^2/a)$, respectively, in the case of a spherical boundary. This is the most significant effect of curvature, and we will return to it shortly.

However, at this point a few comments on the radiation conditions used in obtaining the plane wave reflection coefficients $v_{p\pm}$ and their relation to the spherical problem are in order. Obviously, inside the spherical boundary r = a, there will be a system of 'upgoing' and 'downgoing' traveling waves because of internal reflections at r = a. In the case of a homogeneous sphere, for example, the appropriate solution for (2.20) is

$$\hat{\psi}_1 = B\, j_\ell(k_1 r) \quad ; \quad r < a$$

where k_1 is the wave number in the sphere. The spherical Bessel function $j_\ell(k_1 r)$ represents a system of standing waves and is finite at r = 0. By (2.24) it can be represented as a combination of ingoing and outgoing traveling waves, $h_\ell^{(1)}$ and $h_\ell^{(2)}$, both of which, however, are infinite at r = 0.

Through the device of the rainbow expansion (Bremmer, 1949) the complete response involving $j_\ell(k_1 r)$, say, can be split into an

infinite number of terms, each of which represents a generalized ray reflecting a given number of times at the boundary $r = a$. Some of the individual terms may become infinite at $r = 0$. In the case we are considering of a single boundary, the first term in the expansion represents the generalized ray reflected externally at the boundary $r = a$, the second term represents a generalized ray penetrating the boundary and emerging again with no internal reflections (P in upper mantle seismology), the third represents PP, and so on. See Richards (1970) or Chapman (1969) for a detailed discussion of the rainbow expansion.

The reflection coefficient in the first term of the rainbow expansion can be obtained by applying the usual continuity conditions at $r = a$ and assuming only downgoing waves for $r < a$. Thus the radiation condition applied in the flat case with a negative velocity gradient corresponds to keeping only the first term in the rainbow expansion on transformation to the spherical case. For the positive velocity gradient in the flat case, both upgoing and downgoing waves were retained. This corresponds to obtaining the complete response, and the decomposition into diving waves (3.72) corresponds to the complete rainbow expansion on transformation to the spherical case.

The effects of curvature can be summarized by noting that through the earth-flattening transformation (3.86) the effective

null gradient case actually corresponds to a critical negative velocity gradient, $\gamma = -2n_o^2/a$, as noted above. In geometrical ray theory, this critical gradient corresponds to the case in which the curvature of a ray at its turning point matches the curvature of the earth (see sec. 7.2.3 in Bullen (1963)). Here the ray is trapped and continues around the earth at a constant radius. In this particular case, the transformed reflection coefficient reduces to the plane wave reflection coefficient for two homogeneous media (3.25), and evaluation of the Weyl integral follows standard methods for obtaining the classical head wave result (see Cerveny (1965) or Brekhovskikh (1960))

$$\psi_h \sim \frac{2in_o}{k_o mq\, \rho^{\frac{1}{2}} L^{3/2}}\, e^{i\phi_o}$$

where ϕ_o is the head wave phase (see 3.38). Thus when curvature is included, the results for negative and positive velocity gradients obtained for the flat case apply to physical velocity gradients more negative and less negative than $(-2n_o^2/a)$, respectively. It follows, of course, that there will be an effective positive gradient equal to $(2n_o^2/a)$ when $\gamma = 0$ and the medium below the boundary $r = a$ is homogeneous.

It should be emphasized that this effect of curvature on critically or near-critically refracted waves is independent of

distance, and in principal, should be included even in studies of head wave amplitudes from crustal layers. At the same time, the effect of curvature on waves reflected at the boundary r = a is small and can be neglected under our assumptions. (This follows from the development leading to (3.32) or (3.76) where it was demonstrated that small velocity gradients have a negligible effect on waves reflected from a plane boundary.)

All of the remarks regarding the effects of negative and positive velocity gradients for the plane boundary carry over to the spherical boundary with γ replaced by γ_s. For example, we can use the diving wave results in the case of a positive gradient to assess the validity of ray theory for a homogeneous crust and upper mantle (here $\gamma_s = 2n_o^2/a$). Assuming a 30 km thick crust with a P-wave velocity of 6.4 km/sec over a homogeneous upper mantle with a velocity of 8.0 km/sec (and also assumming that the basic properties of acoustic waves apply to elastic P-waves), we find by (3.82) that for a valid ray-theoretical description, the direct P-wave must bottom at depths greater than 50 km beneath the M-discontinuity for 1-Hz waves. For 5-Hz waves the minimum depth is 20 km. By (3.83), the corresponding minimum distances for an adequate ray-theoretical description of the direct P-wave are 1600 km and 800 km for 1 Hz and 5 Hz waves, respectively.

Finally, there is one further restriction on the results for

a spherical boundary in addition to those summarized at the end of Section 2. Because we have used the linear form of the earth-flattening velocity transformation instead of the exact, exponential form (2.13), there will be a depth ($z < 0$) below which our transformation becomes increasingly inaccurate. For a 1% error, this depth will be approximately given by

$$z_{max} \sim 2 \times 10^{-2}\, a.$$

Accordingly, our results for the spherical boundary are limited in the case of an effective positive gradient to diving waves that bottom at depths less than z_{max}, and in all cases to wave lengths that are less than z_{max}. For example, in the case of the Mohorovičić discontinuity and a homogeneous upper mantle, this maximum depth is approximately 150 km and the maximum wave period is about 20 sec. In practice, the limiting depth and period will usually be imposed by the known velocity structure in the mantle at shallower depths than z_{max} (e.g. the top of the low-velocity zone).

4. Elastic fomulation

In this section we apply the methods developed for acoustic waves to the analogous elastic case. Thus we consider two isotropic elastic half spaces welded together at the boundary $z = 0$. We take the upper half-space to be homogeneous with compressional and shear

velocities α_o and β_o, density ρ_o, and Lamé constants λ_o and μ_o; and we let the lower half space be vertically heterogeneous. As in the acoustic case, our goal is to determine the elastic field generated by a point source in the homogeneous medium and reflected by the boundary and the underlying heterogenous medium. The basic geometric relations for the elastic problem are the same as in the acoustic case (Figure 3a).

Following the arguments presented in the acoustic case, we will take the specific functional forms for the compressional and shear velocities in the heterogeneous medium to be

$$\alpha_1(z) = \alpha_o \left(n_\alpha^2 \pm \gamma_\alpha z \right)^{-\frac{1}{2}} \quad ; \quad z < 0 \tag{4.1}$$

$$\beta_1(z) = \beta_o \left(n_\beta^2 \pm \gamma_\beta z \right)^{-\frac{1}{2}} \quad ; \quad z < 0 \tag{4.2}$$

where n_α and n_β are the compressional and shear indices of refraction across the boundary $z = 0$, and γ_α and γ_β are the corresponding gradient parameters. Again, for empirical reasons, we will let the density variation parallel the velocity variation

$$\rho_1(z) = \rho_o \left(n_\rho^2 \pm \gamma_\rho z \right)^{-\frac{1}{2}} \quad ; \quad z < 0 \tag{4.3}$$

which in turn suggests that the Lamé constants may vary as

$$\begin{pmatrix} \mu_1(z) \\ \lambda_1(z) \end{pmatrix} = \begin{pmatrix} \mu_o \\ \lambda_o \end{pmatrix} \left(n_\mu^2 \pm \gamma_\mu z \right)^{-3/2} \tag{4.4}$$

However, as in the acoustic case, it will turn out that for small gradients the variations in density or in the elastic parameters are not important except near grazing angles of incidence, and all we really require is that their functional forms be consistent with (4.1) and (4.2) through $\alpha = [(\lambda + 2\mu)/\rho]^{\frac{1}{2}}$ and $\beta = [\mu/\rho]^{\frac{1}{2}}$. The variation of elastic velocities as a function of depth is illustrated in Figure 9.

We will not repeat the formal arguments leading to the integral representation in terms of the Weyl integral (3.27) for the elastic case. Instead, we will apply the Weyl integral directly to the elastic plane wave reflection coefficients taking advantage of the properties of the Weyl integral as an operator on plane wave solutions to yield the spherical wave field from a point source. We will treat the SH and P-SV cases separately.

SH motion.-The appropriate potential representation for SH, or torsional, waves is given by (1.12) to be

$$\underline{u} = \text{curl}\left[0,0,\left[\mu(z)\right]^{-\frac{1}{2}} T(\rho,z)\right] \tag{4.5}$$

where the potential, T, satisfies

$$\nabla^2 T + k^2 T = \begin{cases} -\frac{\rho}{\mu}\,\delta(z-z_o)\,\delta(r) & z > 0 \\ 0 & z < 0 \end{cases} \tag{4.6}$$

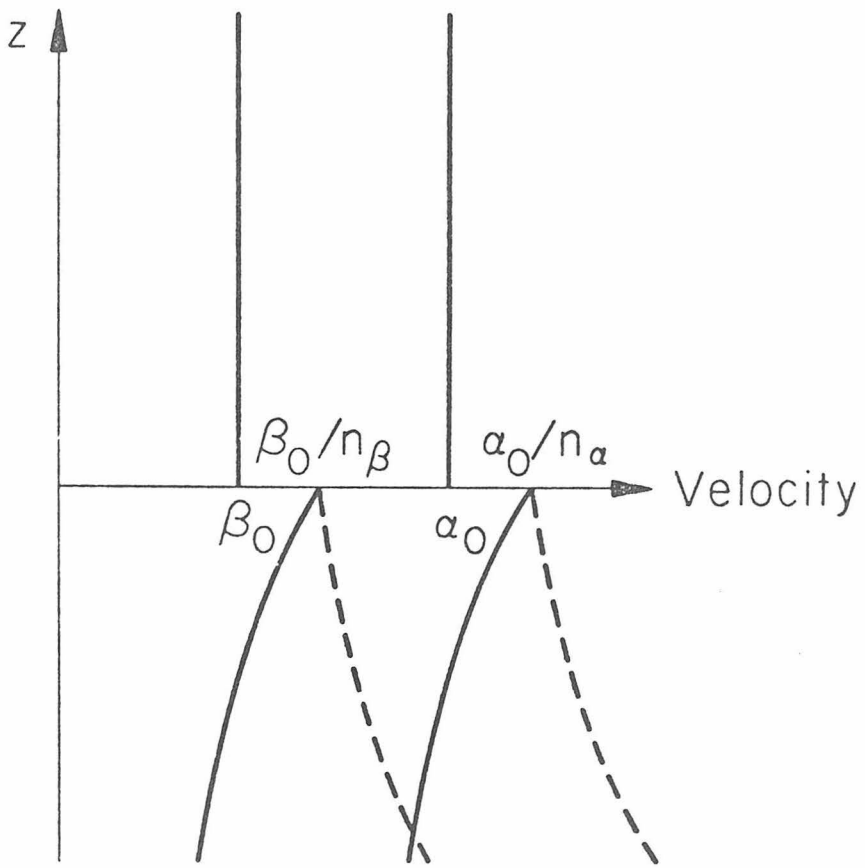

Figure 9

in a cylindrical coordinate system (see 1.12).

To determine the plane-wave reflection coefficient, we will transform to Cartesian coordinates and consider a plane wave propagating in the x-z plane and incident on the boundary at an angle θ. In this case, the SH-wave displacement will be given by

$$\underline{u} = \hat{e}_2 \, \mu^{-\frac{1}{2}}(z) \, \frac{\partial T}{\partial x} \tag{4.7}$$

where $\hat{e}_2$ is the unit vector in the y-coordinate, and the displacement potential will satisfy

$$\nabla^2 T + k^2(z) \, T = 0 \tag{4.8}$$

where by (4.2)

$$k^2(z) = \begin{cases} k_o^2 & z > 0 \\ k_1^2(z) = k_o^2 \, (n_\beta^2 \pm \gamma z) & z < 0 \end{cases} \tag{4.9}$$

The elastic boundary conditions for a welded interface require continuity of displacement and stress. For SH-motion these conditions become

$$\begin{aligned} \underline{u}(0_+) &= \underline{u}(0_-) \\ \tau_{yz}(0_+) &= \tau_{yz}(0_-) \end{aligned} \tag{4.10}$$

respectively (also see Section 2).

We assume a standard variable-separable solution to (4.8) of

the form

$$T(x,z) = X(x)\,\hat{T}(z) \tag{4.11}$$

and obtain

$$\frac{d^2X}{dx^2} + \kappa^2 X = 0 \tag{4.12}$$

$$\frac{d^2\hat{T}}{dz^2} + \left[k^2(z) - \kappa^2 \right] \hat{T} = 0 \tag{4.13}$$

where the separation constant, κ, is identified as the horizontal shear wave number. Equations (4.12) and (4.13) have the same form as (3.6) and (3.7) in the acoustic case, and their solutions are

$$\left.\begin{aligned} X_j(x) &= A_j\, e^{i\kappa x} + B_j\, e^{-i\kappa x} \\ \hat{T}_{oj}(z) &= C_j\, e^{i\eta_\beta z} + D_j\, e^{-i\eta_\beta z} \end{aligned}\right\} \quad j = 1,2 \tag{4.14}$$

$$\begin{pmatrix} \hat{T}_1(z) \\ \hat{T}_2(z) \end{pmatrix} = \begin{pmatrix} E_1 Ai\left(-\zeta_-\, e^{i2\pi/3}\right) \\ E_2 Ai(-\zeta_+) \end{pmatrix} + \begin{pmatrix} F_1 Ai\left(-\zeta_-\, e^{-i2\pi/3}\right) \\ F_2 Bi(-\zeta_+) \end{pmatrix}$$

where the subscript, j, refers to a negative gradient when equal to 1 and a positive gradient when equal to 2, and where

$\eta_\beta = (k_o^2 - \kappa_\beta^2)^{\frac{1}{2}}$, $\zeta_\pm = \varepsilon_\beta^{-2}(n_\beta^2 - p^2 \pm \gamma z)$, $\varepsilon_\beta = (\gamma_\beta/k_o)^{1/3}$, $p = \sin\theta$.

Taking the incident plane wave to have unit amplitude and assuming radiation conditions at $z = -\infty$ analogous to those in the acoustic case for negative and positive gradients, the solution (4.11) becomes

$$T_{oj}(x,z) = e^{i(\kappa x - \eta_\beta z)} + V_{SH} \; ; \; e^{i(\kappa x + \eta_\beta z)} \qquad z > 1 \tag{4.15}$$

$$\begin{pmatrix} T_1(x,z) \\ \\ T_2(x,z) \end{pmatrix} = \begin{pmatrix} U_{SH_1} \, Ai\left(-\zeta_- \, e^{i2\pi/3}\right) \\ \\ U_{SH_2} \, Ai(-\zeta_+). \end{pmatrix} e^{i\kappa_1 x} \qquad z < 1 \tag{4.16}$$

Substituting these solutions into the boundary conditions (4.10) we obtain

$$\mu_o^{-\frac{1}{2}} \left.\frac{\partial T_{oj}}{\partial x}\right|_{z=0_+} = \mu_1^{-\frac{1}{2}}(0) \left.\frac{\partial T_j}{\partial x}\right|_{z=0_-}$$

and

$$\left[\mu_o \frac{\partial}{\partial z}\left[\mu_o^{-\frac{1}{2}} \frac{\partial T_{oj}}{\partial x}\right]\right]_{z=0_+} = \left[\mu_1(0) \frac{\partial}{\partial z}\left[\mu_1^{-\frac{1}{2}}(z) \frac{\partial T_j}{\partial x}\right]\right]_{z=0_-}$$

or

$$\begin{pmatrix} 1 & -s^{\frac{1}{2}} H_j \\ i\eta_\beta & -s^{-\frac{1}{2}} \left[-\frac{1}{2}\frac{\mu_1'}{\mu_1} + H_\pm' \frac{d\zeta_\pm}{dz} \right] \end{pmatrix} \begin{pmatrix} V_{SH_j} \\ U_{SH_j} \end{pmatrix} = \begin{pmatrix} -1 \\ i\eta_\beta \end{pmatrix}; \quad j=1,2$$

where

$$\begin{pmatrix} H_1 \\ H_2 \end{pmatrix} = \begin{pmatrix} Ai & -\zeta_- e^{i2\pi/3} \\ & Ai(-\zeta_+) \end{pmatrix}, \quad s = (\mu_o/\mu_1(0)),$$

and the primes indicate differentiation with respect to z. Solving for the plane-wave reflection coefficients we obtain

$$V_{SH_2} = \frac{Ai(-\zeta_o)\left[iqs - \frac{s}{4}\left(\frac{\varepsilon_\beta}{\eta_\beta}\right)^3 \right] - \varepsilon_\beta^2 Ai'(-\zeta_o)}{Ai(-\zeta_o)\left[iqs + \frac{s}{4}\left(\frac{\varepsilon_\beta}{\eta_\beta}\right)^3 \right] + \varepsilon_\beta^2 Ai'(-\zeta_o)}; \quad \gamma_\beta > 0 \qquad (4.17)$$

and

$$VSH_1 = \frac{Ai(-\zeta_o)\left[iqs + \frac{s}{4}\left(\frac{\varepsilon_\beta}{\eta_\beta}\right)^3 \right] + e^{i2\pi/3} \varepsilon_\beta^2 Ai'(-\zeta_o)}{Ai(-\zeta_o)\left[iqs - \frac{s}{4}\left(\frac{\varepsilon_\beta}{\eta_\beta}\right)^3 \right] - e^{i2\pi/3} \varepsilon_\beta^2 Ai'(-\zeta_o)}; \quad \gamma_\beta < 0 \qquad (4.18)$$

Referring back to the acoustic case, we see that the SH plane-wave reflection coefficients have the same form as the acoustic plane-wave reflections coefficients (3.22) and (3.23). The only difference is that the shear modulus ratio, s, enters the SH reflection coefficients in place of the density ratio, m, in the acoustic case.

It follows that upon substitution of these SH reflection coefficients into the Weyl integral (3.27), the asymptotic evaluation of the integral will proceed exactly as in the acoustic case. Thus, we can take the results for acoustic waves obtained in the previous section for both negative and positive gradients and simply replace m by s to obtain the corresponding expressions for the SH displacement potential for the flat boundary. For completeness, these results are summarized below.

For a negative gradient ($\gamma_\beta < 0$) the refracted part of the field is given by

$$T_{h_1} \sim \begin{cases} T_{h_o}\left[\, 1 - \sigma_1^{3/2} \,\right] e^{i\phi_o} \quad ; & |\sigma_1| << 1 \\ -\sqrt{\dfrac{2\pi k_o}{\rho}}\, \dfrac{\varepsilon^3}{s(1-n_\beta^2)}\, \exp\left[i(\phi_o + \delta_1 + \pi/4) \right. & \\ \left. -\dfrac{\sqrt{3}}{4}\, \dfrac{k_o L\, \varepsilon_\beta^2}{n_\beta} \left(a_1 - \dfrac{\varepsilon}{\sqrt{3}\, s(1-n_\beta^2)^{\frac{1}{2}}} \right) \right] \quad ; & |\sigma_1| >> 1 \end{cases} \tag{4.19}$$

where

$$\sigma_1 = -\, i \left(\frac{3\pi}{8} \right)^{2/3} \frac{k_o L\, \varepsilon_\beta^2}{2n_\beta}\, e^{i\pi/3}$$

$$\delta_1 = \frac{k_o L\, \varepsilon_\beta^2}{4n_\beta}\, a_1 \quad , \quad \text{and}$$

$a_1 = 2.338$ (the first zero of Ai(-a)).

$$T_{h_o} = \frac{2i\, n_\rho}{k_s (1-n_\beta^2)\, \rho^{1/2}\, L^{3/2}} \qquad \text{(the homogeneous head-wave modulus)}$$

$$\phi_o = k_o (L_s + L_r) + k_1 L \qquad \text{(the homogeneous head-wave phase)}$$

For a null gradient ($\gamma = 0$) the refracted field becomes the classical, homogeneous head wave

$$T_h = T_{h_o}\, e^{i\phi_o} \tag{4.20}$$

For a positive gradient ($\gamma > 0$) the refracted field becomes

$$T_{h_2} \sim \begin{cases} T_{h_o} \left[1 + \varepsilon_\beta \sigma_2\, g \right] e^{i\phi_o} & |\sigma_2| << 1 \\ \sum_{n=1}^{\infty} T_d^{(n)} & |\sigma_2| > 1 \end{cases} \tag{4.21}$$

where

$$\sigma_2 = \frac{k_o L \varepsilon_\beta^2}{2n_\beta}$$

$$g = \left[\left(\frac{\pi k_o L}{2n_\beta} \right)^{\frac{1}{2}} e^{-i\pi/4} \left(\frac{1}{2} + e^{-i\sigma_2} \left(\frac{3}{8} \right)^{2/3} \right) - \frac{1}{q_c \ell} \right]$$

and where the nth diving wave, $T_d^{(n)}$, is given by

$$T_d^{(n)} \simeq - e^{i\frac{(n+1)\pi}{2}} \sqrt{\frac{\gamma\beta}{\rho}} \left[\frac{p_n (1-p_n)^{3/2} (n_\beta^2 - p_n^2)^{1/2}}{4(n+1)\, q_n^3 (n_\beta^2 - 2p_n) + \gamma_\beta (n_o^2 - p_n^2)^{\frac{1}{2}} (z+z_o)} \right]^{\frac{1}{2}}$$

$$\cdot V_o^n (1-V_o^2)\, e^{f_n(p_n)} \qquad (4.22)$$

with

$$v_o = \frac{q_n s - p_n}{q_n s + p_n}$$ (the homogeneous plane-wave reflection coefficient).

$$f_n(p_n) = i \left[\rho p_n + (z+z_o)\, q_n + \frac{4(n+1)}{\gamma_\beta} (n_\beta^2 - p_n^2)^{3/2} \right]$$

The field reflected directly at the boundary is given by

$$T_r \simeq \frac{e^{ik_o R_1}}{R_1} v_o \qquad (4.23)$$

for all of the above cases.

To modify these expressions for flat geometry to those appropriate for a spherical boundary at radius r = a, all that is required is to substitute the modified gradient parameter

$$\gamma_{\beta s} = \frac{2n_\beta^2}{a} \pm \gamma_\beta$$

for γ_β and the modified distance factor

$$\rho = a \sin \Delta$$

(where Δ is the angular distance in radians) for ρ.

P-SV motion.-To determine the plane-wave reflection coefficient for P-SV motion, we consider a plane P-wave propagating in the x-z plane at an angle of incidence, θ, with respect to the boundary at z = 0 in a Cartesian coordinate system, as shown in Figure (10). By (1.13) the appropriate potential representation is

$$\underline{u} = f^{-1} \left\{ \text{grad}(f\Phi) + \text{curl curl } (0,0,f\psi) \right\} \tag{4.24}$$

where

$$\Phi = \frac{P}{\rho^{\frac{1}{2}}} \qquad \psi = \frac{S}{\rho^{\frac{1}{2}}} \tag{4.25}$$

and the potential P and S satisfy separate Helmholtz equations

$$\nabla^2 P + h^2(z)\, P \simeq 0 \tag{4.26}$$

$$\nabla^2 S + k^2(z)\, S \simeq 0 \tag{4.27}$$

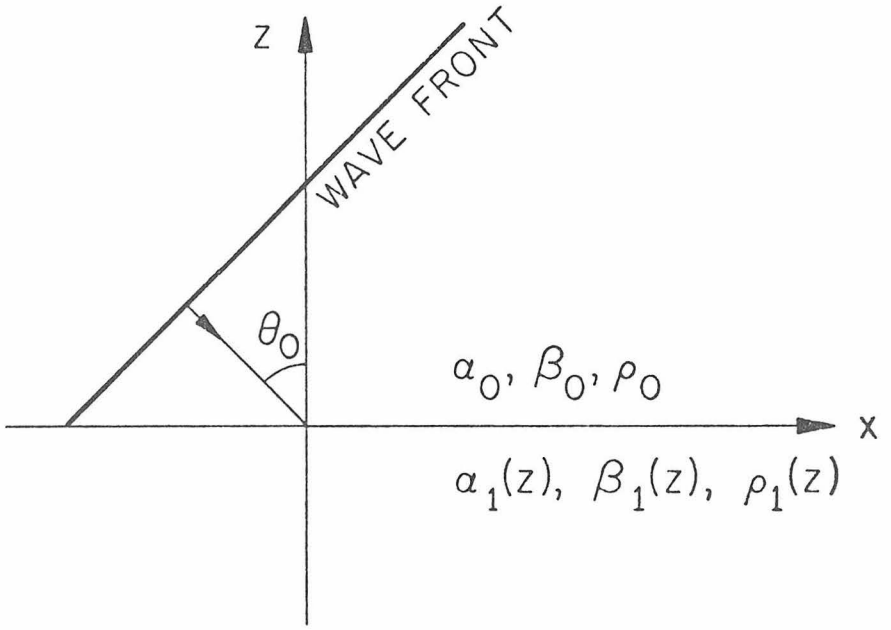
Z
WAVE FRONT
θ_0
$\alpha_0, \beta_0, \rho_0$
X
$\alpha_1(z), \beta_1(z), \rho_1(z)$

Figure 10

at high frequencies as discussed in Section 1. Again, by (4.2), the P and SV wave numbers for $z < 0$ are given by

$$h(z) = \begin{cases} h_o \\ h_o(n_\alpha^2 \pm \gamma_\alpha z)^{\frac{1}{2}} \end{cases} \tag{4.28}$$

$$k(z) = \begin{cases} k_o \\ k_o(n_\beta^2 \pm \beta_\alpha z)^{\frac{1}{2}} \end{cases} \tag{4.29}$$

respectively, where $n_\alpha = \alpha_o/\alpha_1(0)$ and $n_\beta = (\beta_o/\beta_1(0))$.

Using standard vector notation and the properties of the vector operator, $\underline{\nabla}$, we can rewrite (4.24) as

$$\underline{u} = \underline{\nabla}\Phi + \frac{f'}{f}\Phi + \underline{e}_z \frac{f'}{f} \times \underline{\nabla} \times (0,0,\psi) + \underline{\nabla} \times \underline{\nabla} \times (0,0,\psi)$$

Now by (1.7a), the ratio (f'/f) must have the following form for high-frequency P-SV decoupling

$$f'/f = \frac{\lambda + 2\mu}{\lambda + \mu}\left[\frac{\rho'}{\rho} + \frac{2\mu'}{\lambda + 2\mu}\right]$$

where primes indicate differentiation with respect to z. From the form of ρ and μ for $z < 0$ in (4.3) and (4.4), we see that the terms involving the ratio (f'/f) are or order (γ) and (γk_o) in Φ and Ψ, respectively, while the term $\nabla\Phi$ and $\underline{\nabla} \times \underline{\nabla} \times \psi$ are of order (h_o) and $k_o^2)$ respectively. Thus for high frequencies and small gradients

(e.g. $|\gamma/k_o| << 1$) the terms involving the ratio (f'/f) can be neglected, and (4.24) becomes

$$\underline{u} \simeq \text{grad } \Phi + \text{curl curl } (0,0,\psi) \tag{4.30}$$

or in component form

$$\begin{aligned} u_x &= \frac{\partial}{\partial x}\Phi + \frac{\partial^2}{\partial x \partial z}\psi \\ u_z &= \frac{\partial}{\partial z}\Phi - \frac{\partial^2}{\partial x^2}\psi \end{aligned} \tag{4.31}$$

with $\underline{u} = \hat{e}_1 u_x + \hat{e}_3 u_z$.

The appropriate boundary conditions for a plane, welded interface for P-SV motion are

$$u_x(0_+) = u_x(0_-) \quad , \quad u_z(0_+) = u_z(0_-) \tag{4.32}$$

for continuity of displacement and

$$\tau_{xz}(0_+) = \tau_{xz}(0_-) \quad , \quad \tau_{zz}(0_+) = \tau_{zz}(0_-) \tag{4.33}$$

for continuity of stress, where

$$\tau_{xz} = \mu\left(\frac{\partial u_z}{\partial x} + \frac{\partial u_x}{\partial z}\right)$$

$$\tau_{zz} = \lambda\left(\frac{\partial u_x}{\partial x} + \frac{\partial u_z}{\partial z}\right) + 2\mu \frac{\partial u_z}{\partial z}$$

Again, we assume standard variable-separable solutions to (4.26) and (4.27)

$$p(x,z) = X_p(x)\ \hat{P}(z)$$

$$s(x,z) = X_s(x)\ \hat{S}(z)$$

so that we obtain

$$\frac{d^2X_p}{dx^2} + h^2\ X_p = 0$$

$$\frac{d^2\hat{P}}{dz^2} + \left[\ h^2(z) - h^2\ \right]\hat{P} = 0$$

for P motion, and

$$\frac{d^2X_s}{dx^2} + \kappa^2\ X_s = 0$$

$$\frac{d^2\hat{S}}{dz^2} + \left[\ k^2(z) - \kappa^2\ \right]\hat{S} = 0$$

for SV motion. Here the separation constants h and κ are identified as the horizontal components of the P and SV wave numbers, respectively. These equations and their solutions have the same form as in the acoustic and SH cases, and we can write the complete solutions

immediately as

$$P_{oj}(x,z) = e^{i(hx - \eta_\alpha z)} + V_{pp_j}\, e^{i(hx + \eta_\alpha z)} \quad ; \; j=1,2 \quad ; \; z > 0$$

$$\begin{pmatrix} P_1(x,z) \\ \\ P_1(x,z) \end{pmatrix} = \begin{pmatrix} U_{pp_1}\, Ai^{(1)}(-\zeta_{\alpha-}) \\ \\ U_{pp_2}\, Ai(-\zeta_{\alpha+}) \end{pmatrix} e^{ih_1 x} \quad ; \quad z < 0 \tag{4.34}$$

$$S_{oj}(x,z) = V_{ps_j}\, e^{i(\kappa x + \eta_\beta z)} \quad ; \; j = 1,2 \quad ; \quad z > 1$$

$$\begin{pmatrix} S_1(x,z) \\ \\ S_2(x,z) \end{pmatrix} = \begin{pmatrix} U_{ps_1}\, Ai^{(1)}(-\xi_-) \\ \\ U_{ps_2}\, Ai(-\xi_+) \end{pmatrix} \quad ; \quad z < 1 \tag{4.35}$$

where

$$\eta_\alpha = (n_o^2 - h^2)^{\frac{1}{2}} = h_o(1 - p^2)^{\frac{1}{2}} = h_o q$$

$$\eta_p = (k_o^2 - \kappa^2)^{\frac{1}{2}} = h_o(\ell^2 - p^2)^{\frac{1}{2}} = h_o \nu$$

$$\zeta_{\mp} = \varepsilon_\alpha^{-2}(n_\alpha^2 - p^2 \mp \gamma_\alpha z) \quad ; \qquad \varepsilon_\alpha = (\gamma_\alpha / n_o)^{1/3}$$

$$\xi_{\mp} = \varepsilon_b^{-2}(n_b^2 - p^2 \mp \gamma_b z) \quad ; \qquad \varepsilon_b = (\gamma_b / n_o)^{1/3}$$

$$\ell = k_o/h_o = \alpha_o/\beta_o \; , \quad n_b = \ell n_\beta \; , \quad \gamma_b = \ell^2 \gamma_\beta \; , \quad p = \sin\theta$$

and j = 1,2 refers to a negative or positive gradient respectively. We are also using the convention

$$Ai^{(1)}(-\zeta) \equiv Ai\left(-\zeta e^{i2\pi/3}\right)$$

for brevity. In writing the above solutions, we have made the following assumptions:

(1) The incident plane P wave has unit amplitude.

(2) Both P and SV waves may be reflected into the upper homogeneous half space and transmitted into the lower heterogeneous half space.

(3) The radiation conditions for both P and SV waves in the heterogeneous half-space are analogous to those assumed in the acoustic case for negative and positive gradients as $z \to -\infty$.

The four constants, V_{pp}, V_{ps}, U_{pp}, and U_{ps}, can be evaluated by putting (4.34) and (4.35) into the four boundary condition equations (4.32) and (4.33). Making these substitutions, we obtain the four equations

$$\left[\frac{\partial \Phi_{oj}}{\partial x} + \frac{\partial^2 \psi_{oj}}{\partial x \partial z}\right]_{0_+} = \left[\frac{\partial \Phi_j}{\partial x} + \frac{\partial^2 \psi_j}{\partial x \partial z}\right]_{0_-} \tag{4.36a}$$

$$\left[\frac{\partial \Phi_{oj}}{\partial z} - \frac{\partial^2 \psi_{oj}}{\partial x^2}\right]_{0_+} = \left[\frac{\partial \Phi_j}{\partial z} - \frac{\partial^2 \psi_j}{\partial x^2}\right]_{0_-} \tag{4.36b}$$

$$\lambda_o \left[\frac{\partial^2 \Phi_{oj}}{\partial x^2} + \frac{\partial^2 \Phi_{oj}}{\partial z^2} \right]_{0_+} + 2\mu_o \left[\frac{\partial^2 \Phi_{oj}}{\partial z^2} - \frac{\partial^3 \psi_{oj}}{\partial x^2 \partial z} \right]_{0_+} =$$

(4.36c)

$$= \lambda_1 \left[\frac{\partial^2 \Phi_j}{\partial x^2} + \frac{\partial^2 \Phi_j}{\partial z^2} \right]_{0_-} + 2\mu_1 \left[\frac{\partial^2 \Phi_j}{\partial z^2} - \frac{\partial^3 \psi_j}{\partial x^2 \partial z} \right]_{0_-}$$

$$\mu_o \left[2 \frac{\partial^2 \Phi_{oj}}{\partial x \partial z} + \frac{\partial^3 \psi_{oj}}{\partial x \partial z^2} - \frac{\partial^3 \psi_{oj}}{\partial x^3} \right]_{0_+} = \mu_1 \left[2 \frac{\partial^2 \Phi_{ij}}{\partial x \partial z} + \frac{\partial^3 \psi_{1j}}{\partial x \partial z^2} - \frac{\partial^3 \psi_{1j}}{\partial x^3} \right]_{0_-}$$

(4.36d)

where

$$\Phi_{oj} = \rho_o^{-\frac{1}{2}} \left(e^{i\eta_\zeta z} + v_{wj} e^{-i\eta_\zeta z} \right) e^{ihx}$$

$$\Phi_j = U_{pp_j} \rho_1^{-\frac{1}{2}}(z) \Lambda_{\alpha j} e^{ih_1 x}$$

$$\psi_{oj} = V_{ps_j} \rho_o^{-\frac{1}{2}} e^{i(\kappa x - \eta_\beta z)}$$

$$\psi_j = U_{ps_j} \rho_1^{-\frac{1}{2}}(z) \Lambda_{\beta j} e^{i\kappa_1 x} \quad , j = 1,2$$

and we define

$$\begin{pmatrix} \Lambda\alpha_1 \\ \Lambda_{\alpha_2} \end{pmatrix} = \begin{pmatrix} \mathrm{Ai}^{(1)}(-\zeta_-) \\ \mathrm{Ai}(-\zeta_+) \end{pmatrix}_{z=0}$$

$$\begin{pmatrix} \Lambda\beta_1 \\ \Lambda\beta_2 \end{pmatrix} = \begin{pmatrix} \mathrm{Ai}^{(1)}(-\xi_-) \\ \mathrm{Ai}(-\xi_+) \end{pmatrix}_{z=0}$$

Completing the indicated differentiation, we obtain the following fourth order matrix equation.

$$
\begin{bmatrix}
im^{\frac{1}{2}} & \eta_\beta m^{\frac{1}{2}} & -i\Lambda\alpha_j & -i\rho_1^{\frac{1}{2}}\frac{d}{dz}\left(\rho_1^{-\frac{1}{2}}\Lambda\beta_j\right) \\
-i\eta_\alpha m^{\frac{1}{2}} & h^2 m^{\frac{1}{2}} & -\rho_1^{\frac{1}{2}}\frac{d}{dz}\left(\rho^{-\frac{1}{2}}\Lambda\alpha_j\right) & -h^2\Lambda\beta_j \\
-\left[h^2\lambda_o+\eta_\alpha^2(\lambda_o+2\mu_o)\right]m^{\frac{1}{2}} & -2ih^2\eta_\beta\mu_o & E\alpha_j & -2h^2\mu_1\rho_1^{\frac{1}{2}}\frac{d}{dz}\left(\rho^{-\frac{1}{2}}\Lambda\beta_j\right) \\
2\eta_\alpha\mu_o m^{\frac{1}{2}} & i(h^2-\eta_\beta^2)\mu_o m^{\frac{1}{2}} & -2i\mu_1\rho_1^{\frac{1}{2}}\frac{d}{dz}\left(\rho^{-\frac{1}{2}}\Lambda\alpha_j\right) & -E\beta_j(\xi_o)
\end{bmatrix}
\begin{bmatrix} V_{pp_j} \\ V_{ps_j} \\ U_{pp_j} \\ U_{ps_j} \end{bmatrix}
=
\begin{bmatrix} -im^{\frac{1}{2}} \\ -i\eta_\alpha m^{\frac{1}{2}} \\ \left[\lambda_o h^2 + (\lambda_o + 2\mu_o)\,\eta_\alpha^2\right]m^{\frac{1}{2}} \\ 2\eta_\alpha\mu_o m^{\frac{1}{2}} \end{bmatrix}
\quad ; \quad j=1,2 \qquad (4.37)
$$

where

$$E\alpha_j(\zeta_o) = h^2\lambda_1\Lambda\alpha_j - (\lambda_1 + 2\mu_1)\,\rho_1^{\frac{1}{2}}\frac{d^2}{dz^2}\left(\rho_1^{\frac{1}{2}}\Lambda\alpha_j\right)$$

$$E\beta_j(\zeta_o) = i\mu_1\left[h^2\Lambda\beta_j + \rho_1^{\frac{1}{2}}\frac{d^2}{dz^2}\left(\rho_1^{\frac{1}{2}}\Lambda\beta_j\right)\right]$$

Here the derivatives of the terms $(\rho_1^{-\frac{1}{2}}\Lambda\beta)$ and $(\rho_1^{-\frac{1}{2}}\Lambda\alpha)$ with respect to z are given by

$$\frac{d}{dz}\left[\rho_1^{-\frac{1}{2}}\begin{pmatrix}\Lambda\alpha_1\\ \Lambda\alpha_2\end{pmatrix}\right] = h_o\left\{\frac{\rho_o^{-\frac{1}{2}}\varepsilon^3}{4n_\rho^{3/2}}\begin{pmatrix}-Ai^{(1)}(-\zeta_o)\\ Ai(-\zeta_o)\end{pmatrix}\right. \tag{4.38}$$

$$\left. + \rho_1^{-\frac{1}{2}}\varepsilon_\alpha\begin{pmatrix}e^{i2\pi/3}\,Ai^{(1)'}(-\zeta_o)\\ -Ai'(-\zeta_o)\end{pmatrix}\right\}$$

$$\frac{d}{dz}\left[\rho_1^{-\frac{1}{2}}\begin{pmatrix}\Lambda\beta_1\\ \Lambda\beta_2\end{pmatrix}\right] = h_o\left\{\frac{\rho_o^{-\frac{1}{2}}\varepsilon_b^3}{4n_\rho^{3/2}}\begin{pmatrix}-Ai^{(1)}(-\xi_o)\\ Ai(-\xi_o)\end{pmatrix}\right. \tag{4.39}$$

$$\left. + \rho_1^{-\frac{1}{2}}\varepsilon_b\begin{pmatrix}e^{i2\pi/3}\,Ai^{(1)'}(-\xi_o)\\ -Ai'(-\xi_o)\end{pmatrix}\right\}$$

$$\frac{d^2}{dz^2}\left[\rho_1^{-\frac{1}{2}}\begin{pmatrix}\Lambda\alpha_1\\ \\ \Lambda\alpha_2\end{pmatrix}\right] = h_o^2\varepsilon_\alpha\left\{\begin{pmatrix}-\left[\rho_1^{-\frac{1}{2}}\zeta_o\, e^{i\frac{4\pi}{3}} + \frac{3\rho_o^{-\frac{1}{2}}\varepsilon_\alpha^4}{8n_\rho^{7/2}}\right]Ai^{(1)}(-\zeta_o)\\ \\ \left[\rho^{-\frac{1}{2}}\zeta_o - \frac{3\rho_o^{-\frac{1}{2}}\varepsilon_\alpha^4}{8n_\rho^{7/2}}\right]Ai(-\zeta_o)\end{pmatrix}\right.$$

$$\left. - \frac{\rho_o^{-\frac{1}{2}}\varepsilon_\alpha^2}{2n_\rho^{3/2}}\begin{pmatrix}e^{i2\pi/3}\, Ai^{(1)'}(-\zeta_o)\\ \\ Ai'(-\zeta_o)\end{pmatrix}\right\} \tag{4.40}$$

$$\frac{d^2}{dz}\left[\rho_1^{-\frac{1}{2}}\begin{pmatrix}\Lambda\beta_1\\ \\ \Lambda\beta_2\end{pmatrix}\right] = h_o^2\varepsilon_b^2\left\{\begin{pmatrix}-\left[\rho_1^{-\frac{1}{2}}\xi_o\, e^{i\frac{4\pi}{3}} + \frac{\rho_o^{-\frac{1}{2}}\varepsilon_b^4}{8n_\rho^{7/2}}\right]Ai^{(1)}(-\xi_o)\\ \\ \left[\rho_1^{-\frac{1}{2}}\xi_o - \frac{3\rho_o^{-\frac{1}{2}}\varepsilon_b^4}{8n_\rho^{7/2}}\right]Ai(-\xi_o)\end{pmatrix}\right.$$

$$\left. - \frac{\rho_o^{-\frac{1}{2}}\varepsilon_b^2}{2n_\rho^{3/2}}\begin{pmatrix}e^{i2\pi/3}\, Ai^{(1)'}(-\xi_o)\\ \\ Ai'(-\xi_o)\end{pmatrix}\right\} \tag{4.41}$$

where we have taken $\gamma_\rho = \gamma_\alpha = \gamma_\beta$.

It now remains to solve this fourth order system for the plane-wave reflection coefficients V_{pp} and V_{ps}, operate on these reflection coefficients with the Weyl integral (3.28), and evaluate the integral. In principle, we can solve for the reflection coefficients analytically and evaluate the Weyl integral asymptotically as was done for the simpler acoustic and SH wave cases. In fact, we will do this for the case of negative velocity gradients to indicate how the elastic P-SV result for reflected P-waves compares with the result for reflected acoustic waves. However, the result is cumbersome, and in practice it will be more expedient to formally invert the fourth order matrix equation (4.37) and proceed directly with a numerical integration of the Weyl integral.

In carrying out the analytical evaluation of the reflected P wave field for the case of a negative gradient, we will assume $\mu_o = \lambda_o$ and $\mu_1 = \lambda_1$. Substitution of the upper terms in equations (4.38) through (4.41) into the matrix equation (4.37) gives

$$\begin{bmatrix} im^{\frac{1}{2}} & h_o \nu m^{\frac{1}{2}} & -iAi^{(1)}(-\zeta_o) & ih_o G(\zeta_o) \\ -iqm^{\frac{1}{2}} & h_o p^2 m^{\frac{1}{2}} & G(\zeta_o) & -h_o p^2 Ai^{(1)}(-\xi_o) \\ -(1+2q^2)\mu_o m^{\frac{1}{2}} & -2ih_o p^2 \nu \mu_o m^{\frac{1}{2}} & \mu_1 H(\zeta_o) & 2h_o p^2 \mu_1 G(\xi_o) \\ 2q\mu_o m^{\frac{1}{2}} & ih(2p^2-\ell^2)\mu_o m^{\frac{1}{2}} & 2i\mu_1 G(\zeta_o) & i\mu_1 h_o H(\xi_o) \end{bmatrix}$$

$$\begin{bmatrix} V_{pp_1} \\ V_{ps_1} \\ U_{pp_1} \\ U_{ps_1} \end{bmatrix} = m^{\frac{1}{2}} \begin{bmatrix} -i \\ -iq \\ (1-2q^2)\mu_o \\ 2q\mu_o \end{bmatrix} \tag{4.42}$$

where

$$G(\zeta_o) = \frac{m^{\frac{1}{2}} \varepsilon_\alpha^3}{4n_\rho^{3/2}} Ai^{(1)}(-\zeta_o) - \varepsilon\alpha e^{i\frac{2\pi}{3}} Ai^{(1)'}(-\zeta_o) \tag{4.43}$$

$$G(\xi) = \frac{m^{\frac{1}{2}}\varepsilon_b^3}{4n_\rho^{3/2}} \mathrm{Ai}^{(1)}(-\xi_o) - \varepsilon_b e^{i\frac{2\pi}{3}} \mathrm{Ai}^{(1)'}(-\xi_o) \tag{4.44}$$

$$H(\zeta_o) = \left[p^2 + 3\varepsilon_\alpha^2 \left(\zeta_o e^{i4\pi/3} + \frac{3}{8} \frac{\varepsilon_\alpha^4 m^{\frac{1}{2}}}{n_\rho^{7/2}} \right) \right] \mathrm{Ai}^{(1)}(-\zeta_o)$$

$$+ \frac{3}{2} \frac{\varepsilon_\alpha^4 m^{\frac{1}{2}}}{n_\rho^{3/2}} e^{i2\pi/3} \mathrm{Ai}^{(1)'}(-\zeta_o) \tag{4.45}$$

$$H(\xi_o) = \left[-p^2 + \varepsilon_b^2 \left(\xi_o e^{i4\pi/3} + \frac{3}{8} \frac{\varepsilon_b^4 m^{\frac{1}{2}}}{n_\rho^{7/2}} \right) \right] \mathrm{Ai}^{(1)}(-\xi_o)$$

$$+ \frac{\varepsilon_b^4 m^{\frac{1}{2}}}{2n_\rho^{3/2}} e^{i2\pi/3} \mathrm{Ai}^{(1)}(-\xi_o) \tag{4.46}$$

and as before, $p = \sin\theta$, $q = \cos\theta$, with θ as the angle of incidence.

We are interested in comparing the form of the solution for the reflected P-waves with the form of the solution for reflected acoustic waves. Thus we solve (4.42) for V_{pp} using Cramer's rule. By expanding the determinants forming the numerator and denominator of V_{pp} about their third columns, we can express the P-P reflection coefficient in a form analogous to the acoustic reflection coefficient (3.22), that is

$$V_{pp_1} = \frac{Ai^{(1)}(-\zeta_o)\, D - \varepsilon_\alpha e^{i2\pi/3}\, Ai^{(1)'}(-\zeta_o)\, D_1}{Ai^{(1)}(-\zeta_o)\, E - \varepsilon_\alpha e^{i2\pi/3}\, Ai^{(1)'}(-\zeta_o)\, E_1} \tag{4.47}$$

where the terms multiplying $Ai^{(1)}(-\zeta_o)$ and $Ai^{(1)'}(-\zeta_o)$ have the following form

$$\begin{pmatrix} D \\ D_1 \end{pmatrix} = Ai^{(1)}(-\xi_o) \begin{pmatrix} \Omega_1^1 \\ \Omega_2^1 \end{pmatrix} + \varepsilon_b e^{i2\pi/3}\, Ai^{(1)'}(-\xi_o) \begin{pmatrix} \Omega_3^1 \\ \Omega_4^1 \end{pmatrix} \tag{4.48}$$

and

$$\begin{pmatrix} E \\ E_1 \end{pmatrix} = Ai^{(1)}(-\xi_o) \begin{pmatrix} \Omega_1^2 \\ \Omega_2^2 \end{pmatrix} + {}_b e^{i2\pi/3}\, Ai^{(1)'}(-\xi_o) \begin{pmatrix} \Omega_3^2 \\ \Omega_4^2 \end{pmatrix} \tag{4.49}$$

The Ω_i^j are rather complicated algebraic functions of p involving the elastic constants, density, and gradients. The details of this expansion and expressions for the Ω_i^j are given in Appendix V.

As before, the integral expression for the reflected field from a point source is obtained by putting the plane-wave reflection coefficient, V_{pp}, into the Weyl integral. Thus the reflected P-wave field is given by

$$P = e^{i\frac{\pi}{4}} \sqrt{\frac{h_o}{2\pi\rho}} \int_{-\infty}^{\infty} e^{ik_o R(qq_o + pp_o)} V_{pp_1} \frac{p^{\frac{1}{2}}}{q} dp \qquad (4.50)$$

The integrand has branch points at $p = \pm 1$ and $p = 0$ associated with the radicals $q = (1 - p^2)^{\frac{1}{2}}$ and $p^{\frac{1}{2}}$ as in the acoustic case. In addition, there are branch points at $p = \pm \ell$ associated with the radical $\nu = (\ell^2 - p^2)^{\frac{1}{2}}$. Recall that $\ell = (k_o/h_o) = (\alpha_o/\beta_o)$, thus $|\ell| > 1$. We will choose the branch cuts in the same way as in the acoustic case; in particular

$$-\pi/2 < \arg(q) \leq \pi/2$$

$$-\pi/2 < \arg(\nu) \leq \pi/2$$

The position of the branch cuts in the complex P-plane and are shown in Figure (4.4) for the P-SV case.

Furthermore, the integrand now has two lines of poles defined by the zeros of the denominator of V_{pp} instead of the single line associated with the reflection coefficients for the acoustic and elastic SH waves. These lines of poles are approximately located where $Ai^{(1)}(-\zeta_o) = 0$ and $Ai^{(1)}(-\xi_o) = 0$, respectively; both extend into the first quadrant of the complex p-plane at an angle of $\pi/3$ with respect to the real p axis. The poles associated

with the zeros of $Ai^{(1)}(-\zeta_o)$ extend from the point $p = n_\alpha$ on the real p axis, while those associated with the zeros of $Ai^{(1)}(-\xi_o)$ extend from the point $p = n_b$, where $n_b = \alpha_o/\beta_1(0)$(see Figure 4.4)). In most geophysical applications, $\alpha_o > \beta_1(0)$, so that $n_b > 1$, and the second line of poles will not be crossed in deforming the original contour into the steepest descent path as is indicated in Figure (11). However, in the case that $\alpha_o < \beta_1(0)$, the second line of poles will move to the left of $p = 1$, and we get a double head wave contribution; one of the form PP_1P and the other of the form PS_1P.

In this development, we will restrict the compressional velocity in the upper medium to be greater than the shear velocity in the lower medium ($n_b > 1$) and concentrate on the contribution from the poles extending from the compressional-wave index of refraction, n_α. The exponential term in the integrand, and thus the saddle point and steepest-descents contour are the same as in the acoustic case. Hence, by analogy, we can write the saddle-point contribution to the integral as

$$p_r \simeq \frac{e^{ih_o R_1}}{R_1} V_{pp_1} \tag{4.51}$$

which expresses the ray-theoretical P-wave field reflected directly from the boundary, $z = 0$.

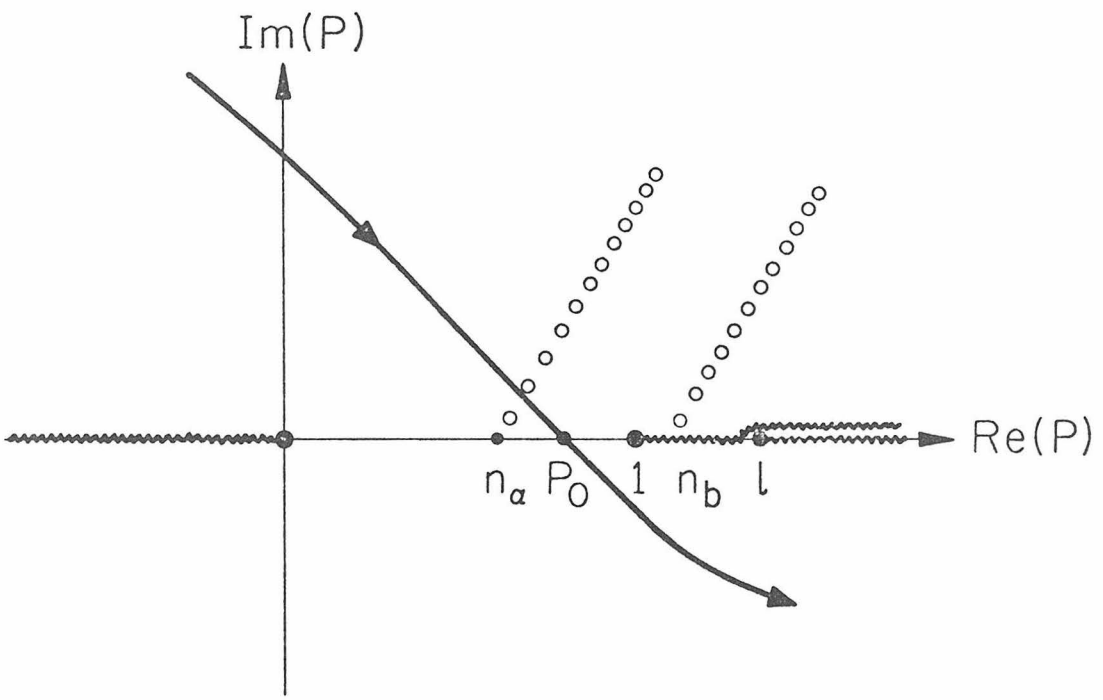

Figure 11

When the angle of incidence, θ_o, is greater than the critical angle for P waves (i.e. $p_o > n_\alpha$), some of the poles associated with the zeros of $Ai^{(1)}(-\zeta_o)$ will be crossed in deforming the original contour into the steepest-descents path. The contribution of these poles to the integral represent the PP_1P head wave. To evaluate the contribution from these poles, we begin as in the acoustic case by expanding the arguments of the Airy functions about $p = n_\alpha$. In particular, we write the argument of $Ai^{(1)}(-\zeta_o)$ as

$$-\zeta_o \, e^{i2\pi/3} = -\tau$$

which gives

$$p \simeq n_\alpha + \frac{\varepsilon_\alpha^2 \tau}{2n_\alpha} \, e^{i\pi/3} \tag{4.52}$$

for $|p - n_\alpha| << 1$ (see the development leading to (3.33)). The argument of $Ai^{(1)}(-\xi_o)$ expressed in terms of τ becomes

$$-\xi_o \, e^{i\frac{2\pi}{3}} = -\varepsilon_b^{-2}(n_b^2 - n_\alpha^2) \, e^{i\frac{2\pi}{3}} - \ell^{-4/3}\tau$$

Under the condition that

$$|\tau| << \left| \frac{(n_b^2 - n_\alpha^2)\ell^{4/3}}{\varepsilon_b^2} \right| ,$$

we can let

$$\xi_o \simeq \varepsilon_b^{-2}(n_b^2 - n_\alpha^2) \tag{4.53}$$

It is evident that as long as $|n_\alpha - n_\beta|$ is not too small (which will be the case in most geophysical situations) and $G_b \ll 1$, the arguments of $Ai^{(1)}(-\xi_o)$ and $Ai^{(1)'}(-\xi_o)$ will be large, and their asymptotic forms (A1-5) and (A1-6) can be used in evaluating contributions to the integral in the vicinity of $p = n_\alpha$.

Let the numerator and denominator of the reflection coefficient be represented as

$$V_{pp} = N_{pp}/D_{pp}.$$

Then the contribution of the N poles crossed in deforming the integration contour into its steepest-descents path when $p_o > n_\alpha$ is given by

$$P_n \sim i\, e^{i\pi/4} \sqrt{\frac{2\pi h_o}{\rho}} \sum_{j=1}^{N} \text{Res}\left[F_{pp}\right] \tag{4.54}$$

where

$$\text{Res}\left[F_{pp}\right] = \left[G_{pp} \frac{\sqrt{p}}{q}\, e^{ih_o R_1 (qq_o + pp_o)} \right]_{\tau=\tau_j} \tag{4.55}$$

and

$$G_{pp} = N_{pp} \Big/ \frac{d}{d\tau} D_{pp} \frac{d\tau}{dp}$$

The approximate locations of the zeros, τ_j, of D_{pp} in the vicinity of $p = n_\alpha$ are

$$\tau_j \simeq a_j - \left[D_{pp} \Big/ \frac{d}{d\tau} D_{pp} \right]_{a_j} \tag{4.56}$$

where a_j is the jth zero of Ai(-x). The derivative term occurring in both (4.55) and (4.56) is

$$\frac{d}{d\tau} D_{pp_1} = Ai(-\tau)\left[\frac{d}{d\tau} E + e_\alpha e^{i2\pi/3} \tau E_1\right]$$

$$- Ai'(-\tau)\left[E + \varepsilon_\alpha e^{i2\pi/3} \frac{d}{d\tau} E_1\right] ,$$

and from (4.52)

$$\frac{d\tau}{dp} \simeq 2n_\alpha \varepsilon^{-2} e^{-i\pi/3} .$$

Substuting the expressions for the D's and E's (4.48) and (4.49) with the Airy functions $Ai^{(1)}(-\xi_o)$ and $Ai^{(1)'}(-\xi_o)$ replaced by their asymptotic forms into the above expressions, we obtain

$$\tau_j \simeq a_j - \varepsilon_\alpha J e^{i2\pi/3} \tag{4.57}$$

where

$$J \simeq \frac{\Omega_2^2 - i(n_b^2 - n_\alpha^2)^{1/2} \Omega_4^2}{\Omega_1^2 - i(n_b^2 - n_\alpha^2)^{1/2} (\Omega_3^2 - \ell^2\Omega_2^2)}$$

and

$$\left[G_{pp}\right]_{\tau=\tau_j} \simeq - i \frac{\varepsilon_\alpha^3}{2n_\alpha} \frac{J\left[\Omega_1^1 - i(n_b^2 - n_\alpha^2)^{1/2}\right]}{\left[i\Omega_1^1 + (n_b^2 - n_\alpha^2)^{1/2} (\Omega_3^2 - \ell^2\Omega_2^2)\right]} \tag{4.58}$$

Expressions for Ω_i^j are given in Appendix V.

The expansion of the argument of the exponential term in (4.55) parallels the acoustic case (see equation (3.38)); in the present case it becomes

$$h_o R_1(qq_o + pp_o) \simeq h_o R \left[p_o\left(n_\alpha + \frac{\varepsilon_\alpha^2 \tau_j\, e^{i\pi/3}}{2n_\alpha}\right) + q_o\left(\sqrt{1-n_\alpha^2} - \frac{\varepsilon_\alpha^2 \tau_j\, e^{i\pi/3}}{2\sqrt{1-n_\alpha^2}}\right)\right]$$

$$\simeq \phi_o + \frac{h_o L \varepsilon_\alpha^2}{2n_\alpha}\, \tau_j\, e^{i\pi/3} \qquad (4.59)$$

where ϕ_o is the classical PP_1P head-wave phase for two homogeneous media and is given by

$$\phi_o = h_o\left[L_s + L_r \right] + h_1 L$$

Thus the residue (4.55) becomes

$$\text{Res}\left[F_{pp}\right] \simeq -\, i\, \frac{\varepsilon_\alpha^3}{2n_\alpha^{1/2} q_{\alpha\alpha}}\, K \exp\left[i\left(\phi_o + \frac{h_o L \varepsilon_\alpha^2}{2n_\alpha}\, \tau_j\, e^{i\pi/3}\right)\right]$$

where $q_\alpha = (1-n_\alpha^2)^{1/2}$ and

$$K = \frac{\left(J(\Omega_1^1 - i(n_b^2 - n_\alpha^2)^{1/2}\right)}{\left[i\Omega_1^2 + (n_b^2 - n_\alpha^2)^{1/2}\,(\Omega_3^2 \ell^2 \Omega_2^2)\right]}$$

The contribution from the first N poles (4.54) describing the PP_1P head-wave potential then becomes

$$P_n \sim \left[\frac{2\pi h_o}{\rho n_\alpha} \right]^{1/2} \frac{\varepsilon_\alpha^3 e^{i(\phi_o + \pi/4)}}{q_\alpha} K \sum_{j=1}^{N} \exp\left[i \frac{h_o L \varepsilon_\alpha^2 \tau_j}{2n_\alpha} e^{i\pi/3} \right] \tag{4.60}$$

This expression has the same form as the analogous results for the acoustic case (3.39). The only difference is that the simple density ratio, m, in the acoustic case is replaced by the complicated ratio of elastic constants, K, multiplying the sum and by the ratio J in τ_j. From the expressions for Ω_i^j in Appendix V and the definition (4.57), we see that J is of the form

$$J = \frac{\mu_o^2 b_1 + \mu_o \mu_1 b_2 + \mu_1^2 b_3}{\mu_o^2 b_4 + \mu_o \mu_1 b_5 + \mu_1^2 b_6}$$

where the b's are complicated algebraic functions of the indices of refraction, n_α, n_β, and ℓ only. Similarly, from the definition of K above, we see that

$$K = \left[\frac{\mu_o^2 b_1^1 + \mu_o \mu_1 b_2^1 + \mu_1^2 b_3^1}{\mu_o^2 b_4^1 + \mu_o \mu_1 b_5^1 + \mu_1^2 b_6^1} \right]^2$$

where the b^{l}'s are in general different functions of n_α, n_β, and ℓ.

The summation in (4.60) is completed exactly as in the acoustic case. We define the parameter

$$\sigma_{\alpha_1} = - i\left(\frac{3\pi}{8}\right)^{2/3} \frac{h_o L\varepsilon_\alpha^2}{2n_\alpha} e^{i\pi/3} \tag{4.61}$$

and follow the development from (3.40) to (3.46), which yields an expression for the PP_1P head-wave potential for $|\sigma_\alpha| << 1$

$$P_n \simeq \frac{2in_\alpha K}{h_o q_\alpha \rho^{\frac{1}{2}} L^{3/2}} e^{i\phi_o}\left[1 - \sigma_{\alpha_1}^{3/2}\right] \tag{4.62}$$

As was also true in the acoustic case, the poles spread out and move away from the real p axis in a positive imaginary direction as $|\sigma_\alpha|$ increases. For $|\sigma_\alpha| >> 1$, the pole nearest the real p axis will dominate, and the asymptotic expression for the PP_1P head wave becomes

$$P_n \simeq - \left[\frac{2\pi h_o}{\rho n_\alpha}\right]^{\frac{1}{2}} \frac{\varepsilon_\alpha^3 K}{q_\alpha} e^{i(\phi_o - \delta_{\alpha_1} + \pi/4)} \cdot \exp\left[-\frac{\sqrt{3}}{4}\frac{h_o L\varepsilon_\alpha^2}{h_\alpha}\left(a_1 + \frac{h_o L\varepsilon_\alpha^3 \, \mathrm{Im}(J)}{4n_\alpha}\right)\right] \tag{4.63}$$

where

$$\delta_{\alpha_1} \simeq \frac{h_o L \varepsilon_\alpha^2}{4n_\alpha} \left(a_j - \frac{h_o L \varepsilon_\alpha^3 \, \mathrm{Re}(J)}{4n_\alpha} \right)$$

Both (4.62) and (4.63) have the same form as their corresponding equations (3.46) and (3.49) in the acoustic case. In particular, we see that the spectral amplitude of the PP_1P head wave for P-SV motion is the same as that for acoustic motion aside from the constant scaling factor, K.

The analysis of the PP_1P "head wave" in the case of a positive velocity gradient will lead to a similar result for small values of the parameter σ_{α_2}. That is, for

$$|\sigma_{\alpha_2}| = \left| \frac{h_o L \varepsilon_{\alpha+}^2}{2n_\alpha} \right| << 1.$$

The spectral amplitude of the PP_1P wave will be the same as for the acoustic case (3.69) except for the ratio of elastic constants, K, multiplying the result. The analysis of the diving wave will be more complicated, however. Mathematically the difficulty arises from the necessity of expanding the reflection coefficient V_{pp}, in terms of both sets of Airy functions, $Ai(-\zeta_+)$ and $Ai(-\xi_+)$. Physically the difficulty is related to the fact that P to SV or SV-P mode conversion will occur at each reflection of the higher order diving waves at the underside of the boundary at $z = 0$. Nevertheless,

we can expect that the direct diving P-wave will have the same form as that for the acoustic case (equation (3.81) with n = 1) with V_o replaced by V_{pp_o}, where V_{pp_o} is the PP reflection coefficient for two homogeneous media.

To convert the results for P-SV motion for a plane boundary to those appropriate for a spherical boundary, it is necessary to see how the continuity conditions across a jump in elastic properties behave under the earth-flattening transformation. This is done in Appendix VI, where we see that the transformed spherical boundary conditions have the same form as the plane boundary conditions when $|\kappa a| >> 1$. Thus for crustal and upper mantle wave propagation problems we can use the results based on the plane layer reflection coefficient noting that the P and SV displacement potentials in a spherical and flat system have the following correspondence

$$P_f \leftrightarrow P \qquad\qquad S_f \leftrightarrow aS$$

where the subscript f refers to the flat system. As indicated in Appendix VI, the factor a (the radius to the boundary), is required in the relation between SV potentials to keep things dimensionally correct. This factor can be included in the SV reflection and transmission coefficients V_{ps} and U_{ps} in (4.35) when making the earth-flattening transformation. It does not

enter into the analysis of the reflection and refraction of P-waves.

Thus to complete the conversion of above results for a plane boundary to those for a spherical boundary at radius r = a for reflected P-waves, it is only necessary to introduce the spherical mapping gradient and replace the distance factor $\rho^{-\frac{1}{2}}$ by $[a \sin \Delta]^{-\frac{1}{2}}$. In this case the mapping applies to both compressional and shear velocities, and we replace the gradient parameters γ_α and γ_β by

$$\gamma_{\alpha s} = \frac{2n_\alpha^3}{a} \pm \gamma_\alpha$$

and

$$\gamma_{\beta s} = \frac{2n_\beta^3}{a} \pm \gamma_\alpha$$

5. Numerical results

We now wish to consider some of the implications of the foregoing analysis in terms of numerical results for several specific models. We will consider numerical results based on both the analytic asymptotic expressions obtained for the refracted and reflected waves as well as results obtained by exact numerical integration of the Weyl integral (2.37) containing the appropriate reflection coefficients. The consideration of both asymptotic solutions and exact numerical solutions together provides insight into the problem that would not be realized through either approach by itself. Through the asymptotic solution we can see explicitly how various physical parameters affect the solution over limited ranges and we can 'understand' the predicted wave phenomena in terms of mode and ray propagation through the study of poles and saddle points. On the other hand exact numerical methods provide a means for obtaining solutions over an arbitrary range of parameters (i.e. arbitrary frequencies and gradients) and may reveal important properties of the wave field for situations in which existing asymptotic solutions do not apply. In the case of a positive velocity gradient, for example, numerical integration reveals some interesting interference properties of the diving wave field in

the intermediate distance range not covered by either wave- or ray-theoretical asymptotic results. The inversion of seismic data can be accomplished quickly and cheaply for situations in which the asymptotic solutions are valid. When conditions are not so favorable (which is probably the case in most situations), more expensive and time-consuming exact numerical methods must be used. However, the process of numerical inversion can often be optimized when asymptotic solutions are available to serve as a guide. Finally, the agreement between asymptotic and exact numerical solutions for appropriate ranges of parameters provides an important internal consistency check on the solutions to the problem as posed.

By exact numerical integration of the integral, we mean that the answer is limited only by computational considerations such as word length and round-off error and not by analytical approximations to the integral itself. Thus the answers obtained by numerical integration of the Weyl integral are not constrained by the assumption of high frequencies and small gradients ($\varepsilon << 1$) made in the analytical evaluation of the integral using the asymptotic forms of the Airy functions occurring in the reflection coefficients. Of course the answer will still be limited by the assumptions made in section 1 which were to put the equations of motion in the form of canonical Helmholtz equations. For acoustic and elastic SH-

motion these assumptions required small density and shear modulus gradients, and for decoupled elastic P-SV motion they required high frequencies. Similarly, in the case of a spherical earth, the 'exact' answer will be limited to the extent that the Weyl integral (2.37) is an approximation to the original integral (2.30) for direct waves from a point source in a spherical earth.

The actual numerical integration is completed in a manner similar to that described by Phinney and Cathles (1969) or Richards (1970). In particular, the original integral along the real p axis is deformed into a finite path in the complex p-plane such that contributions with the appropriate phase (or angle of incidence) are included near the center of the path and such that the integrand decays exponentially toward both ends of the path. This path will often roughly parallel a steepest descents path through the saddle point, although it need not coincide with the true steepest descents path at any point. The integral is then evaluated by applying a standard Simpson integration algorithm separately to the real and imaginary parts of the integrand along this path. Naturally the path must be of sufficient length that the contributions from either end of the path are numerically insignificant with respect to those along the central portion of the path. A single path can be used to evaluate the integral for a range of distances and frequencies thus considerably reducing the computation time. A

modification of the program EXACT based on these principles written by Richards (1970) was used to evaluate the Weyl integral numerically in the examples presented below. A description of this program can be found in Richards' thesis (Richards, 1970).

The Airy functions occurring in the reflection coefficients in the Weyl integral were numerically evaluated using SHARE subroutine HF13, which computes Hankel functions of 1/3 order for complex argument (Berry, 1964). The method used for obtaining Airy functions from one-third order Hankel functions is summarized in Appendix I. Using these procedures in a single precision program on an IBM 360-75 computer, the values of the Airy functions (or the modified Hankel functions discussed in Appendix I) check to an accuracy of at least four significant figures with the tabulated values for modified Hankel functions with complex arguments compiled by the Staff of the Computation Laboratory (1945).

We will begin our discussion of the numerical results for specific models by considering the amplitude spectra of both reflected and refracted waves obtained by the exact numerical integration of the Weyl integral in the case of a flat geometry. This will provide an opportunity to illustrate the integration paths used in doing the numerical integration in the case of both negative and positive velocity gradients as well as in the classical case of a homogeneous refractor. We will then compare the results

obtained by exact numerical integration with the asymptotic solutions obtained in the preceding sections and finally consider the numerical results for some spherical earth models.

Thus, consider the flat acoustic model illustrated in Figure 12 consisting of a homogeneous half space with a velocity of 7.0 km/sec over a half space in which the velocity is 8.0 km/sec at the boundary, below which it may either increase or decrease with depth according to (3.12) and with a density ratio, m, of 1.2 across the boundary. Both the source and receiver are taken to be at a height of 30 km above the boundary. The theoretical amplitudes of three spectral components, 0.75, 1.0, and 1.5 Hz, are plotted as a function of distance from the source for both reflected and refracted waves in Figure 12. These amplitudes were computed by exact numerical integration of the Weyl integral (3.28) as described above for three values of the gradient parameter, γ, -10^{-3}, 0, and $+10^{-3}$ km^{-1} (see equation 3.12). Note that by (3.12a), the corresponding physical velocity gradients in the lower half space are $\pm 5.2 \times 10^{-3}$ km/sec/km.

The ray-theoretical critical distance for this model and source-receiver geometry occurs at 108 km from the source as indicated by the arrows in Figure 12. The reflected and head wave amplitudes for the homogeneous case ($\gamma = 0$) and their relation to the ray-theoretical critical point are just as described earlier by Cerveny (1965, 1966_6). In particular, note that

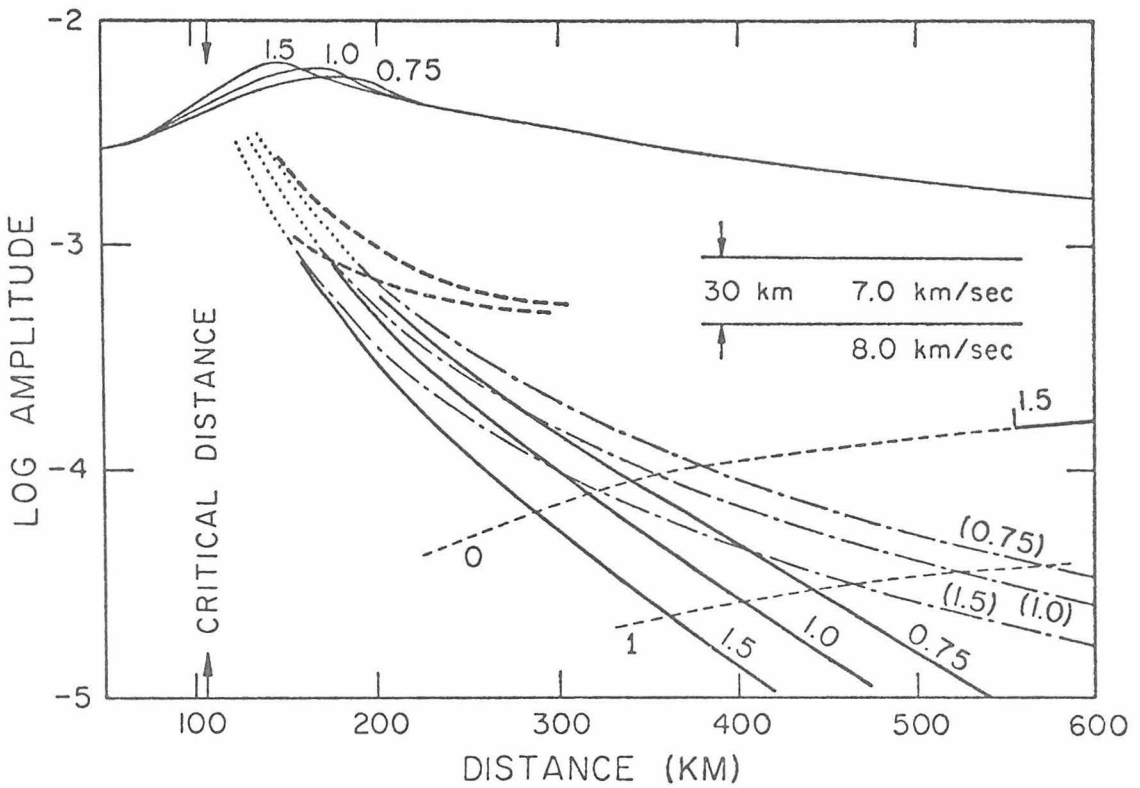
-2
-3
-4
-5
LOG AMPLITUDE
1.5
1.0
0.75
CRITICAL DISTANCE
30 km
7.0 km/sec
8.0 km/sec
1.5
(0.75)
(1.5)
(1.0)
0
1
1.5
1.0
0.75
100
200
300
400
500
600
DISTANCE (KM)

Figure 12.

1) the maximum amplitude of the reflected wave occurs at successively larger distances from the critical point for successively lower frequencies and not at the critical point itself,

2) the reflected wave amplitudes are frequency dependent in the vicinity of the critical point (from about 70 km to 220 km), but on either side of this interval the amplitudes of the three frequencies coincide and the reflected wave can be accurately described by the ray theoretical result (3.32),

3) beyond about 200 km the head wave amplitudes behave according to the classical asymptotic result

$$\Phi_n \propto \frac{2n_o}{k_o(1-n_o^2)m\,\rho^{\frac{1}{2}}\,\gamma^{3/2}}$$

and

4) it is not possible to make a useful distinction between the reflected and head wave contributors to the amplitudes from the vicinity of the critical point out to about 200 km.

The integration paths used in doing the numerical integration for the homogeneous case are shown in Figure 13 a and b. Here the branch cut associated with the reflection coefficient for two homogeneous half spaces (3.25) was chosen such that

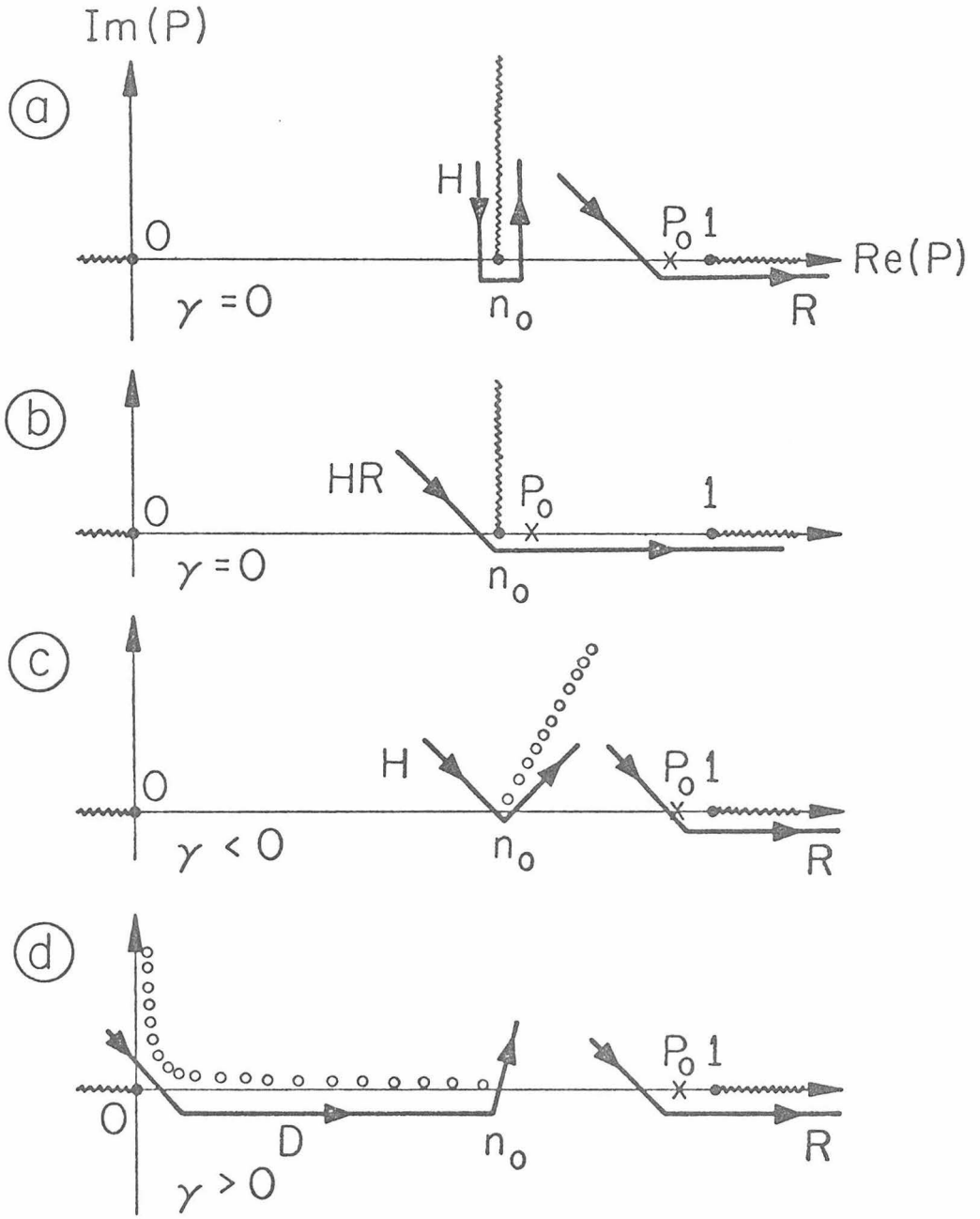
Im(P)
a
H
0
P_0 1
Re(P)
$\gamma = 0$
n_0
R
b
HR
P_0
1
0
$\gamma = 0$
n_0
c
H
P_0 1
0
$\gamma < 0$
n_0
R
d
P_0 1
0
D
n_0
R
$\gamma > 0$

Figure 13.

$$-\frac{\pi}{4} \leq \arg\left[\sqrt{n_o^2 - p^2}\right] < \frac{7\pi}{4}$$

on the upper Riemann sheet. For this choice, the branch cut extends into the positive imaginary half of the p-plane at a right angle to the real axis, and the integrand on either side of the cut decays in an exponential manner away from the branch point on the real axis. When the saddle point (indicated by a cross on the real axis in Figure 13) is a sufficient distance beyond the branch point (corresponding to distances greater than 200 km in Figure 12) it is possible to resolve the separate contributions for the head wave (the branch cut) and the reflected wave (the saddle point) using separate contours as shown in Figure 13a. The contributions of the integrand near the leading and tailing end of these contours are numerically insignificant with respect to the contributions near the branch and saddle points. However, when the saddle point approaches the branch point from the right, the contributions from the tailing end of the branch cut contour and the leading edge of the 'saddle point' contour become significant, and it is no longer possible to make a definite distinction between the head wave and reflected wave contributions. This situation corresponds to the distance interval between the critical point and about 200 km in Figure 12. In this case, the combined contribution is obtained by integrating along the single contour shown in Figure 13b. When

the saddle point is to the left of the branch point, a single straight line contour passing approximately through the saddle point at an angle of $3\pi/4$ is sufficient to obtain the amplitude for the sub-critical reflection.

The 'head wave' amplitudes for the three frequencies in the case of a negative velocity gradient in the lower half-space ($\gamma = -10^{-3}km^{-1}$) are shown as heavy solid lines in Figure 12. Note that they approach the homogeneous head wave amplitudes as the critical point is approached from the right and that they tend to fall off exponentially with increasing distance as predicted by the asymptotic result (3.49). Also note that the spread between frequencies increases with increasing distance such that the high frequency amplitudes fall off at a more rapid rate than the lower frequency amplitudes.

The paths for numerical integration of the Weyl integral in the case of a negative gradient are shown in Figure 13c. As in the homogeneous case, it is possible to separate the 'head' and reflected wave contributions when the saddle point is a sufficient distance to the right of the line of 'head wave' poles. In this case, the 'head wave' contribution is obtained from the V-shaped contour including the lines of poles. The contribution for the reflected wave is obtained from the same contour used in the homogeneous case. Again when the saddle point is sufficiently close to the line of poles, the two contributions

are not distinct, and a single contour like the one shown in Figure 13b is used to obtain the combined contributions of the poles and the saddle point. For the frequencies and gradients we are considering, there is not a significant numerical difference between the amplitudes of the reflected waves in the presence of a negative gradient and those from a homogeneous half-space.

The heavy dashed lines in Figure 12 represent the amplitudes of the 0.75 and 1.5 Hz 'head waves' in the case of a positive gradient in the lower half-space ($\gamma = 10^{-3}$ km^{-1}). Actually these curves represent the envelopes of scalloped amplitude curves generated by the interference of multiple diving waves or normal modes set up between the boundary and the underlying positive velocity gradient. We will consider the details of these scalloped amplitude curves associated with the positive gradient later. Here we only wish to point out the general characteristic of their envelopes. In particular, note that they approach the homogeneous head wave amplitudes as the critical distance is approached and that they decay less rapidly with increasing distance than the homogeneous head wave amplitudes. Also note that the high-frequency curve (1.5 Hz) dies off less rapidly than the low frequency curve (0.75 Hz) with increasing distance. The ray-theoretical amplitudes of the first two diving waves for the positive gradient case are

also plotted in Figure 12 for reference. Note that in this case, the ray-theoretical amplitude for the direct diving wave is only valid beyond 550 km for the 1.5 Hz wave according to the criteria established in section 3 (see equation 3.83). The direct diving wave amplitudes for the 0.75 Hz wave as well as the amplitudes for the diving wave making one reflection for both 1.5 and 0.75 Hz are valid only at distances greater than 600 km. 'Exact' amplitudes for the diving waves were not computed beyond 300 km because the spectrum becomes increasingly rough with distance and the computation time goes up accordingly. These envelope and ray-theoretical amplitude curves are qualitatively similar to those published by Cerveny and Jansky (1966) and Cerveny (1966) for a positive gradient, although these authors as well as Checkin (1965), who did the original analytical work on the effects of positive gradients, do not mention the scalloping of the amplitude curves associated with diving wave interference.

The contours used for numerical integration in the case of the positive gradient are shown in Figure 13d. As before, when the saddle point is a sufficient distance from the last diving wave pole, the diving wave and reflected wave contributions can be numerically separated.

Having established the method for exact numerical integration of the Weyl integral and applied it to the foregoing model, we now

wish to see how the asymptotic analytic solutions compare with the exact answer. For this purpose we will consider acoustic waves in a spherical earth model composed of a crust 30 km thick with an average velocity of 6.4 km/sec and a mantle with a velocity of 8.0 km/sec just below the M discontinuity at a radius of 6367 km. We will take the source and receiver to be located on the 'surface' 30 km above the M-discontinuity, although as indicated earlier the effects of a free surface are not included in these calculations. The theoretical amplitude curves for 1.0 and 5.0 Hz waves refracted by the M-discontinuity in the case of negative and positive velocity gradients of 5×10^{-3} km/sec/km below the M-discontinuity are shown in Figures 14a and 14b, respectively. The ray-theoretical critical distances for this model is at 0.72 degrees or 80 km from the source as indicated by the arrows in Figures 14a and b. The exact amplitude curves for the classical head wave are plotted as a dash-dot line in both Figures for reference.

In Figure 14a the exact theoretical amplitude curves for 1.0 and 5.0 Hz head waves refracted by a mantle with a negative gradient are plotted as solid lines. We see that these curves have the same relation to the exact classical head wave amplitude curves noted in the previous example and illustrated in Figure 12. The dashed curves associated with the two exact curves are the head wave amplitudes predicted by the asymptotic solutions (3.46) for

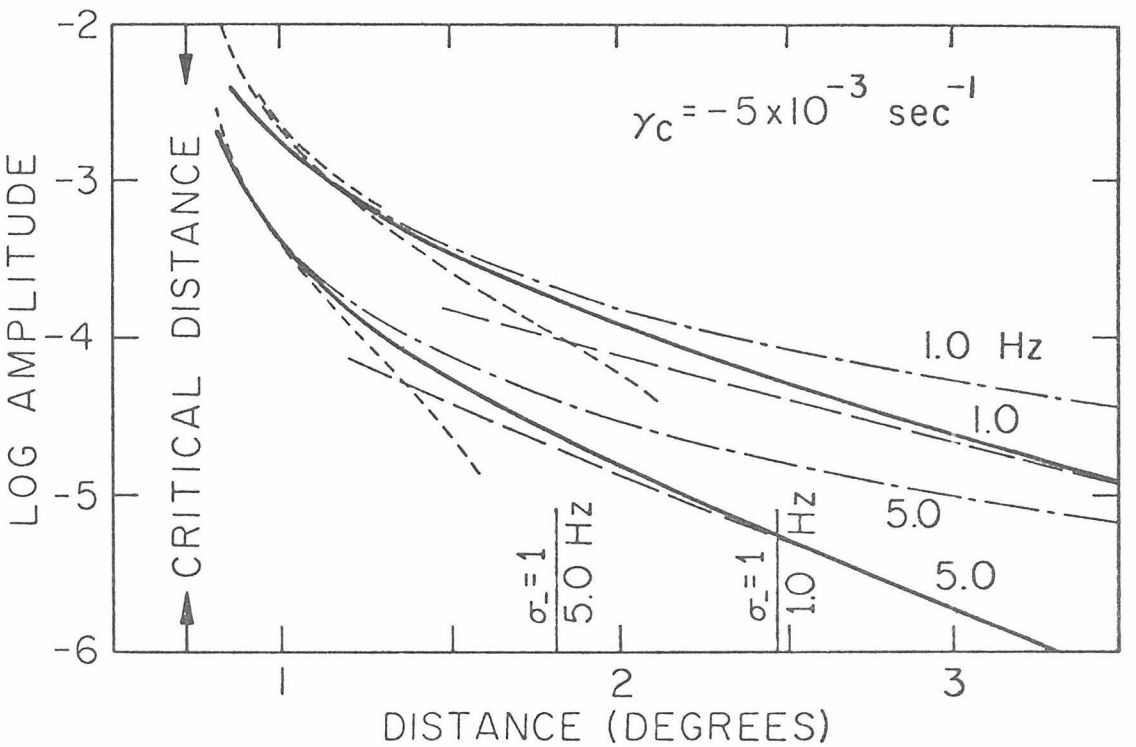
LOG AMPLITUDE
-2
-3
-4
-5
-6
CRITICAL DISTANCE
$\gamma_c = -5 \times 10^{-3}$ sec^{-1}
1.0 Hz
1.0
5.0
5.0
$\sigma = 1$
5.0 Hz
$\sigma = 1$
1.0 Hz
1
2
3
DISTANCE (DEGREES)

Figure 14a.

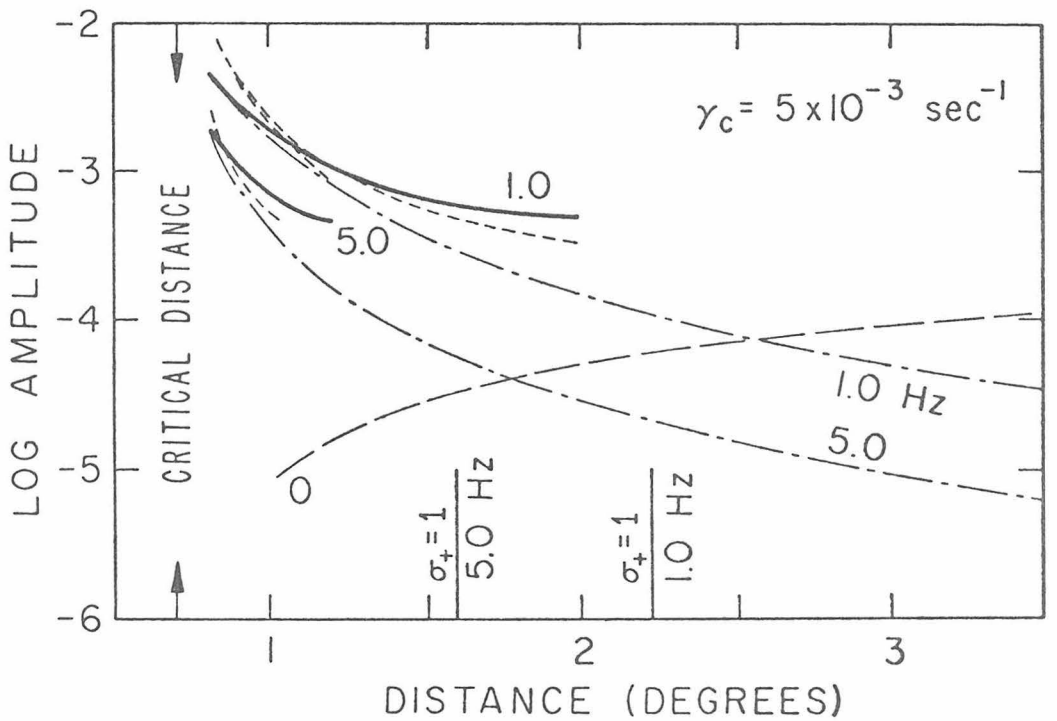
LOG AMPLITUDE
-2
-3
-4
-5
-6
CRITICAL DISTANCE
$\gamma_c = 5 \times 10^{-3}$ sec^{-1}
1.0
5.0
0
1.0 Hz
5.0
$\sigma_+ = 1$
5.0 Hz
$\sigma_+ = 1$
1.0 Hz
1
2
3
DISTANCE (DEGREES)

Figure 14b.

$|\sigma_-| << 1$ and (3.49) for $|\sigma_-| >> 1$. The distances at which σ_- becomes unity for frequencies of 1.0 and 5.0 Hz are also indicated in the figure. It is evident that the asymptotic solutions for $|\sigma_-| >> 1$ (3.49) is a good approximation to the exact solution for both frequencies at distances not too far beyond the point at which $|\sigma_-| = 1$, and that the approximation becomes very good indeed at large distances. On the other hand, the solution for $|\sigma_-| << 1$ (3.46) approximates the exact solution over a fairly short interval (between about 0.8 and 1.0 degrees) at 5.0 Hz, and is not a very useful approximation at all to the 1.0 Hz case. Evidently it is necessary to include more terms than just the first to make the asymptotic solution obtained by summing the poles (3.45) an adequate approximation to the exact solution for the frequencies and gradients considered here. For higher frequencies and smaller gradients these asymptotic approximations improve according to the assumptions made in deriving them; however the approximation for $|\sigma_-| << 1$ keeping only the first term is probably never much better than the asymptotic solution for the classical head wave itself.

In Figure 14b the envelopes of the scalloped amplitudes of the interfering diving waves refracted by a mantle with a positive gradient are plotted as solid lines (see Figure 21 for the exact nature of the amplitude curves). The ray-theoretical amplitude of

the diving wave is also plotted as a solid line beyond the minimum distance for which it provides an adequate description of the 5.0 Hz wave. At shorter distances the ray-theoretical diving wave amplitude is plotted as a dashed line. The 'head wave' amplitudes predicted by the asymptotic solution for $|\sigma_-| << 1$ (3.69) are plotted as short dashed lines for the two frequencies 1.0 and 5.0 Hz, and the distances at which $\sigma_- = 1$ for these two frequencies are also indicated. These curves are smooth and describe the 'head wave' at very small distances from the critical point where the scalloping due to interference has not yet had a chance to develop (i.e., see Figure 17). As was true in the negative gradient case, it appears that the asymptotic solution for the 'head wave' in the case of a positive gradient for $|\sigma_+| << 1$ is of little use when only the first term is retained. Note that the terms involving the derivatives of f(0) in the original Euler-Maclaurin summation formula (3.62) are oscillatory, and as more of these terms are retained, the approximation to the exact scalloped amplitude will improve. Note also that the amplitudes predicted by (3.69) have approximately the same shape as the exact envelope curves, although the predicted curves die off more rapidly with distance than the exact envelopes. However, there is no reason to believe that the two should have any correspondence.

We will use the same basic model of a 6.4 km/sec crust 30 km

thick over a mantle with a 8.0 km/sec velocity immediately below the M-discontinuity to illustrate the effects of curvature and velocity gradients in the mantle on the spectral amplitudes of waves reflected and refracted by the M-discontinuity. The general relations between curvature and velocity gradients in the mantle and their effects on critically and near-critically refracted waves discussed at the end of section 3 are illustrated in Figure 15. Recall in particular, that the classical head wave is generated at the M-discontinuity when the velocity gradient beneath this discontinuity is equal to the negative critical velocity gradient, $\gamma_c = - V/r$, as indicated in Figure 15c. For the model we are considering, this critical velocity gradient is -1.25×10^{-3} km/sec/km, and we will use the classical head wave associated with this gradient as a reference case in each of the following examples. Recall that because of curvature, velocity gradients less negative the critical, null, and positive velocity gradients result in an effective positive velocity gradient as indicated in 15a and 15b, and that velocity gradients more negative than critical result in an effective negative velocity gradient as indicated in Figure 15d.

The theoretical amplitude curves for waves reflected and refracted in the case of a homogeneous crust and mantle ($\gamma_c = 0$, Figure 15b) for three frequencies out to a distance of 30° are shown in Figure 16. The classical head wave amplitudes associated with

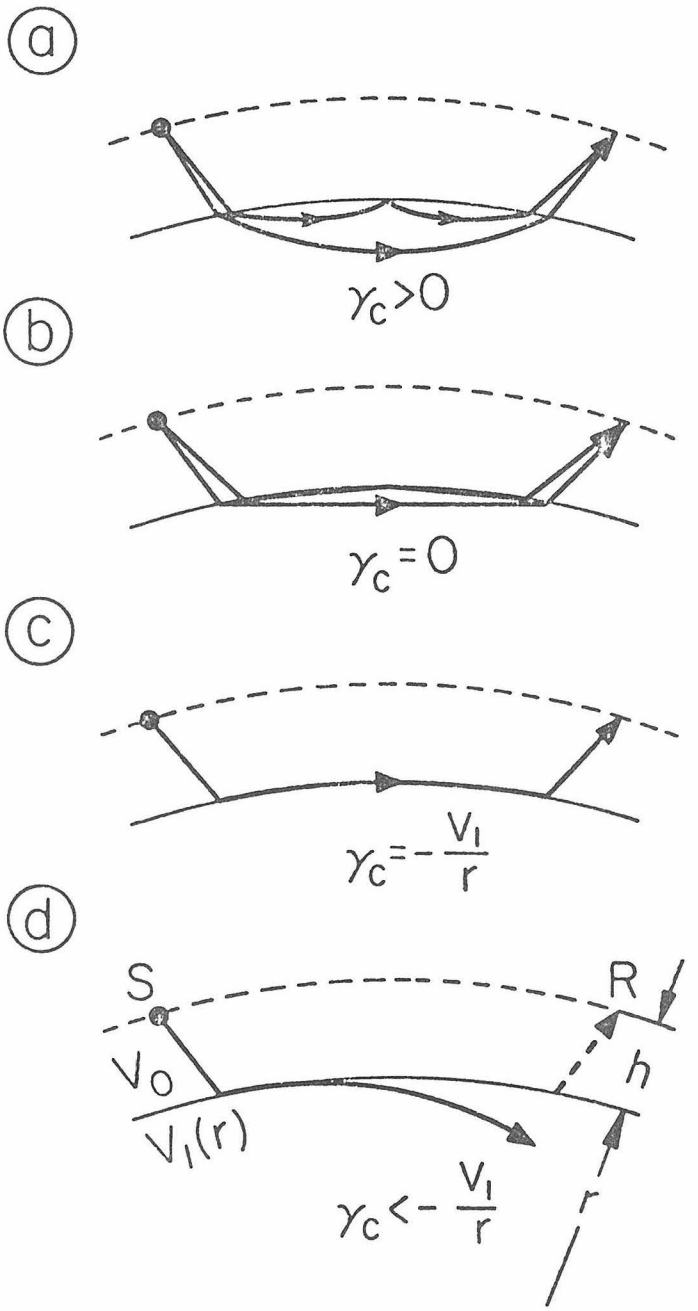
a
$\gamma_c > 0$
b
$\gamma_c = 0$
c
$\gamma_c = -\frac{V_1}{r}$
d
S
R
V_0
$V_1(r)$
h
r
$\gamma_c < -\frac{V_1}{r}$

Figure 15

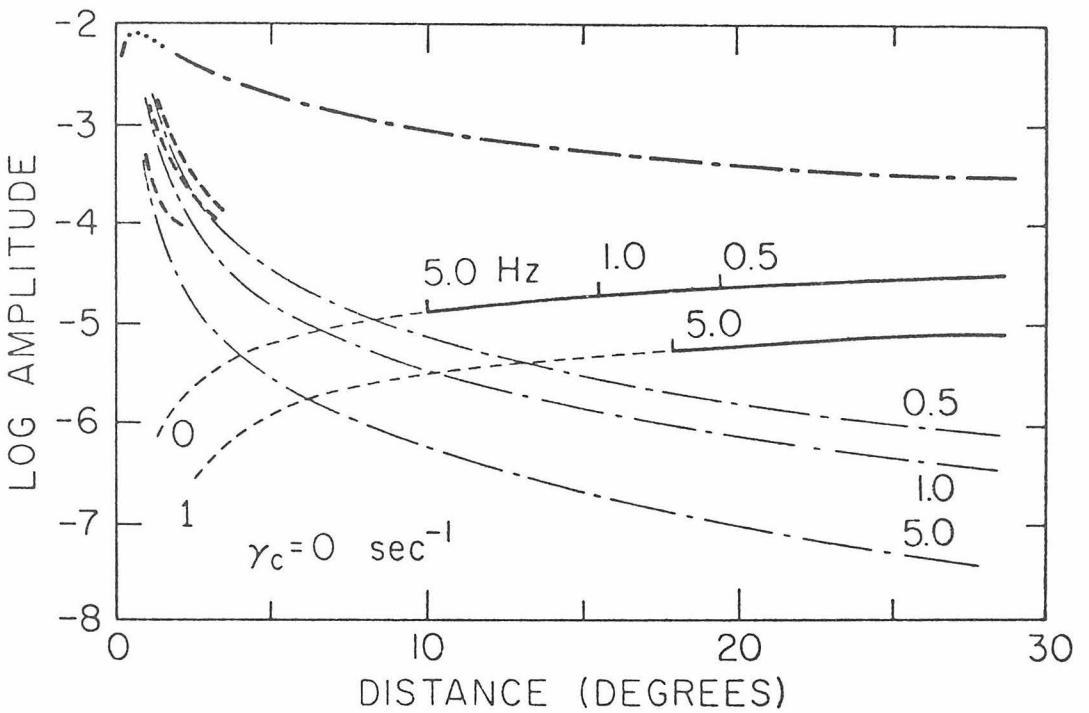
LOG AMPLITUDE
-2
-3
-4
-5
-6
-7
-8
0
10
20
30
DISTANCE (DEGREES)
5.0 Hz
1.0
0.5
5.0
0.5
1.0
5.0
0
1
$\gamma_c = 0$ sec^{-1}

Figure 16

the critical negative gradient are plotted as light dash-dotted lines and the reflected wave amplitude is plotted as a heavy dash-dotted line. The details of the reflected wave amplitudes near the critical distance (Δ = 0.72 degrees) have been omitted. The amplitudes of the first two diving waves (P and PP) are plotted as solid lines with a short vertical bar indicating the minimum distance at which the ray-theoretical description of the wave amplitude becomes valid for the three frequencies 5.0, 1.0, and 0.5 Hz. These distances are approximately 10, 16, and 20 degrees for 5.0, 1.0, and 0.5 Hz waves respectively for the direct diving wave (PP). The direct waves arriving at 10, 16, and 20 degrees from the source have their turning points at depths of 18, 52, and 82 km beneath the M-discontinuity respectively. The PP diving wave arriving at 18 degrees has its turning points at a depth of 13 km below the M-discontinuity.

The envelopes of the amplitudes of the near-critically refracted waves in the vicinity of the critical are plotted as heavy dashed lines. These curves have the same general character as the envelope curves for the positive gradient case in the flat example discussed above. They die off less rapidly with distance than the classical head wave amplitudes and the high frequency components gain on the low frequency components with increasing distance. The details

of these amplitude curves are shown in Figure 17. These theoretical amplitudes were obtained by numerically integrating the Weyl integral along the contour labeled D in Figure 13d. The most significant aspects of these amplitude curves are the following:

1) At small distances beyond the critical point the amplitudes of the waves refracted by the spherical boundary closely follow the exact classical head wave amplitudes (the dash-dotted lines) but have slightly higher amplitudes.

2) As the distance increases away from the critical point, the amplitude curves become noticeably scalloped. This scalloping increases in amplitude and decreases slightly in spatial period with increasing distance.

3) The maxima of the scalloped curves decrease less rapidly with distance than the classical head wave amplitudes, and the maxima of the higher frequency components gain on the lower frequency components with increasing distance as was indicated in describing the envelopes of these curves above.

4) The spatial period of the scalloping decreases with increasing frequency.

The amplitude spectra of the waves refracted by the spherical boundary are plotted in Figure 18 for distances of 1.0 and 3.0 degrees from the source. These amplitude spectra were also

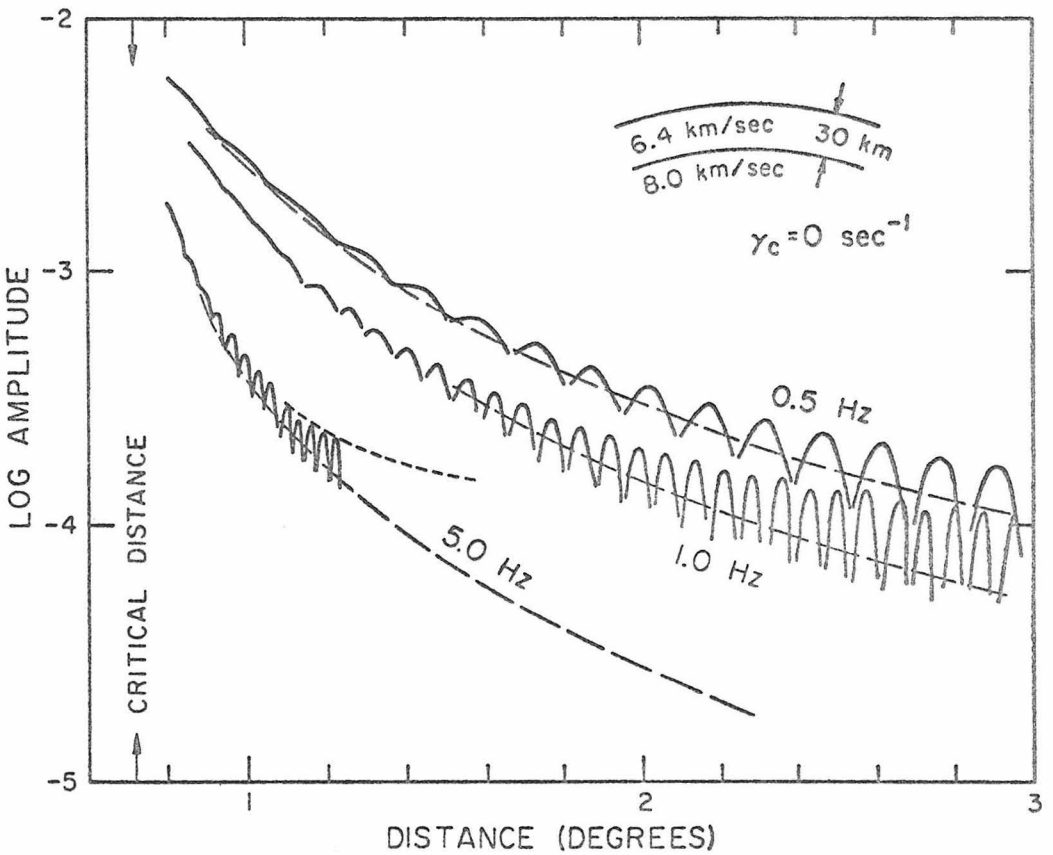
-2
-3
-4
-5
LOG AMPLITUDE
CRITICAL DISTANCE
6.4 km/sec
8.0 km/sec
30 km
$\gamma_c = 0$ sec^{-1}
0.5 Hz
1.0 Hz
5.0 Hz
1
2
3
DISTANCE (DEGREES)

Figure 17.

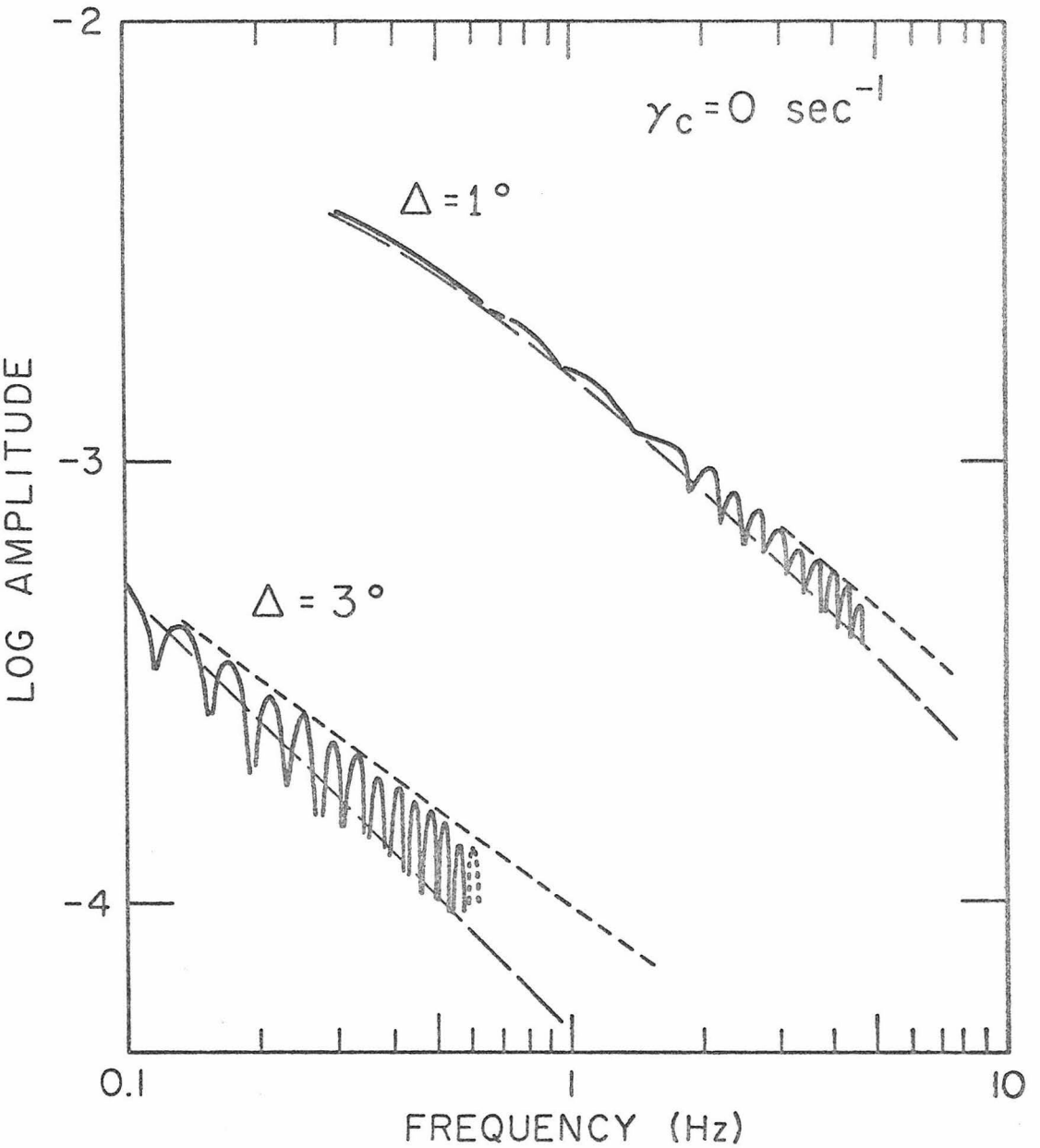
-2
-3
-4
LOG AMPLITUDE
$\gamma_c = 0$ sec^{-1}
$\Delta = 1°$
$\Delta = 3°$
0.1
1
10
FREQUENCY (Hz)

Figure 18.

obtained by numerically integrating the Weyl integral using the contour, D, shown in Figure 13d. At a distance of 1.0 degree from the source the amplitude spectrum of the refracted waves closely follows that of the classical head wave from about 0.3 Hz up to about 1.0 Hz. For frequencies higher than 1.0 Hz, the spectrum of the refracted wave becomes increasingly scalloped and the maximum amplitude of the scalloping dies off slightly less rapidly with increasing frequency than the classical head wave spectrum. The frequency of the scalloping also increases slightly with increasing wave frequency, although not as strongly as is at first apparent on this log frequency plot. At a distance of 3.0 degrees, the spectrum of the refracted wave is already strongly scalloped at a frequency of 0.1 Hz, and the scalloping increases in both amplitude and frequency with increasing wave frequency. The envelope of the scalloped spectrum has a higher amplitude and falls off noticeably less rapidly with frequency than the inverse frequency fall-off of the classical head wave at this distance. We will postpone a discussion of the significance of the scalloped spectrum until the effects of different velocity gradients have been considered; however, it is evident that the scalloping is due to the interference of the multiple diving waves or normal modes propagating in the refracting medium.

The theoretical amplitude curves for waves reflected and refracted in the same earth model but with velocity gradients of $\pm 5 \times 10^{-3}$ sec^{-1} and $\pm 1 \times 10^{-2}$ sec^{-1} in the upper mantle are plotted in Figures 19 and 20 respectively. The amplitude curves for the head waves associated with the negative velocity gradients are shown as heavy solid lines in both figures. These curves exhibit the same general behavior found before in the case of a negative gradient; they approach the classical head wave amplitudes in the vicinity of the critical point and tend toward an exponential decay with increasing distance from the critical point. The effect of the negative gradient to increase the spread between the amplitude curves for different frequency components with distance is quite evident in both figures. The result is that the high frequency components of a head wave are strongly attenuated by the negative velocity gradient, and we can anticipate that when such waves are observed at moderate distance beyond the critical distance, they will have a low amplitude and low frequency character. Note that the effect of doubling the negative velocity gradient from -5×10^{-3} sec^{-1} (Figure 19) to -1×10^{-2} sec^{-1} (Figure 20) results in an order of magnitude decrease in the amplitude of the 1.0 Hz wave at 5.0 degrees. The amplitudes of the 5.0 and 0.5 Hz waves are decreased by greater and lesser amounts, respectively. This sensitivity of the head wave amplitudes to small differences in velocity gradients provides

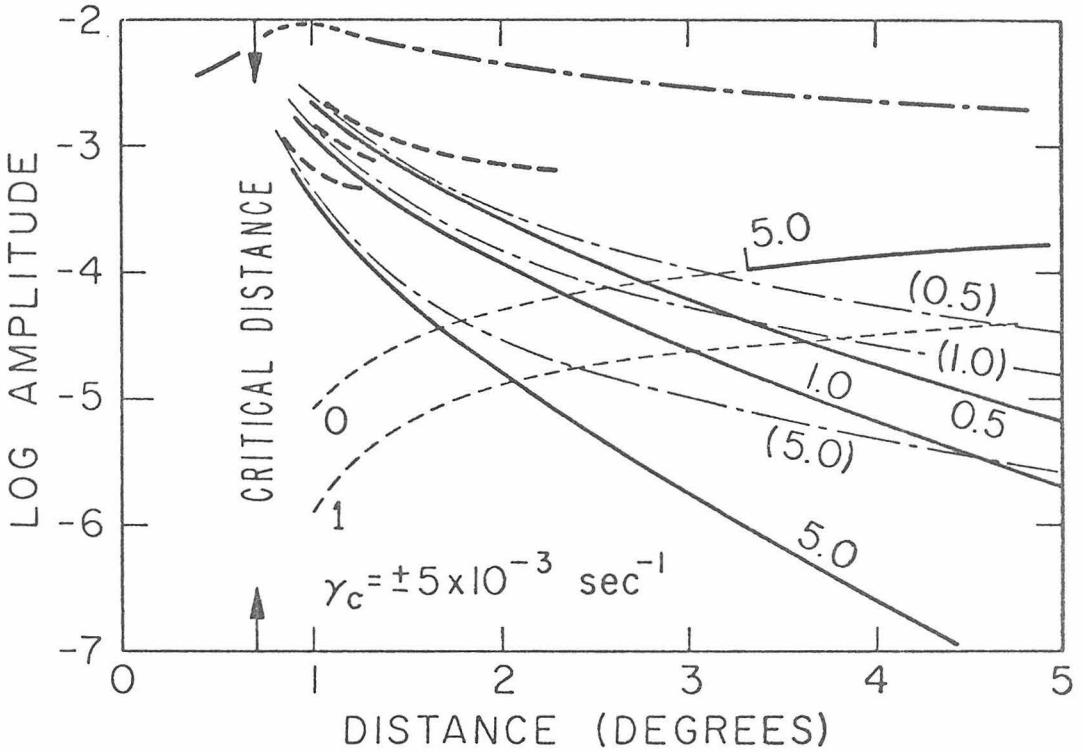
LOG AMPLITUDE
-2
-3
-4
-5
-6
-7
0
1
2
3
4
5
DISTANCE (DEGREES)
CRITICAL DISTANCE
$\gamma_c = \pm 5 \times 10^{-3}$ sec^{-1}
5.0
(0.5)
(1.0)
1.0
0.5
(5.0)
5.0
0
1

Figure 19.

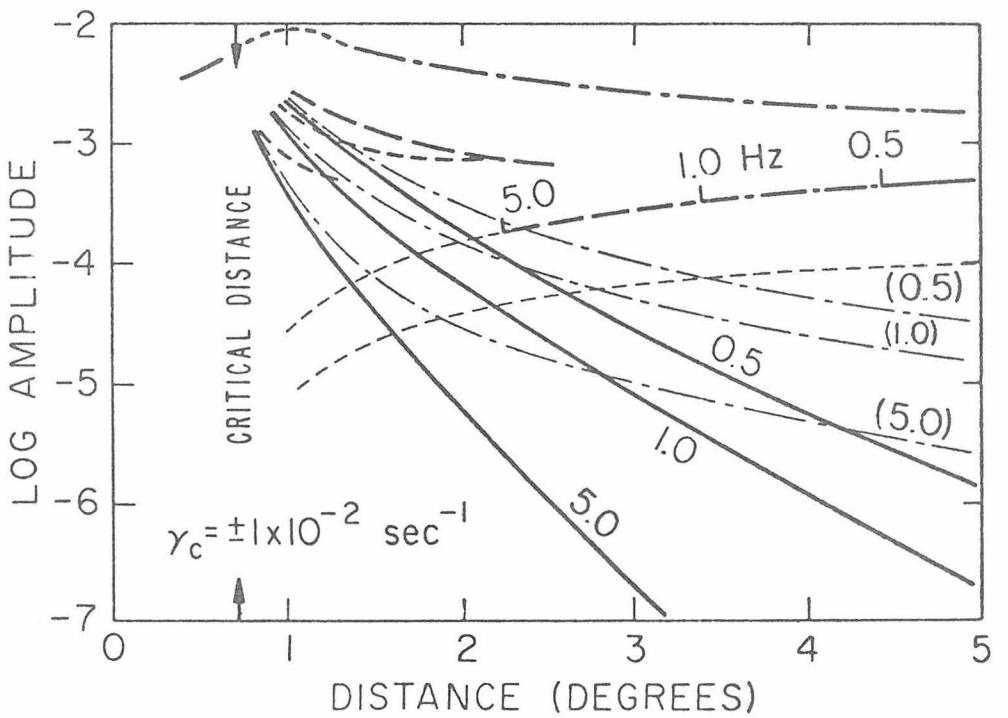
LOG AMPLITUDE
-2
-3
-4
-5
-6
-7
0
1
2
3
4
5
DISTANCE (DEGREES)
CRITICAL DISTANCE
$\gamma_c = \pm 1 \times 10^{-2}$ sec^{-1}
1.0 Hz
0.5
5.0
(0.5)
(1.0)
0.5
(5.0)
1.0
5.0

Figure 20

a potentially useful criteria for detecting negative velocity gradients in major seismic refractors.

The ray-theoretical amplitudes of the first two diving waves (the direct P and the reflected PP paths) are also plotted in Figures 19 and 20. As before, the minimum distances at which the ray-theoretical amplitudes become valid for the three frequency components are indicated by short vertical bars. Comparing the positions of these bars in Figures 19 and 20 with those plotted for the case of a homogeneous mantle in Figure 16, we can see how increasingly strong positive gradients serve to reduce the minimum distance for a valid ray-theoretical description of a given frequency component in the direct diving wave. For example, as the velocity gradient increases from zero in the homogeneous case through 5×10^{-3} to 1×10^{-2}, the minimum distance at which the ray-theoretical amplitude of the 5.0 Hz diving wave reduces from 10 degrees, through 3.2 degrees to 2.2 degrees with the lower frequency component following a similar pattern. A second effect of an increase in the positive gradients is to increase the amplitudes of the diving waves at a given distance. From Figures 19 and 20, we see that a doubling of the positive gradient from 5×10^{-3} to 1×10^{-2} sec^{-1} increases the amplitudes of both the P and PP diving waves by a factor of about 2.5 at 5 degrees.

The envelopes of the amplitudes of the interfering diving

wave modes near the critical distance (indicated by the heavy dashed lines in Figures 19 and 20) fall off less rapidly with distance for increasing positive gradients. Note also that these envelopes tend to level off at amplitudes corresponding to the maximum ray-theoretical amplitudes for the direct diving wave. The details of the amplitude curves for the interfering diving wave modes near the critical distance for the case of a 5×10^{-2} sec^{-1} gradient are shown in Figure 21. Comparing these curves with those plotted in Figure 17 for the homogeneous mantle, we see that the scalloping is more pronounced at a given distance and the envelopes of the scalloped curves fall off less rapidly with distance than for the 5×10^{-3} sec^{-1} gradient than for the homogeneous mantle. (Recall that the homogeneous mantle has an effective positive gradient of 1.25×10^{-3} sec^{-1} due to curvature of the M-discontinuity.)

The theoretical spectral amplitudes of the interfering diving waves at distances of 1.0 and 3.0 degrees from the source for a 5×10^{-3} sec^{-1} gradient are plotted in Figure 22. Again, comparing these curves with those in Figure 18 for the homogeneous mantle, we see that the scalloping is more pronounced and the envelopes die off less rapidly with frequency than those in the homogeneous case. Note in particular that the envelope of the scalloped spectral amplitude curve at 3.0 degrees is almost flat, i.e. it approaches the spectrum of the source, which in this case is a delta function.

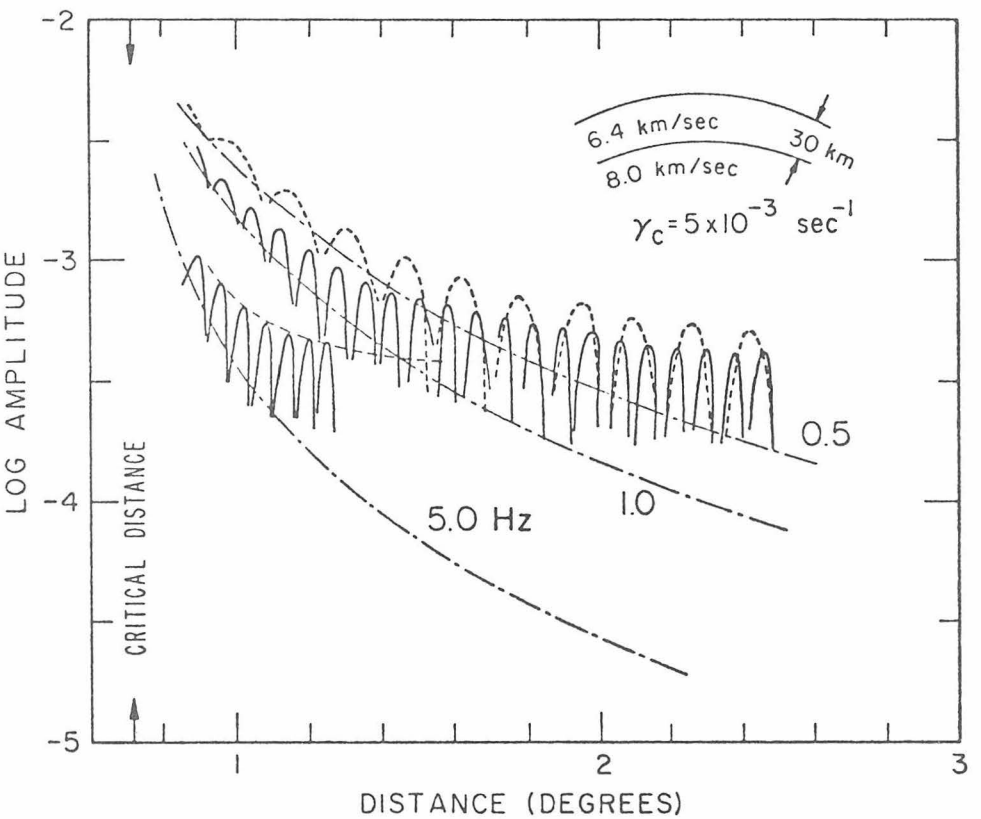
-2
-3
-4
-5
LOG AMPLITUDE
CRITICAL DISTANCE
1
2
3
DISTANCE (DEGREES)
6.4 km/sec
8.0 km/sec
30 km
$\gamma_c = 5 \times 10^{-3}$ sec^{-1}
0.5
1.0
5.0 Hz

Figure 21

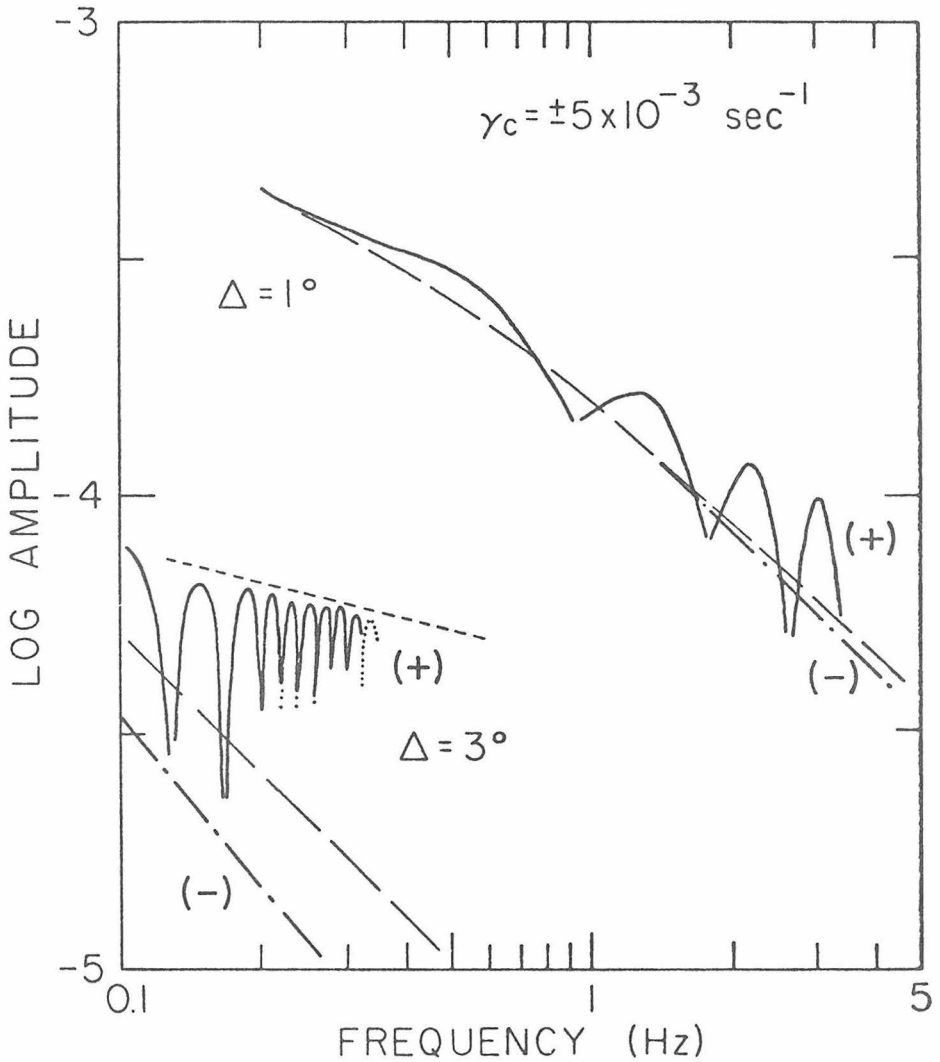
-3
-4
-5
LOG AMPLITUDE
$\gamma_c = \pm 5 \times 10^{-3}$ sec^{-1}
Δ = 1°
(+)
(−)
(+)
Δ = 3°
(−)
0.1
1
5
FREQUENCY (Hz)

Figure 22

At large distances where the individual diving waves are well separated in time, we expect the spectrum of an individual diving wave to be that of the source and be flat as well.

The amplitude spectra of the head waves from the negative gradient -5×10^{-3} sec^{-1} are also shown in Figure 22 (they are plotted as heavy dash-dotted lines). Note that they are smooth and fall off more rapidly with frequency than the inverse frequency fall off of the classical head wave. This feature of the head-waves from a negative gradient was alluded to above when we pointed out the larger spread in their amplitude curves compared to the classical head wave amplitude curves. The effect of increasingly strong negative gradients is to increase the rate of fall-off of the head wave spectral amplitudes with frequency as can be seen in Figures 19 and 20. This attenuation of high frequency with respect to low frequency components by the negative velocity gradient is just the opposite behavior one might intuitively expect if one's 'intuition' is based primarily on a surface wave analog. In particular, it may at first sight seem reasonable to expect the longer wave lengths to 'feel' the lower velocities at depth and to be selectively leaked off as was suggested by Archambeau et al. (1969). On the other hand, as was pointed out in the introduction, the problem of the effect of a negative gradient on a critically refracted wave is mathematically akin to a diffraction problem. Thus, if one's

intuition happens to be based on a diffraction analog, the theoretically predicted relative attenuation of high frequencies would have been anticipated.

The sensitivity of the spectral-amplitude fall-off with frequency to velocity gradients in the refracting horizon summarized in Figure 22 provides an additional criteria for determining velocity gradients using near-critical wave data. At the same time, it is clear that these propagation effects on near-critical waves should be recognized and taken into account in studies of source parameters using body wave spectra.

The interpretation of the scalloped amplitude curves and spectra of the interfering diving waves or modes associated with the positive velocity gradient is directly related to the problem of interpreting the spectrum of a number of wave forms spread over an extended interval in the time domain. For this reason, the spectral amplitude curves for the positive gradient case (including the homogeneous case with curvature) cannot be readily interpreted in terms of first arrival amplitudes in the range beyond a short distance from the critical point to the minimum distance at which the ray-theoretical description of the diving waves becomes valid.

In principle, it is possible to in some sense obtain the spectral amplitude of the 'first arriving' energy by choosing the contour for numerical integration such that only contributions with

a limited range of phase velocities (or angles of incidence) are included. In the case of the classical head wave or the head wave from a negative gradient this is a simple matter because the dominant contributions from the contours labeled H in Figures 13a and 13c come from the immediate vicinity of the branch point or the end of the line of poles, which corresponds to the angle of incidence of the critical ray ($p \sim n_o$). However, in the case of a positive gradient, the diving wave contribution is spread out along the real axis from $p \sim n_o$ to $p = 0$ under the line of poles (see Figure 13d), and there is no simple criteria for judging just where a contour should cut through the line of poles to limit the range of phase velocities contributing to the integral. A different spectral result is obtained depending on where the contour cuts through the line of poles in the interval $0 < p < n_o$. This is directly analogous to the fact that a different spectral result is obtained in the Fourier analysis of a time series depending on where the time series is truncated following its onset. It is because of this complication that the frequency-domain, wave-theoretical description of waves refracted by a medium with an effective positive gradient is not well-suited to the study of first motion amplitudes in the region of diving wave interference. In this case, there is clearly some value in attempting to complete the analysis by taking the inverse Fourier transform of the frequency-domain solution convolved with

a band-limited source to express the solution in the time domain.

Because the theoretical scalloped diving-wave spectral amplitudes presented above were obtained using the contour, D, shown in Figure 13d, contributions from all the normal modes (poles) propagating in the lower, positive gradient medium are included. These included modes with high phase velocities and low group velocities that 'feel' the deeper regions of the velocity profile. Thus, because the actual velocity profile used in obtaining these results (3.12) deviates from the exact spherical mapping profile (2.13) at depth, we cannot expect the details of these scalloped amplitudes curves to correspond to those that would be obtained for the exact exponential profile. It remains as a future task to assess the effects of the deeper regions of the velocity profiles on the spectral amplitude of the entire diving wave series, as well as to obtain a time-domain representation for the first arrivals.

6. Conclusions

The problem of waves generated at a point source and reflected by a closed spherical boundary within which the medium is radially heterogeneous can be expressed in terms of spherical waves reflected from a vertically heterogeneous half space by 1) applying an earth-flattening transformation to the radial differential equation and 2) using the Watson transform to convert the solution from a sum over discrete mode numbers to an integral over continuous wave numbers. Curvature enters the 'equivalent' half-space problem through an effective velocity gradient superimposed on the original physical velocity variation. The result is an integral expression (the Weyl integral) containing the spherical reflection coefficient for the radially heterogeneous medium that represents a valid solution to the original spherical problem for high frequency waves with source and receiver positions small distances above the boundary with respect to the radius of the boundary. In principle, this integral representation can be used to obtain expressions for waves reflected by prescribed velocity distributions at arbitrary depths within the spherical boundary. This approach is well suited to the study of acoustic waves in fluid media and SH waves in elastic media; it can also be used to study P-SV waves in elastic media provided a potential representation is used that results in the high-frequency decoupling of P- and SV-waves.

In applying the above approach to the analysis of waves critically refracted by a discontinuous increase in velocity at a spherical boundary we find that in the special case of a critical negative velocity gradient (a physical gradient equal and opposite to the effective curvature gradient), the critically refracted wave assumes the form of the classical head wave for a plane boundary between two homogeneous media. Mathematically, this true head wave arises from the contribution of a branch cut in the complex wave-number plane associated with a radical in the reflection coefficient. In the case of a physical velocity gradient more negative than the critical gradient, the spectral amplitude of the resulting critically refracted wave decays more rapidly with distance than the classical head wave. For narrow bandwidth data, this decay cannot be distinguished from the effect of anelasticity (Q^{-1}) on a classical head wave. However, the frequency dependence of the two effects is different, and in principle, it should be possible to separate the effects of negative gradients and anelasticity with broad band data. Finally, in the case of physical gradients that are positive, null, or less negative than the critical gradient, the spectral amplitude of the near-critical waves decays less rapidly with distance than the classical head wave. At sufficiently large distances, or for sufficiently strong positive gradients, the refracted waves separate into an infinite series of diving, immersed waves, the first of which represents the direct wave (or cord wave in the case

of a spherical boundary between two homogeneous media).

Mathematically, the near-critical waves in the case of velocity gradients either greater or less than the critical gradient arise from the contribution of a line of poles associated with the zeros of the denominator of the appropriate reflection coefficient. As the velocity gradient approaches the critical gradient from either side, the poles move together and collapse into the classical head wave branch cut. In the case of a moderate negative velocity gradient, the poles spread apart and extend upward in the positive imaginary half of the complex wave number plane at an angle of $\pi/3$ with respect to the real axis. These poles behave very much like the scattering poles that give rise to the diffracted wave in the core shadow (see Nussenzveig, 1965; Richards, 1970; or Chapman, 1970). The wave number, k, enters the contribution from these poles to the near-critical wave as $k^{1/3}$, which is also characteristic of diffracted waves. Thus we find that in very real sense, the near-critical wave associated with a velocity gradient less than the cricital gradient is a diffraction phenomenon. When the physical velocity gradient is greater than the critical gradient, the poles lie just above the real wave number axis. These poles also have the character of scattering poles, but for moderate gradients or large distances, it is convenient for analytical reasons to expand the reflection coefficient into a series whose terms arise from an

infinite number of saddle points along the real axis. Each of these saddle points gives a contribution that can be identified with the ray path of a wave reflecting a given number of times from the bottom of the discontinuity. Examples of such waves in the earth are given by the phases PP...P in the upper mantle or PKK...KP in the core. At sufficiently large distances, these diving waves can be described quite adequately in terms of geometrical ray theory, and indeed the ray-theoretical methods described by Bullen (1963) are generally successful in predicting amplitudes of the direct P- and S-waves at teleseismic distances.

Thus the true head wave in the classical sense is a fragile thing. Its character is destroyed by small velocity gradients in the refracting horizon as well as by slight curvature of the boundary. Cerveny (1966) recognized this and concluded that there is no practical sense in using head wave amplitude to determine absorption coefficients. However, it is just the sensitivity of the near-critical wave to small velocity gradients that makes the study of its amplitude potentially useful for determining the fine velocity structure in the crust and upper mantle. For example, with the prospect of broad band digital field instruments of the type described by Burke et. al. (1970), the outlook for using the spectral amplitudes of critically refracted waves to separate absorption and gradients effects in the major crust and upper mantle refractors is extremely promising.

This is particularly true for the longer period body waves (from 5 to 20 sec), which are both less attenuated by the propagation characteristics of critically refracted waves and less effected by the small scale heterogeneities in the crust and upper mantle which result in the notorious scatter in short period body wave amplitudes. On the other hand, because of the sensitivity of the spectral amplitudes of near-critical waves to small velocity gradients in the major refractors, it is clear that these propagation effects must be considered in studies of source parameters of local earthquakes using body wave spectra as described by Thatcher and Hanks (1971).

Chapter 2

1. Introduction

Much of our current knowledge of crustal and upper mantle structure is based on ray-theoretical methods of interpreting seismic reflection and refraction data. These methods are quite adequate in many situations, but as we attempt to extract more information from the seismograms and consider finer details of crustal structure, we find that in a number of important situations ray theory is inadequate and a higher order wave theory is required.

We found in the first chapter that although the travel times of critically refracted, or head waves are correctly predicted by ray theory, their amplitudes are not. Furthermore, we found that the spectral amplitudes of near-critical waves and head waves are extremely sensitive both to small velocity gradients directly beneath the refracting boundary and curvature along the refracting boundary. Thus attempts at complete interpretation of seismic-refraction data must consider both travel time and amplitudes of the various refracted branches in light of wave-theoretical results. It is clear, for example, that attempts to determine anelasticity (Q^{-1}) or velocity gradients in crustal horizons from refraction data using ray theory can lead to serious error and must be reevaluated in terms of the wave-theoretical results.

The purpose of this chapter is two-fold. First we wish to consider published amplitude data for the major refraction branches (Pg, P* and Pn) in terms of the effects of small velocity gradients, as developed in Chapter 1, together with the effects of anelastic attenuation in a preliminary attempt to determine the possible existence and distribution of velocity gradients in the mantle lid and well established crustal horizons. Secondly, we wish to evaluate the plausibility of the inferred velocity gradients in light of physical properties of crustal rocks measured in the laboratory and their relation to heat flow and geothermal gradients.

Throughout this Chapter the following convention will be adopted for major compressional wave phases propogating in the crust and upper mantle:

Pg - 1st arrivals critically refracted or nearly critically refracted from the upper crystalline horizon having a P-wave velocity of 6.0 $\pm$ 0.2 km/sec.

P* - 1st arrivals critically refracted or nearly critically refracted from an horizon of moderate depth having a P-wave velocity of 6.8 $\pm$ 0.2 km/sec.

Pn - 1st arrivals refracted from the M-discontinuity.

$\bar{P}$ - The extension of Pg following Pn as a train of strong secondary arrivals presumably involving multiple reflected

waves or a guided mode of propagation in the crust.

(This follows the convention introduced by Gutenberg.)

In addition, we will make a distinction between a purely anelastic Q, defined by

$$Q^{-1} = (1/2\pi)\,\Delta W/W$$

where W is the total elastic energy stored per unit volume per cycle, and ΔW is the fraction of W dissipated per cycle, and an effective Q, which will be designated as Q'. Under Q' we will include processes that result in either the real or apparent attenuation (or gain) of seismic waves regarded as propagating through perfectly elastic, homogeneous media. Such processes include scattering by inhomogeneities with dimensions of the order of a wavelength and velocity gradients, as well as the anelastic Q defined above.

2. Effects of velocity gradients and anelasticity on critically refracted waves.

The effects of small velocity gradients in the refractor and curvature of the refractor boundary on the spectral amplitudes of near-critical waves and head waves are summarized by equations (4.19) through (4.23) and by Figures 13, 16, 19, and 20 in Chapter 1. If the refracting medium has a critical negative velocity gradient (or is homogeneous in a flat geometry) and is anelastic with a frequency-independent Q, the asymptotic expression for the head wave

amplitude is given by

$$A \sim A_o e^{\frac{-kL}{2Q}} \tag{1}$$

where A_o is the classical head-wave amplitude

$$A_o \propto \frac{1}{k \rho^{1/2} L^{3/2}} \tag{2}$$

k is the wave number, and L is the distance traveled along the refractor as described in Chapter 1. The effect of anelasticity in the case of a critical gradient is compared with the effects of sub-critical gradients in Figures 23 and 24 for various frequencies and Q's together with curves showing the exact solutions for the effects of negative gradients obtained by the numerical integration of the Weyl integral.

As can be seen in Figure 24, the effects on the head wave amplitude fall-off with distance due to a Q of 300 in a homogeneous refractor and to a lossless refractor with a negative gradient of 10^{-3} km^{-1} are quite similar. In fact, considering the usual scatter in amplitude data, it is not practical to attempt to distinguish between the two effects for narrow band width spectral amplitude data. In principle, however, spectral ratio techniques similar to that described by Kanamori (1967) could be used to discriminate between the two effects for data of sufficiently wide band width.

Figure 25 summarizes the effects of gradients in the refracting

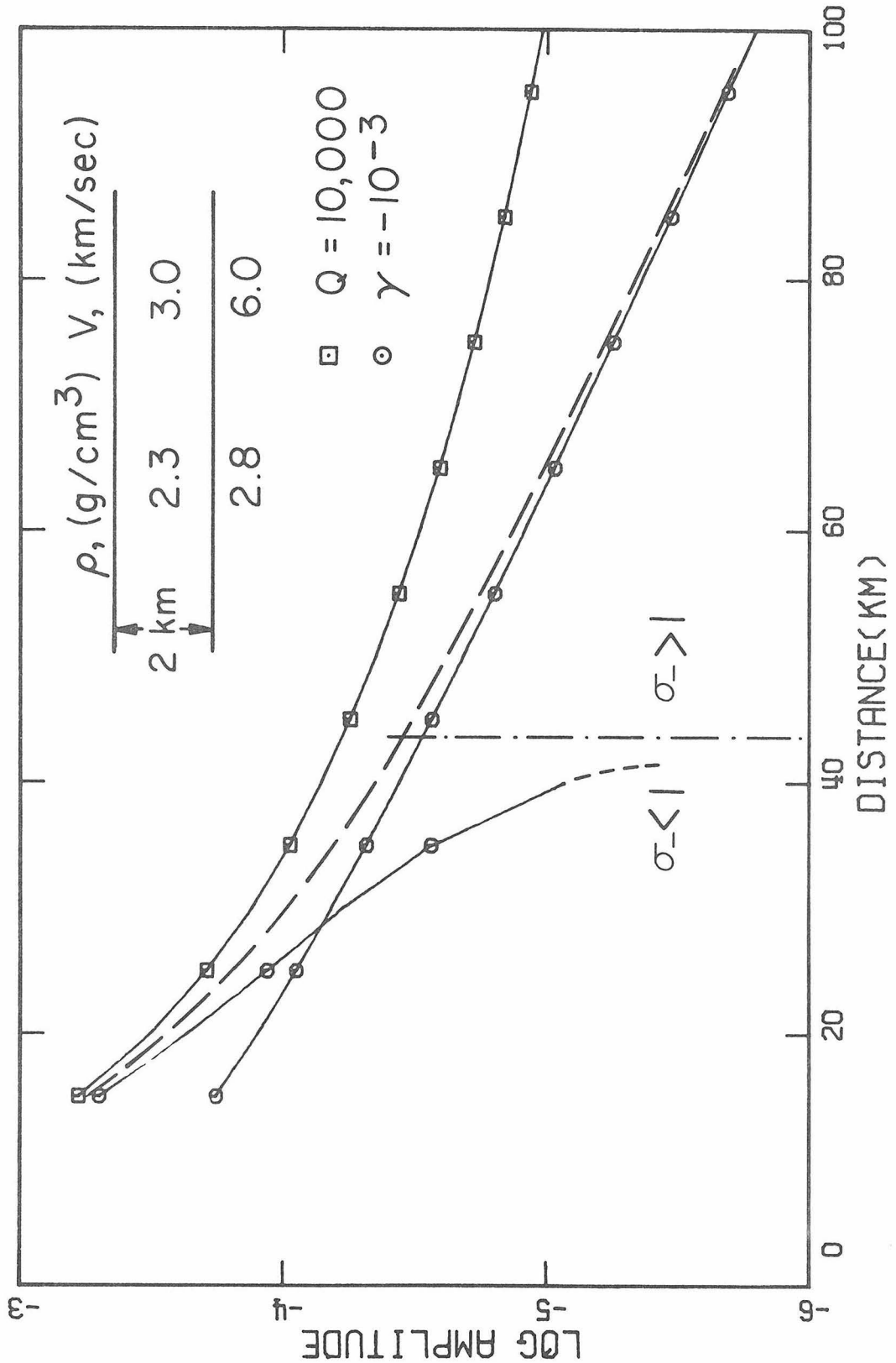
LOG AMPLITUDE
-3
-4
-5
-6
0
20
40
60
80
100
DISTANCE(KM)
σ_<1
σ_>1
Q = 10,000
γ = -10^-3
ρ, (g/cm^3) V, (km/sec)
2 km
2.3
3.0
2.8
6.0

Figure 23

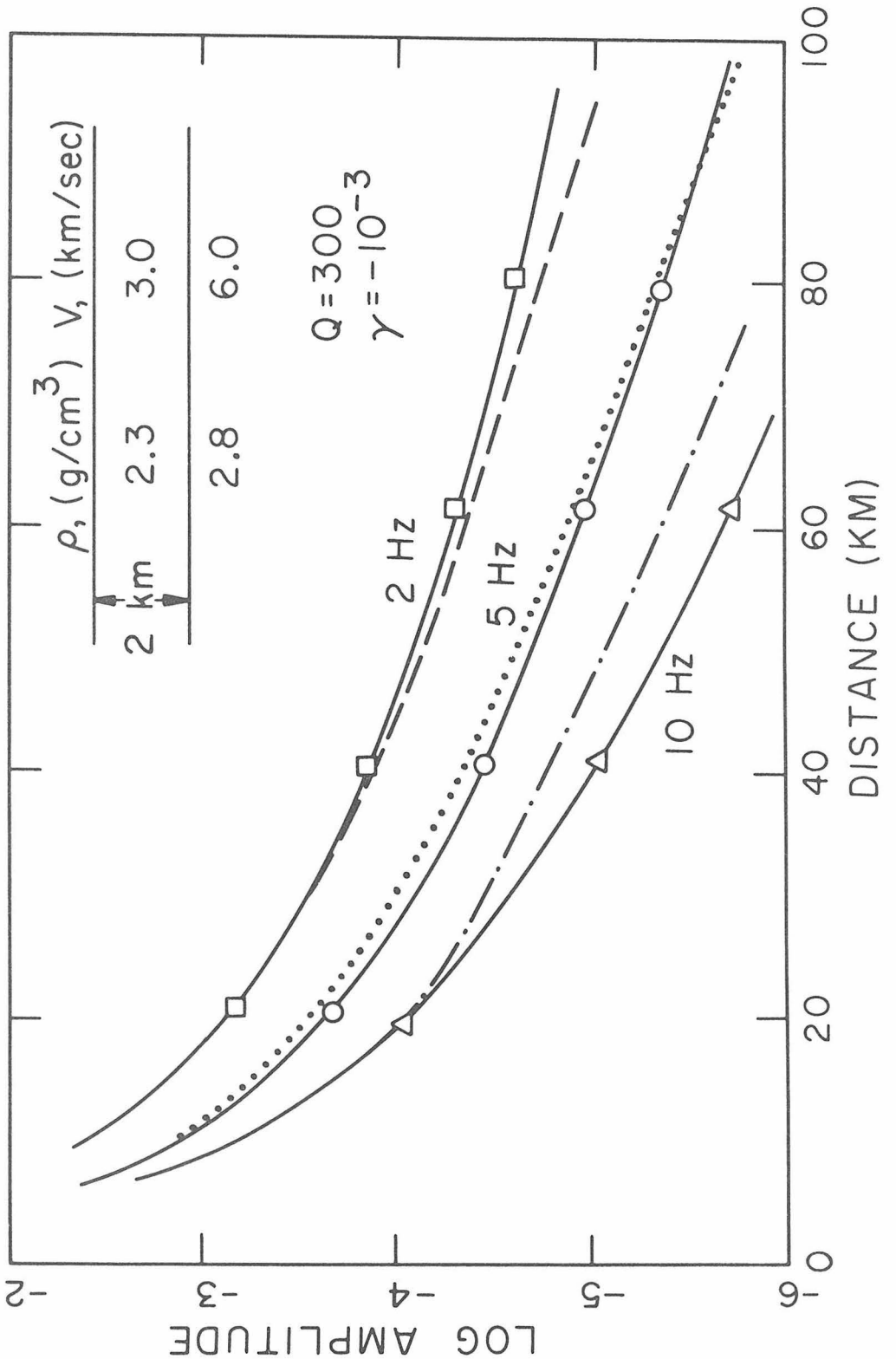
LOG AMPLITUDE
-2
-3
-4
-5
-6
0
20
40
60
80
100
DISTANCE (KM)
2 Hz
5 Hz
10 Hz
Q=300
γ=-10^-3
ρ, (g/cm^3) V, (km/sec)
2 km
2.3
3.0
2.8
6.0

Figure 24

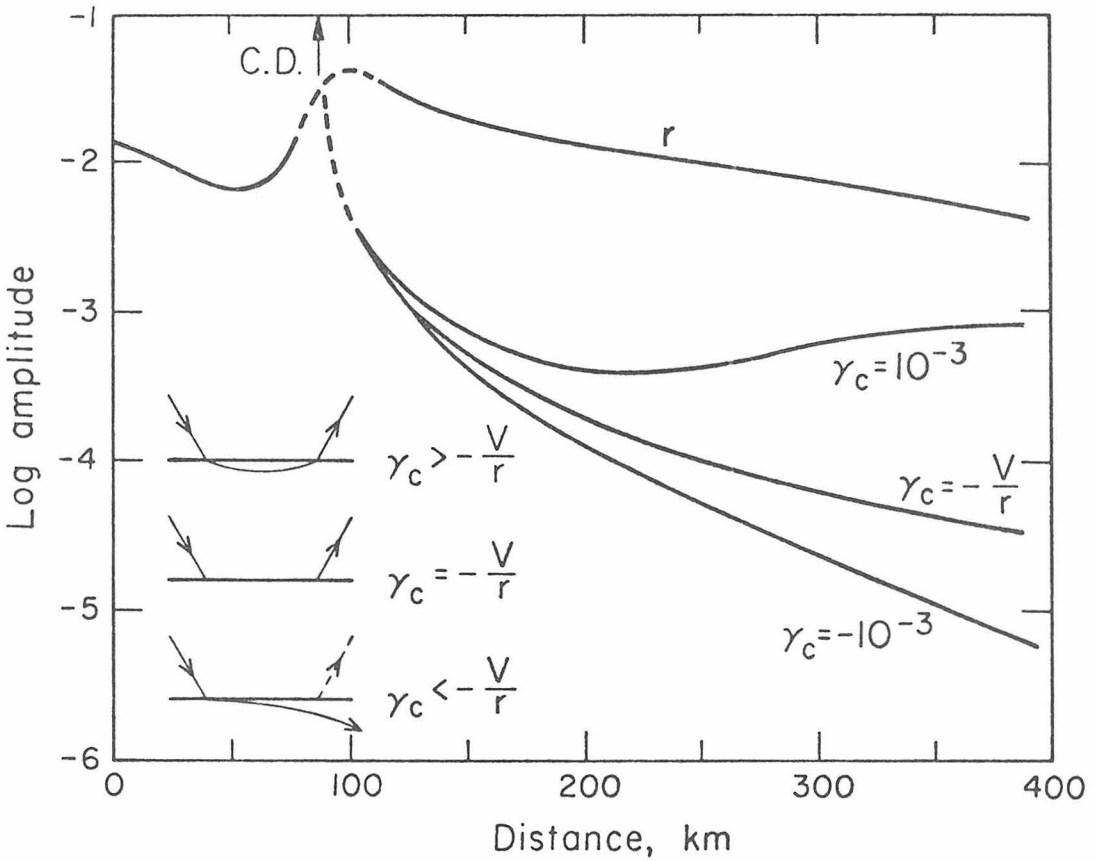
-1
-2
-3
-4
-5
-6
Log amplitude
C.D.
r
$\gamma_c = 10^{-3}$
$\gamma_c = -\frac{V}{r}$
$\gamma_c = -10^{-3}$
$\gamma_c > -\frac{V}{r}$
$\gamma_c = -\frac{V}{r}$
$\gamma_c < -\frac{V}{r}$
0
100
200
300
400
Distance, km

Figure 25

medium on head wave amplitudes found in Chapter 1. The reflected wave amplitude, which is essentially unaffected by small gradients in the lower medium, is shown for reference.

3. Analysis of Published Amplitude Data

A number of authors reporting on crustal and upper mantle seismic refraction measurements include amplitude data for first arrivals defining the major branches of the observed travel time curves. Typically the amplitudes are obtained by measuring the first peak-to-trough displacement on the seismogram and correcting for instrument response to ground displacement. The dominant period of the arrival is usually estimated as twice the time between the first peak and trough (i.e., see Eaton, 1963). In effect, then, we will be considering displacement amplitudes of a single spectral component (for crustal arrivals this component is commonly about 5 Hz and for Pn arrivals it is commonly between 2 and 4 Hz), and thus, as was noted in the preceding section, we cannot expect to distinguish between the effects of anelasticity (Q^{-1}) and negative gradients using these data. In most cases the amplitude data were taken just as published. In a few cases, the most distant amplitude points were omitted when it was clear from the accompanying discussion that these measurements were uncertain because of low signal to noise ratios.

Layer velocities and depths were taken from interpretations

given in the respective papers. In carrying out the analysis described below, the velocity structure above the particular refracting horizon of interest was replaced by single velocity representing the average velocity structure as seen by a wave near the critical angle of incidence. This is necessary because the theory developed in Chapter 1 is based on a single, homogeneous 'layer' over the refracting medium. For this purpose, the average velocity is defined such that both the vertical travel time (i.e. the intercept time) and the ray-theoretical critical distance of the refracted travel time branch are conserved. According to this definition, the average velocity of the overlying structure, V_a, is found from the following two equations

$$H(1 - V_a^2/V_n^2)^{\frac{1}{2}}/V_a = \sum_{i=1}^{m} h_i \, (1 - V_i^2/V_n^2)^{\frac{1}{2}}/V_i \qquad (3)$$

$$H \frac{(V_a/V_n)}{(1-V_a^2/V_n^2)^{\frac{1}{2}}} = \sum_{i=1}^{m} h_i \frac{(V_i/V_n)}{(1-V_i^2/V_n^2)^{\frac{1}{2}}} \qquad (4)$$

where V_i = velocity in the ith layer

h_i = thickness of the ith layer

V_n = velocity of the refractor, and

H = the effective thickness of the overlying structure with velocity, V_a.

Here equation (3) expresses the conservation of vertical travel time and (4) expresses the conservation of critical distance. Note that in general the effective thickness, H, will differ from the reported model thickness,

$$T = \sum_{i=1}^{m} h_i \quad .$$

However, in all cases, the two thicknesses differ by less than 10%. Furthermore, the method of fitting the data described below is considerably less sensitive to small variations in layer thickness than it is to small variations in the critical distance (which is directly related to L in equations 1 and 2). In fact, this is the reason for constraining the critical distance to be constant rather than the layer thickness in the averaging process. Equations 3 and 4 can be solved explicitly for the average velocity and effective depth. The result is

$$V_a = V_n \left[\frac{C_1^2 V_n^2}{H^2} + 1 \right]^{-\frac{1}{2}} \qquad (5)$$

$$H = \left[C_1 C_2 V_n \right]^{\frac{1}{2}} \qquad (6)$$

where C_1 and C_2 are the values of the sums on the right hand sides of equations 3 and 4, respectively.

The approach taken in analyzing these amplitude data was to

initially regard the first arrivals as classical head waves propagating through a refractor with a critical velocity gradient $\gamma_c = - V_n/r$, (or a homogeneous refractor with $\gamma = 0$ in the flat case) as illustrated in Figure 4, and to attribute any systematic deviation of their amplitudes from this ideal case to an effective Q(Q'). The Q' for each set of arrivals was obtained by fitting the following form of equation (1) through the appropriate amplitude (A) vs distance (ρ) data

$$A = \frac{b}{\sqrt{\rho}\, L^{3/2}} e^{-\alpha L} \tag{7}$$

Here α and b are adjustable parameters with

$$\alpha = \frac{\pi f}{Q' V_n} \tag{8}$$

where f = frequency and V_n = the P-wave velocity of the refracting horizon. The actual fit was made by taking the log of equation (7) and using a standard least-squares estimation of nonlinear parameters algorithm (Share program #3094).

Using the effects summarized in Figure 25 as a guide, the results of this process are interpreted in the following manner:

1) A negative Q' implies a gradient greater than critical

($\gamma_i = - V_n/r \sec^{-1}$) in the refractor. A negative anelastic Q is not physically possible in a passive system such as the earth, but as indicated in Figure 25, velocity gradients greater than critical in the refracting horizon results in an effective increase in amplitudes with respect to the critical case.

2) $|Q'| \geq 1000$ implies a near critical velocity gradient in the refractor, depending on the degree of true anelasticity (Q^{-1}) in the refractor.

3) $0 > Q' < 1000$ implies a) velocity gradient less than critical, b) a moderate to high anelasticity (Q^{-1}), or c) scattering by relief on the refractor.

In the above interpretations of Q', we have ignored the effects of possible lateral velocity variations within the refracting horizon. Of course, this effect can potentially have a strong influence on body wave amplitudes and Q' as we are using it here. But in most cases both the data and existing theory are inadequate to take it into proper account. We will also ignore the effect of a dipping refractor. It can be shown that small dips have only a very minor effect on the fall-off of head wave amplitudes, and we will not consider data from profiles in which the layers appear to be strongly dipping.

The theoretical results summarized above have been applied to

the data for which $0 < Q' < 1000$ in an attempt to estimate maximum negative gradients in the respective refracting horizons. Because of the problems involved in interpreting the theoretical spectral amplitudes of the interfering diving waves in terms of first arrival amplitudes as discussed in Section 5 of Chapter 1, we will make only a qualitative evaluation of gradients greater than critical using the data considered here.

In attempting a quantitative evaluation of gradients less than critical, it turns out that in most cases the asymptotic expression for head wave amplitudes for $|\sigma_-| \ll 1$ or $|\sigma_-| \gg 1$ (i.e. see equations 3.46 and 3.49 in Chapter 1) cannot be used to obtain uniformly valid fits over the entire distance range covered by the data sets. This situation arises because the parameter σ_- becomes unity at an intermediate distance in the data sets as is illustrated in Figure 23. To handle these cases, an empirical corresponding was established between gradients and Q''s by fitting equation (7) through points obtained from numerical integration of the Weyl integral for a number of gradients. The resulting empirical curve relating Q' and negative gradients is shown in Figure 26 as a straight line fitted through these points in a least-squares sense on a log-log plot. The values of the gradient obtained from this empirical curve are within 15% of values that would

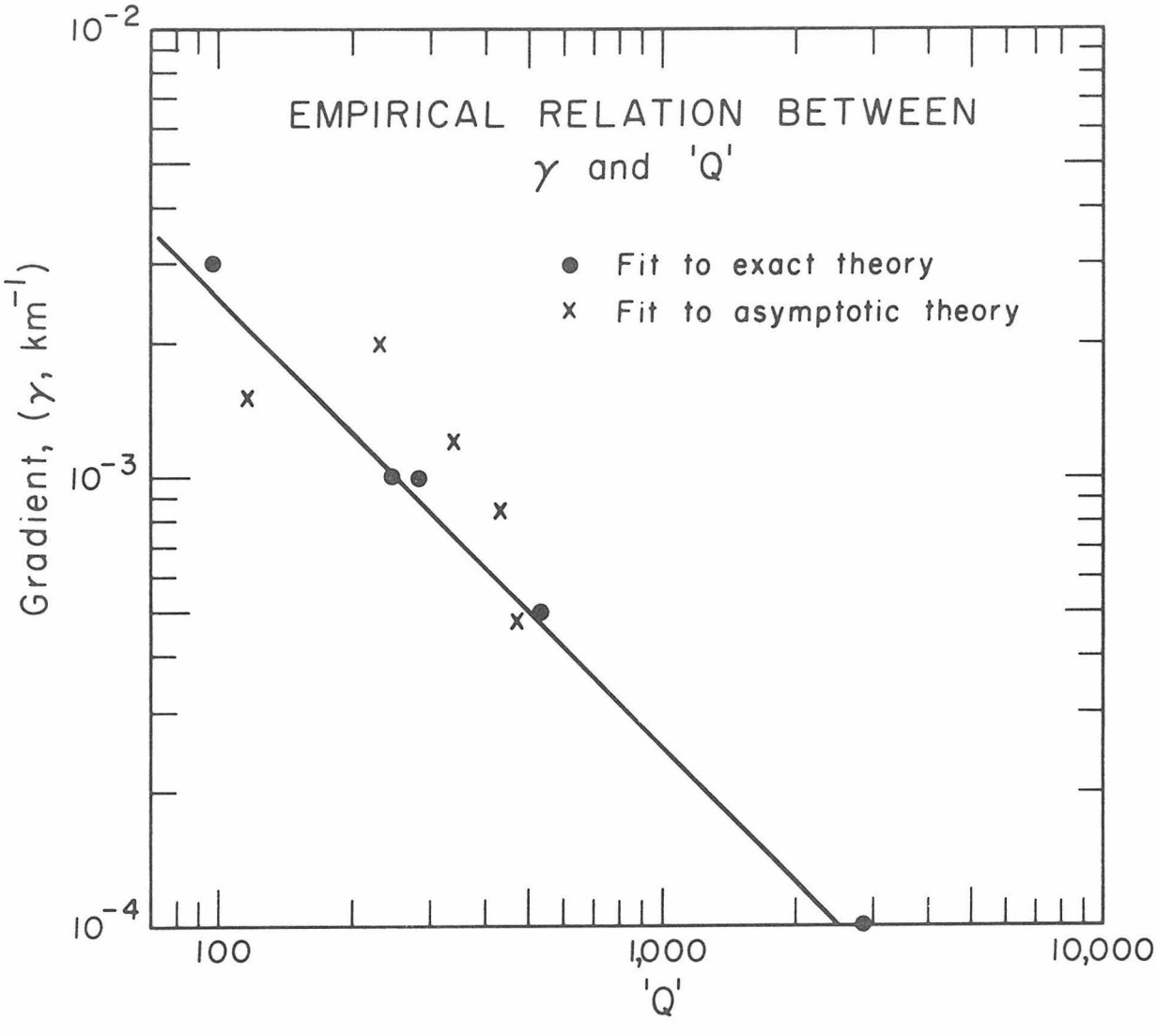
EMPIRICAL RELATION BETWEEN
γ and 'Q'
Fit to exact theory
Fit to asymptotic theory
Gradient, (γ, km⁻¹)
10⁻²
10⁻³
10⁻⁴
100
1,000
10,000
'Q'

Figure 26

be obtained if theoretical amplitude curves based on numerical integration of the Weyl integral had been fitted to the data. Attempts to determine the gradient directly by fitting the asymptotic expression for $|\sigma_-| >> 1$ (3.49) through selected data sets are indicated by crosses, and as can be seen in the figure, the results differ from the empirical curve by as much as a factor of two for low Q' values.

Crustal amplitude data - The majority of the data used in this analysis of crustal data are first arrival amplitudes of the Pg branch. This branch is generally well recorded in the distance interval 5 km to 10 km from the shot point out to 100 km or more. The 6.0 ± 0.2 km/sec Pg refracting horizon is commonly found at depths of 0.5 km to 4 km and is overlain by material with P-wave velocities ranging between 2 km and 4 km/sec. Exceptions to this are:

1) The San Francisco to Fallon amplitude data presented here are for the 5.36 km/sec 'Pg' branch recorded between 20 km to 100 km east of San Francisco (Eaton, 1963). 'Pg' velocities of 5.6 km/sec or lower are common in central California east of the San Andreas fault and are presumably representative of the Franciscan basement.

2) The amplitude data for the Snake River Plain (Hill and Pakiser, 1966), Lake Superior (O'Brien, 1968) and Mississippi (Warren et al., 1966) are from the P* branch refracted from an

intermediate layer (6.8 ± 0.2 km/sec) at depths between 10 km and 16 km.

Figures 27 through 31 are plots of the crustal amplitude data used in this study showing the fit for Q' according to equations (1) and (8) for each data set. The results of the analysis of these data in terms of Q' and velocity gradients are summarized in Table 1 and Figure 32.

The scatter typical in crustal body wave amplitude data is evident in Figures 27-31. A measure of this scatter is given by the standard error for Q^{-1} in Table 1. From this table, we see that the standard error is at best one-tenth of Q'^{-1}, and that in about 20% of the cases it is actually larger than Q'^{-1}. Thus, although arguments based on the results for any single profile cannot carry much weight, consistent trends between profiles within a given region are regarded as significant.

The most obvious trend in the results is that the bulk of the Pg data in the Basin and Range Province have a Q' less than 1000, while most of the data elsewhere have a Q' that is either greater than 1000 or negative. Hence, according to our criteria for interpreting Q', the Pg refractor (the upper part of the crystalline crust) may have slight negative velocity gradients in the Basin and Range Province, while the gradient is either nearly critical or slightly positive elsewhere.

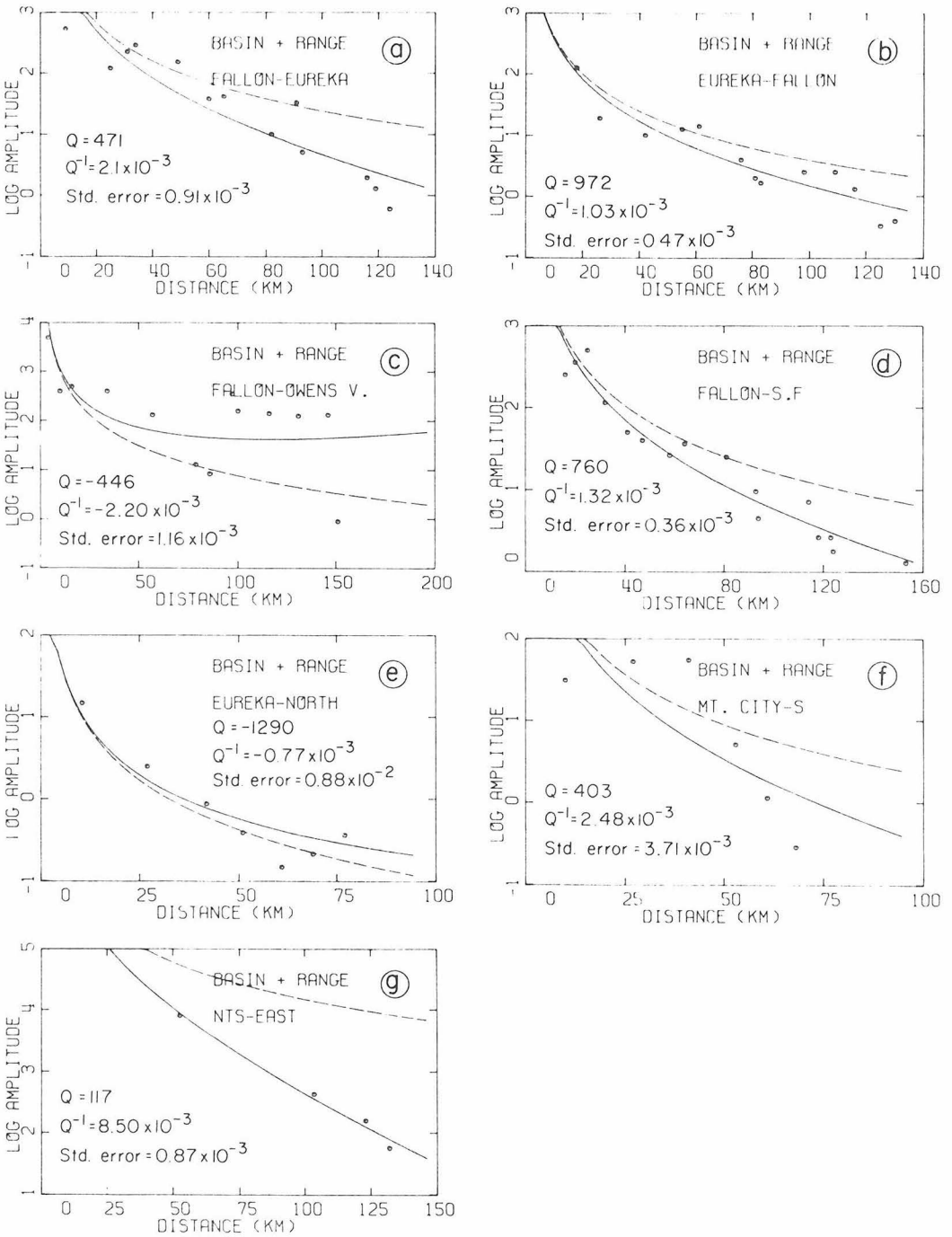
BASIN + RANGE
FALLON-EUREKA
Q = 471
$Q^{-1} = 2.1 \times 10^{-3}$
Std. error = 0.91×10^{-3}
LOG AMPLITUDE
DISTANCE (KM)
BASIN + RANGE
EUREKA-FALLON
Q = 972
$Q^{-1} = 1.03 \times 10^{-3}$
Std. error = 0.47×10^{-3}
BASIN + RANGE
FALLON-OWENS V.
Q = -446
$Q^{-1} = -2.20 \times 10^{-3}$
Std. error = 1.16×10^{-3}
BASIN + RANGE
FALLON-S.F
Q = 760
$Q^{-1} = 1.32 \times 10^{-3}$
Std. error = 0.36×10^{-3}
BASIN + RANGE
EUREKA-NORTH
Q = -1290
$Q^{-1} = -0.77 \times 10^{-3}$
Std. error = 0.88×10^{-2}
BASIN + RANGE
MT. CITY-S
Q = 403
$Q^{-1} = 2.48 \times 10^{-3}$
Std. error = 3.71×10^{-3}
BASIN + RANGE
NTS-EAST
Q = 117
$Q^{-1} = 8.50 \times 10^{-3}$
Std. error = 0.87×10^{-3}

Figure 27

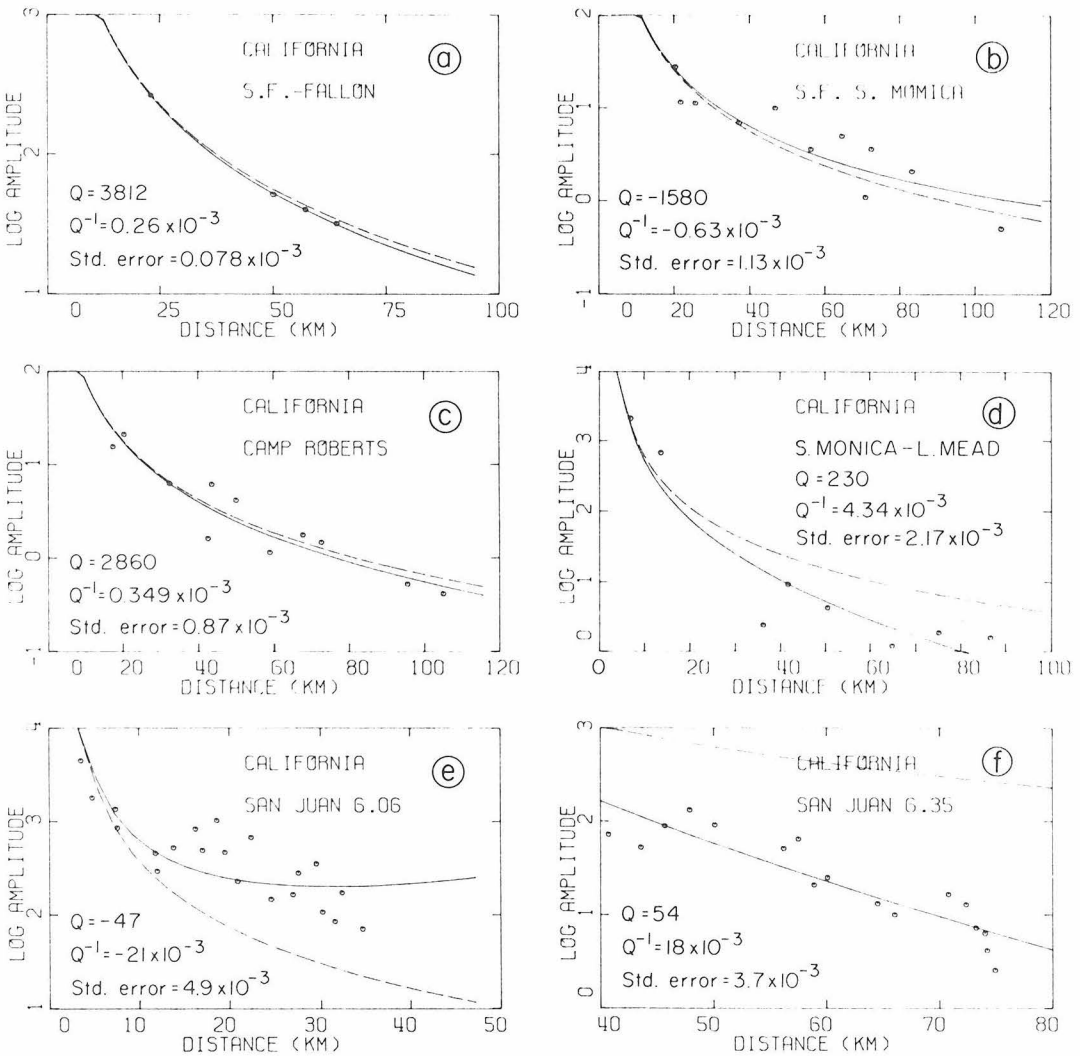
CALIFORNIA
S.F.-FALLON
Q=3812
$Q^{-1}=0.26\times10^{-3}$
Std. error=0.078×10^{-3}
CALIFORNIA
S.F. S. MONICA
Q=-1580
$Q^{-1}=-0.63\times10^{-3}$
Std. error=1.13×10^{-3}
CALIFORNIA
CAMP ROBERTS
Q=2860
$Q^{-1}=0.349\times10^{-3}$
Std. error=0.87×10^{-3}
CALIFORNIA
S. MONICA-L. MEAD
Q=230
$Q^{-1}=4.34\times10^{-3}$
Std. error=2.17×10^{-3}
CALIFORNIA
SAN JUAN 6.06
Q=-47
$Q^{-1}=-21\times10^{-3}$
Std. error=4.9×10^{-3}
CALIFORNIA
SAN JUAN 6.35
Q=54
$Q^{-1}=18\times10^{-3}$
Std. error=3.7×10^{-3}
LOG AMPLITUDE
DISTANCE (KM)

Figure 28

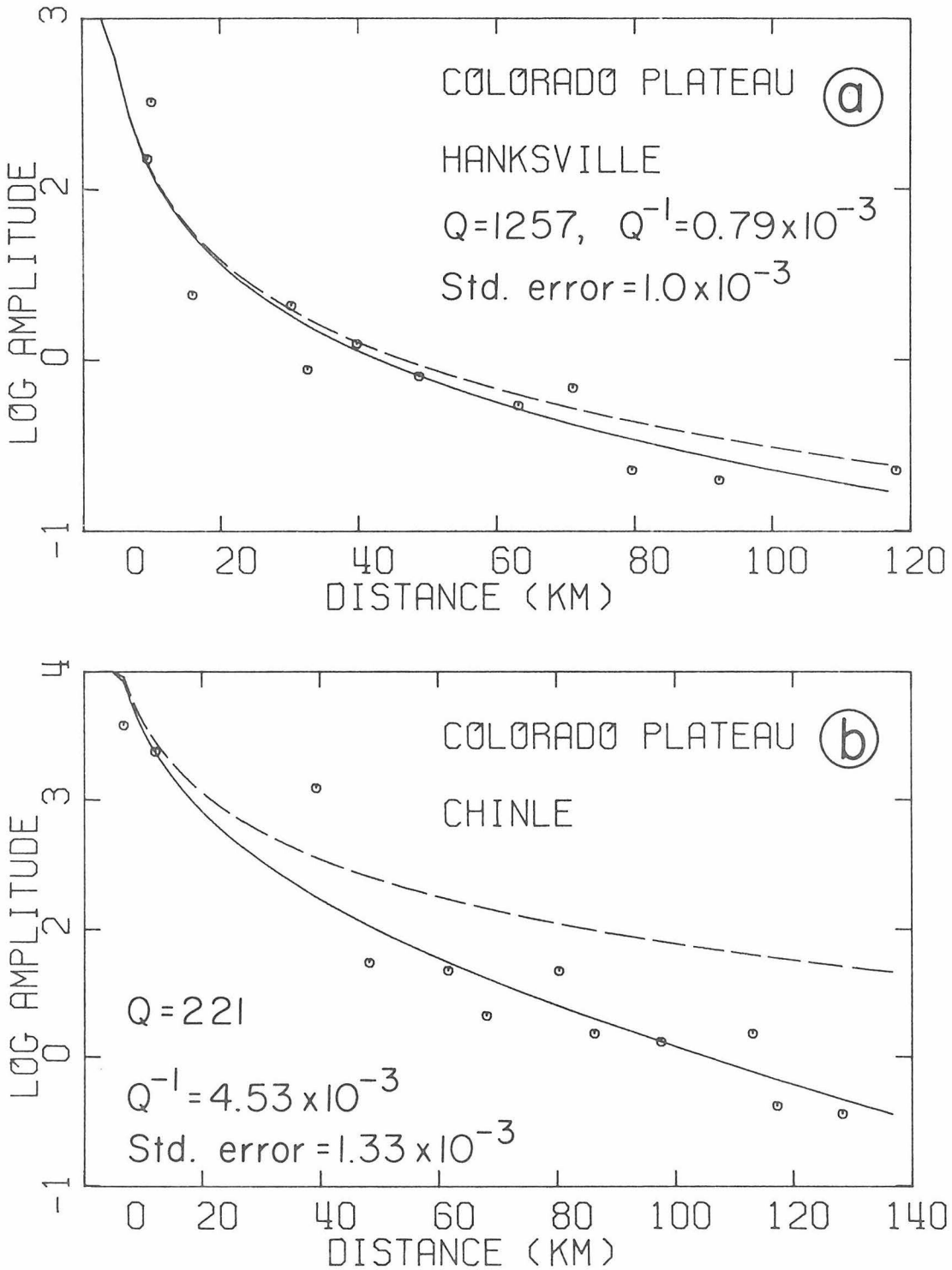
COLORADO PLATEAU
a
HANKSVILLE
Q=1257, $Q^{-1}=0.79\times10^{-3}$
Std. error = 1.0×10^{-3}
LOG AMPLITUDE
DISTANCE (KM)
COLORADO PLATEAU
b
CHINLE
Q=221
$Q^{-1}=4.53\times10^{-3}$
Std. error = 1.33×10^{-3}
LOG AMPLITUDE
DISTANCE (KM)

Figure 29

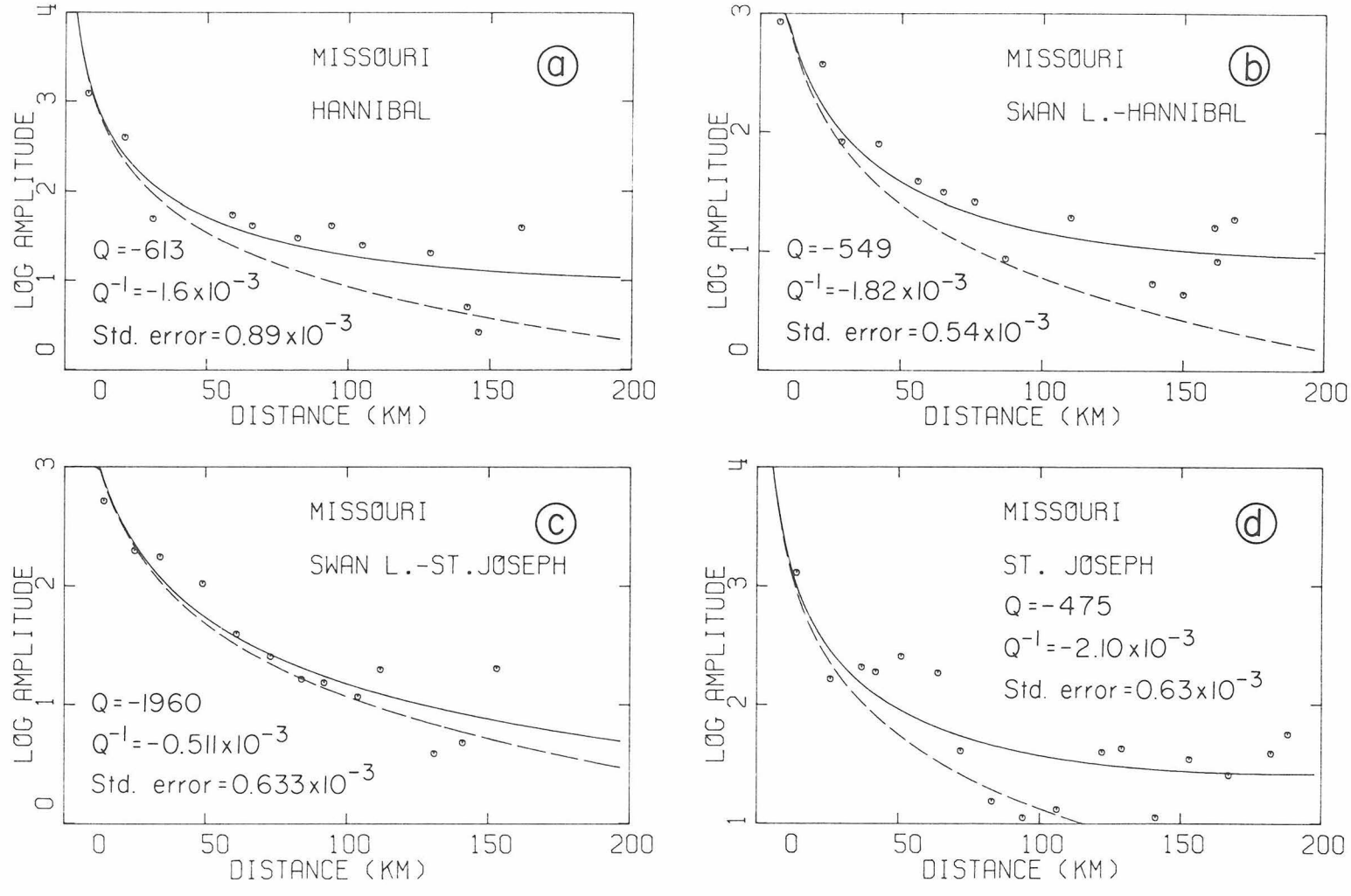
MISSOURI
HANNIBAL
a
Q=-613
$Q^{-1}=-1.6\times10^{-3}$
Std. error=0.89×10^{-3}
MISSOURI
SWAN L.-HANNIBAL
b
Q=-549
$Q^{-1}=-1.82\times10^{-3}$
Std. error=0.54×10^{-3}
MISSOURI
SWAN L.-ST.JOSEPH
c
Q=-1960
$Q^{-1}=-0.511\times10^{-3}$
Std. error=0.633×10^{-3}
MISSOURI
ST. JOSEPH
d
Q=-475
$Q^{-1}=-2.10\times10^{-3}$
Std. error=0.63×10^{-3}
LOG AMPLITUDE
DISTANCE (KM)
0
50
100
150
200

Figure 30

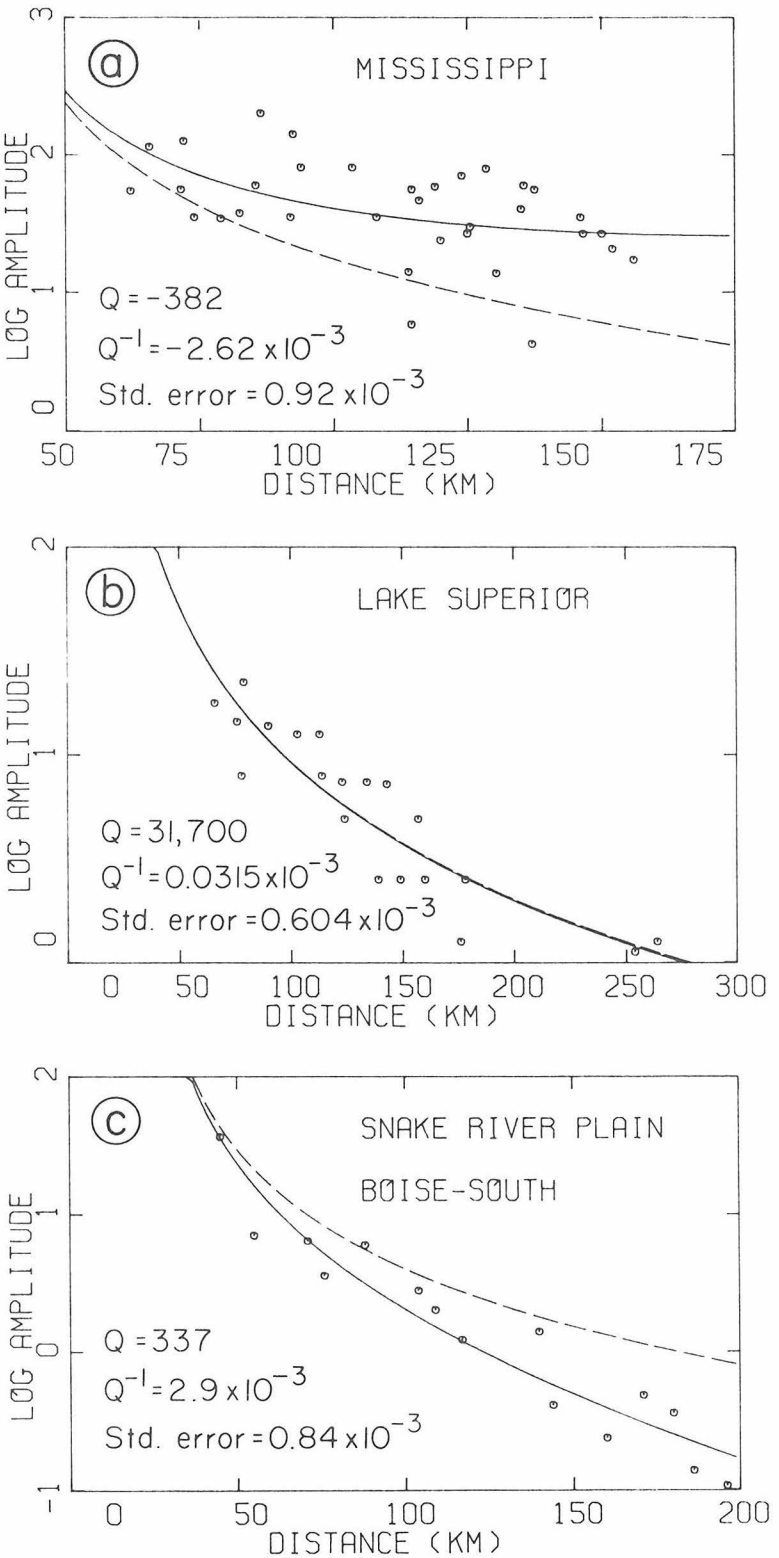
a
MISSISSIPPI
LØG AMPLITUDE
Q = -382
$Q^{-1} = -2.62 \times 10^{-3}$
Std. error = 0.92×10^{-3}
DISTANCE (KM)
b
LAKE SUPERIØR
LØG AMPLITUDE
Q = 31,700
$Q^{-1} = 0.0315 \times 10^{-3}$
Std. error = 0.604×10^{-3}
DISTANCE (KM)
c
SNAKE RIVER PLAIN
BØISE-SØUTH
LØG AMPLITUDE
Q = 337
$Q^{-1} = 2.9 \times 10^{-3}$
Std. error = 0.84×10^{-3}
DISTANCE (KM)

Figure 31

The results for the two P* data sets show a Q' of 337 for the Snake River Plain, 32,000 for Lake Superior, and -382 for Mississippi. Again, this may be interpreted as a possible negative gradient (-4.5×10^{-5} sec^{-1}) in the upper part of the 6.7 km/sec refractor under the Snake River Plain and a null or slightly positive gradient under Lake Superior and Mississippi.

An interesting exception to the generally high or negative Q' values found for California is provided by the Pg amplitude data along the profile southeast from San Juan in the Gabilan range described in a preliminary report by Stewart (1968). The Pg branch from 3.5 km to 40 km southeast of the San Juan shot point has an apparent velocity of 6.06 km/sec and a slightly negative Q'. Between 40 km and 75 km southeast of the shot point the first arrivals define an apparent velocity of 6.35 km/sec. The amplitudes of these first arrivals fall off quite rapidly with distance giving a Q' of only 54. If these results are treated in a straightforward manner assuming horizontal layers and using the Q'-gradient relation described above, we would expect a slight positive velocity gradient beneath the 6.06 km/sec refractor and a negative gradient of 2×10^{-2} km/sec/km beneath the 6.35 km/sec refractor.

The values of Q' determined in this paper for first arrival crustal body waves tend to average somewhat higher than the values of crustal Q determined by Sutton *et al.* (1967) and Press (1964),

using Pg ($\overline{P}$ according to the convention used in this paper) and Lg amplitudes. They report values of Q generally less than 500 in the western U. S. and greater than 500 in the east. The maximum value in the eastern U.S. reported by Sutton et al. (1967) is 1000. $\overline{P}$ and Lg are both presumed to be guided waves involving most of the crust, and thus Q determined from these phases represents minimum averages for the entire crust. The values are minimum estimates because the effects of mode leakage and scattering have been neglected. Most of the propagation paths studied by these authors cross one or more geologic province boundaries, and such boundaries can have a severe scattering effect on $\overline{P}$ (and presumably Lg as well). Thus we might expect that the true anelastic Q of the crust (particularly in the western U.S., where province boundaries tend to be relatively close together) is actually significantly higher than reported in these papers. In fact, Clowes and Kanasewich (1970) report Q values for the lower crust in southern Alberta of 1500 based on the spectral analysis of deep crustal reflections.

However, it should be realized that if the Q values reported by Sutton et al. (1967) and Press (1964) for the western U.S. do represent the actual anelastic Q of the crust, the somewhat higher Q' values found in this paper for the Basin and Range Province would imply slightly positive velocity gradients for the crystalline crust of this province as well.

In Figure 32 contours have been drawn which roughly separate regions having Q' values greater than 1000 (or negative values) from the region having Q' values less than 1000. Considering the scatter in the amplitude data, the 1000 Q' contour corresponds remarkably well with the 2.0 HFU contours presented by Archambeau et al. (1968) (Figure 32), or Roy et al. (1970)(Figure 33). The low Q' values (and possible negative velocity gradients) in the Basin and Range and Snake River Plain fall in the high heat flow province ($q > 2$ $\mu cal/cm^2/sec$), while the higher Q' values (and positive velocity gradients) fall in the low heat flow provinces ($q < 2$ $\mu cal/cm^2/sec$). Correlations also hold for other geophysical parameters characteristic of the heat flow provinces. For example, low Q' values are generally associated with low Pn velocities and lower average crustal velocities in the Basin and Range, while high or negative Q' values are associated with high Pn velocities and higher average crustal velocities in the eastern U.S. and the California coast (see Pakiser and Steinhart, 1964).

Pn amplitude data - A considerable body of Pn amplitude data has been reported in the literature based on recordings of both high-energy chemical explosions and nuclear events. In this study of Pn first motion amplitudes, we will limit our consideration primarily to data recorded from nuclear events. First arrivals from nuclear explosions are commonly well recorded to distances

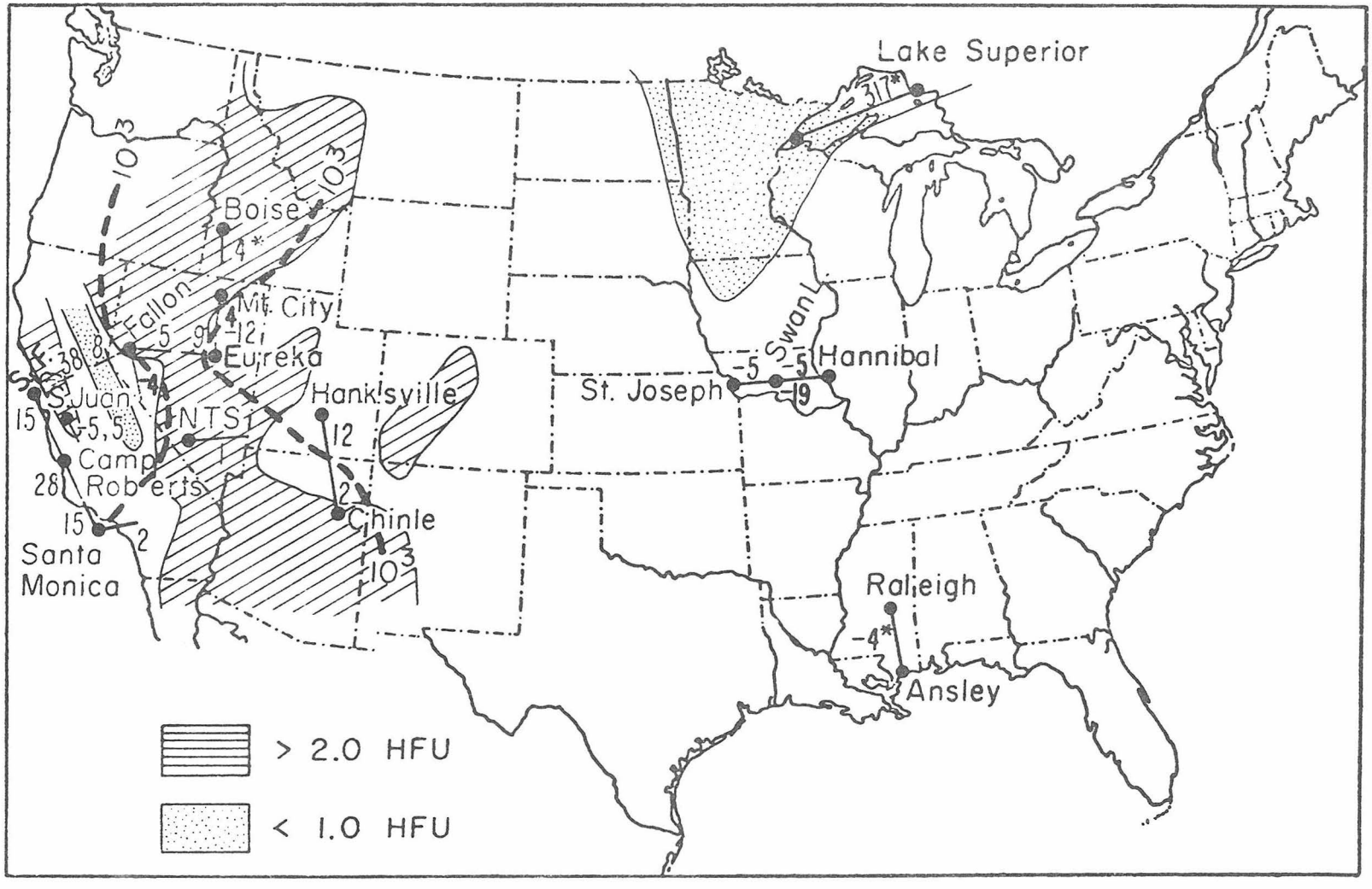
Lake Superior
317*
Boise
14*
Fallon
Mt. City
Eureka
Hanksville
NTS
Camp Roberts
Chinle
Santa Monica
St. Joseph
Swan L
Hannibal
Raleigh
Ansley
> 2.0 HFU
< 1.0 HFU

Figure 32

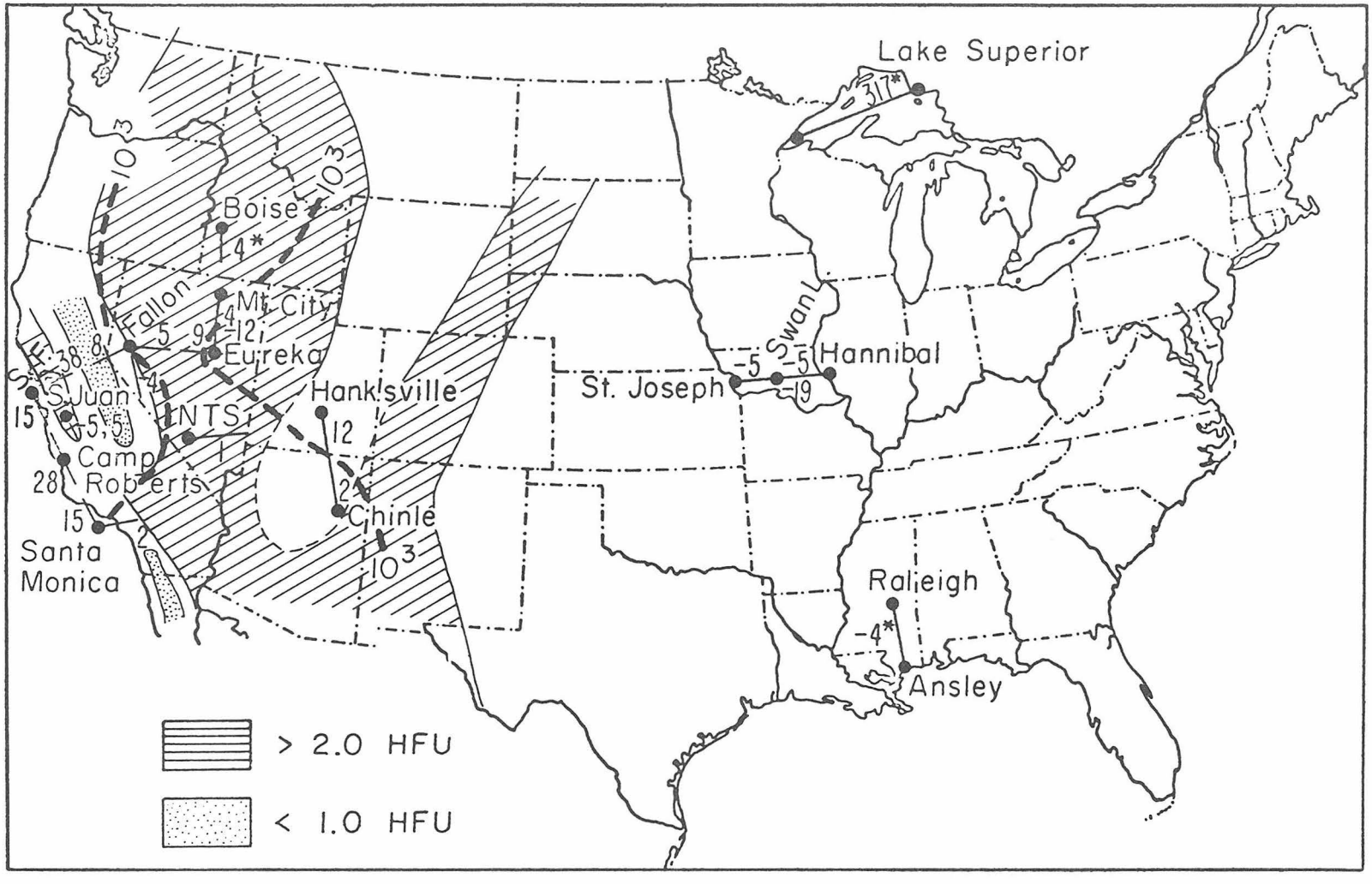
Lake Superior
3 1*
Boise
14*
Fallon
5
9
4
12
Mt. City
Eureka
38
8
4
St. Juan
5
5
NTS
Hanksville
12
2
Cihinle
10 3
Camp
Roberts
28
15
2
Santa
Monica
Swan L.
5
5
19
Hannibal
St. Joseph
Ralieigh
4*
Ansley
> 2.0 HFU
< 1.0 HFU

Figure 33

beyond 500 km, and we can be reasonably assured that the amplitude measurements based on these arrivals are significant. On the other hand, Pn arrivals from chemical explosions are generally not reliably recorded at distances much beyond 300 km, and the first motion of the arrivals is commonly near the noise level at even smaller distances. A singular exception to this is provided by the EARLY RISE series of chemical explosions detonated in Lake Superior in 1966 (Iyer, et al., 1969). First arrivals from these explosions were well recorded to distances of 2000 km and beyond, and we will include some of these data recorded in the central and eastern United States in this analysis. We will also include one set of oceanic Pn amplitude data from a profile described by Helmberger and Morris (1969) over the proposed Mohole site northeast of the Hawaiian Islands.

Figures 34 through 37 are plots of the Pn amplitude data used in this study showing the fit for Q' according to equations (7) and (8) for each data set. The results of the analysis of these data in terms of Q' and velocity gradients are summarized in Table 2 and Figure 38.

Referring to Figures 34-37, we see that there is considerable scatter in the Pn amplitude data. As was true for the crustal amplitude data, the standard error for the Pn data is at best

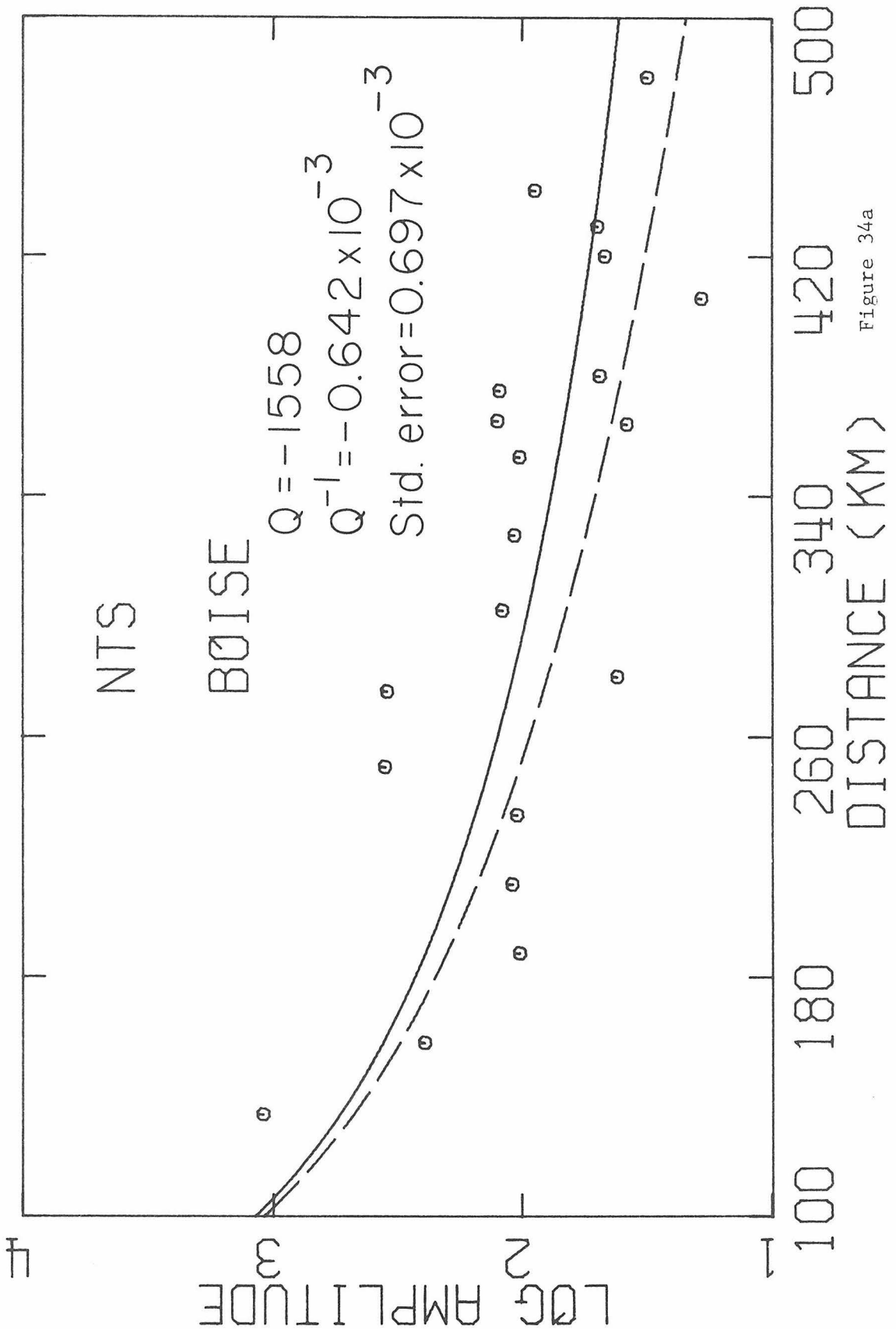
NTS
BOISE
Q=-1558
Q^{-1}=-0.642x10^{-3}
Std. error=0.697x10^{-3}
LOG AMPLITUDE
DISTANCE (KM)
1
2
3
4
100
180
260
340
420
500

Figure 34a

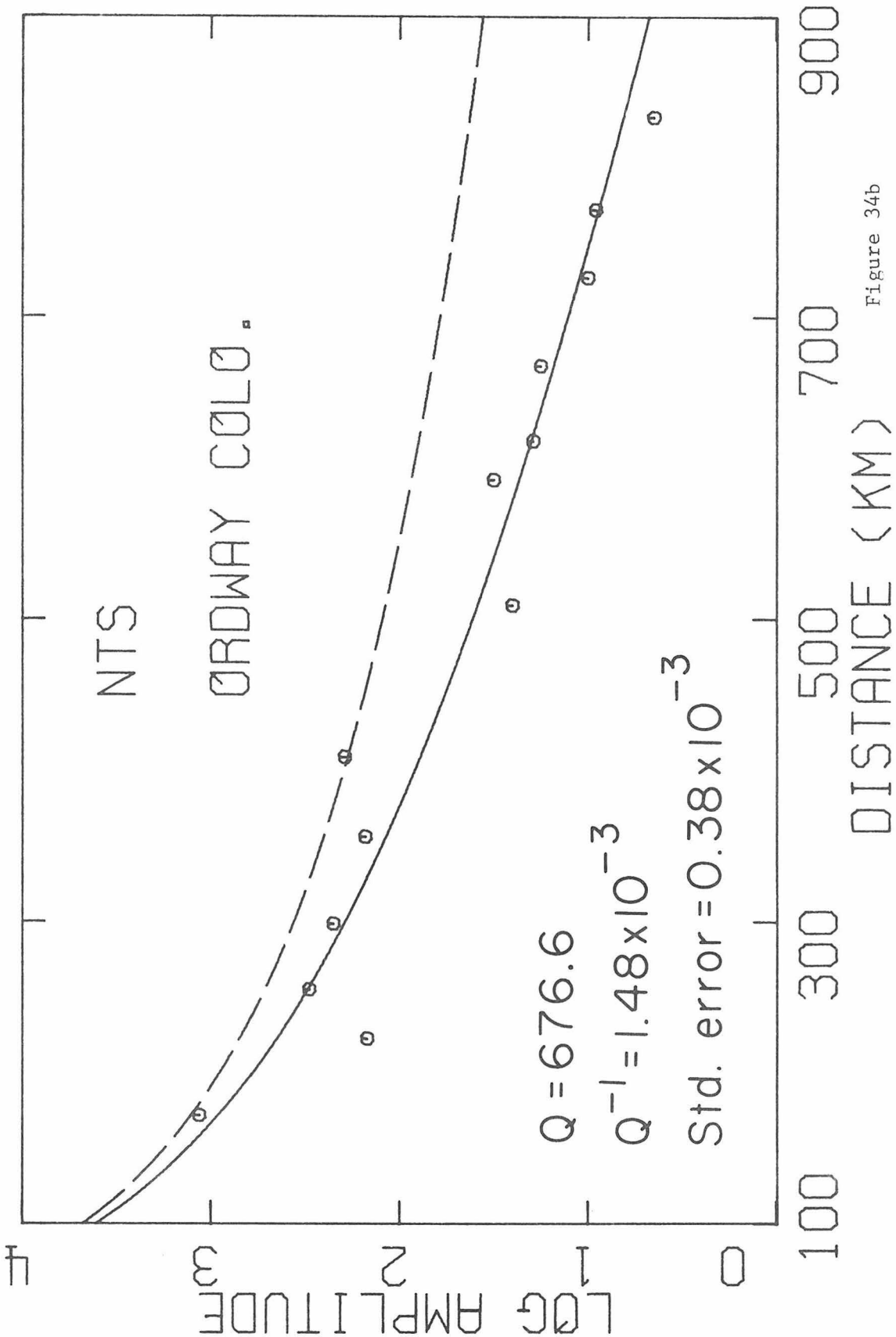
NTS
ORDWAY COLO.
Q=676.6
$Q^{-1}=1.48\times10^{-3}$
Std. error=0.38×10^{-3}
LOG AMPLITUDE
DISTANCE (KM)
0
1
2
3
4
100
300
500
700
900

Figure 34b

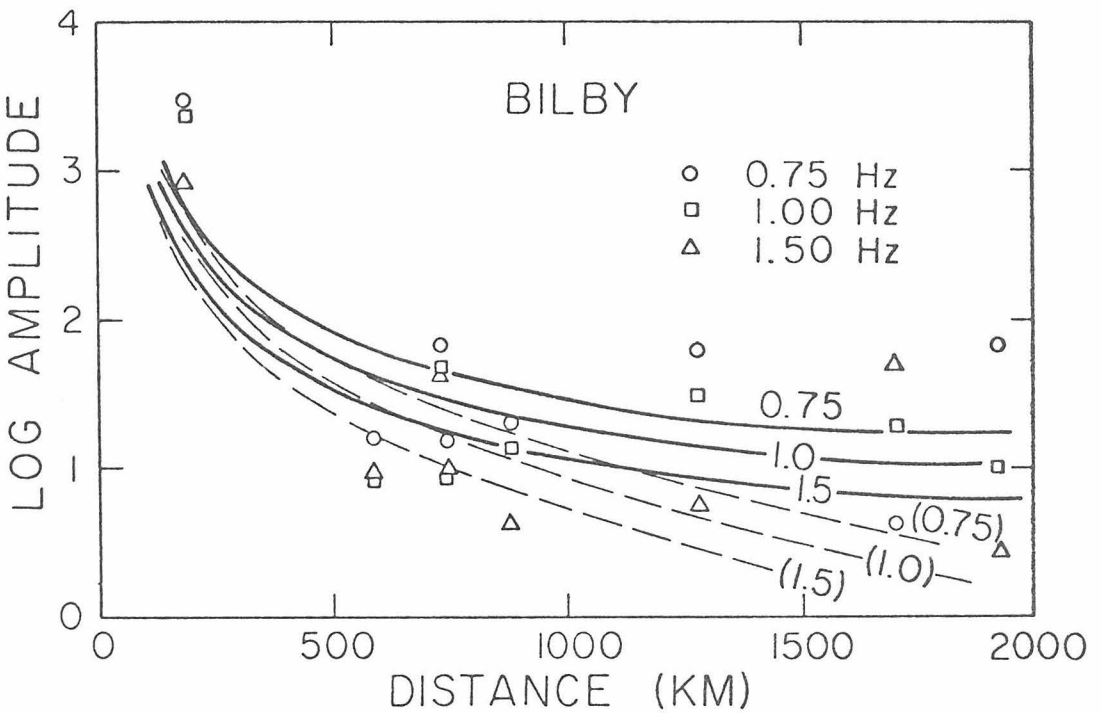
BILBY
0.75 Hz
1.00 Hz
1.50 Hz
0.75
1.0
1.5
(0.75)
(1.0)
(1.5)
LOG AMPLITUDE
DISTANCE (KM)
0
1
2
3
4
0
500
1000
1500
2000

Figure 34c.

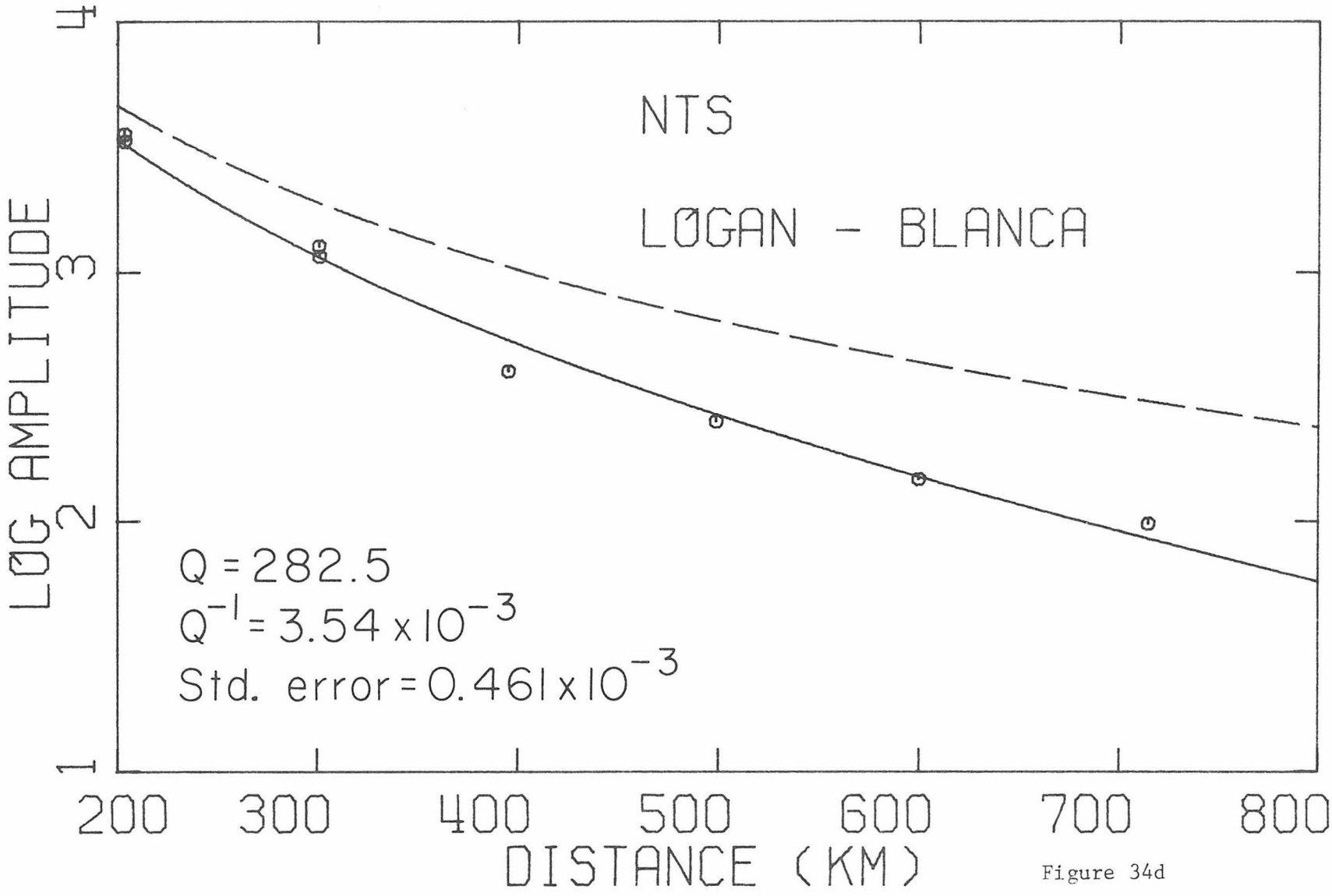
NTS
LØGAN - BLANCA
LØG AMPLITUDE
4
3
2
1
Q = 282.5
$Q^{-1} = 3.54 \times 10^{-3}$
Std. error = 0.461×10^{-3}
200
300
400
500
600
700
800
DISTANCE (KM)

Figure 34d

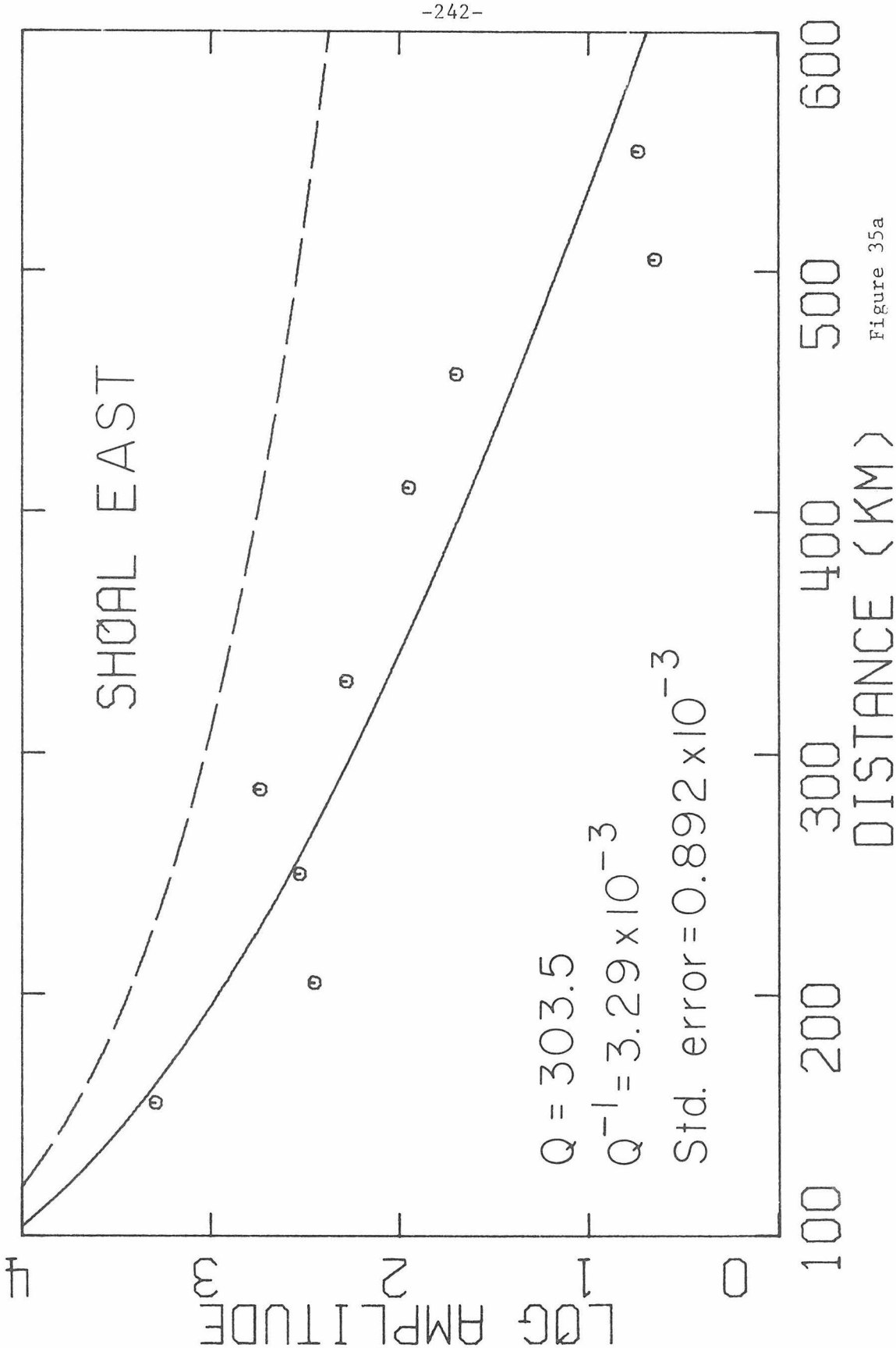
SHOAL EAST
Q = 303.5
$Q^{-1} = 3.29 \times 10^{-3}$
Std. error = 0.892×10^{-3}
LOG AMPLITUDE
0
1
2
3
4
100
200
300
400
500
600
DISTANCE (KM)

Figure 35a

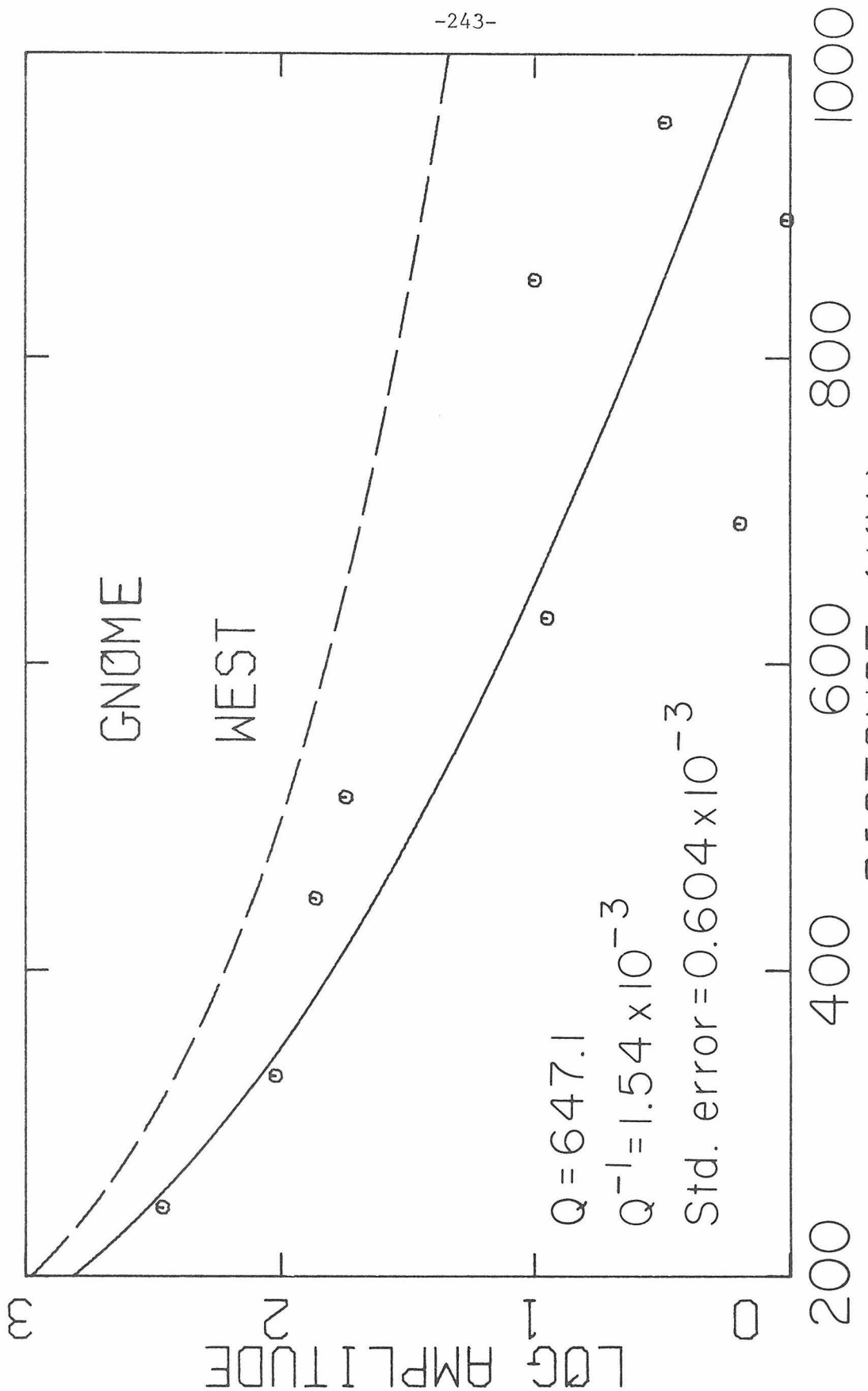
GNOME
WEST
Q=647.1
$Q^{-1}=1.54\times10^{-3}$
Std. error=0.604×10^{-3}
LOG AMPLITUDE
DISTANCE (KM)
0
1
2
3
200
400
600
800
1000

Figure 35b

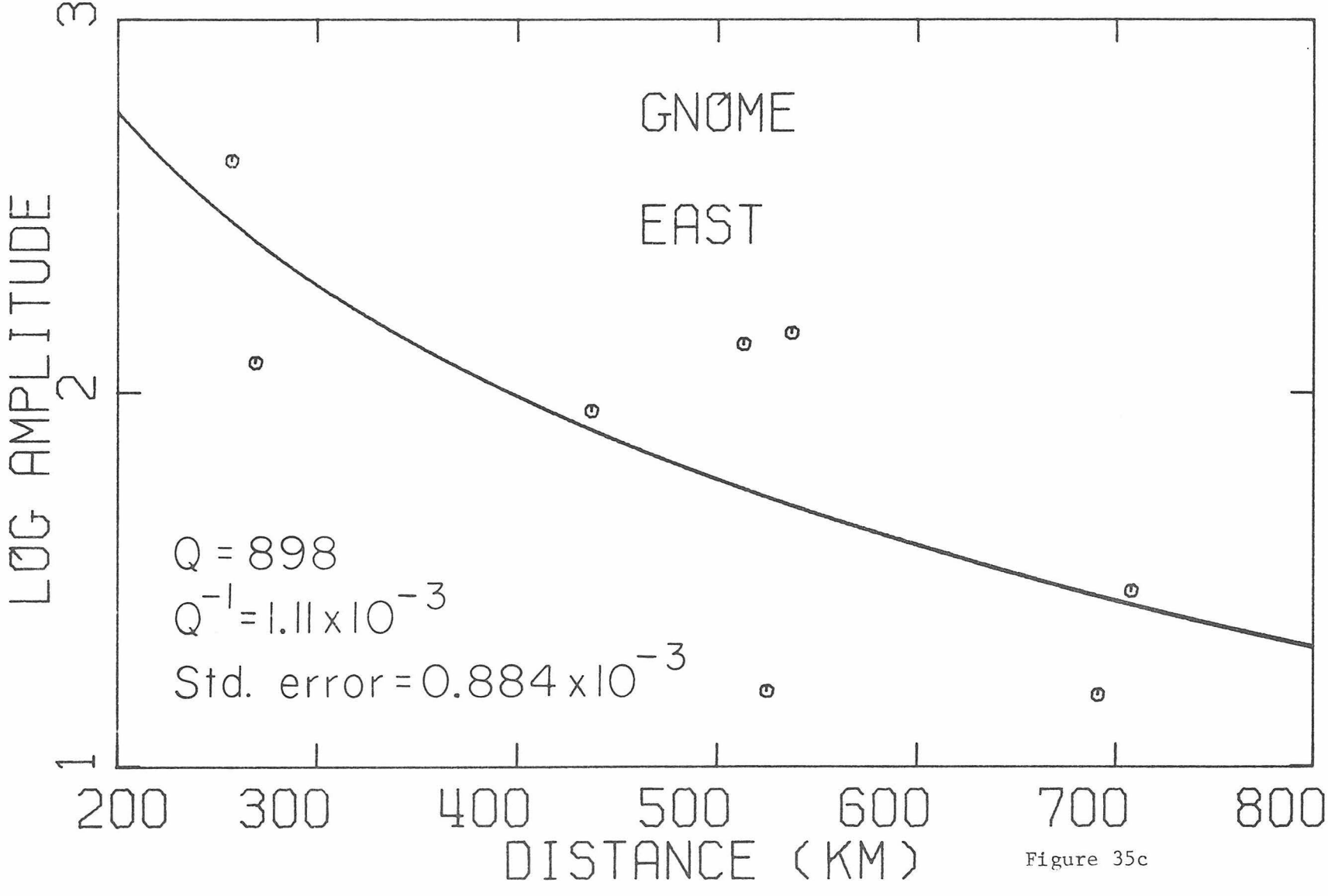
GNOME
EAST
LOG AMPLITUDE
3
2
1
200
300
400
500
600
700
800
DISTANCE (KM)
Q = 898
$Q^{-1} = 1.11 \times 10^{-3}$
Std. error = 0.884×10^{-3}

Figure 35c

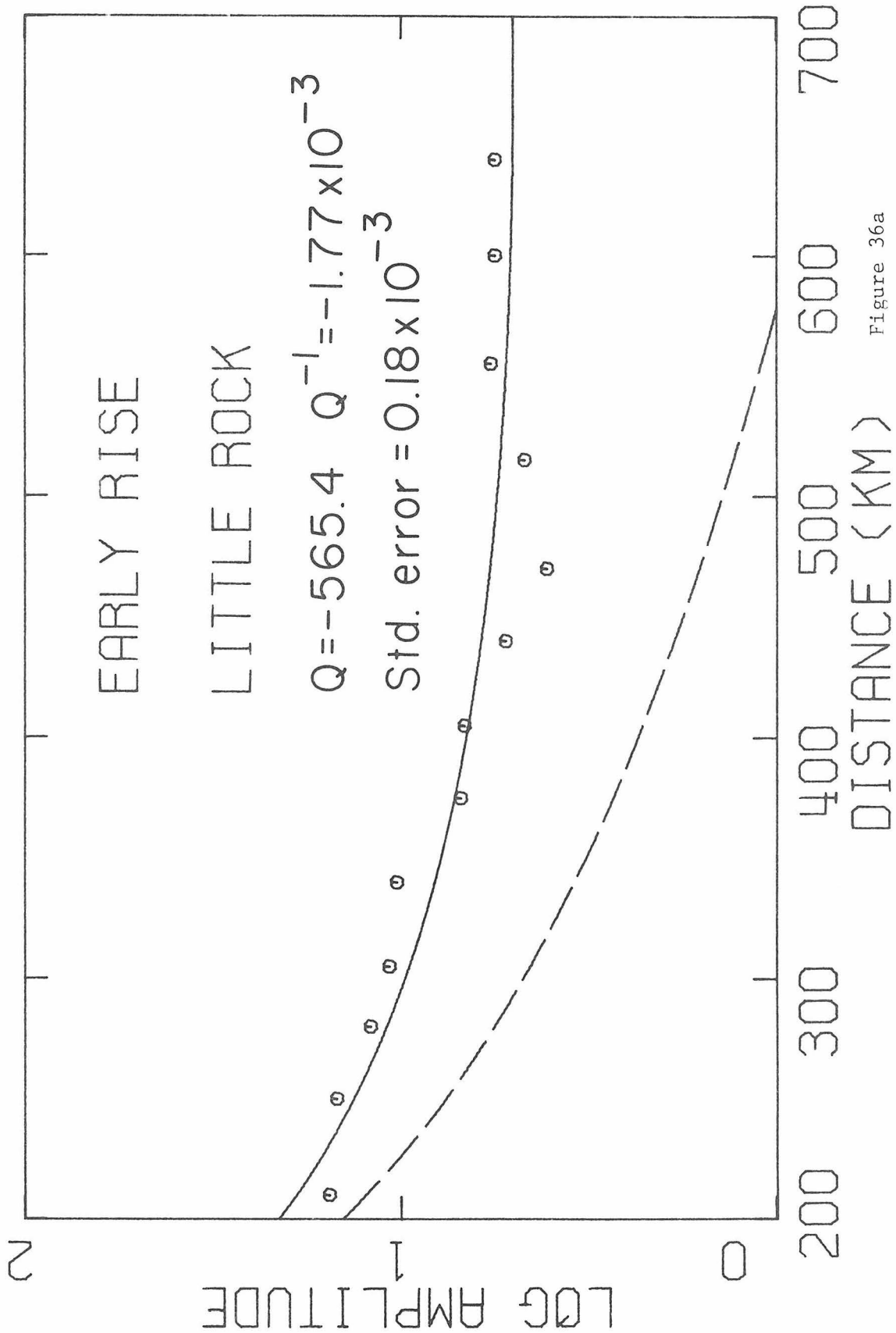
EARLY RISE
LITTLE ROCK
Q=-565.4 Q⁻¹=-1.77x10⁻³
Std. error = 0.18x10⁻³
LOG AMPLITUDE
DISTANCE (KM)
2
1
0
200
300
400
500
600
700

Figure 36a

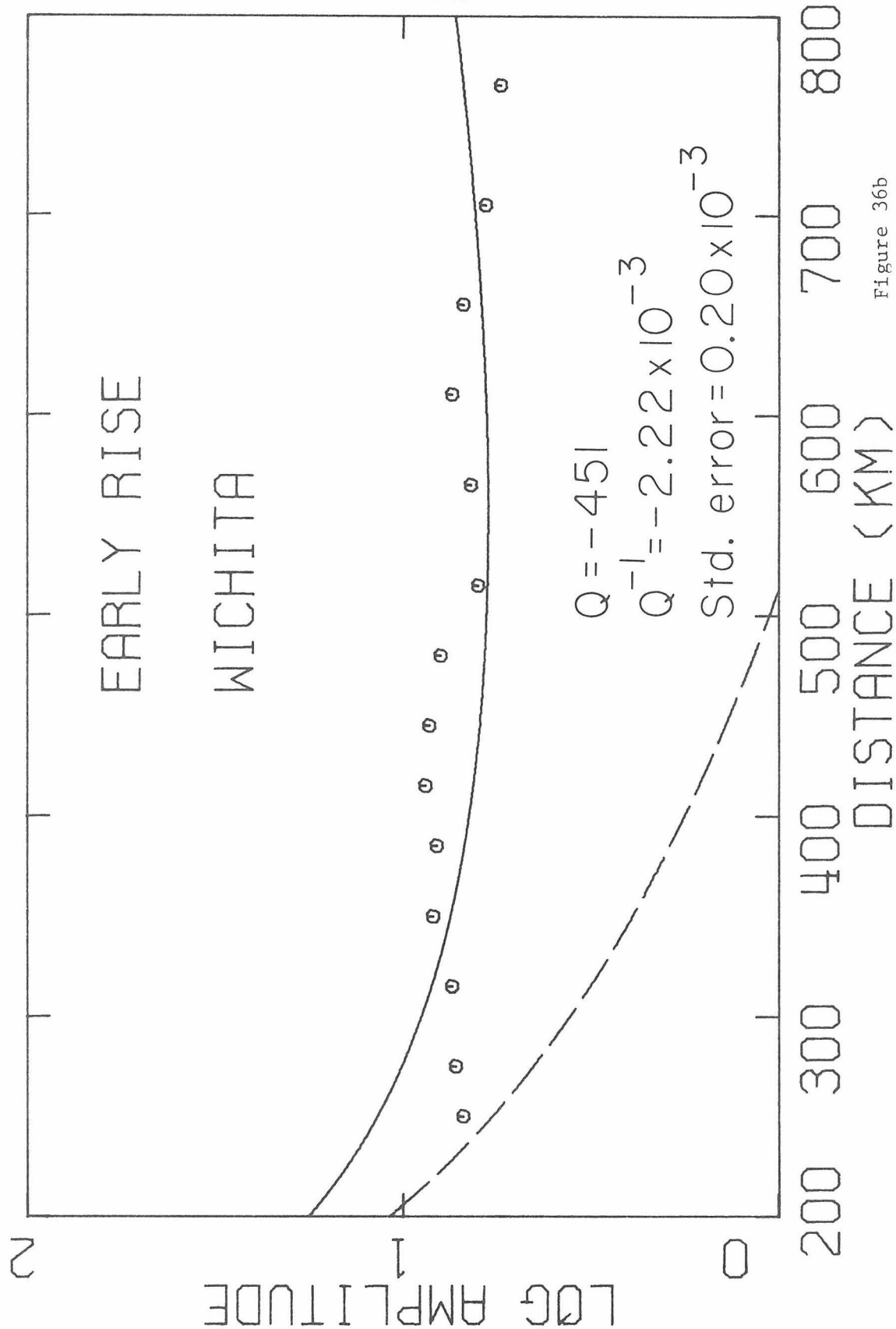
EARLY RISE
WICHITA
Q = -451
$Q^{-1} = -2.22 \times 10^{-3}$
Std. error = 0.20×10^{-3}
LOG AMPLITUDE
2
1
0
200
300
400
500
600
700
800
DISTANCE (KM)

Figure 36b

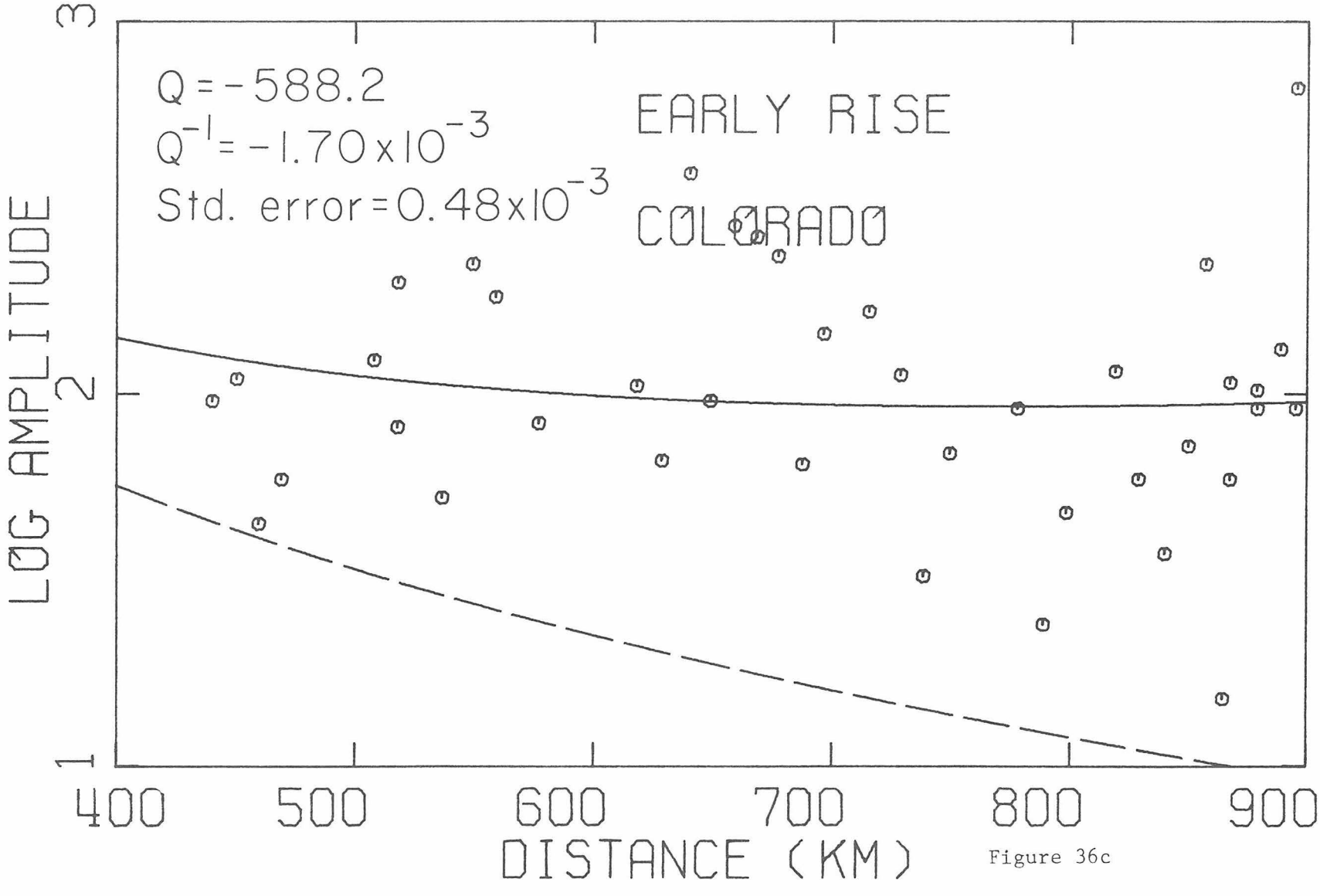
Q = -588.2
$Q^{-1} = -1.70 \times 10^{-3}$
Std. error = 0.48×10^{-3}
EARLY RISE
COLORADO
LOG AMPLITUDE
3
2
1
400
500
600
700
800
900
DISTANCE (KM)

Figure 36c

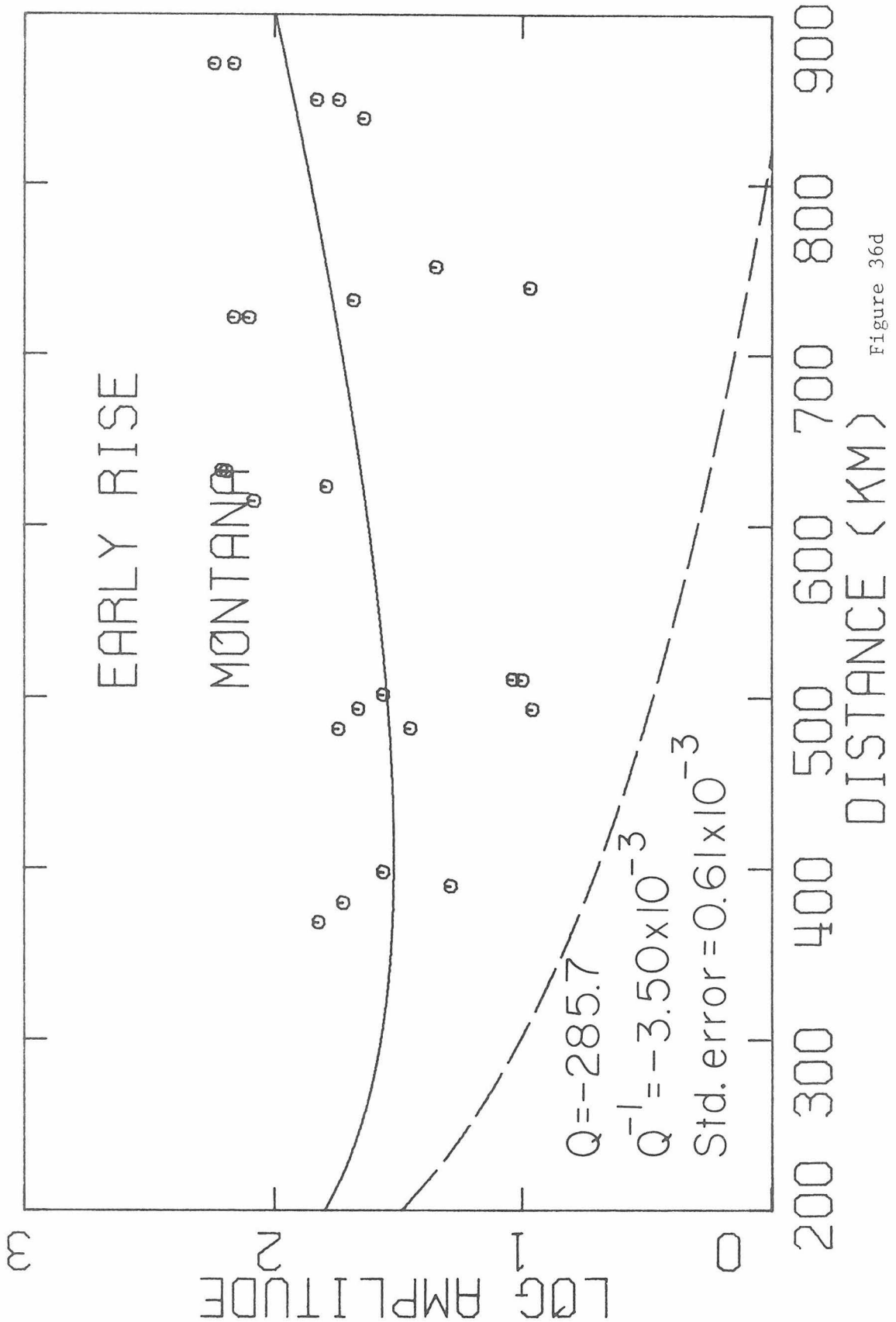
EARLY RISE
MONTANA
Q=-285.7
$Q^{-1}=-3.50\times10^{-3}$
Std. error=0.61×10^{-3}
LOG AMPLITUDE
DISTANCE (KM)
0
1
2
3
200
300
400
500
600
700
800
900

Figure 36d

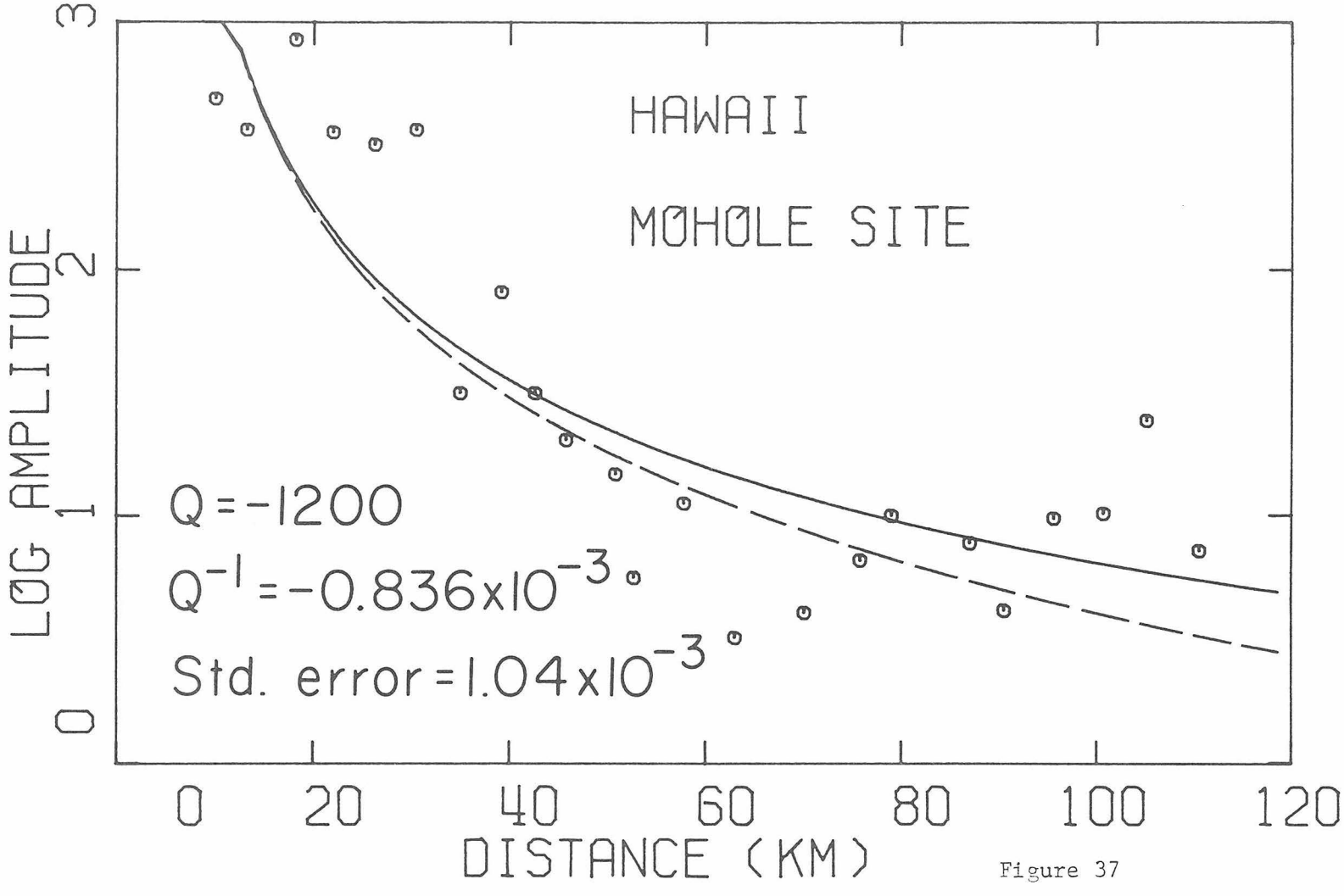
HAWAII
MOHOLE SITE
Q = -1200
$Q^{-1} = -0.836 \times 10^{-3}$
Std. error = 1.04×10^{-3}
LOG AMPLITUDE
0
1
2
3
0
20
40
60
80
100
120
DISTANCE (KM)

Figure 37

one-tenth of $(Q')^{-1}$ as shown in Table 2. However, in this case the standard error values are all less than the $(Q')^{-1}$ (with the single exception of the NTS-Boise data, in which case the standard error is slightly larger than $(Q')^{-1}$) suggesting that the Pn amplitudes are, in general, better behaved than the crustal data. Nevertheless, we still cannot place much weight on the results for any given profile, but must look for trends in the data common to a given region.

As can be seen in Figure 38, there is a consistent and marked difference in the Q' values between the profiles radiating from Lake Superior and the EARLY RISE events in the eastern United States and the profiles in the western United States associated with various nuclear events. The Q' values for the EARLY RISE profiles are consistently less than -600 indicating an appreciable gain of the observed data with respect to the classical head wave amplitude with distance. This relative gain can be clearly seen in Figures 36a-36d; here all of the data points lie distinctly above the dashed line defining the classical head wave amplitude. On the other hand, the Q' values associated with profiles in the western United States are positive (indicating a slight amplitude loss with distance). The relation of these data with respect to the reference head wave amplitudes are illustrated in Figures 34 and 35. The Q' value associated with the oceanic profile is -1200, and as shown in Figure

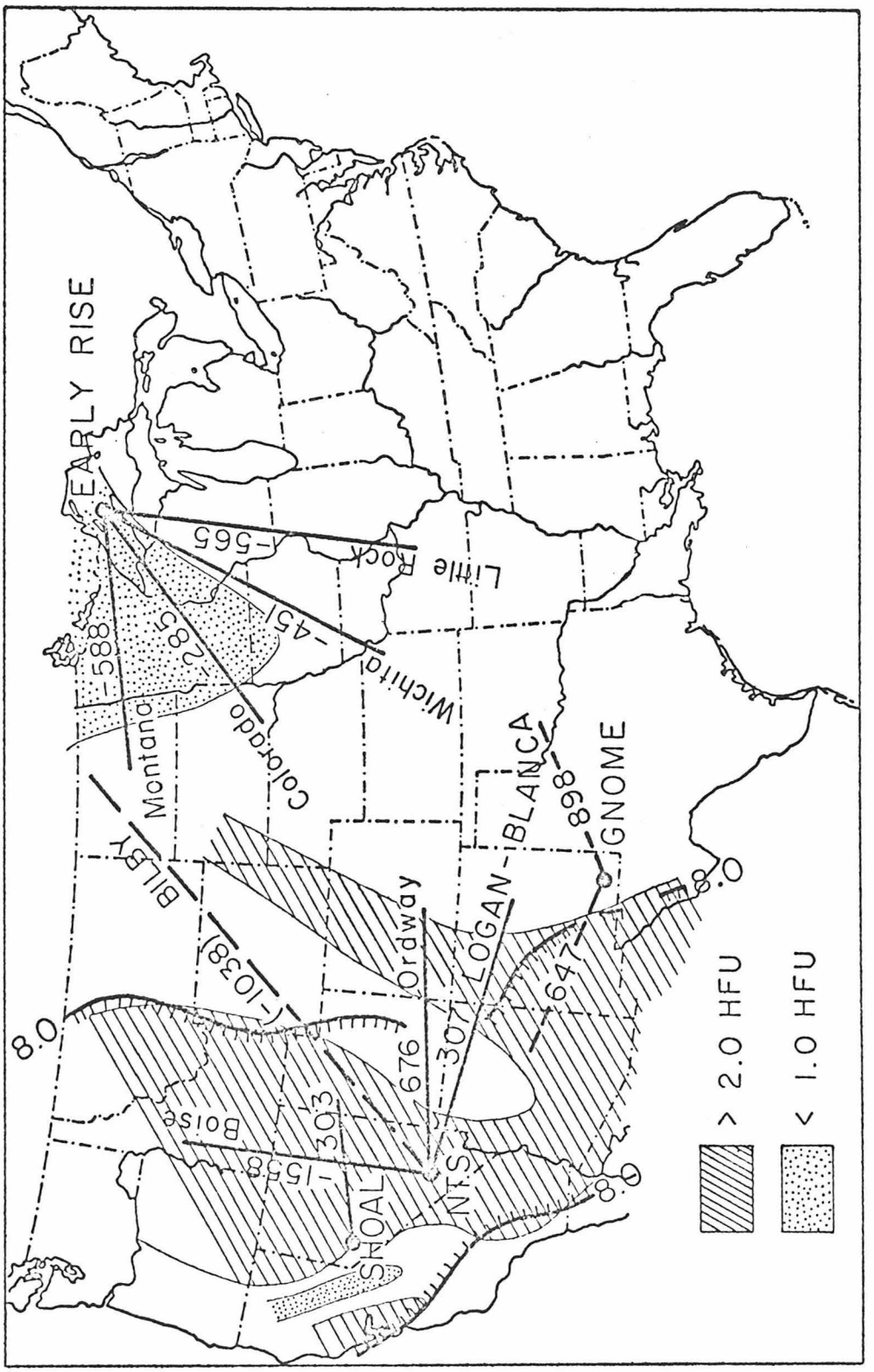
EARLY RISE
Little Rock
Wichita
Colorado
Montana
Billy
Ordway
BLANCA
GNOME
LOGAN
SHOAL
Boise
8.0
> 2.0 HFU
< 1.0 HFU

Figure 38

36, the least-squares fit though the data falls off slightly less rapidly with distance than the classical head wave.

Simply on the basis that clear P-wave arrivals were recorded out to distances of 2000 km from 10,000 pound chemical explosions in Lake Superior, it seems evident that the P-wave velocity in the upper mantle under much of eastern North America must increase in some manner with depth to focus much of the initially downward radiated energy back to the surface. In fact, published velocity structures based on the EARLY RISE data are composed almost entirely of positive velocity gradients and abrupt increases in velocity with only minor velocity reversals. (See Julian, 1970; Iyer et al., 1969; Green and Hales, 1968, and Lewis and Meyer, 1968.) Most of these studies are based on an inversion of travel-time data with only a qualitative reference to amplitudes. However, Julian (1970) considered the absolute amplitude data using a quantitative estimate of the EARLY RISE source function together with a first-order ray theory. He concluded that positive velocity gradients on the order of at least 2×10^{-3} sec^{-1} are required in the upper mantle to explain the large amplitudes of the observed data.

According to the ray-theoretical asymptotic solution for diving waves in a spherical earth developed in Chapter 1, first-order ray theory should provide an adequate description of first arrival amplitudes of 2 Hz waves (the dominant frequency of the EARLY RISE

source) propagating through a mantle with a 2×10^{-3} sec^{-1} gradient beyond about 600 km. Julian's analysis included data beyond this distance, and his results should be valid in this respect.

Comparison of the general trend in the EARLY RISE amplitude data and its relation to the classical head wave amplitude curves in Figures 36a-36d with the theoretical amplitude curves for diving waves in a spherical earth in Figures 19 and 20, shows that velocity gradients on the order of 5×10^{-3} sec^{-1} in the mantle lid beneath the eastern United States are quite reasonable. However, on the basis of this rather cursory treatment of the data, we can only say that the velocity beneath the M discontinuity increases in some average way at a rate on the order of 2×10^{-3} to 5×10^{-5} sec^{-1}, and not necessarily in a smooth continuous gradient.

It has been recognized for some time that Pn amplitudes recorded in the western United States from nuclear events decay more rapidly with distance than predicted by classical body wave theory. Reported Pn amplitude decays proportional to Δ^{-3} are well established in the literature (see Romny, 1959; Ryall and Stuart, 1963; and Hill and Pakiser, 1966; for examples). Here we note that at large distances from the critical point, the classical head wave amplitude decays approximately as Δ^{-2}. This relative decay of observed Pn amplitudes with respect to the classical head

wave is generally confirmed by the data presented in Figures 35 and 36a-36d. On the basis of the criteria for interpreting Q' values established earlier, we conclude that velocity gradients more negative than the critical gradient may be characteristic of the mantle lid in the western United States. According to the empirical relation between Q' and γ in Figure 26, these gradients could be as low as -6.8×10^{-3} sec^{-1} east of the SHOAL event (near Fallon, Nevada) and southeast of NTS (the LOGAN-BLANCA profiles). The NTS-Boise profile has a Q' of -1558, suggesting a small effective positive gradient, or a nearly homogeneous mantle. The data recorded to the east and to the west of the GNOME event in southeastern New Mexico (Romny, et al., 1962) have Q' values of 898 and 647 suggesting subcritical gradients of -2.7×10^{-3} and -3.5×10^{-3} sec^{-1}, respectively. These results are summarized in Table 1.

The BILBY Pn data summarized in Figure 34c and represented by the long dashed line in Figure 38 are taken from Archambeau et al. (1969). The data points represent the Fourier spectral amplitudes of the Pn arrival at 0.45, 1.0, and 1.5 Hz recorded on LRSM stations along two profiles extending roughly northwest and southeast from NTS. The data extend to nearly 2000 km from the source at NTS, although Pn becomes a second arrival beyond about 1000 km. Where it occurs as a second arrival, the Pn phase was identified using

a non-linear polarization filter (Archambeau, et al, 1969). Because these data are combined from two azimuths and cover such a large distance range (each profile crosses several geologic provinces), they can be regarded as sampling the mantle lid under the west-central section of the United States in some average sense. Considering the scatter in the spectral amplitude points, it is somewhat surprising that the least-square fits to each frequency have the close relationship to each other and to the classical head wave curves shown in Figure 34c. Note that the least-square curves have essentially the same separation as the classical head wave amplitude curves but that they fall off somewhat less rapidly with distance than the reference curves. Comparing these curves with the theoretical amplitude curves for a homogeneous crust and upper mantle in Figure 16 (which is based on a structure very similar to that obtained by Archambeau et al., 1969, using the BILBY data), we see that the difference between the observed amplitudes and the classical head wave amplitude in Figure 34a is somewhat less than the predicted difference between the classical head wave and the direct diving wave at distances between 1500 and 2000 km (13 to 18 degrees) in Figure 16. Accordingly, we can interpret these data as suggesting that, on the average, the mantle lid under the west-central United States has a slight negative velocity gradient. This gradient cannot be as negative as the critical gradient

(-1.2×10^{-3} sec^{-1}) and is probably at most a null gradient (depending on the physical Q in the lid). This is consistent with the result obtained by Archambeau et al. (1969). Using a ray-theoretical analysis of these amplitude data, they conclude that the mantle lid has a negative velocity gradient on the order of -1×10^{-3} sec^{-1}.

The Q' values associated with the profiles described above are plotted on a map of the United States in Figure 38 together with contours showing the distribution of heat flow according to Roy et al (1971) and Pn velocities according to Pakiser and Steinhart (1964). It is evident from this map that positive Q values (and possible negative velocity gradients) correlate with the high heat flow (greater than 2.0 HFU) and low Pn velocities (less than 8.0 km/sec) associated with the tectonically active western United States. On the other hand, the small, negative Q' values (positive velocity gradients) are confined to the stable eastern United States where the heat flow is normal or low (less than 1.0 HFU) and the Pn velocities are 8.0 km/sec or greater.

4. Velocity and Geothermal Gradients

The correlation of the low Q' values found for both crustal and Pn amplitude data with the high heat-flow, tectonically active

western United States may be due to a combination of any of the following factors:

(1) Scattering may be a more important factor in the tectonic provinces than in the stable, relatively unfaulted eastern crust. The major fault blocks in the Basin and Range, for example, have characteristic widths of 25 km to 50 km. The Pg crustal phase is normally recorded as a first arrival out to distances of 100 km and thus we might expect to see the effects of these major faults as rather abrupt changes in Pg amplitudes at discrete distances rather than the more nearly random scatter typically observed for the Basin and Range Pg amplitudes. Of course, smaller, more closely spaced faults could effectively produce the observed low Q' values and cannot be ruled out. The relief on the M-discontinuity inferred by Hill and Pakiser (1966) from Pn time delays on the NTS Boise profile would certainly effect the observed Pn amplitudes, and no doubt some of the scatter in the amplitude data can be attributed to such effects. In the case of negative or near critical velocity gradients in the mantle lid, relief on the M-discontinuity would serve to decrease the observed Q' values by scattering the head wave. However, in the case of a positive gradient in the mantle lid, the principle effect of such relief would be to focus and defocus the emerging diving waves resulting in peaks and troughs

in the amplitude data but not a net decrease in the average level of the amplitudes with distance. Thus, although we may attribute the Pn low Q' values in the west more to relief on the M-discontinuity than to negative gradients in the mantle lid, it is unlikely that the mantle lid has a significant positive gradient.

(2) A temperature dependent anelastic Q may also explain the observed correlation of low Q' and high heat flow. According to geotherms published by Roy et al. (1968) and Lachenbruch (1970), the temperature in the Basin and Range is higher by 30° to 50°C at depths of 3 to 5 km and about 300°C at the base of the crust than temperatures at equivalent depths under the eastern United States. Q shows a strong temperature dependence at high pressures for many materials (Jackson and Anderson, 1970), but the appropriate measurements have not been made on rocks at temperatures and pressures typical of the crust and mantle lid, nor has a likely mechanism been proposed. Thus a temperature-dependent Q remains a possible, but presently inaccessible factor.

(3) Finally, we consider the possibility that temperature is a dominant factor controlling velocity gradients in major refracting horizons in the crust and upper mantle and that the low Q' values in the western high heat flow province are primarily due to negative velocity gradients associated with high geothermal gradients. The

velocity gradient in a rock of homogeneous composition and structure is related to pressure and temperature effects according to

$$\frac{dV_p}{dz} = \left(\frac{\partial V_p}{\partial P} \right)_T \frac{dP}{dz} + \left(\frac{\partial V_p}{\partial T} \right)_P \frac{dT}{dz} \qquad (9)$$

where z is a depth coordinate, $\frac{dP}{dz}$ and $\frac{dT}{dz}$ are the lithostatic and geothermal gradients respectively, and $\left(\frac{\partial V_p}{\partial p} \right)_T$ and $\left(\frac{\partial V_p}{\partial T} \right)_P$ are obtained from laboratory measurements on the variation of P-wave velocities (V_p) due to pressure and temperature.

The temperature curves published by Roy et al. (1968) for their heat flow provinces indicate that crustal geothermal gradients in the Basin and Range and eastern United States are about 30°/km and 15°/km, respectively. According to the temperature curves published by Lachenbruch (1970) and to recent work on the systematic inversion of temperature data for geothermal structure by Minster and Archambeau (1970), the crustal gradient may be as high as 40°/km and 20°/km for the Basin and Range and eastern United States. According to these same workers, geothermal gradients in the mantle lid are about 20°/km and 10°/km under the Basin and Range and eastern United States, respectively, although these values are less certain from those in the crust.

Lithostatic gradients in the crust are essentially determined by local density and should be about 0.27 kb/km in the crystalline "granitic" crust, 0.3 kb/km in the more basic "intermediate" layer,

and 0.33 kb/km in the mantle lid.

Hughes and Maurette (1956) have measured variations in both compressional and shear waves in granites for crustal temperatures and pressures. From their data we can estimate values for $\left(\frac{\partial V_p}{\partial T}\right)_P$ and $\left(\frac{\partial V_p}{\partial P}\right)_T$ at pressure-temperature conditions approximate for the upper part of the crystalline crust, which we will take to be 1 kb and 100°C. At 1 kb the average of $\left(\frac{\partial V_p}{\partial T}\right)_P$ is approximately 9.0×10^{-4} km/sec/C°, using the data for the granites published by Hughes and Maurette (1956) or the curves given by Press and Biehler (1964) based on these data.

Extrapolation of values for $\left(\frac{\partial V_p}{\partial P}\right)_T$ measured in the laboratory to actual conditions in the upper crust involves some difficulties. Velocities of samples measured in the laboratory rise rapidly with increasing pressures up to about 1 kb as cracks and open spaces in the sample are closed. Beyond 1 kb the velocity increases with pressure much more slowly. Presumably rocks that have been in place at pressures in the order of 0.5 to 1 kb for geologic time periods have had any original cracks or open spaces closed by non-elastic flow or creep processes so that the high pressure derivatives measured in laboratory samples in this pressure range are considerably higher than values that would be measured <u>in situ</u>. Furthermore, Nur and Simmons (1969) have shown that at pressures less than 1 kb, P-wave velocities are significantly higher in water-saturated samples

than in dry samples and that the knee in the pressure-velocity curve is shifted to lower pressures. Accordingly variations in P-wave velocities on the high pressure side of the knee (between 1 and 2 kb) were used to estimate $\left(\frac{\partial V_p}{\partial P} \right)_T$ from Hughes and Maurette's data. The average results for three granites at 100°C gives $\left(\frac{\partial V_p}{\partial P} \right)_T \sim 0.07$ kb/km.

When these values are put into equation (9), we obtain

$$\frac{dV_p}{dz} = \begin{cases} -0.008 \text{ km/sec/km under the Basin and Range} \\ 0.005 \text{ km/sec/km under the eastern U. S.} \end{cases}$$

which indicates that it is reasonable to expect negative velocity gradients in the upper part of the crystalline crust in the high heat flow Basin and Range Province and small positive gradients in the normal eastern United States in accord with our interpretation of Pg Q' values in terms of velocity gradients.

A similar calculation using data published by Hughes and Maurette (1957) for basic igneous rocks gives the following result for velocity gradients at the top of the intermediate layer under the Snake River Plain, Lake Superior, and Mississippi.

$$\frac{dV_p}{dz} = \begin{cases} -0.016 \text{ km/sec/km under Snake River Plain} \\ -0.003 \text{ km/sec/km under Lake Superior} \end{cases}$$

In this calculation the partial derivatives for pressure and temperature were evaluated at 3 kb and 200°C and geothermal gradients

of 30°C/km were assumed for the Snake River Plain and 15°C/km for Lake Superior and Mississippi. In fact, it turns out that at depths much below 5 km, the pressure partials are quite small, and for any reasonable geothermal gradients it is difficult to avoid negative velocity gradients in chemically homogeneous horizons in the lower crust and upper mantle using Hughes and Maurette's data.

The analogous calculation for velocity gradients expected in the mantle lid under the western tectonic provinces and the stable eastern provinces is based on pressure and temperature data for olivine (forsterite) reported by Anderson and Sammis (1970). The pertinent values are

$$\left(\frac{\partial V_p}{\partial P} \right)_{298°K} = 10.3 \times 10^{3} \text{ km/sec/kb}$$

$$\left(\frac{\partial V_p}{\partial T} \right)_{1 \text{ bar}} = -4.1 \times 10^{4} \text{ km/sec/°K} \quad ,$$

which when put in equation (9) together with the geothermal gradients appropriate for the mantle lid mentioned above yield

$$\frac{dV_p}{dz} = \begin{cases} -4.8 \times 10^{-3} \text{ sec}^{-1} \text{ under the western United States} \\ -0.7 \times 10^{-3} \text{ sec}^{-1} \text{ under the eastern United States} \end{cases}$$

However, the partial derivative data used in this calculation were measured at room temperature and pressure instead of at upper mantle temperatures and pressures (Anderson et al., 1968). Correction of the partial derivative data to the appropriate P-T conditions would serve to increase the magnitude of the temperature partial with respect to the pressure partial (Sammis, 1971), and the proper velocity gradients are probably somewhat more negative than those obtained above. Thus, again, it is difficult to avoid negative velocity gradients in a mantle lid of uniform composition assuming reasonable geothermal gradients.

In computing velocity gradients by equation (9), we are taking the difference between two small relatively uncertain quantities; thus the above should be taken as plausibility arguments. As was indicated earlier, the geothermal gradients could be as high as 40°/km and 20°/km in the crust under the Basin and Range and eastern United States, which would result in negative velocity gradients in both regions. On the other hand, Birch's velocity-temperature measurements (Birch, 1958) give temperature partial derivatives nearly an order of magnitude smaller than those of Hughes and Maurette, which would result in positive velocity gradients everywhere. (However, Hughes and Maurette's values seem to be more in line with recent measurements on single crystals and powdered ceramics - see Anderson and Sammis (1970)). Finally, we note that if a given

refracting horizon has a vertical variation in composition, C, a term $\left(\frac{\partial V_p}{\partial C}\right)\frac{dC}{dz}$ must be added to equation (7), which could change the sign of a velocity gradient computed assuming homogeneity.

Conclusions

The amplitude spectra of critically refracted waves (head waves) are sensitive to small velocity gradients in the refracting horizon, and in principle, the analysis of amplitudes of these waves provides a direct method for determining either negative or positive velocity gradients in crustal and upper mantle refracting horizons. However, for narrow band width data it is not possible to distinguish between the effects of small negative velocity gradients and anelasticity (Q) or scattering. In this case it is only possible to estimate maximum negative velocity gradients from the effective Q(Q') of the amplitude data, which is a measure of the decay or gain with distance of observed amplitudes with respect to theoretical amplitudes for head waves refracted from critical velocity gradients in a spherical earth (or a homogeneous medium in a flat earth).

Q' values computed for critically refracted first arrival Pg, P*, and Pn amplitudes recorded in the continental United States show an inverse correlation with heat flow. Crustal Q' values in the eastern United States and west coast normal heat flow provinces

are greater than 1000 or negative, which according to theoretical results on the effects of small gradients on head wave amplitudes implies critical, null, or small positive velocity gradients for the upper portions of the crystalline crust ("granitic layer") and intermediate layer in these regions. Crustal Q' values in the Basin and Range high heat flow province, which probably includes the Snake River Plain, are generally less than 1000. Similarly, Q' values for Pn amplitudes are small and negative in the stable eastern United States and predominantly positive in the tectonically active western United States. The positive Q' values common to the western United States may be due to

1) scattering of the critically refracted waves by relief on the refractor associated with major crustal faulting (as in the Basin and Range province),

2) a temperature dependent anelastic Q,

3) negative velocity gradients in the major crustal and upper mantle horizons associated with high geothermal gradients.

Available information is insufficient to quantitatively assess effects of the first two, and they remain as possible contributing factors. The third factor can be assessed quantitatively and is found to be consistent with the observed Q' - heat flow correlation. The values of Q' found for Basin and Range Pg amplitudes can be

interpreted as being due to negative velocity gradients of the order of 1 x 10^{-2} km/sec/km in at least the upper section of the crystalline crust (the 6.0 km/sec "granitic" horizon). Heat flow work suggests that the crustal geothermal gradients in the Basin and Range heat flow province is 30°/km or possibly somewhat higher. This gradient combined with partial derivatives of P-wave velocities in granites with respect to pressure and temperature measured in the laboratory suggests negative velocity gradients in the upper crystalline crust of about 0.8 x 10^{-2} km/sec/km under the Basin and Range. The lower geothermal gradients (about 15°/km) associated with the normal heat flow province combined with the same partial derivative data suggest positive velocity gradients of about 0.5 x 10^{-2} km/sec/km in the upper crystalline crust. Thus velocity gradients in the upper part of the crystalline crust (Pg refractor) determined from Pg amplitudes and geothermal gradients agree reasonably well in the Basin and Range and eastern United States - west coast heat flow provinces.

Similar calculations assuming geothermal gradients of 30°/km under the Snake River Plain and 15°/km under Lake Superior and Mississippi suggests negative velocity gradients of 1.6 x 10^{-2} km/sec/km in the intermediate layer under the Snake River Plain, 0.3 x 10^{-2} km/sec/km under Lake Superior and Mississippi. These

velocity gradients are more negative than those implied by the Q' values obtained from the P* amplitude data. If we take this result at face value, then a compositional gradient (e.g. increasing mafic content with depth) is required in the upper part of the intermediate layer to bring the velocity gradient estimated from the geothermal gradient in line with that estimated from Q'. However, neither the amplitude nor the thermal data are of sufficient accuracy for this conclusion to warrant much confidence.

On the basis of laboratory measurements of pressure and temperature partials for olivine and inferred geothermal gradients at the base of the crust of 10°C/km under the stable eastern province, and 20°C/km under the tectonic western provinces, it appears that velocity gradients in the mantle lid are in the neighborhood of -0.8×10^{-3} sec^{-1} in the eastern provinces, and -4.7×10^{-3} sec^{-1} in the western provinces. Negative velocity gradients of this order are consistent with Q' values for Pn in the western tectonic provinces, and it is reasonable to expect that at least part of the relative attenuation of Pn amplitudes in these provinces is due to negative velocity gradients in an essentially homogeneous mantle lid. On the other hand, the positive velocity gradients in the mantle lid under the eastern United States required by the high Pn amplitudes are difficult to reconcile with the data from laboratory physical

property measurements and geothermal gradients for a lid of uniform composition. If we accept Julian's (1970) estimate for velocity gradients in the upper mantle under the eastern United States of 2×10^{-3} sec^{-1} and the pressure and temperature partials for olivine given above, then by (7) we would require a geothermal gradient of 3.5°C/km or less in a mantle lid of uniform composition. By all estimates this is too low, and we conclude that the mantle lid under the eastern United States very likely has a compositional gradient of some sort to counter the effect of the geothermal gradient on the velocity gradient. It remains to be seen whether such a gradient can be attributed to a systematic change in basic mineralogy with depth or to a temperature-dependent dehydration reaction as in the case of serpentine.

The positive velocity gradient for the mantle lid implied by the negative Q' for Hawaii (Mohole site) oceanic Pn amplitudes occurs in a region of normal oceanic heat flow (Sclater and Corry, 1967). Assuming a uniform mantle lid and using the pressure and temperature partials given by Anderson and Sammis (1970) for olivine, the geothermal gradient in the mantle lid under the Mohole site must be less than 8°C/km to give a positive velocity gradient. Again, a compositional gradient in the mantle lid is required to give a positive velocity gradient if the geothermal gradient is greater than 8°C/km, and evidently the oceanic geothermal gradient may be

as high as 20°C/km (Slater and Francheteau, 1970).

Thus on the basis of Pg amplitudes and thermal data, we conclude that a slight P-wave low velocity zone may exist in the upper crystalline crust in the Basin and Range high heat flow province and that such zones are unlikely in the eastern United States and west coast normal heat flow provinces. In the Basin and Range Province the crustal low velocity zone would have the form of a gradual decrease in velocity from the top of the crystalline crust downward (at a maximum rate of about 1×10^{-2} km/sec/km) and would terminate more or less abruptly at the top of the intermediate layer. An abrupt, pronounced crustal low velocity zone at depths of about 10 km of the type proposed by Muller and Landisman (1966) could be present but would be difficult to detect using the data and methods described in this paper.

Similarly, the mantle lid under the tectonically active western United States may have a slight negative velocity gradient, but the Pn amplitude data require a positive velocity gradient for the mantle lid under the stable, eastern United States. A systematic change in composition with depth is required in the eastern mantle lid on the basis of laboratory physical-properties measurements and anticipated geothermal gradients.

Chapter 3

1. Introduction

The massive Miocene basalt fields of the Columbia Plateau in eastern Washington and Oregon hold an intriguing but poorly understood relation to the development of western North America in terms of recently advanced ideas in plate tectonics (Atwater, 1970). Surprisingly, very little is known about the deep crustal and upper mantle structure of this important tectonic unit. An opportunity to obtain some deep seismic-refraction data in the Columbia Plateau was provided by the series of high-energy chemical explosions detonated in Greenbush Lake, British Columbia, by the Dominion Observatory of Canada under project EDZOE. This chapter is a summary of the results obtained by recording these shots along a profile directly south across the Columbia Plateau from the Canadian border into central Oregon.

The location of the Columbia Plateau and its relation to major geologic units in the Pacific Northwest is shown in Figure 39. An excellent summary of the general geologic and tectonic setting of the Columbia Plateau is given by Waters (1962). The Columbia Plateau is one of the largest flood basalt provinces in the world. It is composed of massive tholeiitic basalt flows of Miocene and early Pliocene age (the Columbia River basalts). On the west, it is bounded by the more recent andesitic volcanoes of the High

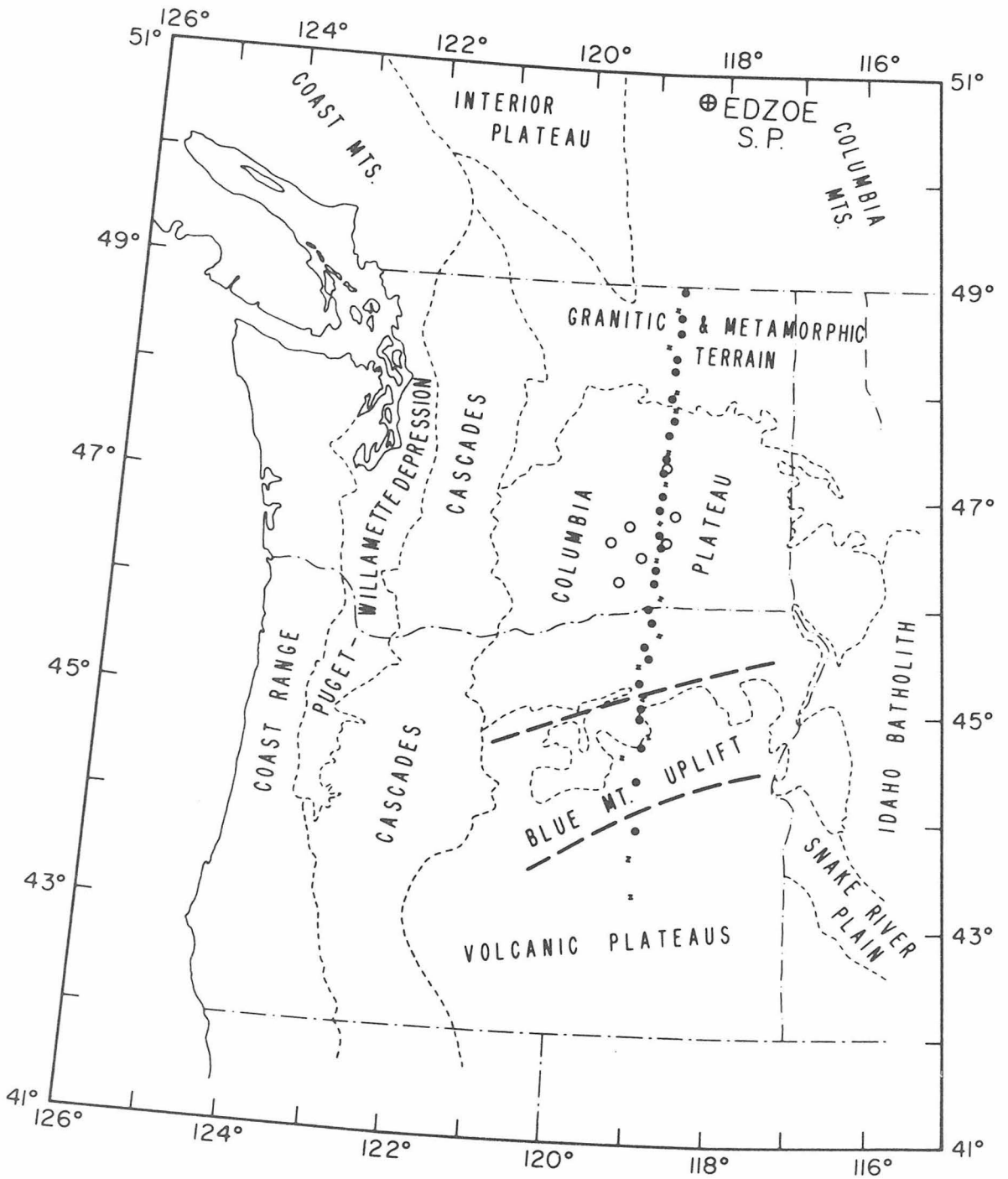
126°
124°
122°
120°
118°
116°
51°
49°
47°
45°
43°
41°
COAST MTS.
INTERIOR PLATEAU
EDZOE S.P.
COLUMBIA MTS.
GRANITIC & METAMORPHIC TERRAIN
WILLAMETTE DEPRESSION
CASCADES
COLUMBIA PLATEAU
COAST RANGE
PUGET-
CASCADES
BLUE MT. UPLIFT
IDAHO BATHOLITH
SNAKE RIVER PLAIN
VOLCANIC PLATEAUS

Figure 39

Cascades, and to the south it is separated from the high-alumina basalt fields of eastern Oregon by the Blue Mountain uplift. The Columbia River basalts lap against the Cretaceous Idaho Batholith to the east and Paleozoic granitic and metamorphic terrain to the north and northeast. A direct connection is made to the related Pliocene-Pleistocene basalt flows of the western Snake River Plain at the southeastern corner of the Plateau between the Blue Mountains and the Idaho Batholith. Potassium-Argon dating put the age of the Columbia River basalts somewhere between 12 and 16 m.y. (Swanson, 1967).

Published models of the crustal structure in the Pacific Northwest (Washington and Oregon) are based largely on regional studies of body wave travel-times from local earthquakes (Dehlinger, Chiburis, and Collver, 1965; and Dehlinger, Couch, and Gemperle, 1968) and surface wave phase velocities (Chiburis, 1966). These studies suggest that the crust east of the Cascades is about 40 km thick and that the P-wave velocity in the mantle just below the M-discontinuity is 7.9 km/sec. Johnson and Couch (1970) obtained data from the series of EDZOE explosions along two profiles that cut diagonally across the Cascades to the northwest of the Columbia Plateau. They conclude that the crust thins from about 35 km thick near Revelstoke, B.C. (adjacent to the EDZOE shot point) to between

25 and 30 km under the Cascades, and that the Cascades lack a significant root. In making their interpretation of these data, Johnson and Couch (1970) assume an upper mantle P-wave velocity of 7.96 km/sec based primarily on the earlier work of Dehlinger et al. (1965, 1968).

Some relatively detailed crustal seismic-refraction studies have been made in areas adjacent to the Columbia Plateau. White et al. (1968) conclude that the crust in southern British Columbia north of the Columbia Plateau is 30 to 35 km thick with a P-wave velocity of 6.1 km/sec from their interpretation of a series of reversed seismic-refraction profiles. They indicate that the true Pn velocity (the P-wave velocity just below the M-discontinuity) is 7.8 to 8.0 km/sec depending on the dip of the M-discontinuity. White and Savage (1965) report a crustal thickness in excess of 40 km in the vicinity of Vancouver Island, British Columbia, and a shallow ($\sim$ 10 km) 6.7-km/sec crustal layer, which may be related to the Eocene mafic volcanic rocks and associated gravity high in northwestern Washington described by Stuart (1961). The Snake River Plain to the southeast of the Columbia Plateau is commonly regarded as a closely related tectonic unit (i.e. a flood basalt plain). Hill and Pakiser (1966) interpreted a series of reversed seismic-refraction profiles across the western Snake River Plain in terms of crust 45 km thick composed of a 5.2-km/sec layer 10 km thick

over a 6.7-km/sec layer about 35 km thick. They find the Pn velocity under the Snake River Plain to be 7.9 km/sec. Prodehl (1970) derived a similar model making a reinterpretation of these same data.

2. Observations.

As part of project EDZOE, the Dominion Observatory of Canada detonated a series of 20 high-energy chemical explosions in Greenbush Lake, British Columbia, in August of 1969. The charges of the explosions were approximately equivalent to 10,000 lbs of geogel, although the first nine shots were partial misfires resulting in a smaller effective charge for these shots. The coordinates of all the shots are given as 50.782°N latitude and 118.344°W longitude. The shots were detonated in about 60 meters of water and at an elevation of about 982 meters.

Seismic waves from the explosions were recorded along a profile extending 800 km due south from the shot point from the Canadian border into central Oregon as shown in Figure 39. A total of 42 sites were occupied along this profile by three recording units. Two of the recording units used were California Institute of Technology trailers, which are capable of recording three seismic channels plus timing on film and magnetic tape. For this experiment, the output of a single, vertical seismometer with a natural period of

1.0 sec was recorded at two levels on tape and a single level on film. The third unit was used as a standard U. S. Geological Survey eight-channel seismic-refraction truck. This unit recorded the output of six vertical seismometers with a natural period of 1.0 sec equally spaced in a linear array 2.5 km long. In addition, the output of a pair of horizontal seismometers, located near one of the verticals in the array, was recorded to provide one three-component station. The output of all eight seismic channels was recorded at two levels on photographic paper and magnetic tape. Timing for all three units was based on WWV or WWVB radio signals and is accurate to a tenth of a second or better. Data were also obtained from the EDZOE events on the seven-station Hanford array located in the central part of the Columbia Plateau and operated by the U.S. Geological Survey. The data from this array are telemetered to the National Center for Earthquake Research in Menlo Park, California and recorded on 35 mm film. The location of the Hanford array stations are indicated by open circles in Figure 39. The locations and elevations of all the recording sites used in this study are tabulated in Table 3.

Distances between the shot point and receivers were computed using a program for a spherical earth written by Bruce Julian (1970). These distances together with the total travel-times and the travel-times reduced by $T-\Delta/8.0$ sec for first arrivals and prominent later

arrivals are listed in Table 4. The reduced travel-times of these arrivals are plotted as a function of distance from the shot point in Figure 40. A record section of the seismic waves recorded by the eight-channel mobile unit along this profile is plotted in Figure 41. Each trace in the figure is taken from one of six comprising the 2.5 km array. An effort was made to choose a trace for plotting that was in some sense representative of the character of the arrivals on all six traces. The generally high quality of the data recorded out to more than 700 km is evident in this record section.

3. Interpretation.

Crustal structure - All of the first arrivals recorded along this profile are on the Pn travel-time branch. That is, the first arrivals are waves that have traveled downward through the crust from the shot point to be critically refracted at the M-discontinuity and thence propagated along this boundary as a head wave at the P-wave velocity of the mantle lid. As is evident from Figures 40 and 41, an average line drawn through the first arrivals has a slightly negative slope in these reduced travel-time plots. Thus the average phase velocity of Pn along this profile is slightly greater than the reducing velocity of 8.0 km/sec. However, because this profile is unreversed, it is not possible to unambiguously determine the

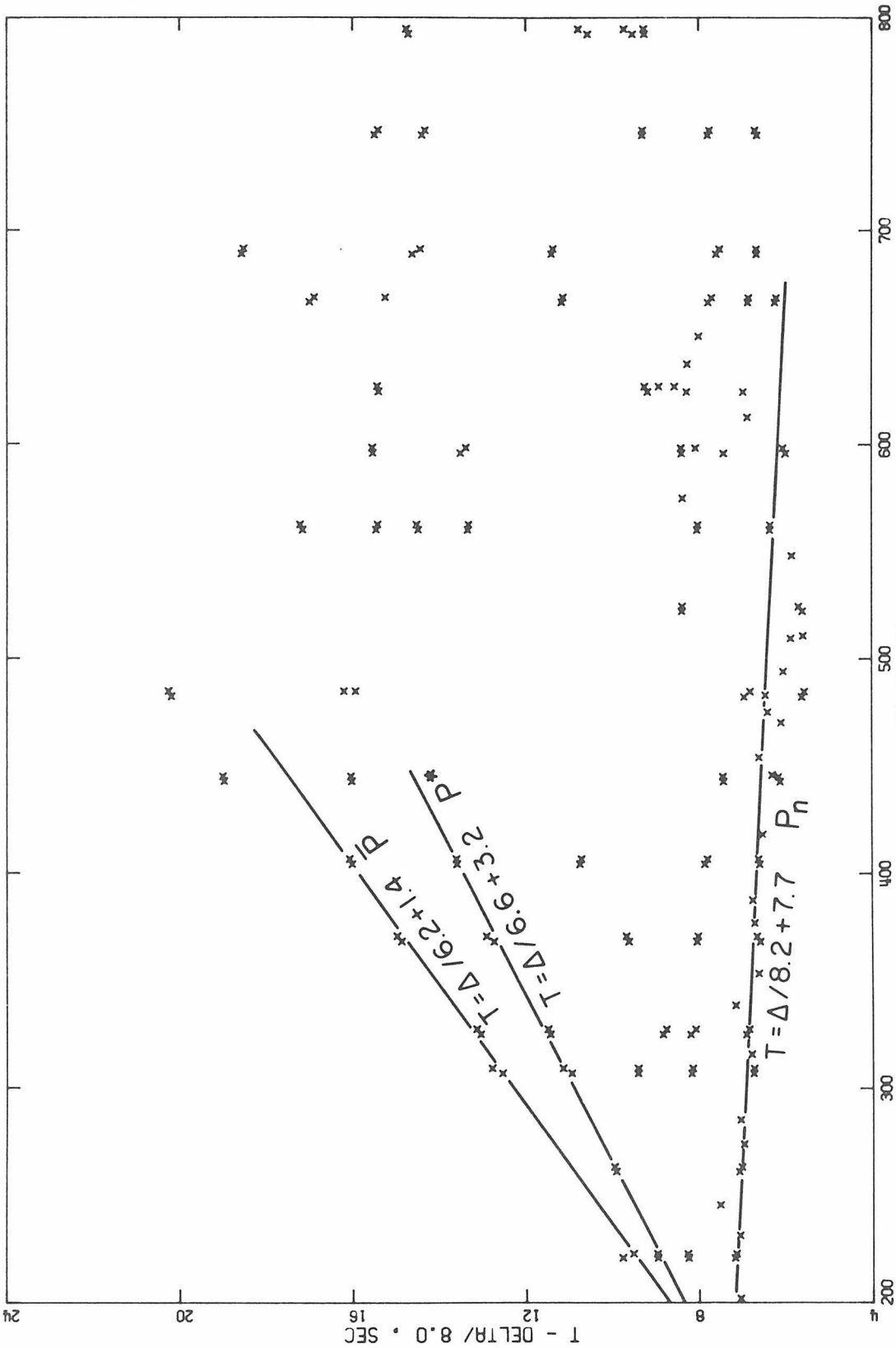

Figure 40

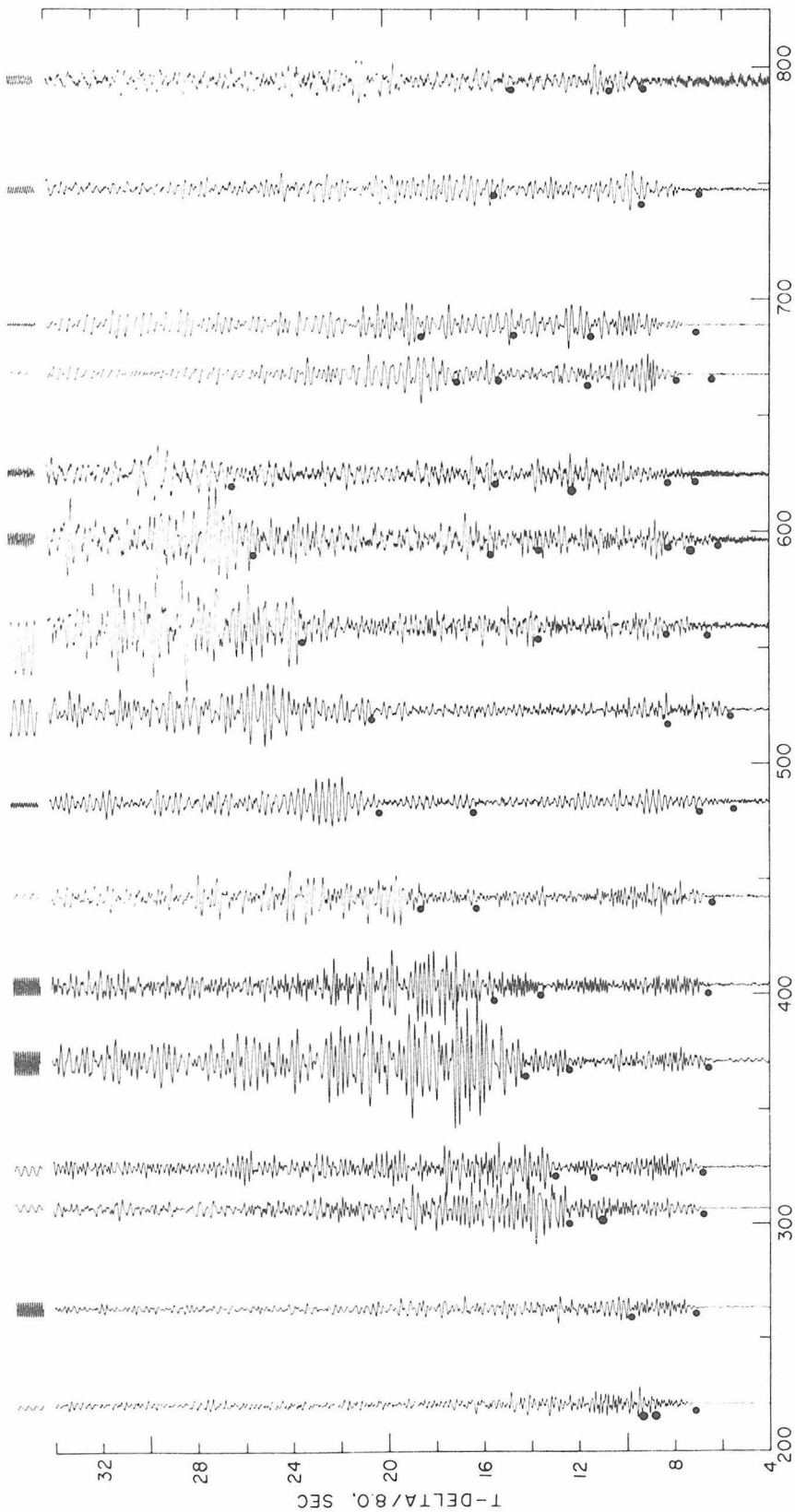
T-DELTA/8.0, SEC
32
28
24
20
16
12
8
4
DELTA, KM
200
300
400
500
600
700
800

Figure 41

true P-wave velocity of the mantle at the M-discontinuity from this phase velocity. Here we will assume a Pn velocity of 7.9 km/sec based on the regional travel-time data from local earthquakes in the Pacific Northwest published by Dehlinger et al. (1965).

Perhaps the most striking aspect of the Pn arrivals in Figures 40 and 41 is the group of early arrivals between 400 and 600 km from the shot point. These arrivals are as much as 0.9 sec early with respect to a line, $T = \Delta/8.2 + 7.7$, drawn through the first arrivals on either side of this distance range (see Figure 20). These early arrivals were recorded in the central part of the Columbia Plateau, just north of the Oregon-Washington border (see Figure 39) in the Pasco Basin, and they indicate strong lateral variations in the crustal and upper mantle structure in this vicinity.

A set of strong secondary arrivals following the Pn arrivals of successively larger times with distance are clearly visible on the record section in Figure 41. In fact, they are the most prominent event on the seismograms. These arrivals represent the $\overline{P}$ phase in crustal seismology, and the sustained character of the phase is most likely due to multiple critical reflections and refractions within the crust between the M-discontinuity and the surface. The onset of the $\overline{P}$ phase has an apparent velocity of about 6.2 km/sec (see Figure 40), which may in some sense approximate the average velocity within the crust.

A set of weaker, but still distinct arrivals can be seen one to two seconds ahead of the $\overline{P}$ phase out to about 400 km in Figure 41. These arrivals have an apparent velocity of about 6.6 km/sec as indicated in Figure 40 and are interpreted here as waves that have been critically refracted by the "intermediate" layer in the crust (the P* phase).

Figure 42 shows a crustal model along this profile through the Columbia Plateau based on an interpretation of the arrival described above. The crustal structure for the granitic-metamorphic terrain north of the Plateau was obtained by interpreting the Pn and P* travel-time branches using standard seismic-refraction methods and assuming: (1) the upper crust has a P-wave velocity of about 6.0 km/sec as found by White et al. (1968) a short distance to the north, (2) the intermediate layer is approximately horizontal and has a P-wave velocity of 6.6 km/sec, and (3) the upper mantle P-wave velocity is 7.9 km/sec (as indicated above). The result is a crust composed of a 6.0 km/sec layer about 22 km thick over 6.6 km/sec layer 8 to 15 km thick with a total thickness of about 35 km. The base of the crust in this model dips at a small angle (about 1.5°) to the north. The average crustal velocity for this model seen by a ray critically reflected from the M-discontinuity is about 6.2 km/sec, which is consistent with the phase velocity of the onset of the $\overline{P}$ event. This structure is in reasonable agreement with that

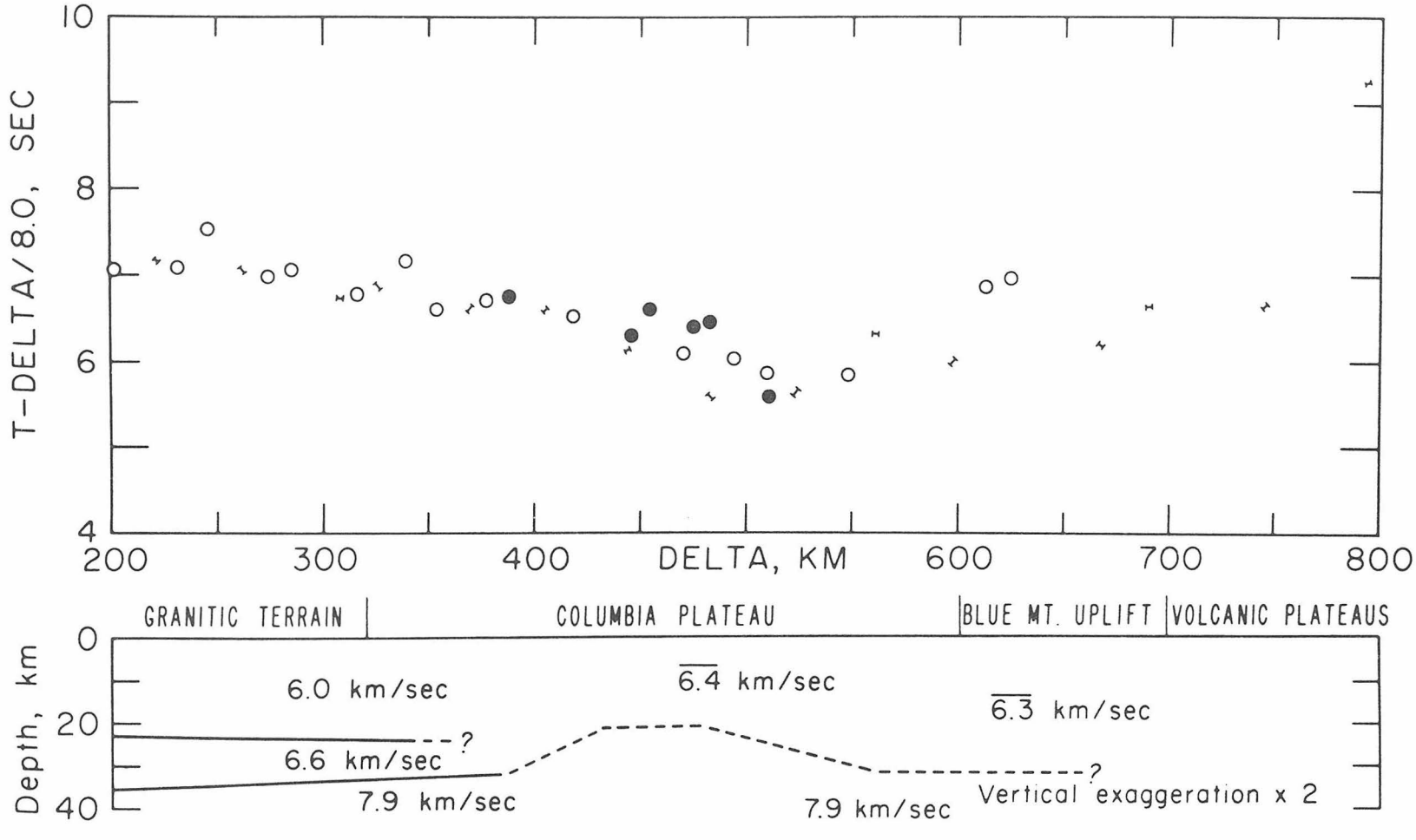
T-DELTA/8.0, SEC
10
8
6
4
200
300
400
DELTA, KM
600
700
800
GRANITIC TERRAIN
COLUMBIA PLATEAU
BLUE MT. UPLIFT
VOLCANIC PLATEAUS
Depth, km
0
20
40
6.0 km/sec
6.6 km/sec
7.9 km/sec
6.4 km/sec
6.3 km/sec
7.9 km/sec
Vertical exaggeration x 2

Figure 42

obtained by White et al. (1968) in British Columbia just to the north, although these authors did not present any evidence for an intermediate layer in the lower crust.

The structure of the M-discontinuity south of the granitic-metamorphic terrain under the Columbia Plateau and the Blue Mountain uplift is based on the observed variations in Pn arrival times plotted above the structure section in Figure 42. Variations in Pn arrival times (Pn delays) provide a direct measure of variations in P-wave travel-times through the crust from the M-discontinuity to the surface under the recording stations. Thus, in the absence of additional information on velocity structure within the crust, Pn delays provide a measure of variations in the ratio of crustal thickness to the average P-wave velocity in the crust along the profile. Using the crust under the granitic-metamorphic terrain as a reference (a 35 km thick crust with an average P-wave velocity of 6.2 km/sec), we can consider two extreme interpretations of the variations in Pn arrival times plotted in Figure 42:

1) Crustal thickness is essentially constant along the profile and the early Pn arrivals over the Columbia Plateau are due entirely to an increase in the average P-wave velocity in the crust from 6.2 km/sec in the granitic-metamorphic terrain to about 7.0 km/sec in the Columbia Plateau, or

2) The average crustal P-wave velocity is essentially constant along the profile and the early Pn arrivals are due entirely to a decrease in crustal thickness from 35 km under the granitic terrain to about 20 km under the Columbia Plateau.

The first interpretation can be dispensed with because of the high average crustal P-wave velocity required to explain the data. P-wave velocities as high as 7.0 km/sec have been reported for the lower portions of the crust in some regions, but it is difficult to believe that the average velocity for the entire crust can be anywhere near this value. On the other hand, the second interpretation can be retained as a possible model; there is nothing at this stage to indicate that the crust under the Columbia Plateau cannot be as thin as 20 km.

The model shown in Figure 42 is a compromise between the above two interpretations. Here, using the velocity structure for the western Snake River Plain reported by Hill and Pakiser (1966) as a guide, we assume an average crustal velocity of 6.4 km/sec for the Columbia Plateau and obtain a crustal thickness of about 23 km. The average crustal velocity south of the Columbia Plateau was arbitrarily chosen to be 6.3 km/sec, which gives a crustal thickness of about 30 km under the Blue Mountain uplift.

Theoretical travel-times for the model in Figure 42 were computed using a ray-tracing program for waves in a laterally heterogeneous,

spherical earth written by Bruce Julian (1970). As shown in Figure 43, the agreement between observed and theoretical Pn travel-times is quite good. Thus, although the details of the structure shown in Figure 42 may change as more data accumulates, it seems clear that the crust under the central part of the Columbia Plateau is substantially thinner, and probably has a somewhat higher P-wave velocity, than the crust in the granitic-metamorphic terrain to the north and the Blue Mountains to the south.

Upper mantle structure - Beyond about 500 km, a number of events occur on the seismograms between Pn and $\overline{P}$ as can be seen in the record section (Figure 41). Note in particular the rather abrupt increase in signal level at $T-\Delta/8.0 = 12$ to 16 seconds between records on either side of $\Delta = 550$ km. These events are very likely associated with waves that have penetrated into the upper mantle beneath the Columbia Plateau. However, the identification of these phases is much less certain than is the case for the crustal arrivals, and the following interpretation of these events in terms of upper mantle structure must be regarded as tentative.

Consider first the set of arrivals that follow Pn by 2 to 3 seconds starting just beyond 500 km. These arrivals have a slightly higher apparent velocity than Pn and may be explained in terms of waves refracted by an abrupt increase in velocity from about 8.0 to 8.4 km/sec at a depth of about 100 km. Evidence for a similar

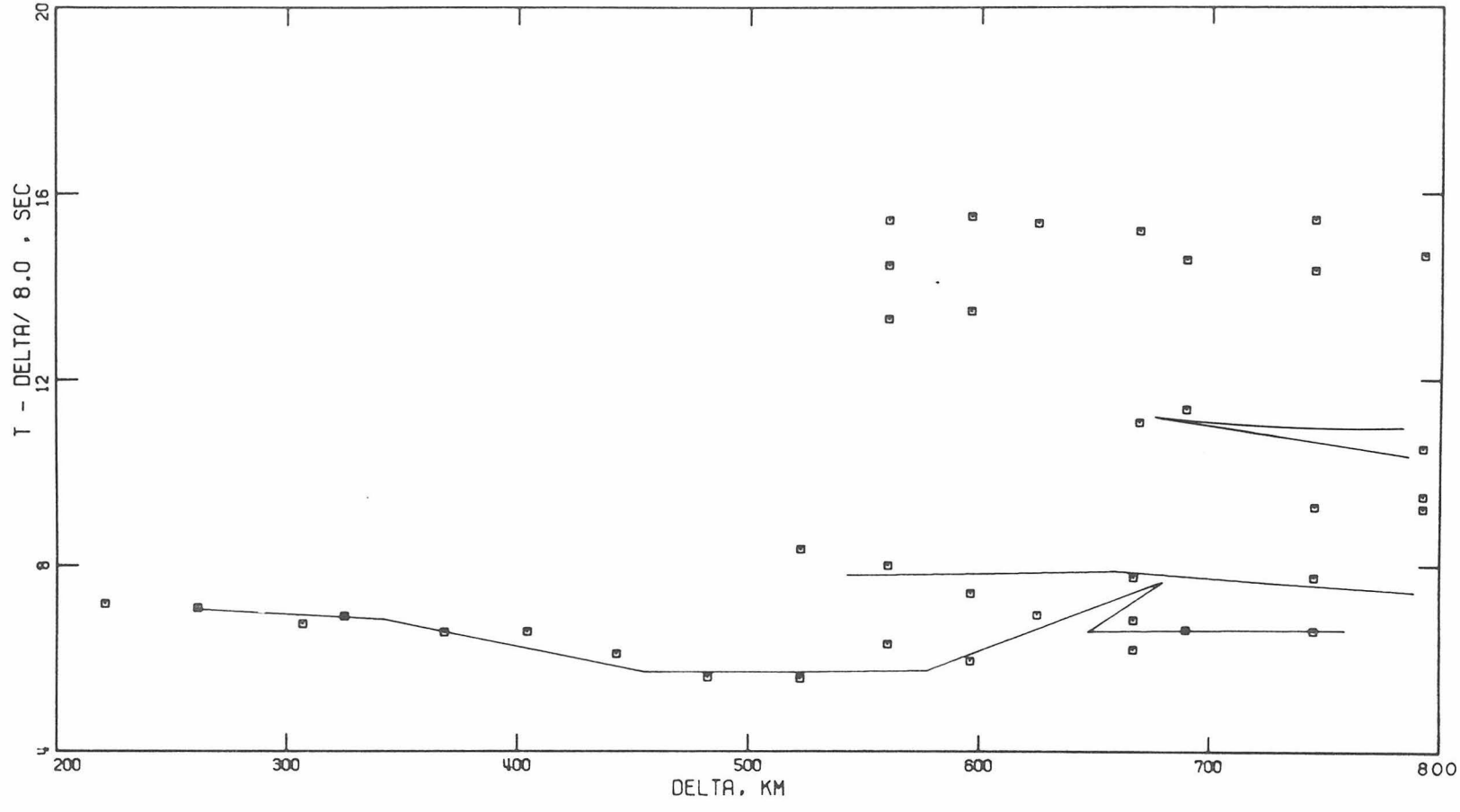
T - DELTA/ 8.0 , SEC
20
16
12
8
4
200
300
400
500
600
700
800
DELTA, KM

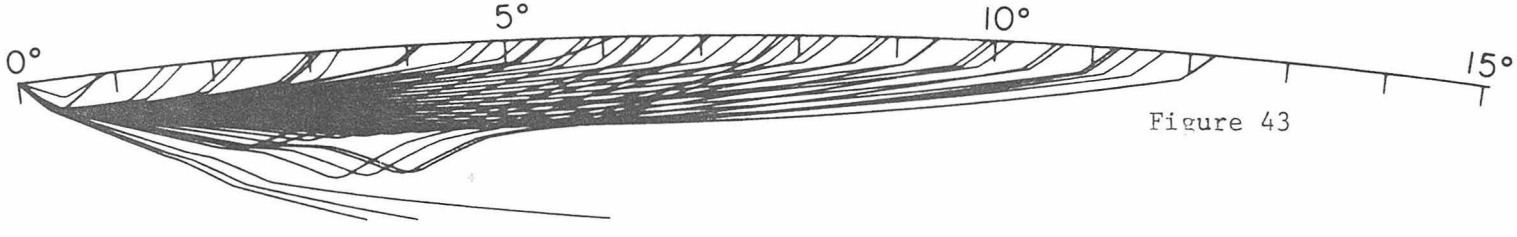
0°
5°
10°
15°

Figure 43

high velocity horizon at depths of 70 to 120 km beneath the eastern United States has been found in data from the EARLY RISE experiment interpreted by Green and Hales (1968), Lewis and Meyer (1968), and Julian (1970). Hales et al. (1970) also find evidence for a high velocity horizon (8.6 km/sec) at a depth of 60 km beneath the Gulf of Mexico, from their interpretation of long-range seismic-refraction data between Florida and Mexico.

A later group of arrivals can be seen to begin about 8 sec behind Pn at 560 km and at successively smaller times behind Pn with increasing distance. These arrivals are characterized by a somewhat lower frequency and general increase in amplitude with respect to the coda of the preceding few seconds, although the amplitude increase is not consistent from record to record. We tentatively identify these arrivals as waves reflected from the bottom of the low velocity zone. If this identification is correct, it would appear that the cusp for this reflection occurs at about 550 km (at smaller distances, the seismograms are relatively quiet in this time interval).

Two models of the upper mantle have been constructed to explain these arrivals. They are plotted in Figure 44 together with the model constructed by Julian (1970) using data recorded along a profile due north from the Nevada Test Site (NTS). The profile from NTS north is parallel to, and about 100 km to the east of the profile we are considering here. The first model (CP1) includes

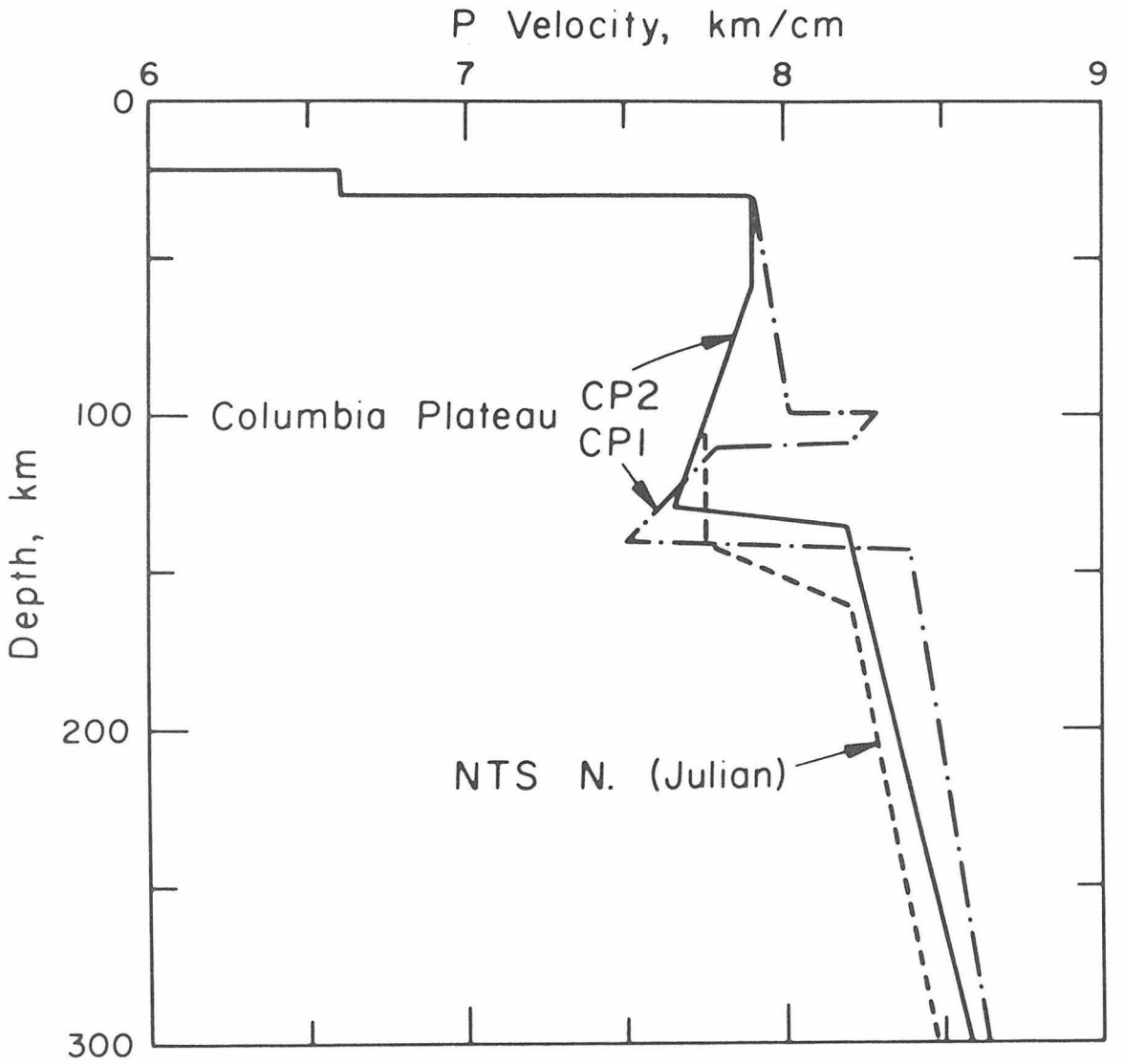
P Velocity, km/cm
6
7
8
9
0
100
200
300
Depth, km
Columbia Plateau
CP2
CP1
NTS N. (Julian)

Figure 44

the 8.4 km/sec horizon at a depth of 100 km. This horizon is only about 10 km thick and serves as a lid to a rather deep (in velocity) low velocity zone. The low velocity zone bottoms very abruptly at a depth of about 145 km. The second model (CP2) does not include the high velocity horizon at 100 km, but grades directly into a wedge shaped low velocity zone beginning at 60 km and ending at about 130 km. The 100 km high velocity horizon is omitted in the second model on the hypothesis that the first set of arrivals described above has an alternate explanation such as lateral refraction or reverberation within a gradient or transition zone.

Theoretical travel-times for both these models were computed using a ray-tracing program for a spherical earth with lateral variations (Julian, 1970). The theoretical travel-times for CP1 are plotted in Figure 43 and those for CP2 in Figure 45. In Figure 43, we see that theoretical travel-times from both the 8.4 km/sec horizon at 100 km and the bottom of the low velocity zone agree reasonably well with the picked arrivals, although the cusp of the reflection from the low velocity zone occurs at about 650 km instead of 550 km as suggested by the observed arrivals. To bring the cusp back toward 550 km, it would be necessary to further decrease the velocity in the low velocity zone and move the bottom of the zone to a shallower depth in CP1. In Figure 45, we see again that the theoretical travel times for the reflection from the bottom of the

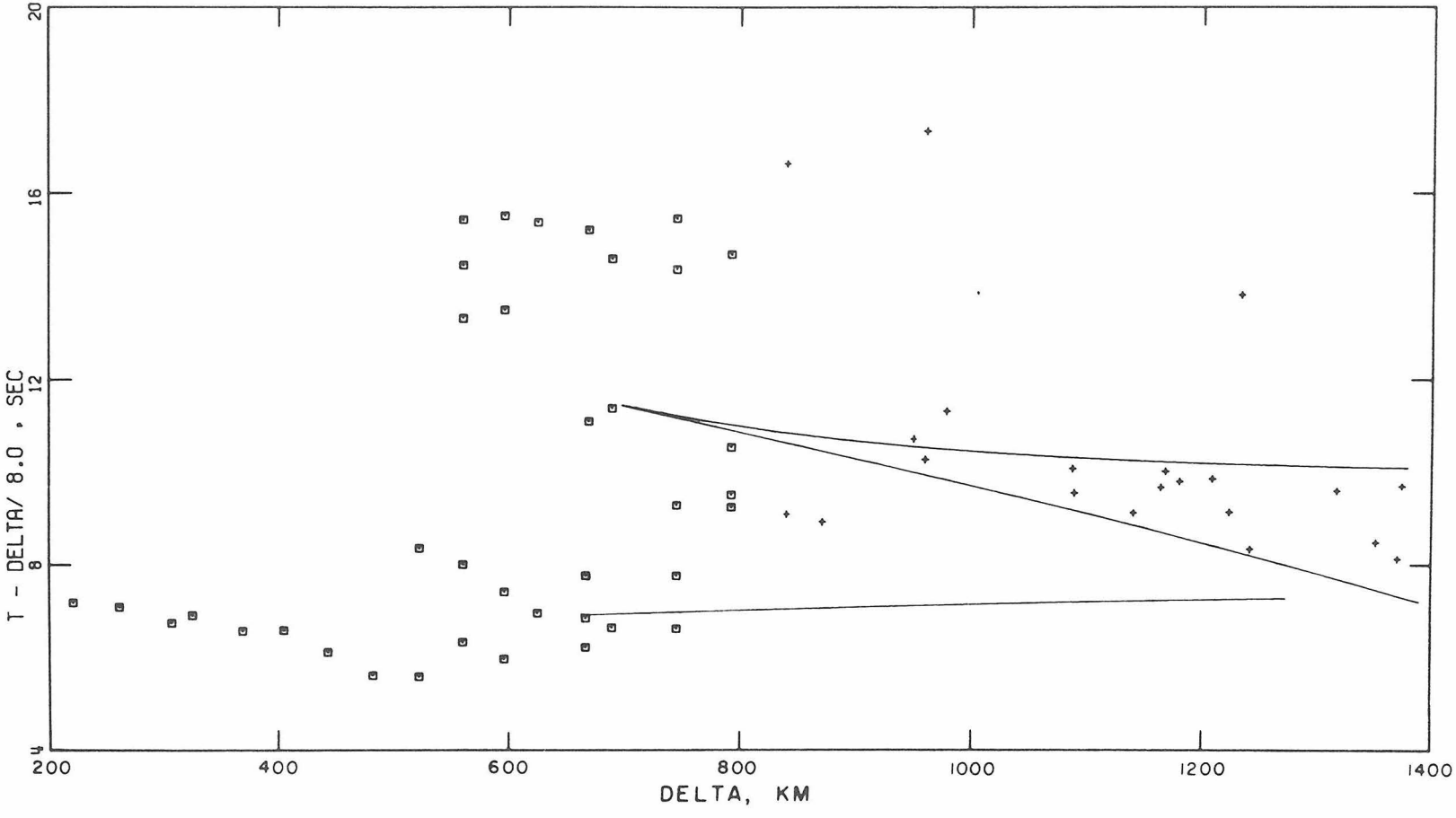
T - DELTA/ 8.0 , SEC
20
16
12
8
4
200
400
600
800
1000
1200
1400
DELTA, KM

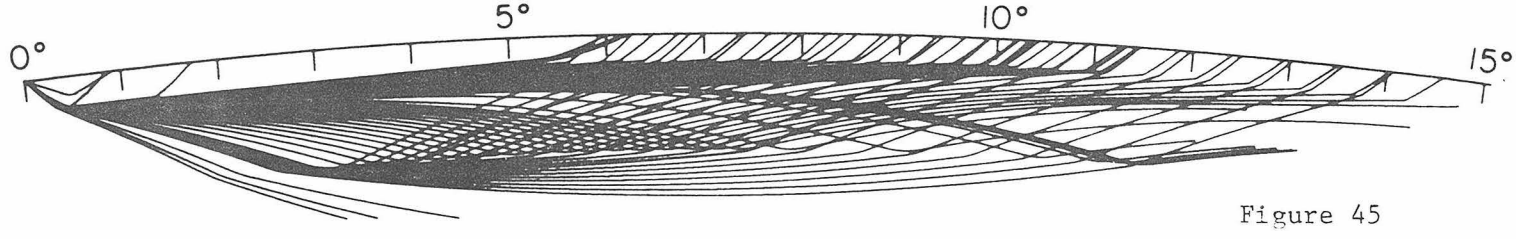
0°
5°
10°
15°

Figure 45

low velocity zone in CP2 agree with the times of the picked arrivals, but that the cusp occurs at too large a distance. As before, to move the theoretical cusp back it would be necessary to decrease the velocity in the low velocity zone and have it bottom to a shallower depth. The points plotted as crosses between 800 and 1400 km in this figure are the first arrivals refracted from the bottom of the low velocity zone recorded on the profile north of NTS as interpreted by Julian (1970). This NTS north data samples an equivalent section of the mantle 100 km due east of the Columbia Plateau profile. The fact that the NTS data are essentially continuous with the events identified as reflections from the bottom of the low velocity zone in the Columbia Plateau provides some assurance that these events were identified correctly - assuming, of course, that the upper mantle structure does not change significantly over the 100 km between the profiles.

The models shown in Figure 44 may serve as a first approximation to the actual structure in the upper mantle under the Columbia Plateau. However, it should be realized that the inversion of body wave travel time data is at best non-unique, and thus considering the limited data set available in this analysis, these models must be regarded as tentative approximations.

4. Summary and Conclusions

Early Pn arrivals recorded across the Columbia Plateau from the EDZOE explosions indicate that the crust under the Plateau is both thinner and has a higher average P-wave velocity than the 35 km thick - 6.2 km/sec crust under the granitic-metamorphic terrain of northeastern Washington. If the average P-wave velocity in the crust under the Columbia Plateau is similar to that of the western Snake River Plain (both are flood basalt provinces), then the crust thins to about 23 km under the central part of the Plateau and has an average P-wave velocity of 6.4 km/sec. The P-wave velocity of the mantle at the M-discontinuity in this region is assumed to be about 7.9 km/sec on the basis of travel time curves for the Pacific Northwest from local earthquakes (Dehlinger et al., 1969).

Secondary arrivals following Pn by 2 to 8 seconds at distances beyond 500 km suggest that a thin (10 km thick) horizon with a P-wave velocity of 8.4 km/sec may exist at a depth of about 100 km and that this horizon is underlain by a rather sharp low velocity zone extending to a depth of about 140 km. If the thin high-velocity horizon at 100 km is not present (and the associated arrivals have another explanation) the low velocity zone may extend over a depth interval from 60 to 130 km. Either interpretation of upper mantle structure is based on a limited data set and must be regarded as tentative.

Hales (1969) has summarized some of the evidence for a high-velocity horizon at a depth of 80 to 90 km beneath the eastern United States. He postulates that this horizon may represent a phase transition from spinel to garnet peridotite. The inferred 8.4 km/sec horizon at 100 km beneath the Columbia Plateau may represent such a phase transition. An alternate explanation of the arrivals following Pn by 2 to 3 seconds at distances beyond 500 km is that they represent lateral refractions from the postulated down-going lithosphere beneath the 'island-arc' structure of the Cascade Range (Atwater, 1970). Julian (1970) has found some evidence to support the existence of such a structure in the distribution of teleseismic P residuals from the Puget Sound earthquake of April 29, 1965. Confirmation of either of these possibilities must await more complete studies.

Hamilton and Myers (1966) have suggested that the flood basalt provinces of the Columbia Plateau and the Snake River Plain are the result of major crustal rifting in the Cenozoic. Hill and Pakiser (1966) came to a similar conclusion for the Snake River Plain; they found no evidence of the typical 6.0 km/sec continental crust, but rather a 10 km thick layer of 5.4 km/sec 'eruptive volcanics' underlain by a 35 km thick layer of 6.6 km/sec 'intruded mafic rocks'. It remains to be seen whether or not the velocity structure within the Columbia Plateau is analogous to that of the Snake River Plain,

but the present data are at least consistent with the rifting hypotheses.

However, there is one striking difference between the Columbia Plateau and the Snake River Plain - that of crustal thickness. The crust under the Columbia Plateau is thin (25 km or less) while that under the Snake River Plain is thick (40 km or more). This difference is directly reflected in Pn delays over each region (Hill and Pakiser, 1966). If the two regions are in fact genetically the same, perhaps this difference is related to the evolutionary development of a continental flood basalt province, with the Snake River Plain representing the younger, currently active stage.

The earliest Pn arrivals in the Columbia Plateau are associated with the Pasco Basin, a region just north of the Oregon-Washington border and approximately in the center of the Columbia River lava field. Hence, this is also the region of the thinest crust and/or highest crustal P-wave velocity. Danes (1969, and personal communication, 1970) has established a network of stations in eastern Washington and found a 50 to 60 milligal gravity high approximately centered over the Pasco Basin. On the basis of these observations, it seems likely that the Pasco Basin area may have been a primary source region, at least in the early stages in the development of the Columbia Plateau. The only major source areas for the Columbia River basalts recognized from field observations

of exposed flows and dike systems are limited to the southern and southwestern edges of the Columbia Plateau (Waters, 1961, and Swanson, 1967). However, it is not unreasonable to expect that early sources associated with initial rifting of the crust may now be deeply buried beneath later flows from peripheral sources.

REFERENCES

Abramowitz, M. and I.A. Stegun, Handbook of Mathematical Functions, U.S. Nat'l. Bur. Stan., 1964.

Anderson, D.L. and M.N. Toksoz, Surface waves on a spherical earth, J. Geophys. Res., 68, 3483-3500, 1963.

Anderson, D. L., and C. Sammis, Partial melting in the upper mantle, Phys. Earth Planet. Interiors, 3, 41-50, 1970.

Anderson, O. L., E. Schreiber, and R. C. Liebermann, Some elastic constant data on minerals relevant to geophysics, Rev. Geophys., 6, 491-524, 1968.

Archambeau, C. B., E. A. Flinn, and D. G. Lambert, Fine structure of the upper mantle, J. Geophys. Res., 74, 5825-5865, 1969.

Archambeau, C. B., R. F. Roy, D. D. Blackwell, D. L. Anderson, L. Johnson, and B. Julian, A geophysical study of continental structure (abstract), Trans. Amer. Geophys. Union, 49, 328, 1968.

Atwater, T., Implications of plate tectonics for the Cenozoic tectonic evolution of western North America, Geol. Soc. America Bull., 81, 3513-3536, 1970.

Berry, L. A., Computation of Hankel functions, U.S. Nat'l., Bur. Stan. Tech. Note 216, 1964.

Berry, M. J. and G. F. West, Reflected and head wave amplitudes in a medium of several layers, in The Earth Beneath the Continents, edited by J. S. Steinhart and T. J. Smith, American Geophysical Union Geophysical Monograph 10, Washington, D. C., 464-481, 1966.

Bhattacharya, S. N., Exact solutions of SH wave equations for inhomogeneous media, Bull. Seism. Soc. Am., 60, 1847-1860, 1971.

Birch, F., Interpretation of the seismic structure of the crust in the light of experimental studies of wave velocities in rocks, in Contributions in Geophysics in Honor of Beno Gutenberg, pp. 158-170, Pergamon Press, London, 1958.

Biswas, N. N., and L. Knopoff, Exact earth-flattening calculations for Love waves, Bull. Seism. Soc. Am., 60, 1123-1137, 1970.

Brekhovskikh, L. M., Waves in Layered Media, 561 pp. Academic Press, New York, 1960.

Brekhovskikh, L. M., The reflection of spherical waves at a plane interface between two media, J. Tech. Physics [U.S.S.R], 18, 455-482, 1948 (in Russian).

Bremmer, H., Terrestrial Radio Waves, Elsevier Pub. Co., New York, 343 pp., 1949.

Brune, J. N., Tectonic stress and the spectra of seismic shear waves, J. Geophys. Res., 75, 4997-5009, 1970.

Budden, K. G., The Wave-Guide Mode Theory of Wave Propagation, Prentice-Hall, Englewood, N.J., 1960.

Budden, K.G., The Wave-Guide Mode Theory of Wave Propogation, Prentice-Hall, Englewood, N.J., 325 p., 1961.

Bullen, K.E., An Introduction to the Theory of Seismology, Cambridge University Press, London, 381 p., 1963.

Burke, M. D., E. R. Kanasewich, J. P. Malinsky, J. F. Montalbetti, A wide-band digital seismograph system, Bull. Seism. Soc. Am., 60, 1417-1426, 1970.

Cagniard, L., Reflection et refraction des ondes progressives seismiques, Gauthier-Villars, Paris, 1939.

Cerveny, V., The dynamic properties of reflected and head waves around the critical point, Prace. Geofys. Ustavu. Cesk. Akad. Ved., Geofysikalni Sbornik, pp. 135-245, 1965.

Cerveny, V., On dynamic properties of reflected and head waves in the n-layered earth's crust, Geophys.J. Roy. Astr. Soc., 11, pp. 139-147, 1966.

Cerveny, V., and J. Jansky, On some dynamic properties of the diving wave, Proc. of the 7th Assembly of the European Seismological Comm., pp. 397-402, Copenhagen, 1967.

Chapman, C. H., Seismic wave diffraction theory, Ph.D. Thesis, Christ's College, Cambridge, 212 p., 1969.

Chekin, B. S., The effect on a head wave of small inhomogeneities in a refracting medium, Izv. Earth Physics Ser., No. 3,, pp. 1-10, 1965.

Chekin, B. S., On the reflection of elastic, spherical waves from an inhomogeneous half space, Izv. Geophys. Ser., No. 5, pp. 711-717, 1964.

Chiburis, E. F., Crustal structures in the Pacific northwest states from phase-velocity dispersion of seismic surface waves, Ph.D. Thesis, Oregon State University, 170 p., 1966.

Clowes, R. M., and E. R. Kanasewich, Seismic attenuation and nature of reflecting horizons within the crust, J. Geophys. Res., 75, 6693-6705, 1970.

Daneš, Z. F., Gravity results in western Washington, EOS, Trans. Am. Geophys. Union, 50, 548-550, 1969.

Dehlinger, P., E. F. Chiburis, and M. M. Collver, Local travel-time curves and their geologic implications for the Pacific northwest states; Bull. Seism. Soc. Am., 55, 587-607, 1965.

Dehlinger, P., R. W. Couch, and M. Gemperle, Continental and oceanic structure from the Oregon Coast westward across the Juan de Fuca Ridge, Canadian J. Earth Sci., 5, 1079-1090, 1968.

Dix, C. H., Seismic Prospecting for Oil, Harper and Brothers, New York, 414 p., 1952.

Eaton, J. P., Crustal structure from San Francisco, California, to Eureka, Nevada, from seismic-refraction measurements, J. Geophys. Res., 68, 5789-5806, 1963.

Epstein, P. S., Reflection of waves in an inhomogeneous absorbing medium, Proc. Nat. Acad. Sci. Wash., 16, p. 627, 1930.

Erdelyi, A., W. Magnus, F. Oberhettinger, and F. G. Tricomi, Higher Transcendental Functions, Volume II, Bateman Manuscript Project, McGraw-Hill, New York, 396, 1953.

Ewing, W. M., W. S. Jardetzky, and F. Press, Elastic Waves in Layered Media, McGraw-Hill, N.Y. 380 p., 1957.

Fuchs, K., The reflection of spherical waves from transition zones with arbitrary depth-dependent elastic moduli and density, J. Phys. Earth, 16, Special Issue, pp. 27-41, 1968.

Gilbert, F., and D. V. Helmberger, Generalized ray theory for a layered sphere, Geophysical J., in press, 1971.

Grant, F. S., and G. F. West, Interpretation Theory in Applied Geophysics, McGraw-Hill, New York, 584 p., 1965.

Green, R. W.E., and A. L. Hales, The travel times of P waves to 30° in the central United States and upper mantle structure, Bull. Seism. Soc. Am., 58, 267-289, 1958.

Hales, A. L., A seismic discontinuity in the lithosphere, Earth and Planet. Sci. Letters, I, 44-46, 1969.

Hales, A. L., C. E. Helsley, and J. B. Nation, P travel times for an oceanic path, J. Geophys. Res., 75, 7362-7381, 1970.

Hamilton,W., and W. B. Myers, Cenozoic tectonics of the western United States, Rev. Gophys., 4, 509-549, 1966.

Healy, J. H., Crustal structure along the coast of California from seismic refraction measurements, J. Geophys. Res., 68, 5777-5787, 1963.

Healy, J. H., and D. H. Warren, Explosion seismic studies in North America, in The Earth's Crust and Upper Mantle, Geophys. Monograph 13, ed. by P. J. Hart, pp. 208-220, American Geophysical Union, Washington, D. C., 1969.

Heelan, P. A., On the theory of head waves, Geophysics, 18, 871-893, 1953.

Helmberger, D. V., the crust-mantle transition in the Bering Sea, Bull. Seism. Soc. Am., 58, 178-214, 1968.

Helmberger, D. V., and G. B. Morris, A travel time and amplitude interpretation of a marine refraction profile: primary waves, J. Geophys. Res., 74, 483-494, 1969.

Hill, D. P., and L. C. Pakiser, Crustal structure between the Nevada Test Site and Boise, Idaho from seismic-refraction measurements in Earth Beneath the Continents, Geophys. Monogra. 10, edited by Steinhart and Smith, pp. 391-419, American Geophysical Union, Washington, D. C. 1966.

Hirasawa, T., and M. J. Berry, Reflected and head waves from a linear transition layer in a fluid medium, Bull. Seis. Soc. Am., 61, pp. 1-26, 1971.

Hoop, A. T. de, A modification of Cagniard's method for solving seismic pulse problems, Appl.Sci.Res.B, 8, pp.349-356, 1960.

Hron, F., and E. R. Kanasewich, Synthetic seismograms for deep seismic sounding studies using asymptotic ray theory, Bull. Seis. Soc. Am. (in press), 1971.

Hughes, D. S., and C. Maurette, Variation of elastic wave velocities in granites with pressure and temperature, Geophysics, 21, 277-284, 1956.

Hughes, D. S., and C. Maurette, Variation of elastic wave velocites in basic igneous rocks with pressure and temperature, Geophysics, 22, 23-31, 1957.

Iyer, H. M., L. G. Pakiser, D. J. Stuart, and D. H. Warren, Project Early Rise: Seismic probing of the upper mantle, J. Geophys. Res., 74, 4409-4441, 1969.

Jackson, D. D., and D. L. Anderson, Physical mechanisms of seismic-wave attenuation, Rev. Geophys. Space Phys., 8, 1-64, 1970.

James, D. E., and J. S. Steinhart, Structure beneath the continents: A critical review of explosions studies 1960-1965, in The Earth Beneath the Continents, Geophys. Monograph 10, edited by J. S. Steinhart and T. J. Smith, pp. 293-333, American Geophysical Union, Washington, D. C., 1966.

Jeffreys, H., On compressional waves in two superposed layers, Proc. Camb. Phil. Soc., 33, 472-481, 1926.

Johnson, L. R., Array measurements of P velocities in the upper mantle, J. Geophys. Res., 6309-6325, 1967.

Johnson, S. H., and R. W. Couch, Crustal structure in the north Cascade mountains of Washington and British Columbia from seismic refraction measurements, Bull. Seism. Soc. Am., 60, 1259-1269, 1970.

Julian, B. R., Regional variations in upper mantle structure beneath North America, Ph.D. Thesis, California Institute of Technology, Pasadena, 208 p., 1970.

Kanamori, H., Spectrum of short-period core phases in relation to the attenuation in the mantle, J. Geophys. Res., 72, 2181-2186, 1967.

Karal, F. C. Jr., and J. B. Keller, Elastic wave propagation in homogeneous and inhomogeneous media, J. Acoust. Soc. Am., 31, 694-705, 1959.

Kline, M., An asymptotic solution of Maxwell's equations, Comm. Pure Appl. Math., 4, 225-263, 1951.

Knopoff, L., and J. F. Gilbert, Diffraction of elastic waves by the core of the earth, Bull. Seism. Soc. Am., 31, 694-705, 1959.

Kovach, R. L., and D. L. Anderson, Long-period Love waves in a heterogeneous spherical earth, J. Geophys. Res., 67, 5243-5255, 1962.

Lachenbruch, A. H., Crustal temperature and heat production: implications of the linear heat-flow relation, J. Geophys. Res., 75, 3291-3300, 1970.

Langer, R. E., The asymptotic solutions of ordinary linear differential equations of the second order, with special reference to a turning point, Trans. Amer. Math. Soc., 67, 1949.

Lewis, B.T.R., and R. P. Meyer, A seismic investigation of the upper mantle to the west of Lake Superior, Bull. Seism. Soc. Am., 58, 565-596, 1968.

Nakamura, Y., Head waves from a linear transition layer in a liquid, J. Geophys. Res., 69, 4349-4354, 1964.

Minster, Jean B., and Charles B. Archambeau, Systematic inversion of continental heat flow and temperature data, Abstract, Amer. Geophys. U. Meeting, December 7-10, San Francisco, 1970.

Muller, S., and M. Landisman, Seismic studies of the earth's crust in continents, 1: Evidence for a low-velocity zone in the upper part of the lithosphere, Geophys. J. Roy. Astr. Soc., 10, 525-538, 1966.

Nur, A., and G. Simmons, The effect of saturation on velocity in low porosity rocks, Earth Planet. Sci. Lett., 7, 183-193, 1969.

Nussenzveig, H. M., High frequency scattering by an impenetrable sphere, Ann. Phys., 34, 23-95, 1965.

O'Brien, P.N.S., Lake Superior crustal structure - a reinterpretation of the 1963 seismic experiment, J. Geophys. Res., 73, 2669-2689, 1968.

Onda, I., Reflection of waves from a point source with special remarks on total reflection of spherical waves, Bull. Earthquake Res. Institute, 46, 1183-1205, 1968.

Pakiser, L. C. and J. S. Steinhart, Explosion studies in the western hemisphere, in Research in Geophysics, vol. 2, Solid Earth Interface Phenomena, edited by H. Odishaw, pp. 123-147, Chapter 5, MIT Press, Cambridge, 1964.

Pekeris, C. L., Accuracy of the earth-flattening approximation in the theory of microwave propagation, Physical Review, 70, 518-522, 1946.

Phinney, R. A., Reflection of acoustic waves from a continuously varying interfacial region, Rev. Geophys. Space Phys., 8, 517-532, 1970.

Phinney, R. A., and S. S. Alexander, P wave diffraction theory and the structure of the core-mantle boundary, J. Geophys. Res., 71, 5959-5975, 1966.

Phinney, R. A., L. M. Cathles, Diffraction of P by the core: a study of long period amplitudes near the edge of the shadow, J. Geophys. Res., 74, 1556-1574, 1969.

Press, F., Seismic wave attenuation in the crust, J. Geophys. Res., 69, 4417-4418, 1964.

Press, F., and S. Biehler, Inferences on crustal velocities and densities from P wave delays and gravity anomalies, J. Geophys. Res., 69, 2949-2995, 1964.

Prodehl, C., Seismic refraction study of crustal structure in the western United States, Geol. Soc. Am. Bull., 81, 2629-2646, 1970.

Richards, P. G., A contribution to the theory of high frequency elastic waves, with applications to the shadow boundary of the Earth's core, Ph.D. Thesis, California Institute of Technology, 278p., 1970.

Richards, P. G., Potentials for elastic displacement in spherically symmetric media, J. Acoust. Soc. Am., in press, 1971.

Roller, J. C., Crustal structure in the eastern Colorado Plateau Province from seismic refraction measurements, Bull. Seism. Soc. Am., 55, 107-119, 1965.

Roller, J. C., and J. H. Healy, Seismic-refraction measurements of crustal structure between Santa Monica Bay and Lake Mead, J. Geophys. Res., 68, 5837, 1963.

Roller, J. C., and W. H. Jackson, Seismic wave propagation in the upper mantle: Lake Superior Wisconsin to central Arizona, J. Geophys. Res., 71, 5933-5941, 1966.

Romny, C., Amplitudes of seismic body waves from underground nuclear explosions, J. Geophys. Res., 64, 1489-1498, 1959.

Romny, G., B. G. Brooks, R. H. Mansfield, D. S. Carter, J. N. Jordan, and D. W. Gordon, Travel times and amplitudes of principal body phases recorded from GNOME, Bull. Seism. Soc. Am., 52, 1057-1074, 1962.

Roy, R. F., D. D. Blackwell, and E. R. Decker, Continental Heat Flow, Symposium Dedicated to Francis Birch, ed. E. G. Robertson, McGraw-Hill, New York (in press), 1970.

Roy, R. F., D. D. Blackwell, and F. Birch, Heat generation of plutonic rocks and continental heat flow provinces, Earth Planet. Sci. Lett., 5, 1-12, 1968.

Ryall, A., and D. J. Stuart, Travel times and amplitudes from nulcear explosions, Nevada Test Site to Ordway, Colorado, J. Geophys. Res., 68, 5821-5835, 1963.

Sammis, C., Seismological application of lattice theory, Ph.D. Thesis, California Institute of Technology, Pasadena, California, 1971.

Sato, R., Body wave amplitudes near shadow boundary-SH waves, J. Phys. Earth, 16, 55-59, 1968a.

Sato, R., Effect of spherical crustal layering (SH waves), J. Phys. Earth, 16, 1-6, 1968b.

Sclater, J. G., and J. Francheteau, The implications of terrestrial heat flow observations on current tectonic and geochemical models of the crust and upper mantle of the earth, Geophys. J. R. Astr. Soc., 20, 509-542, 1970.

Sclater, J. G., and C. E. Corry, Heat flow, Hawaiian area, J. Geophys. Res., 72, 3711-3715, 1967.

Scholte, J. G. J., On seismic waves in a spherical earth, Komnkl. Ned. Meterol. Inst. Publ. 65, 1956.

Staff of the Computation Laboratory, Tables of the modified Hankel functions of order one-third and their derivatives, Harvard University Press, Cambridge, 235 p, 1945.

Stewart, S. W., Crustal structure in Missouri by seismic-refraction methods, Bull. Seism. Soc. Am., 58, 291-323, 1968.

Stewart, S. W., Preliminary comparison of seismic travel times and inferred crustal structure adjacent to the San Andreas fault in the Diablo and Gabilan ranges of central California, in Proc. of Conference on Geologic Problems of San Andreas Fault System, edited by W. R. Dickinson and A. Grantz, Stanford University Publications, Geological Sciences, 11, 218-230, Stanford, California, 1968.

Stoker, J. J., Water waves, Interscience, New York, 567p., 1957.

Stuart, D. J., Gravitv study and crustal structure in western Washington, U. S. Geol. Surv. Profess. Paper 424-C, C273-C276, 1961.

Sutton, G. H., W. Mitronovas, and P. W. Pomeroy, Short-period seismic energy radiation patterns from underground nuclear explosions and small-magnitude earthquakes, Bull. Seism. Soc. Am., 57, 249-267, 1967.

Swanson, D. A., Yakima basalt of the Tieton River area, south-central Washington; Geol. Soc. Am. Bull., 78, 1077-1110, 1967.

Teng, T., and P. G. Richards, Diffracted P, SV and SH waves and their shadow boundary shifts, J. Geophys. Res., 74, 1537-1555, 1969.

Thatcher, W., and T. C. Hanks, Source dimensions, seismic moment and stress drop from shear wave spectra of local earthquakes in the southern California region (abstract), EOS, Trans. Am. Geophys. U., 52, 275, 1971.

Warren, D. H., J. H. Healy, and W. H. Jackson, Crustal seismic measurements in southern Mississippi, J. Geophys. Res., 71, 3437-3458, 1966.

Waters, A. C., Stratigraphic and lithologic variations in the Columbia River basalt, Am. J. Sci., 259, 583-611, 1961.

Waters, A. C., Basalt magma types and their tectonic associations - Pacific northwest of the United States, American Geophys. Union Geophys. Mon. 6, 158-170, 1962.

White, W. R. H., M. N. Bone, and W. G. Milne, Seismic refraction surveys in British Columbia, 1941-1966; A preliminary interpretation in the crust and upper mantle of the Pacific area, L. Knopoff, C. L. Drake and P. J. Hart, Editors, Am. Geophys. Union, Geophys. Mon. 12, 81-93, 1968.

White, W. R. H., and J. C. Savage, A seismic refraction and gravity study of the earth's crust in British Columbia, Bull. Seism. Soc. Am., 55, 436-486, 1965.

Appendix I

Some Properties of Airy Functions

Solutions to Stokes' differential equation

$$\frac{d^2U}{d\zeta^2} + \zeta U = 0 \qquad \text{(A1-1)}$$

can be expressed either in terms of one-third order Bessel functions or as Airy functions. One-third order Hankel functions, which are the most commonly used Bessel function representations for solutions to (A1-1), possess a branch point at $\zeta = 0$. This branch point is artificial in the sense that it is nullified by a function of ζ multiplying the Hankel function required to give the proper solution. Nevertheless, great care must be taken in the analytic continuation of the Hankel function from any $(\zeta\ e^{i\eta\pi})$ to any (ζ) across the branch point. These unnecessary complications associated with the branch cut in the Hankel functions can be avoided by using the Airy function representation for solutions to (A1-1). Airy functions are entire and single-valued in the finite complex ζ plane, which is an obvious advantage in analysis.

In wave propagation problems it is convenient to work with the following two pairs of independent solutions to Stokes' equation (A1-1):

$$U(\zeta) = Ai(-\zeta),\quad Bi(-\zeta) \qquad \text{(A1-2)}$$

and

$$U(\zeta) = Ai\left(-\zeta e^{\pm i\frac{2\pi}{3}}\right) \qquad \text{(A1-3)}$$

For sufficiently large argument ($|\zeta| > 3$ for most purposes) the first pair (A1-2) represent standing waves (for $\zeta > 0$) or exponentially growing and decaying waves (for $\zeta < 0$), and the second pair (A1-3) represent downgoing and upgoing traveling waves.

The following properties of Airy functions are summarized here for convenient reference; most can be found in standard references; (i.e. Abramowitz and Stegun, 1964). However, some of the properties of $Ai\left(-\zeta e^{\pm i2\pi/3}\right)$ given below are not commonly tabulated. For a detailed discussion of the analytic properties of Airy functions see Chapter 15 in Budden (1961).

The relation between the pairs of solutions (A1-2 and A1-3) is given by 10.4.9 in Abramowitz and Stegun (1964) as

$$Ai\left(-\zeta e^{\pm i\frac{2\pi}{3}}\right) = \frac{1}{2} e^{\pm i\frac{\pi}{3}}\left[Ai(-\zeta) \mp i\, Bi(-\zeta)\right] \qquad \text{(A1-4)}$$

It follows immediately that

$$Ai'\left(-\zeta e^{\pm i\frac{2\pi}{3}}\right) = \frac{1}{2} e^{\mp i\frac{\pi}{3}}\left[Ai'(-\zeta) \mp i\, Bi'(-\zeta)\right] \qquad \text{(A1-5)}$$

where the prime indicates differentiation with respect to the argument.

Asymptotic forms for the pair (A1-2) and their derivatives for large argument are

$$\begin{aligned} \mathrm{Ai}(-\zeta) &\sim \pi^{-\frac{1}{2}}\, \zeta^{-\frac{1}{4}} \sin(\omega + \pi/4) \\ \mathrm{Ai}(\zeta) &\sim \frac{1}{2}\, \pi^{-\frac{1}{2}}\, \zeta^{-\frac{1}{4}}\, e^{-\omega} \\ \mathrm{Ai}'(-\zeta) &\sim -\, \pi^{-\frac{1}{2}}\, \zeta^{\frac{1}{4}} \cos(\omega + \pi/4) \\ \mathrm{Ai}'(\zeta) &\sim -\, \frac{1}{2}\, \pi^{-\frac{1}{2}}\, \zeta^{\frac{1}{4}}\, e^{-\omega} \end{aligned} \qquad \text{(A1-6)}$$

and

$$\begin{aligned} \mathrm{Bi}(-\zeta) &\sim \pi^{-\frac{1}{2}}\, \zeta^{-\frac{1}{2}} \cos(\omega + \pi/4) \\ \mathrm{Bi}(\zeta) &\sim \pi^{-\frac{1}{2}}\, \zeta^{-\frac{1}{4}}\, e^{\omega} \\ \mathrm{Bi}'(-\zeta) &\sim \pi^{-\frac{1}{2}}\, \zeta^{\frac{1}{4}} \sin(\omega + \pi/4) \\ \mathrm{Bi}'(\zeta) &\sim \pi^{-\frac{1}{2}}\, \zeta^{\frac{1}{4}}\, e^{\omega} \end{aligned} \qquad \text{(A1-7)}$$

where

$$\omega = \frac{2}{3}\, \zeta^{3/2} \qquad \text{(A1-8)}$$

(Abramowitz and Stegun, 1964, sec 10.4).

From (A1-4), (A1-5), (A1-6), (A1-7), we have

$$\mathrm{Ai}\left(-\zeta e^{\pm\, i\frac{2\pi}{3}}\right) \sim \mp\, \frac{1}{2}\, e^{\pm\, i\, \frac{\pi}{3}} \left[\frac{e^{\pm\, i(\omega + \frac{\pi}{4})}}{\pi^{\frac{1}{2}}\, \zeta^{\frac{1}{4}}} \right] \qquad \text{(A1-9)}$$

$$\mathrm{Ai}'\left(-\zeta e^{\pm i\frac{2\pi}{3}}\right) \sim -\frac{1}{2}\, e^{\mp i\frac{\pi}{3}} \left[\frac{\zeta^{\frac{1}{4}}\, e^{\pm i(\omega+\frac{\pi}{4})}}{\pi^{\frac{1}{2}}}\right] \qquad \text{(A1-10)}$$

Relations between the pair (A1-3) and Hankel functions of one-third order are

$$\mathrm{Ai}\left(-\zeta e^{\pm i\frac{2\pi}{3}}\right) = \pm\frac{1}{2}\sqrt{\frac{\zeta}{3}}\; H^{\binom{1}{2}}_{-1/3}(\omega) \qquad \text{(A1-11)}$$

$$\mathrm{Ai}'\left(-\zeta e^{\pm i\frac{2\pi}{3}}\right) = \frac{\zeta}{2\sqrt{3}}\; e^{\pm i\frac{7\pi}{6}}\; H^{\binom{1}{2}}_{-2/3}(\omega) \qquad \text{(A1-12)}$$

These can be deduced using (A1-1), (A1-2), and relations 10.4.15 through 10.4.21 in Abramowitz and Stegun (1964) reproduced below:

$$\mathrm{Ai}(-\zeta) = \frac{1}{2}\sqrt{\frac{\zeta}{3}}\left[e^{i\pi/6}\, H^{(1)}_{1/3}(\omega) + E^{-i\pi/6}\, H^{(2)}_{1/3}(\omega)\right] \qquad \text{(A1-13)}$$

$$\mathrm{Ai}'(-\zeta) = \frac{1}{2}\,\frac{\zeta}{\sqrt{3}}\left[e^{-i\pi/6}\, H^{(1)}_{2/3}(\omega) + e^{i\pi/6}\, H^{(2)}_{2/3}(\omega)\right]$$

$$\mathrm{Bi}(-\zeta) = \frac{i}{2}\sqrt{\frac{\zeta}{3}}\left[e^{i\pi/6}\, H^{(1)}_{1/3}(\omega) - e^{-i\pi/6}\, H^{(2)}_{1/3}(\omega)\right] \qquad \text{(A1-14)}$$

$$\mathrm{Bi}'(-\zeta) = \frac{i}{2}\,\frac{\zeta}{\sqrt{3}}\left[e^{-i\pi/6}\, H^{(1)}_{2/3}(\omega) - e^{i\pi/6} H^{(2)}_{2/3}(\omega)\right]$$

In working numerical computations, Airy functions can be evaluated for complex argument using the SHARE program #1489 (NBS HF13), which computes Hankel functions of one-third and two-third orders, together with the properties of modified Hankel functions of one-third order and their tabulated values for complex argument (Staff of the Computation Laboratory, 1945).

Modified Hankel functions of one-third order are defined in terms of Hankel functions as (loc. cit: 1945)

$$
\begin{aligned}
h_1(\zeta) &= \left(\frac{2}{3}\,\zeta^{3/2}\right)^{1/3} H^{(1)}_{1/3}\left(\frac{2}{3}\,\zeta^{3/2}\right) \\
h_2(\zeta) &= \left(\frac{2}{3}\,\zeta^{3/2}\right)^{1/3} H^{(2)}_{1/3}\left(\frac{2}{3}\,\zeta^{3/2}\right) \\
h_1'(\zeta) &= \left(\frac{2}{3}\right)^{1/3} \zeta\, H^{(1)}_{-2/3}\left(\frac{2}{3}\,\zeta^{3/2}\right) \\
h_2'(\zeta) &= \left(\frac{2}{3}\right)^{1/3} \zeta\, H^{(2)}_{-2/3}\left(\frac{2}{3}\,\zeta^{3/2}\right)
\end{aligned}
\qquad \text{(A1-15)}
$$

In turn, Airy functions can be defined in terms of modified Hankel functions as (loc. cit., 1945)

$$
\begin{aligned}
\mathrm{Ai}(-\zeta) &= \frac{1}{2k}\, h_1(\zeta) + \frac{1}{2k^*}\; h_2(\zeta) \\
\mathrm{Ai}'(-\zeta) &= -\frac{1}{2k}\, h_1'(\zeta) - \frac{1}{2k^*}\; h_2'(\zeta)
\end{aligned}
\qquad \text{(A1-16)}
$$

and

$$\mathrm{Bi}(-\zeta) = \frac{i}{2k}\, h_1(\zeta) - \frac{i}{2k^*}\, h_2(\zeta)$$

$$\mathrm{Bi}'(-\zeta) = \frac{-i}{2k}\, h_1'(\zeta) + \frac{i}{2k^*}\, h_2'(\zeta) \qquad \text{(A1-17)}$$

where

$$k = (12)^{1/6}\, e^{-i\pi/6}\,, \quad k^* = (12)^{1/6}\, e^{i\pi/6}$$

Furthermore, from the properties of Airy functions given above, we obtain the additional relations

$$\mathrm{Ai}\left(-\zeta e^{i\frac{2\pi}{3}}\right) = \frac{1}{2k}\, e^{i\frac{\pi}{3}}\, h_1(\zeta)$$

$$\mathrm{Ai}\left(-\zeta e^{-i\frac{2\pi}{3}}\right) = \frac{1}{2k^*}\, e^{-i\frac{\pi}{3}}\, h_2(\zeta)$$

$$\mathrm{Ai}'\left(-\zeta e^{i\frac{2\pi}{e}}\right) = -\frac{1}{2k}\, e^{-i\frac{\pi}{3}}\, h_1'(\zeta) \qquad \text{(A1-18)}$$

$$\mathrm{Ai}'\left(-\zeta e^{-i\frac{2\pi}{3}}\right) = -\frac{1}{2k^*}\, e^{i\frac{\pi}{3}}\, h_2'(\zeta).$$

Because of the symmetry relations between modified Hankel functions

$$h_1(\zeta^*) = \left[\, h_2(\zeta) \,\right]^*, \quad h_2(\zeta^*) = \left[\, h_1(\zeta) \,\right]^*$$

$$h_1'(\zeta^*) = \left[\, h_2'(\zeta) \,\right]^*, \quad h_2'(\zeta^*) = \left[\, h_1(\zeta) \,\right]^* \qquad \text{(A1-19)}$$

it is only necessary to evaluate both kinds of functions in the upper half of the complex ζ-plane to obtain values for any one kind of function over the entire ζ-plane. (Note that similar symmetry relations also hold for Airy functions.)

The SHARE subroutine HF13 computes values for $H_\nu^{(k)}(\omega)$ in the following form

$$H_\nu^{(k)}\left[(\omega R,\omega I)\ e^{ib2\pi}\right] = e^{M}(HR,HI) \qquad \text{(A1-20)}$$

where $k = 1,2$; $\nu = 1/3,2/3$; $b = -1,0,1$, $\omega R = \text{Real}(\omega)$, $\omega I = \text{Imag}(W)$, and $-\pi \quad \arg(\omega) < \pi$. For Airy functions

$$\omega = \frac{2}{3}\ \zeta^{3/2}$$

and we must consider the mapping of the upper half of the ζ-plane to ω-plane (keeping in mind the cut in the ω-plane) to determine the proper values of b to be used in (A1-20). If we let

$$\zeta = r\ e^{i\phi} \quad \text{and} \quad \omega = \rho\ e^{i\varepsilon}$$

we can see from Figure (A1-1) that the proper choice of b is given by

$$\begin{aligned} &0 \leq \phi \leq \frac{2\pi}{3}\ , \quad 0 \leq \theta \leq \pi && b = 0 \\ &\frac{2\pi}{3} < \phi \leq \pi\ , \quad -\pi < \theta \leq -\frac{\pi}{2} && b = 1 \end{aligned} \qquad \text{(A1-21)}$$

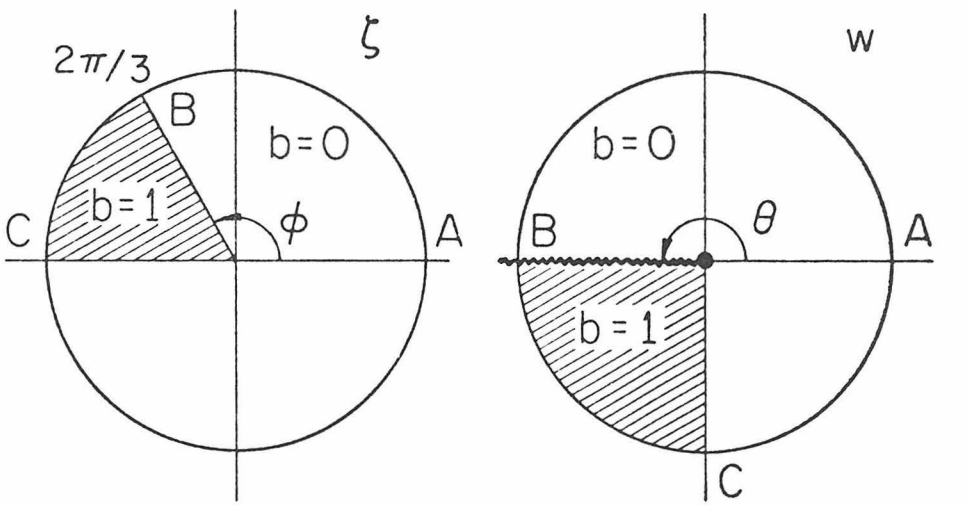

$\zeta = re^{i\phi}$ $\qquad$ $w = \rho e^{i\phi} = \frac{2}{3} r^{3/2} e^{i3\phi/2}$

Figure A1-1

Thus, Airy functions can be evaluated over the entire ζ- plane using relations (A1-15) and (A1-16) together with either (A1-17) or (A1-18); by putting $b = 0$ for $0 \leq \arg(\zeta) \leq 2\pi/3$ and $b = 1$ for $2\pi/3 < \arg(\zeta) \leq \pi$ in (A1-20); and by using the symmetry relations (A1-19) for $\pi \leq \arg(\zeta) \leq 2\pi$.

Because the exponent, M, in (A1-20) can become very large (and result in numerical overflow in a computer), it is convenient to work with ratios of Airy functions when possible. This can be done for the reflection coefficients in Chapter 1, and we note the following useful relations:

$$\frac{Ai'\left(-\zeta e^{i\,2\pi/3}\right)}{Ai\left(-\zeta e^{i\,2\pi/3}\right)} = -e^{-i\frac{2\pi}{3}}\,\frac{h_1'(\zeta)}{h_1(\zeta)} \qquad \text{(A1-22)}$$

and

$$\frac{Ai'(-\zeta)}{Ai(-\zeta)} = -e^{i\,\frac{2\pi}{3}}\,\frac{h_1'\left(\zeta e^{-i\,2\pi/3}\right)}{h_1\left(\zeta e^{-i\,2\pi/3}\right)} \qquad \text{(A1-23)}$$

Appendix II

A Justification of the Radiation Condition for the Negative Gradient Half-Space

In developing the solution for spherical waves reflected from a half-space with a negative velocity gradient, we assumed that the appropriate radiation condition was for the wave at $z = -\infty$ to be downgoing. Here we present two arguments to justify this assumption. The first involves showing that the asymptotic form of the reflection coefficient obtained by making this assumption is identical with the asymptotic expansion of the reflection coefficient obtained for the case in which the negative velocity gradient is terminated at a finite depth by a constant velocity, homogeneous half-space. In this case the appropriate radiation condition for a wave incident on the layer from above is that the wave emerging from beneath the heterogeneous layer be downgoing. The second argument involves showing that the backscattering from the particular velocity gradient considered (3.12) becomes arbitrarily small as $z \to -\infty$.

Consider a heterogeneous fluid layer of thickness, h, bounded above and below by homogeneous fluid half-spaces with the origin of a Cartesian coordinate system placed at the upper boundary of the layer as shown in Figure (A2-1). We will take the variation of

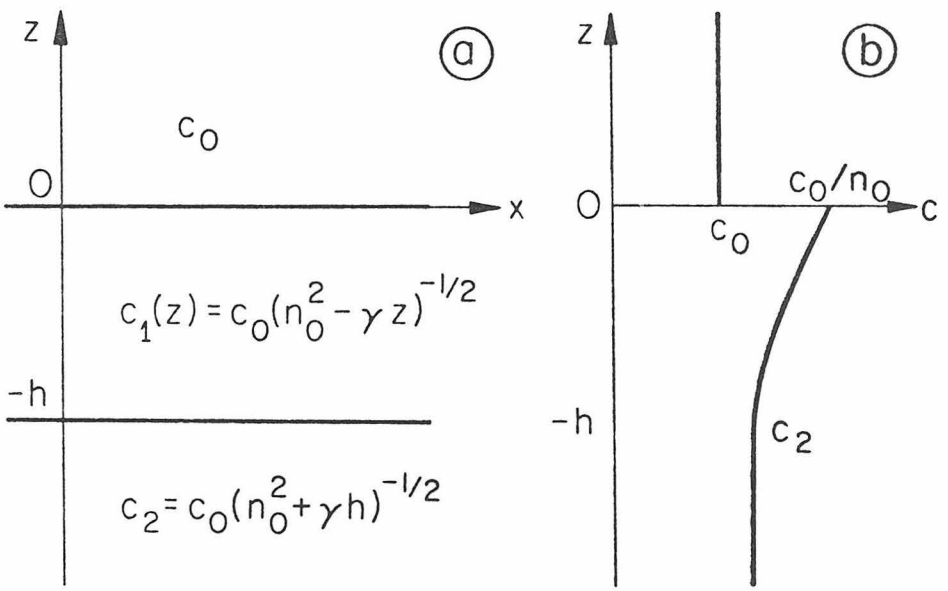
z
a
c_0
0
x
$c_1(z) = c_0(n_0^2 - \gamma z)^{-1/2}$
-h
$c_2 = c_0(n_0^2 + \gamma h)^{-1/2}$
z
b
0
c_0/n_0
c
c_0
-h
c_2

Figure A2-1

acoustic velocity with depth to be given by

$$C(z) = \begin{cases} C_o & z > 0 \\ C_1(z) = C_o(n_o^2 - \gamma z)^{\frac{1}{2}} & 0 > z > -h \\ C_2 = C_o(n_o^2 + \gamma h)^{-\frac{1}{2}} & z < -h \end{cases} \qquad \text{(A2-1)}$$

where the velocity variation in the heterogeneous layer, $C_1(z)$, has the same form as (3.12). We will assume that the density variation parallels the velocity variation.

Because we are interested in the general form of the reflection coefficient, it will be sufficient to determine the plane-wave coefficient, keeping in mind that the cylindrical case can be obtained simply by including the factor $(i/\eta_o)\, e^{i\eta_o z_o}$ (see equation 3.42). Thus we consider a plane wave of unit amplitude incident on the upper boundary of the homogeneous layer at a angle, θ. In this case the solutions to the equations of motion (Helmholtz equations) will be

$$\begin{aligned} \psi_o &= e^{i(\kappa_o x + \eta_o z)} + V_1\, e^{i(\kappa_o x + \eta_o z)} && z > 0 \\ \psi_1 &= \left[V_2\, \mathrm{Ai}^{(1)}(-\zeta) + V_3\, \mathrm{Ai}^{(2)}(-\zeta) \right] e^{i\eta_1 z} && 0 > z > -h \\ \psi_2 &= V_4\, e^{i(\kappa_2 x - \eta_2 z)} && z < -h \end{aligned} \qquad \text{(A2-2)}$$

where

$$Ai^{(1)}(-\zeta) \equiv Ai\left(-\zeta e^{i2\pi/3}\right), \quad Ai^{(2)}(-\zeta) \equiv Ai\left(-\zeta e^{-i2\pi/3}\right)$$

$$\zeta = \varepsilon^{-2}(n_o^2 - p^2 - \gamma z)$$

$$p = \sin\theta \quad , \quad \varepsilon = (\gamma/k_o)^{1/3}$$

as in section 3 of Chapter 1. Here we allow both upgoing and downgoing waves in the heterogeneous layer and require only downgoing waves in the lower half space.

Applying the continuity conditions (3.2) and (3.3) to (A2-2) at the upper boundary (z = 0) of the heterogeneous layer, we obtain

$$\begin{pmatrix} 1 & -m^{\frac{1}{2}}Ai^{(1)}(-\zeta_o) & -m^{\frac{1}{2}}Ai^{(2)}(-\zeta_o) \\ iq_o & -m^{-\frac{1}{2}}A^{(1)}(-\zeta_o) & -m^{-\frac{1}{2}}A^{(2)}(-\zeta_o) \end{pmatrix} \begin{pmatrix} V_1 \\ V_2 \\ V_3 \end{pmatrix} = \begin{pmatrix} -1 \\ iq_o \end{pmatrix} \tag{A2-3}$$

where

$$A^{(1)}(-\zeta_o) = Ai^{(1)}(-\zeta_o)\, D_o + \varepsilon\, e^{i2\pi/3}\, Ai^{(1)'}(-\zeta_o)$$

$$A^{(2)}(-\zeta_o) = Ai^{(2)}(-\zeta_o)\, D_o + \varepsilon\, e^{-i\pi/3}\, Ai^{(2)'}(-\zeta_o)$$

$$\zeta_o = \varepsilon^{-2}(n_o^2 - p_o^2) \quad , \; D_o = \varepsilon^3/4n_o^3 m,$$

$$q_o = \cos\theta_o \quad , \quad m = (\rho_1(0)/\rho_o)$$

Solving (A2-3) for the reflection coefficient, V_1, we can write

$$V_1 = \frac{1 - \frac{i}{q_o} R}{1 + \frac{i}{q_o} R} \tag{A2-3a}$$

where

$$R = \frac{V_2 \, A^{(1)}(-\zeta_o) + V_3 \, A^{(2)}(-\zeta_o)}{V_2 \, Ai^{(1)}(-\zeta_o) + V_3 \, Ai^{(2)}(-\zeta_o)} \tag{A2-4}$$

Here we note that if $V_2 = 0$, the reflection coefficient, V_1, reduces to the plane wave reflection coefficient for the negative gradient half-space (3.22).

To evaluate the constants V_1 and V_2, we next apply the continuity conditions to the lower boundary of the heterogeneous layer ($z = -h$). In this case

$$\begin{pmatrix} Ai^{(1)}(-\zeta_2) & Ai^{(2)}(-\zeta_2) \\ A^{(1)}(-\zeta_2) & A^{(2)}(-\zeta_2) \end{pmatrix} \begin{pmatrix} V_2 \\ V_3 \end{pmatrix} = V_4 \, e^{-i\eta_2 h} \begin{pmatrix} 1 \\ iq_2 \end{pmatrix} \tag{A2-5}$$

where

$$A^{(1)}(-\zeta_2) = Ai^{(1)}(-\zeta_2) \, D_2 + \varepsilon \, e^{i 2\pi/3} \, Ai^{(1)'}(-\zeta_2)$$

$$A^{(2)}(-\zeta_2) = Ai^{(2)}(-\zeta_2) \, D_2 + \varepsilon \, e^{-i 2\pi/3} \, Ai^{(2)'}(-\zeta_2)$$

$$\zeta_2 = \varepsilon^{-2}(n_o^2 - p_o^2 + \gamma h) \qquad , \qquad D_2 = \frac{\varepsilon^3}{4}\,(n_o^2 + \gamma h)^{-1}$$

Thus we see that

$$V_2 = V_4 \frac{\left[A^{(2)}(-\zeta_2) - iq \;\; Ai^{(2)}(-\zeta_2) \right]}{\Delta} \tag{A2-6}$$

$$V_3 = V_4 \frac{\left[iq_3 \; Ai^{(1)}(-\zeta_2) - A^{(1)}(-\zeta_2) \right]}{\Delta} \tag{A2-7}$$

where

$$\Delta = A^{(2)}(-\zeta_2) \; Ai^{(1)}(-\zeta_2) - A^{(1)}(-\zeta_2) \; Ai^{(2)}(-\zeta_2)$$

Substitution of these expressions for V_1 and V_2 into (A2-4) gives the following result for R,

$$R = \frac{A^{(1)}(-\zeta_o) + f \; A^{(2)}(-\zeta_o)}{Ai^{(1)}(-\zeta_o) + f \; Ai^{(2)}(-\zeta_o)} \tag{A2-8}$$

where

$$f = \frac{iq_2 \; Ai^{(1)}(-\zeta_2) - A^{(1)}(-\zeta_2)}{-iq_2 \; Ai^{(2)}(-\zeta_2) + A^{(2)}(-\zeta_2)}$$

We are interested in the form of the reflection coefficient, V_1, (A2-3a) when the thickness of the layer is large with respect to the wave lengths considered and the characteristic dimension of the gradient. Thus when $|\gamma h| >> 1$ and $\varepsilon << 1$

$$|\zeta_2| = |\varepsilon^{-2}(n_o^2 - p_o^2 + \gamma h)| >> 1,$$

and we can use the asymptotic forms for the Airy functions with arguments $(-\zeta_2)$ given in Appendix I. In addition, note the following relations:

$$\lim_{h\to\infty} D_2 = \lim_{h\to\infty} \frac{\gamma}{4k_o} (n_o^2 + \gamma h)^{-1} = 0$$

$$\lim_{h\to\infty} q_2 = \lim_{h\to\infty} \left[1 - (n_o^2 + \gamma h)^{-\frac{1}{2}} p_o \right] = 1$$

Accordingly, we find that

$$\lim_{h\to\infty} f = - e^{2i(W_2 + 7\pi/12)} \qquad \text{(A2-9)}$$

where

$$W_2 = \frac{2}{3} \varepsilon^{-3}(n_o^2 - p_o^2 + \gamma h)^{3/2}$$

Dividing both numerator and denominator of (A2-8) by $Ai^{(1)}(-\zeta_o)$, we can write R in the following form

$$R = \frac{g_1 + fg_2}{1 + fg_3} \tag{A2-10}$$

with

$$g_1 = A^{(1)}(-\zeta_o)/Ai^{(1)}(-\zeta_o)$$

$$g_2 = A^{(2)}(-\zeta_o)/Ai^{(1)}(-\zeta_o)$$

$$g_3 = Ai^{(2)}(-\zeta_o)/Ai^{(1)}(-\zeta_o)$$

Using (A2-10) it is now possible to put the reflection coefficient, V_1, in a form that contains the reflection coefficient for a negative gradient half-space, V_{p-}, as a separate term, i.e.

$$V_1 \simeq \frac{V_{p-} + Q_-}{1 + Q_+} \tag{A2-11}$$

where

$$Q_{\mp} = \frac{\left(f\ g_3 \mp \frac{i}{qm}\ g_2\right)}{1 + \frac{i}{qm}\ g_1}$$

Our goal is to expand (A2-11) into an infinite series with V_{P-} as the leading term. To accomplish this, we will use the asymptotic forms of the Airy functions for $|\zeta_o| >> 1$ given in Appendix I.

Thus we find

$$g_1 \sim D_o - i\,\varepsilon\zeta_o^{1/2} = -\,i\,\varepsilon\zeta_o^{1/2} + O(\varepsilon^3)$$

$$g_2 \sim i\,\varepsilon\zeta_o^{1/2}\, e^{-i(2W_o + 7\pi/6)} + O(\varepsilon^3)$$

$$g_3 \sim -\, e^{-i(2W_o + 7\pi/6)}$$

where $$W_o = \frac{2}{3}\ \varepsilon^{-3}(n_o^2 - p_o^2)^{3/2}$$

and we require

$$\left|\varepsilon^{-2}(n_o^2 - p_o^2)\right| >> 1$$

(i.e. the gradient is small, and the angle of incidence is not too near the critical angle). Using these approximate relations for the g's, we find

$$\begin{pmatrix} Q_- \\ Q_+ \end{pmatrix} \sim e^{i2\phi} \begin{pmatrix} V_o \\ 1 \end{pmatrix} \qquad \text{(A2-12)}$$

where

$$\phi = (W_3 - W_1)$$

and

$$V_o = \frac{mq_o - \sqrt{n_o^2 - p_o^2}}{mq_o + \sqrt{n_o^2 - p_o^2}}\ ,$$

which we recognize as the plane-wave reflection coefficient for two homogeneous half-spaces (3.25).

Combining (A2-11) and (A2-12), we see that

$$V_1 \simeq \frac{V_{p-} + e^{i2\phi} V_o}{1 + e^{i2\phi}}$$

which, on expanding the denominator, can be written as

$$V_1 \simeq \left(V_{p-} + e^{i2\phi} V_o \right) \left(1 - e^{i2\phi} + e^{i4\phi} + \cdots (-1)^n e^{i2n\phi} + \cdots \right) \tag{A2-13}$$

In Section 3 of Chapter 1, we saw that when the asymptotic forms of the Airy functions were used in the plane-wave reflection coefficient for the negative gradient, V_{p-}, it reduced to the reflection coefficient for two homogeneous half-spaces. That is for

$$\left| \varepsilon^{-2} (n_o^2 - p_o^2) \right| >> 1$$

then

$$V_{p-} \sim V_o$$

when V_o is substituted for V_{p-} in (A2-13) and the multiplication is carried out, all of the terms cancel but the first, and we are left with

$$V_1 \sim V_o \tag{A2-14}$$

Thus the asymptotic form for the reflection coefficient for the negative-gradient layer defined by (A2-1) with the proper radiation condition applied to waves in the lower, homogeneous half space reduces to the asymptotic form of the reflection coefficient for the negative-gradient half-space based on the assumed radiation condition of downgoing waves at $z = -\infty$.

We now turn to the problem of showing that the backscattering due to the heterogeneity of the negative gradient becomes arbitrarily small as $z \to -\infty$. In Chapter 3 of his book on waves in layered media, Brekhovskikh (1960) develops an expression describing the relative size of the first order waves backscattered by the heterogeneity of a continuous nonoscillatory velocity gradient. His approach is based on assuming a generalized form of the WKB solution.

$$\phi\alpha\ f(x)\left[\ \chi_1\ \exp\left(ik_o\int_0^z n\ \cos\ \theta\ dz\right)\right. \\ \left. +\ \chi_2 \exp\left(-ik_o\int_0^z n\ \cos\ \theta\ dz\right)\right. \tag{A2-15}$$

in a heterogeneous medium. Here χ_1 and χ_2 are undetermined functions of z satisfying

$$\frac{d\chi_1}{dz} = \varepsilon\lambda_1(z)\ \chi_2(z) \\ \frac{d\chi_2}{dz} = \varepsilon\lambda_2(z)\ \chi_2(z) \tag{A2-16}$$

where

$$\varepsilon = \frac{1}{2}\left[\frac{d}{dz} \ln\left(\frac{\cos\theta}{n}\right) \right]$$

$$\lambda_1(z) = \exp\left(-2ik_o \int_0^z n \cos\theta \, dz \right)$$

$$\lambda_2(z) = \exp\left(2ik_o \int_0^z n \cos\theta \, dz \right)$$

In these equations $n = n(z)$ is an index of refraction with respect to the point $z = 0$, and

$$\cos\theta = \frac{1}{n}(n^2 - \sin^2\theta)$$

where θ is an angle of incidence. Note that for small gradients γ, the term, ε, will be a small quantity since

$$\frac{d}{dz}\left(\ln \frac{\cos\theta(z)}{n(z)} \right) = O(\gamma).$$

The approach is to solve (A2-16) by successive approximations. Solutions to the coupled pair of equations (A2-16) can be expressed as two convergent series

$$\chi_1 = \chi_1^{(0)} + \varepsilon\chi_1^{(1)} + \cdots + \varepsilon^n\chi_1^{(n)} + \cdot$$

$$\chi_2 = \chi_2^{(0)} + \varepsilon\chi_2^{(1)} + \cdots + \varepsilon^n\chi_1^{(n)} + \cdot\cdot$$

(Brekhovskikh, 1960). When these are substituted into (A2-16) and the coefficients of like powers of ε are equated, the following recursion relations between successive approximations are obtained

$$\frac{d\chi_1^{(m)}}{dz} = \lambda_1(z)\chi_2^{(m-1)}(z)$$

$$\frac{d\chi_2^{(m)}}{dz} = \lambda_2(z)\,\chi_1^{(m-1)}(z).$$

We are interested in comparing the first-order backscattered wave with the direct, zeroth-order down-going wave, i.e.

$$\frac{d\chi_1^{(1)}}{dz} = \lambda_1(z)\,\chi_2^{(0)}$$

where $\chi_2^{(0)}$ is constant in the zeroth-order WKB approximation. Putting this relation in (A2-16) and integrating, we obtain

$$\varepsilon\chi_2^{(1)} = \frac{1}{2}\,\chi_1^{(0)}\int_{\infty}^{z}\left[\frac{d}{dz}\ln\left(\frac{\cos\theta}{n}\right)\right]\exp\left(2ik_o\int_0^{z} n\cos\theta\,d\zeta\right)dz\ .$$

For the first-order backscattering term to be small in (A2-15), we require the above integral to be small. This will be true if the integral over each half period of the exponential is small. Assuming that the gradient changes only slightly over one wave length, the quantity in the brackets will vary slowly and

can be taken outside the integral. Thus the modulus of the integral over one half period will be no greater than

$$\frac{\lambda_o}{4n \cos\theta} \frac{d}{dz} \left(\ln \frac{\cos\theta}{n} \right),$$

where $\lambda_o/4n\cos\theta$ is the approximate magnitude of the half-period of the exponential. Hence the requirement for small backscattering becomes

$$\left| \frac{\lambda_o}{4n_o \cos\theta} \frac{d}{dz} \left(\frac{\cos\theta}{n} \right) \right| << 1 \qquad \text{(A2-17)}$$

(Brekhovskikh, 1960).

For the velocity gradient we are considering, $n^2 = n_o^2 - \gamma z$ (see equation 3.12). In this case

$$\frac{d}{dz} \left(\frac{\cos\theta}{n} \right) = \frac{\gamma}{(n_o^2 - \gamma z)} \left[\frac{n_o^2 - \sin^2\theta - \gamma z}{2(n_o^2 - \gamma z)(n_o^2 - \sin^2\theta \cdot \gamma z)} \right]$$

so that

$$\left| \frac{\lambda_o}{4\cos^2\theta} - \frac{d}{ez} \left(\frac{\cos\theta}{n} \right) \right| = \left| \left[\gamma \lambda_o n^2 (n_o^2 - \sin^2\theta - \gamma z) \right] \times \left[4(n_o^2 - \sin^2\theta)(2n_o^4 + \gamma n_o^2 z - \gamma^2 z^2)(n_o^2 - \sin^2\theta - \gamma z)^{\frac{1}{2}} \right]^{\frac{1}{2}} \right|$$

Now since the numerator is of order z and the denominator is of order $z^{5/2}$, we have

$$\lim_{z \to -\infty} \left| \frac{\lambda_o}{4\cos^2\theta} \frac{d}{dz}\left(\frac{\cos\theta}{n}\right) \right| = 0$$

and the backscattering term becomes arbitrarily small as $z \to -\infty$.

We justify the radiation condition assumed for the negative-gradient half space on the basis of these two arguments. In particular we have shown that the reflection coefficient for the well-posed problem of waves reflected from the negative-gradient layer between two homogeneous half spaces is equivalent to the reflection coefficient obtained for the negative-gradient half space assuming downgoing waves at $z = -\infty$ when the layer thickness is large with respect to the characteristic dimension of the gradient and the wave length. The demonstration that waves back-scattered by the negative gradient disappear as $z \to -\infty$ is consistent with the assumption that only down-going waves exist in the neighborhood of $z = -\infty$.

Appendix III

Convergence of the Integral Representation for $D_{-3/2}$ Over the Modified Contour Γ_2.

The integral representation for the parabolic-cylinder function $D_{-3/2}(z)$ is of the form

$$I_{\Gamma_1} = \int_0^\infty e^{-zt - t^2/2}\, t^{\frac{1}{2}}\, dt \qquad \text{(A3-1)}$$

(Erdelyi, et al., vol. 2, 1953). The integral we wish to evaluate (3.65) is of the form

$$I_{\Gamma_2} = \int_{\Gamma_2} e^{-zt - t^2/2}\, t^{\frac{1}{2}}\, dt \qquad \text{(A3-2)}$$

where $z = \rho\, e^{i(\pi/4-\delta)}$, $\delta > 0$ (see 3.64), and Γ_2 extends from the origin at an angle of $\pi/4$ to infinity in the complex t-plane as shown in Figure (A3-1).

Let $t = s\, e^{i\phi}$. Then (A3-1) and (A3-2) can be written as

$$I_{\Gamma_1} = \int_0^\infty \exp\left[- \rho s\, e^{i(\pi/4-\delta)} - \frac{1}{2} s^2 \right] s^{\frac{1}{2}}\, ds \qquad \text{(A3-3)}$$

over Γ_1, and

$$I_{\Gamma_2} = e^{i(3\pi/8)} \int_0^\infty \exp\left[- \rho s\, e^{i(\pi/4-\delta)} - \frac{1}{2} s^2\, e^{i(\pi/2)} \right] s^{\frac{1}{2}} ds$$

(A3-4)

over Γ_2. To demonstrate the equivalence of I_{Γ_1} and I_{Γ_2}, we close the contour between Γ_1 and Γ_2 along C, where C is defined by

$$t = R\, e^{i\phi} \quad , \quad 0 \leq \phi \leq \pi/4$$

(see Figure (A3-1)). The integral over C is given by

$$I_c = iR^{3/2} \int_0^{\pi/4} \exp\left[- \rho R\, e^{i(\phi + \frac{\pi}{4} - \delta)} - \frac{1}{2} R^2\, e^{i2\phi} \right] e^{i\frac{3\phi}{2}}\, d\phi$$

or

$$I_c = iR^{3/2} \int_0^{\pi/4} \left[\exp\left\{ - \left[\rho R \cos(\phi + \pi/4 - \delta) + \frac{R^2}{2} \cos 2\phi \right] \right\} \cdot \exp\left\{ -i \left[\rho R \sin(\phi+\pi/4-\delta) + \frac{R^3}{2} \sin 2\phi + \frac{3\phi}{2} \right] \right\} \right] d\phi$$

(A3-5)

Now as $R \to \infty$, the integrand is dominated by a term of the form $R^{3/2} \exp(-\rho\varepsilon R)$ since even at $\phi = \pi/4$, $\cos(\phi+\pi/4-\delta) \sim \varepsilon > 0$. Thus

$$\lim_{R\to\infty} I_c = 0,$$

and because there are no singularities included in the contour

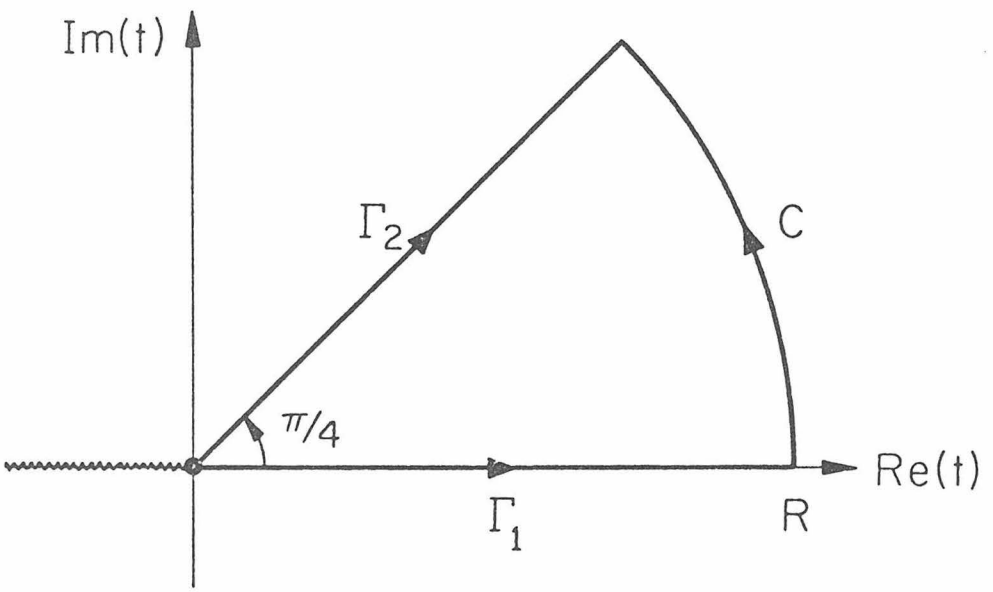

Figure A3-1

$$I_{\Gamma_1} - I_{\Gamma_2} = 0$$

or

$$I_{\Gamma_1} = I_{\Gamma_2} = D_{-3/2}(z)\ \Gamma(3/2)\ e^{z^2/4} \qquad \text{(A3-6)}$$

which is the desired result.

Appendix IV

Geometrical Ray Theory for the Positive Gradient Acoustic Case

In this appendix, we develop some aspects of geometrical ray theory that will be useful in discussing the wave-theoretical solutions to the positive-gradient, acoustic case. The velocity distribution is taken as defined by (3.12). The point source and receiver are located at $(0,z_o)$ and (ρ,z) with respect to the velocity discontinuity at $z = 0$, as shown in Figure (A4-1).

From (3.1) we have the following variation of the index of refraction with depth

$$n(z) = \begin{cases} 1 & z > 0 \qquad \text{(A4-1)} \\ (n_o^2 + \gamma z)^{\frac{1}{2}} & z < 0 \qquad \text{(A4-2)} \end{cases}$$

By Snell's law

$$n(z) \sin \theta(z) = \sin \theta_o . \qquad \text{(A4-3)}$$

where θ_o is the angle of incidence of a given ray at the boundary $z = 0$. As in section 3, Chapter 1, we let $p = \sin \theta$, so that (A4-3) becomes

$$p(z) = \frac{p_o}{(n_o^2 + \gamma z)^{\frac{1}{2}}} . \qquad \text{(A4-4)}$$

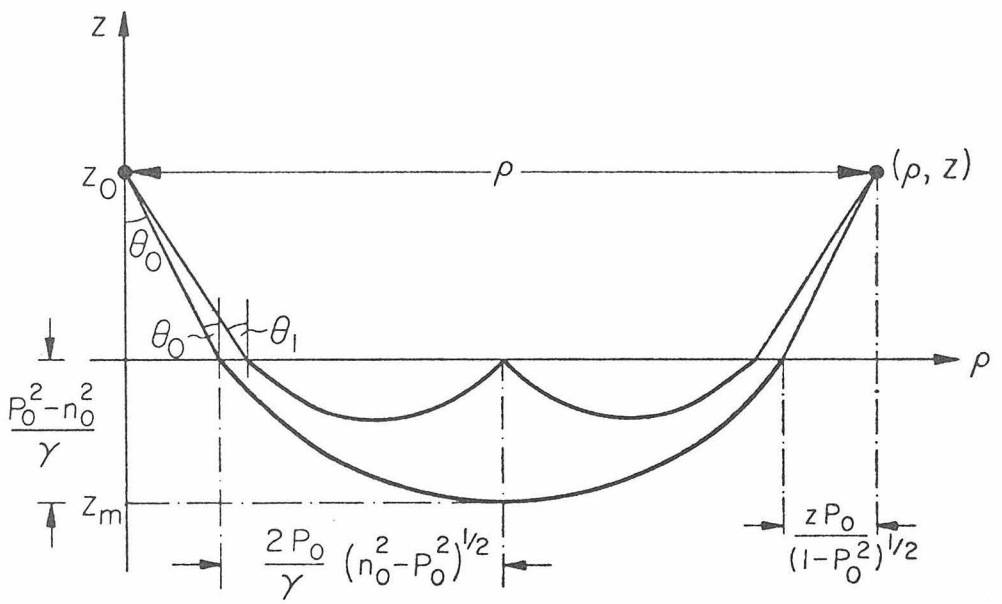
z
z_0
ρ
(ρ, z)
θ_0
θ_0
θ_1
ρ
$\frac{P_0^2-n_0^2}{\gamma}$
z_m
$\frac{2P_0}{\gamma}(n_0^2-P_0^2)^{1/2}$
$\frac{zP_0}{(1-P_0^2)^{1/2}}$

Figure A4-1a

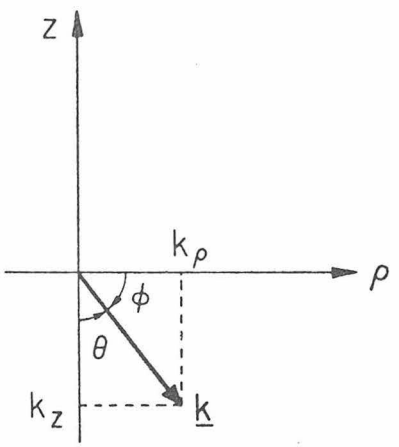

$$\theta = \phi + \frac{\pi}{2}$$

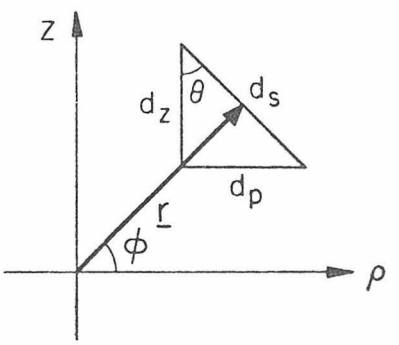

$$\frac{dr}{dz} = -\tan\theta$$

$$\frac{dz}{ds} = -\cos\theta$$

Figure A4-1b

The maximum depth of penetration into the lower medium, z_m, for a ray with an angle of incidence, θ_n, is obtained directly from (A4-4) by noting that at this depth; $p(z) = 0$. Thus

$$z_m = \frac{p_o^2 - n_o^2}{\gamma} \qquad \text{(A4-5)}$$

which is identical with the equation defining the loci of turning points for the positive gradient case discussed in section 3. (See Figure 4 also.)

The horizontal distance covered by the ray in the lower medium, ρ_1, can be found using the relation

$$\frac{d\rho}{dz} = -\tan\theta(z) = \frac{-p(z)}{(1-p^2(z))^{\frac{1}{2}}}$$

Thus

$$\rho(z) = -\int_o^z \frac{p_o\,dz}{(n_o^2 - p_o^2 + \gamma z)^{\frac{1}{2}}}$$

or

$$\rho(z) = \frac{2p_o}{\gamma}\left[(n_o^2 - p_o^2)^{\frac{1}{2}} - (n_o^2 - p_o^2 + \gamma z)^{\frac{1}{2}}\right] \qquad \text{(A4-6)}$$

The distance covered by the ray reaching its maximum depth, z_m, is thus

$$\rho_m = \frac{2p_o}{\gamma}\sqrt{n_o^2 - p_o^2} \qquad \text{(A4-7)}$$

Noting that the horizontal distance covered by a ray between the source and the boundary and between the boundary and the receiver is

$$\rho_c = (z + z_o) \frac{p_o}{\sqrt{1-p_o^2}} ,$$

we obtain for the total horizontal distance covered by the ray leaving the source at an angle θ

$$\rho_t = \rho_c + \rho_m$$

or

$$\rho_t = \frac{p_o}{\sqrt{1-n_o^2}} (z + z_o) + \frac{4p_o}{\gamma} \sqrt{n_o^2 - p^2} \qquad \text{(A4-8)}$$

The total horizontal distance covered by a ray that reflects n times at the boundary $z = 0$ before returning to the upper half space is

$$\rho_t = \frac{p_n}{\sqrt{1-p_n^2}} (z + z_o) + \frac{4(n+1)\, p_n}{\gamma} (n_o^2 - p_n^2)^{\frac{1}{2}} \qquad \text{(A4-9)}$$

where $p_n = \sin \theta_n$, and θ_n is the angle of incidence. For a fixed ρ_z, this equation defines the relation between the angles of incidence for the direct diving ray, θ_o, and the ray making n reflections, θ_n.

The geometry of a ray path in the lower medium can be found by re-writing (A-6) in the following form:

$$\left[\rho_1 - \frac{2p_o}{\gamma} (n_o^2 - p_o^2)^{\frac{1}{2}} \right] = (r_o^2 - p_o^2 + \gamma z)^{\frac{1}{2}}$$

or by squaring both sides and using (A4-7)

$$(\rho_1 - \rho_m)^2 = \gamma \left[\frac{n_o^2 - p_o^2}{\gamma} + z \right] \qquad \text{(A4-10)}$$

This is the equation of a parabola with its vertex at $(\rho,z) = \rho_m, \left(- \frac{n_o^2 - p_o^2}{\gamma} \right)$, its focus at $(\rho,z) = \left[\rho_m, -\left(\frac{n_o^2 - p_o^2}{\gamma} - \gamma/4 \right) \right]$, and with a latus rectum of γ. (See Figure(A4-2)).

The ray-theoretical phase (eiconal) is given by

$$\phi = \int_s \underline{k} \cdot d\underline{s} \qquad \text{(A4-11)}$$

where $\underline{k}$ is the wave number vector and $d\underline{s}$ is a vector increment along the ray path s in our coordinate system (Figure (A4-1))

$$\underline{k} = - k_o \cos \theta(z) + k_o \sin \theta(z) = - k_z + k_\rho$$

where $|\underline{k}| = k_o$, $\theta(z)$ is the local angle of incidence, and the vertical and horizontal components of the wave number, k_z and k_ρ, are given by

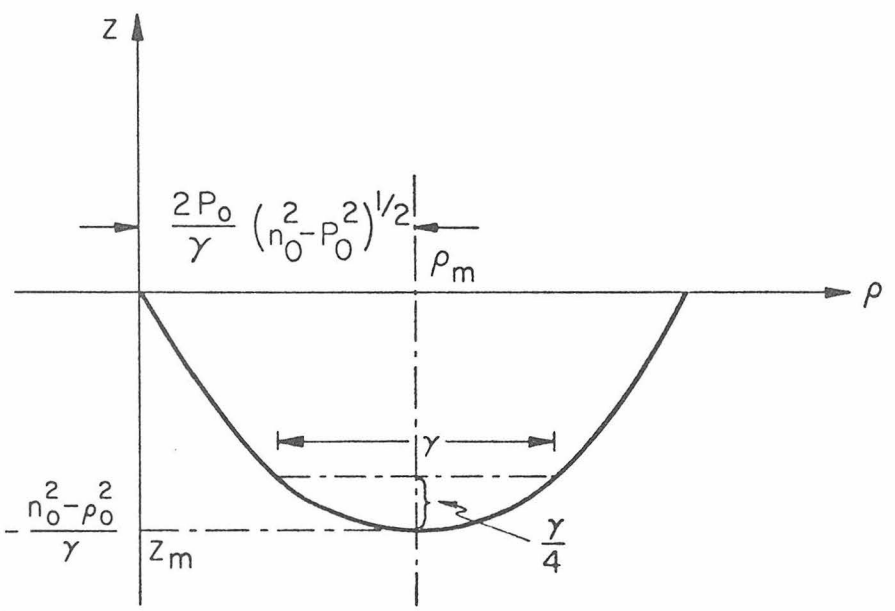
z
$\frac{2P_o}{\gamma}\left(n_o^2-P_o^2\right)^{1/2}$
ρ_m
ρ
γ
$\frac{n_o^2-\rho_o^2}{\gamma}$
z_m
$\frac{\gamma}{4}$

Figure A4-2

$$k_z(z) = \begin{cases} k_o \cos \theta_o & z > 0 \\ k_o n(z) \cos \theta(z) & z < 0 \end{cases} \qquad \text{(A4-12)}$$

and

$$k_\rho = k_o \sin \theta_o. \qquad \text{(A4-13)}$$

where $\cos \theta(z) = (1-p^2(z))^{\frac{1}{2}}$. Using the forms for $p(z)$ and $h(z)$ given by (A4-4) and (A4-2), the integral for the phase (A4-11) becomes

$$\phi = k_o \left\{ \int_o^r p_o d\rho - \int_{z_o}^o q_o dz - 2 \int_o^{z_\omega} (n_o^2 - p_o^2 + \gamma z)^{\frac{1}{2}} dz + \int_o^z q_o \, dz \right\}$$

or

$$\phi = k_o \left[p_o \rho + (z + z_o) q_o + \frac{4}{3\gamma} (n_o^2 - p_o^2)^{3/2} \right] \qquad \text{(A4-14)}$$

This is the ray-theoretical phase of a wave leaving the source at an angle θ_o, bottoming at depth, z_m, in the lower medium, and arriving at (z,r). The phase of a wave that reflects n times at the boundary z = 0 before leaving the lower medium to arrive at (z,r) is given by

$$\phi_n = k_o \left[p_n \rho + (z + z_o) q_o + \frac{4(n+1)}{3\gamma} (n_o^2 - p_n^2)^{3/2} \right] \qquad \text{(A4-15)}$$

where $q_b = (1 - p_n^2)$, $p_n^2 = \sin^2 \theta_n$, and θ_n is the angle of incidence (see (A4-9)). This expression for ϕ_n is purely geometric; it does not include the phase shift associated with the reflection coefficient for a wave incident at the boundary z = 0 from below, nor does it include a wave-theoretical $-\pi/2$ phase shift acquired at each bottoming (turning) point.

The travel time along a ray is given by

$$t = \int_S \frac{ds}{c(s)}$$

where c(s) is the material velocity along the ray path S. In this case

$$t = -\int_0^z \frac{dz}{\sqrt{1-p^2(z)}\, c(z)}$$

Using (3.1) and (A4-4), the total travel time for a ray bottoming once in the lower medium will be

$$t = -\int_{z_o}^{o} \frac{dz}{q_o c_o} - \frac{2}{c_o} \int_o^{z_m} \frac{(n_o^2 + \gamma z)\, dz}{(n_o^2 - p_o^2 + \gamma z)^{1/2}} + \int_o^z \frac{dz}{q_o c_o}$$

or

$$t = \frac{1}{c_o} \left[\frac{(z + z_o)}{q_o} + \frac{4}{3\gamma} (n_o^2 + 2p_o^2) (n_o^2 - p_o^2)^{1/2} \right] \qquad \text{(A4-16)}$$

The total travel time for a ray reflecting n times at the boundary $z = 0$ is

$$t_n = \frac{1}{c_o}\left[\frac{(z + z_o)}{q_n} + \frac{4(n+1)}{3\gamma}\ (n_o^2 + 2p_n^2)(n_o^2 - p_n^2)^{\frac{1}{2}}\right] \qquad \text{(A4-17)}$$

From this expression, it is evident that energy following the direct diving ray will be a first arrival, and that energy following rays that reflect a successively greater number of times at the boundary $z = 0$ will arrive at successively later times.

Appendix V

Inversion of the P-SV Boundary Conditions for the PP Reflection Coefficient - Negative Gradient Case

The fourth order matrix equation (4.42) expressing the boundary conditions for P-SV motion when the lower half-space has negative compressional and shear velocity gradients is of the form

$$\underline{\underline{M}}\underline{V} = \underline{a} \tag{A5-1}$$

Solving this equation for the first element in $\underline{V}$ (i.e. V_{pp}) by Cramer's rule gives

$$V_{pp} = \frac{\det \underline{\underline{N}}}{\det \underline{\underline{M}}} \tag{A5-2}$$

where the matrix $\underline{\underline{N}}$ is formed by replacing the first column in $\underline{\underline{M}}$ by the vector $\underline{a}$. By expanding each of the determinants in (A5-2) about their third columns (the columns containing the Airy functions $Ai^{(1)}(-\zeta_o)$ and $Ai^{(1)'}(-\zeta_o)$) we obtain

$$\begin{pmatrix} \det \underline{\underline{N}} \\ \det \underline{\underline{M}} \end{pmatrix} = -iAi^{(1)}(-\zeta_o)\begin{pmatrix} C_1^1 \\ C_1^2 \end{pmatrix} - G(\zeta_o)\begin{pmatrix} C_2^1 \\ C_2^2 \end{pmatrix} + \mu_1 H(\zeta_o)\begin{pmatrix} C_3^1 \\ C_3^2 \end{pmatrix} - 2i\mu_1 G(\zeta_o)\begin{pmatrix} C_4^1 \\ C_4^2 \end{pmatrix} \tag{A5-3}$$

where C_i^1 and $C_i^2 (i = 1,4)$ are the appropriate cofactors of the matrices $\underline{\underline{N}}$ and $\underline{\underline{M}}$, respectively. These equations can be rewritten using the definitions of $G(\zeta_o)$ and $H(\zeta_o)$ (equations (4.43) and (4.45)) as

$$\begin{pmatrix} \det \underline{\underline{N}} \\ \\ \det \underline{\underline{M}} \end{pmatrix} = - \mathrm{Ai}^{(1)}(-\zeta_o) \begin{pmatrix} D \\ \\ E \end{pmatrix} + \varepsilon_\alpha \, e^{i 2\pi/3} \, \mathrm{Ai}^{(1)'}(-\zeta_o) \begin{pmatrix} D_1 \\ \\ E_1 \end{pmatrix}$$

where

$$\begin{pmatrix} D \\ \\ E \end{pmatrix} = \begin{pmatrix} C_1^1 \\ \\ C_1^2 \end{pmatrix} - \pi_o \mu_1 \begin{pmatrix} C_3^1 \\ \\ C_3^2 \end{pmatrix} + \frac{\varepsilon_\alpha^3 \, m^{\frac{1}{2}}}{4 n_\rho^{3/2}} \begin{pmatrix} C_2^1 + 2i\mu_1 \, C_4^1 \\ \\ C_2^2 + 2i\mu_1 \, C_4^2 \end{pmatrix} \qquad \text{(A5-4)}$$

and

$$\begin{pmatrix} D_1 \\ \\ E_1 \end{pmatrix} = \begin{pmatrix} C_2^1 + 2i\mu_1 \, C_4^1 \\ \\ C_2^2 + 2i\mu_1 \, C_4^2 \end{pmatrix} - \frac{3}{2} \frac{\varepsilon_\alpha^3 \, m^{\frac{1}{2}}}{n_\rho^{3/2}} \begin{pmatrix} C_3^1 \\ \\ C_3^2 \end{pmatrix} \qquad \text{(A5-5)}$$

with

$$\pi_o = p^2 + 3\varepsilon_\alpha^2 \left(\zeta_o \, e^{i 4\pi/3} + \frac{3}{8} \frac{\varepsilon_\alpha^3 \, m^{\frac{1}{2}}}{n_\rho^{3/2}} \right)$$

The cofactors, C_i^j, have the following form

$$C_1^j = h_o^2 m \begin{vmatrix} -iq & p^2 & -p^2 Ai^{(1)}(-\xi_o) \\ \delta_j(1+2q^2)\mu_o & -2ip^2\nu\mu_o & 2p^2\mu_1 G(\xi_o) \\ 2\mu_o q & i(\ell^{-2}+2p^2)\mu_o & i\mu_1 H(\xi_o) \end{vmatrix}$$

$$C_2^j = h_o^2 m \begin{vmatrix} -\delta_j i & \nu & iG(\xi_o) \\ \delta_j(1+2q^2)_o & -2ip^2\nu\mu_o & 2p^2\mu_1 G(\xi_o) \\ 2\mu_o q & i(\ell^{-2}+2p^2)\mu_o & i\mu_1 H(\xi_o) \end{vmatrix}$$

$$C_3^j = h_o^2 m \begin{vmatrix} -\delta_j i & \nu & i\,G(\xi_o) \\ -iq & p^2 & -p^2 Ai^{(1)}(-\xi_o) \\ 2\mu_o q & i(\ell^{-2}+2p^2)\mu & i\mu_1 H(\xi_0) \end{vmatrix}$$

and

$$C_4^j = h_o^2 m \begin{vmatrix} -\delta_j i & \nu & iG(\xi_o) \\ -iq & p^2 & -p^2 Ai^{(1)}(\xi_o) \\ \delta_j(1+2q^2)_o & -2ip^2\nu\mu_o & 2p^2\mu_1 G(\xi_o) \end{vmatrix}$$

where $j = 1,2$ and

$$\delta_j = \begin{cases} 1 & j = 1 \\ -1 & j = 2. \end{cases}$$

Since the factor $h_o^2 m$ is common to all terms in the numerator and denominator of the reflection coefficient, V_{pp}, it will cancel, and we will not include it in what follows.

To express the D's and E's in the form of equations (4.48) and (4.49), we expand each of the above cofactors about their third columns. Thus

$$C_1^j = -p^2 Ai^{(1)}(-\xi_o) g_1^j - 2p^2\mu_1 G(\xi_o) g_2^j + i\mu_1 H(\xi_o) g_3^j$$

$$C_2^j = iG(\xi_o) g_1^j - 2p^2\mu_1 G(\xi_o) g_4^j + i\mu_1 H(\xi_o) g_5^j$$

$$C_3^j = iG(\xi_o) g_2^j + p^2 Ai^{(1)}(-\xi_o) g_4^j + i\mu_1 H(\xi_o) g_6^j$$

$$C_4^j = iG(\xi_o)g_3^j \qquad + p^2 Ai^{(1)}(-\xi_o)g_6^j \qquad +2p^2\mu_1 G(\xi_o)g_6^j$$

where g_i^j $(i = 1, 6;\ j = 1, 2)$ are the appropriate cofactors. Substituting for the definitions of (4.44) and (4.46), $G(\xi_o)$ and $H(\xi_o)$ in the above and neglecting terms of order ε_α^3 in (A5-4) and (A5-5) we obtain (4.48) and (4.49)

$$\begin{pmatrix} D \\ \\ D_1 \end{pmatrix} = Ai^{(1)}(-\xi_o)\begin{pmatrix} \Omega_1^1 \\ \\ \Omega_2^1 \end{pmatrix} + \varepsilon_b\, e^{i2\pi/3}\, Ai^{(1)'}(-\xi_o)\begin{pmatrix} \Omega_3^1 \\ \\ \Omega_4^1 \end{pmatrix}$$

$$\begin{pmatrix} E \\ \\ E_1 \end{pmatrix} = Ai^{(1)}(-\xi_o)\begin{pmatrix} \Omega_1^2 \\ \\ \Omega_2^2 \end{pmatrix} + \varepsilon_b\, e^{i2\pi/3}\, Ai^{(1)'}(-\xi_o)\begin{pmatrix} \Omega_3^2 \\ \\ \Omega_4^2 \end{pmatrix}$$

with

$$\left.\begin{aligned} \Omega_1^j &= -p^2\left(g_1^j + \pi_o\mu_1 g_4^j\right) + i\mu_1\pi_1\left(g_3^j - \pi_o\mu_1 g_6^j\right) \\ \Omega_2^j &= i\mu_1(\pi_1 + 2p^2)g_5^i \\ \Omega_3^j &= \mu_1(2p^2 + i\pi_o)g_2^j \\ \Omega_4^j &= 2p^2\mu_1\left(g_4^j - 2i\mu_1 g_6^j\right) - i\left(g_1^j + 2i\mu_1 g_3^j\right) \end{aligned}\right\} \qquad \text{(A5-6)}$$

where $j = 1,2$ and

$$\pi_1 = - p^2 + \varepsilon_b^2 \left(\xi_o \, e^{i 4\pi/3} + \frac{m^{\frac{1}{2}} \, \varepsilon_b^4}{8 n_\rho^4} \right)$$

The cofactors g_i^j $(i=1,6;\ j=1,2)$ are given by

$$\left.\begin{aligned}
g_1^j &= i\mu_o \left[\delta_j (1 + 2q^2)(2p^2 - \ell^2) + 4qp^2\nu \right] \\
g_2^j &= -\mu_o q \ell^2 \\
g_3^j &= - \mu_o p^2 \left[2q\nu + \delta_j (1 - 2q^2) \right] \\
g_4^j &= \mu_o \left[\delta_j (2p^2 - \ell^2) - 2q\nu \right] \\
g_5^j &= - \delta_j 3\mu_o \nu \\
g_6^j &= i(-\delta_j p^2 + q\nu)
\end{aligned}\right\} \qquad \text{(A5-7)}$$

In the evaulation of the contribution of the poles of V_{pp} to the integrand (4.54), the Ω_i^j will be evaluated with p given by (4.52). Accordingly, in (A5-7)

$$\begin{aligned}
p &= n_\alpha + 0(\varepsilon_\alpha^2) \\
q &= q_\alpha + 0(\varepsilon_\alpha^2) \qquad ; \ q_\alpha = (1-n_\alpha^2)^{\frac{1}{2}} \\
\nu &= \nu_\alpha + 0(\varepsilon_\alpha^2) \qquad ; \ \nu_\alpha = (\ell^2 - n_\alpha^2)^{\frac{1}{2}}
\end{aligned}$$

$$\pi_o = n_\alpha^2 + 0(\varepsilon_\alpha^6)$$

$$\pi_1 = -n_\alpha^2 + (n_b^2 - n_\alpha^2)\, e^{i4\pi/3} + 0(\varepsilon_\alpha^6).$$

When these are substituted into (A5-6), we obtain the following expressions for the Ω_i^j

$$\Omega_1^j \simeq -i\mu_o^2 n_\alpha^2 \left[4q_\alpha n_\alpha^2 \nu_\alpha + \delta_j (1 + 2q_\alpha^2)(2n_\alpha^2 - \ell^2) \right]$$

$$-\mu_o \mu_1 \left\{ i\pi_1 n_\alpha^2 \left[2q_\alpha \nu_\alpha + \delta_j (1+2q_\alpha^2) \right] + n_\alpha^4 \left[\delta_j (2n_\alpha^2 - \ell^2) - 2q_\alpha \nu_\alpha \right] \right\}$$

$$+ \mu_1^2 \pi_1 n_\alpha^2 (-\delta_j n_\alpha^2 + q_\alpha \nu_\alpha)$$

$$\Omega_2^j \simeq -\delta_j i 3\mu_o \mu_1 \nu_\alpha (\pi_1 + 2n_\alpha^2)$$

$$\Omega_3^j \simeq -\mu_o \mu_1 q_\alpha \ell n_2^2 (2 + i)$$

$$\Omega_4^j \simeq \mu_o^2 \left[4q_\alpha n_\alpha^2 \nu_\alpha + \delta_j (1 + 2q_\alpha^2)(2n_\alpha^2 - \ell^2) \right]$$

$$+ \delta_j 2\mu_o \mu_1 n_\alpha^2 (1 - \ell^2)$$

$$+ 4\mu_1^2 n_\alpha^2 (-\delta_j n_\alpha^2 + \nu_\alpha q_\alpha)$$

where $j = 1,2$ and $\delta_j = \begin{cases} 1 & j=1 \\ -1 & j=2 \end{cases}$.

Appendix VI

Earth-Flattening Transformation of the P-SV Displacement Potentials

In this appendix we develop the form of the continuity conditions for the decoupled P-SV displacement potentials across a discontinuous jump in elastic properties at r = a under the earth-flattening transformation. The analogous transformation for SH motion was presented in Section 2 of Chapter 1.

Following the argument leading to (4.30), the decoupled P-SV potential representation in a spherical system can be written as

$$\underline{u}(\underline{r}) \simeq \text{grad } \Phi + \text{curl curl } (r\psi,0,0) \tag{A6-1}$$

when $|\gamma_s/n_o| << 1$ and $|\gamma_\beta/k_o| << 1$. From (1.7) we have

$$\Phi_s = \frac{P(\underline{r})}{[\rho(r)]^{\frac{1}{2}}} \quad , \qquad \psi_s = \frac{S(\underline{r})}{[\rho(r)]^{\frac{1}{2}}} \tag{A6-2}$$

Assuming no dependence of the ϕ coordinate, (A6-1) can be written in component form as

$$\underline{u}(\underline{r}) \simeq \underline{e}_r \left[\frac{\partial}{\partial r} P - \frac{1}{r \sin\theta} \frac{\partial}{\partial \theta} \left(\sin\theta \frac{\partial}{\partial \theta} S \right) \right]$$

$$+ \underline{e}_\theta \frac{1}{r} \left[\frac{\partial}{\partial \theta} P + \frac{\partial^2}{\partial r \partial \theta} (rS) \right] \qquad \text{(A6-3)}$$

where $\underline{e}_r$ and $\underline{e}_\theta$ are unit vectors in the r and θ directions, respectively.

The potentials P and S approximately satisfy the Helmholtz equation at high frequencies

$$\nabla^2 P + h^2 P \simeq 0 \qquad \text{and} \qquad \nabla^2 S + k^2 S \simeq 0$$

and their eigenfunctions are

$$P^{(\ell)} = (\ell + 1/2)\, \hat{\psi}_\ell(r)\, P_\ell(\cos\theta)$$

$$S^{(\ell)} = (\ell + 1/2)\, \hat{\Phi}_\ell(r)\, P_\ell(\cos\theta) \qquad \text{(A6-4)}$$

where

$$\hat{\psi}_\ell(r) = \hat{P}_\ell(r)/[\rho(r)]^{1/2}$$

$$\hat{\Phi}_\ell(r) = \hat{S}_\ell(r)/[\rho(r)]^{1/2} \qquad \text{(A6-5)}$$

and $\hat{P}_\ell(r)$ and $\hat{S}_\ell(r)$ are solutions to equation (2.6).

The boundary conditions at r = a require continuity of displacement, or

$$[u_r]_{a+} = [u_r]_{a-}$$

$$[u_\theta]_{a+} = [u_\theta]_{a-} \tag{A6-7}$$

where u_r and u_θ are the r and θ components of the displacement $\underline{u}(r)$ in (A6-3), and continuity of stress, or

$$[\sigma_{rr}]_{a+} = [\sigma_{rr}]_{a-}$$

$$[\sigma_{r\theta}]_{a+} = [\sigma_{r\theta}]_{a-} \tag{A6-8}$$

In spherical coordinates the stresses are related to displacements by

$$\sigma_{rr} = \lambda \left[\frac{\partial u_r}{\partial r} + \frac{2u_r}{r} + \frac{\partial u_\theta}{r\partial\theta} + \frac{\cot\theta}{r} u_\theta \right] + 2\mu \frac{\partial u_r}{\partial r}$$

$$\sigma_{r\theta} = \mu \left[\frac{1}{r} \frac{\partial u_r}{\partial\theta} + \frac{\partial u_\theta}{\partial r} - \frac{u_\theta}{r} \right] \tag{A6-9}$$

Substituting (A6-4) into the first displacement boundary condition (A6-8) using (A6-3), we have

$$\left\{ P_\ell(x) \frac{d}{dr} \hat{\psi}_\ell - \frac{1}{r \sin\theta} \hat{\Phi}_\ell \frac{d}{d\theta} \left[\sin\theta \frac{d}{d\theta} P_\ell(x) \right] \right\}_{r=a\pm}$$

where we understand that $\left\{ \quad \right\}_{r=a\pm}$ means

$$\left\{ \quad \right\}_{a+} = \left\{ \quad \right\}_{a-}$$

and $P_\ell(x) = P_\ell(\cos\theta)$. Noting that

$$\frac{1}{\sin\theta}\frac{d}{d\theta}\left[\sin\theta \frac{d}{d\theta} P_\ell(x) \right] = (1-x^2)\, P''_\ell(x) - 2xP'_\ell(x)$$

and then that the two terms on the right are the first two terms in Legendre's equation we obtain

$$\frac{1}{\sin\theta}\frac{d}{d\theta}\left[\sin\theta \frac{d}{d\theta} P_\ell(x) \right] = -\ell(\ell+1)\, P_\ell(x)$$

since $P_\ell(x)$ is a solution to the homogeneous Legendre equation. The Legendre polynomials $P_\ell(x)$ thus cancel, and the r-component of the displacement boundary oondition becomes

$$\left\{ \frac{d}{dr}\hat{\psi}_\ell + \frac{\ell(\ell+1)}{a}\hat{\Phi}_\ell \right\}_{r=a\pm} \tag{A6-10}$$

The θ-component of the displacement boundary condition is

$$\left\{ \hat{\psi}_\ell \frac{d}{d\theta} P_\ell(x) + \frac{d}{dr}(r\hat{\Phi}_\ell)\frac{d}{d\theta} P_\ell(x) \right\}_{r=a\pm}$$

Here the θ derivatives of $P_\ell(x)$ cancel, and we are left with

$$\left\{ \hat{\psi}_\ell + \frac{d}{dr}\,(r\hat{\Phi}_\ell) \right\}_{r=a\pm} \tag{A6-11}$$

The σ_{rr} stress boundary condition is

$$\left\{(\lambda+2\mu)\left[P_\ell(x)\,\frac{d}{dr}\left(\frac{d}{dr}\,\hat{\psi}_\ell + \frac{\ell(\ell+1)}{r}\,\hat{\Phi}_\ell\right)\right] + \frac{2\lambda}{r}\,P_\ell(x)\left(\frac{d}{dr}\,\hat{\psi}_\ell + \frac{\ell(\ell+1)}{r}\,\hat{\Phi}_\ell\right)\right.$$

$$\left. + \frac{\lambda}{r}\left(\hat{\psi}_\ell + \frac{d}{dr}\,(r\hat{\Phi}_\ell)\right)\left[\frac{d^2}{d\theta^2}\,P_\ell(x) + \cot\theta\,\frac{d}{d\theta}\,P_\ell(x)\right]\right\}_{a\pm}$$

Again, we note that

$$\frac{d^2}{d\theta^2}\,P_\ell(x) + \frac{\cos\theta}{\sin\theta}\,\frac{d}{d\theta}\,P_\ell(x) = (1-x^2)\,P_\ell''(x) - 2xP_\ell'(x)$$

$$= -\,\ell(\ell+1)\,P_\ell(x)$$

so the P_ℓ's cancel, and we have

$$\left\{(\lambda+2\mu)\,\frac{d}{dr}\left[\frac{d}{dr}\,\hat{\psi}_\ell + \frac{\ell(\ell+1)}{a}\,\hat{\Phi}_\ell\right] + \frac{\lambda}{a}\left[2\left(\frac{d}{dr}\,\hat{\psi}_\ell + \frac{\ell(\ell+1)}{a}\,\hat{\Phi}_\ell\right)\right.\right.$$

$$\left.\left. - \frac{\ell(\ell+1)}{a}\left(\hat{\psi}_\ell + \frac{d}{dr}\,(r\hat{\Phi}_\ell)\right)\right]\right\}_{r=a\pm} \tag{A6-12}$$

Finally, the $\sigma_{r\theta}$ stress boundary condition is

$$\left\{ \mu \left[\frac{1}{r} \left(\frac{d}{dr} \hat{\psi}_\ell + \frac{\ell(\ell+1)}{r} \hat{\Phi}_\ell \right) \frac{d}{d\theta} P_\ell(x) + \left(\frac{d}{dr} \hat{\psi}_\ell + \frac{d^2}{dr^2} (r\hat{\Phi}_\ell) \right) \frac{d}{d\theta} P_\ell(x) \right. \right.$$

$$\left. \left. - \frac{1}{r} \left[\hat{\psi}_\ell + \frac{d}{dr} (r\hat{\Phi}_\ell) \right] \frac{d}{d\theta} P_\ell(x) \right] \right\}_{r=a\pm}$$

Again, the θ derivatives of $P_\ell(x)$ cancel, and we have

$$\left\{ \mu \left[\frac{1}{a} \left(\frac{d}{dr} \hat{\psi}_\ell + \frac{\ell(\ell+1)}{a} \hat{\Phi}_\ell \right) + \frac{d}{dr} \left(\frac{1}{r} \hat{\psi}_\ell + \frac{d}{dr} (r\hat{\Phi}_\ell) \right) \right. \right.$$

$$\left. \left. - \frac{1}{a} \left(\hat{\psi}_\ell + \frac{d}{dr} (r\hat{\Phi}_\ell) \right) \right] \right\}_{r=a\pm} \qquad \text{(A6-13)}$$

We now introduce the earth-flattening transformation (2.12) on the independent variable

$$r = a\, e^{z/a}$$

and the dependent variables

$$\hat{\psi}_\ell(r) = \left(\frac{a}{r} \right)^{1/2} \hat{\psi}(z), \qquad \Phi_\ell(r) = \left(\frac{a}{r} \right)^{1/2} \hat{\Phi}(z)$$

into the boundary conditions (A6-10) through (A6-13) and complete the implicit derivatives. The result is

$$\left\{\left(\hat{\psi}' - \frac{\hat{\psi}}{a}\right) + \frac{\ell(\ell+1)}{a}\,(a\hat{\Phi})\right\}_{z=0\pm} \tag{A6-14}$$

$$\left\{\hat{\psi} + a\hat{\Phi}' + \frac{1}{2}\,\hat{\Phi}\right\}_{z=0\pm} \tag{A6-15}$$

$$\left\{(\lambda + 2\mu)\left[\hat{\psi}'' - \frac{2}{a}\,\psi' + \frac{3}{4a^2} + \frac{\ell(\ell+1)}{a}\left(\hat{\Phi}' - \frac{3}{2}\,\frac{\hat{\Phi}}{a}\right)\right]\right.$$
$$\left. + \lambda\left[\frac{2}{a}\,\hat{\psi}' - \frac{1}{a^2}\,\hat{\psi} - \frac{\ell(\ell+1)}{a^2}\left(\hat{\psi} + a\left(\hat{\Phi}' - \frac{1}{2a}\,\hat{\Phi}\right)\right)\right]\right\}_{z=0\pm} \tag{A6-16}$$

and

$$\left\{\mu\left[2\,\frac{\hat{\psi}}{a} - 2\,\frac{\hat{\psi}}{a} + a\hat{\Phi}'' + \hat{\Phi}\left(\frac{\ell(\ell+1)}{a^2} + \frac{3}{2}\right)\right]\right\}_{z=0\pm} \tag{A6-17}$$

where the primes indicate differentiation with respect to z.

For body wave problems in the crust and upper mantle, $|\kappa^2 a^2| >> 1$. Thus from (2.12) we will have $\kappa^2 a^2 \simeq \ell(\ell+1)$. Furthermore, we will have

$$|\hat{\psi}'| \propto |\eta_\alpha \hat{\psi}| >> \left|\frac{\hat{\psi}}{a}\right|$$

and

$$|\hat{\Phi}| \propto |\eta_\beta \hat{\Phi}| >> \left|\frac{\hat{\Phi}}{a}\right|$$

where η_α and η_β are vertical components of the compressional and shear wave numbers. Thus, neglecting terms of order $(\eta a)^{-1}$ in the

above equations, we obtain the following approximate spherical boundary conditions,

$$\left.\begin{array}{c} \left\{ \hat{\psi}' + \kappa^2(a\hat{\Phi}) \right\}_{z=0\pm} \\ \left\{ \hat{\psi} + (a\hat{\Phi}') \right\}_{z=0\pm} \\ \left\{ (\lambda+2\mu)\left[\hat{\psi}'' + \kappa^2(a\hat{\Phi}') \right] - \lambda\kappa^2\left[\hat{\psi} + (a\hat{\Phi}') \right] \right\}_{z=0\pm} \\ \mu \left\{ 2\hat{\psi}'\left[+ (a\hat{\Phi}'') + \kappa^2(a\hat{\Phi}) \right] \right\}_{z=0\pm} \end{array}\right\} \qquad \text{(A6-18)}$$

The analogous boundary conditions for a plane boundary are given by (4.36a) - (4.36d). The eigenfunctions for the P and SV displacement potentials in Cartesian coordinates are of the form.

$$P_f = \hat{\psi}_f(a)\, e^{\pm i\kappa_\alpha x} \quad , \quad S_f = \hat{\Phi}_f(z)\, e^{\pm i\kappa_\beta x} \qquad \text{(A6-19)}$$

where we let

$$\hat{\psi}_f(z) = \frac{\hat{P}(z)}{[\rho(z)]^{\frac{1}{2}}} \quad , \quad \hat{\Phi}_f(z) = \frac{\hat{S}(z)}{[\rho(z)]^{\frac{1}{2}}} \qquad \text{(A6-20)}$$

and $\hat{P}(z)$ and $\hat{S}(z)$ are solutions to (2.7). Substituting (A6-18) and (A6-19) into the boundary condition equations (4.36a) through (4.36d), we obtain

$$\left\{ \hat{\psi}_f' + \kappa_\alpha^2 \hat{\Phi}_f \right\}_{z=0\pm}$$

$$\left\{ \hat{\psi}_f + \hat{\Phi}_f' \right\}_{z=0\pm}$$

$$\left\{ (\lambda+2\mu) \left[\hat{\psi}_f'' + \kappa_\alpha^2 \hat{\Phi}_f' \right] - \lambda\kappa_\alpha^2 \left[\hat{\psi}_f + \hat{\Phi}_f' \right] \right\}_{z=0\pm} \qquad \text{(A6-21)}$$

$$\left\{ \mu \left[2\hat{\psi}_f' + \hat{\Phi}_f'' + \kappa_\alpha^2 \hat{\Phi}_f \right] \right\}_{z=0\pm}$$

Comparing (A6-20) with (A6-17), we see that the approximate spherical boundary conditions for $|\kappa a| >> 1$ are equivalent to the exact flat boundary conditions and that the corresponding potentials are related by

$$\hat{\psi}_f = \hat{\psi}_\ell \quad , \quad \hat{\Phi}_f = (a\hat{\Phi}_\ell)$$

or

$$P_f = P \quad , \quad S_f = aS$$

The factor a (the radius to the boundary) in the transformation of the SH potentials serves to keep the correspondence dimensionally correct. From the original definitions of the potentials (1.7) and (1.11), it is evident that the spherical SV-potential has the dimensions of area while the flat SV-potential has the dimensions of volume. The P-potential has the dimensions of area in both cases.

Table Headings

Table 1. Summary of Q' and velocity gradients from crustal amplitude data. Std. error refers to Q'^{-1} fit to amplitude data according to equation (7). γ is gradient parameter in equation (3.12) and γ_c is velocity gradient related to γ by equation (3.12a). 'Crit.' and '+' in γ and γ_c columns indicate near critical ($\sim -1.2 \times 10^{-3}$ sec^{-1}), and positive gradients, respectively. *Easton (1963), †Hill and Pakiser (1966), ‡Ryall and Stuart (1963), §Healy (1963), // Roller and Healy (1963), ¶Stewart (1968), **Roller (1965), ††Stewart (1968), ‡‡Warren et al. (1966), §§O'Brien (1968).

Table 2. Summary of Q' and velocity gradients from Pn amplitude data. Std. error refers to Q'^{-1} fit to amplitude data according to equation (7). γ(km^{-1}) is index of refraction gradient and γ_c (sec^{-1}) is velocity gradient (see equation 3.12a in Chapter 1). 'Crit.' and '+' indicate near critical ($\sim -1.2 \times 10^{-3}$ sec^{-1}) and positive gradients, respectively. *Hill and Pakiser (1966), †Ryall and Stuart (1963), ‡Archambeau et al. (1969), §Romny (1959), // Roller and Jackson (1966), ¶Romny et al. (1962), **Green and Hales (1968), ††Iyer et al. (19), §§Helmberger and Morris (1969).

Table 3. List of station locations and elevations for the Columbia Plateau profile. T4 and T5 are sites occupied by the two California Institute of Technology trailers; R1 and R6 are sites of first and last seismometers in the 6-element, 2.5-km array set up for the U.S. Geological Survey recording unit; H1 through H7 are locations of stations in the Hanford array.

Table 4. Distances and travel-times for stations on the Columbia Plateau profile from the EDZOE explsions. EDZ-5 refers to the fifth shot in the EDZOE series. "Corrected time' is actual travel-time between source and reciever;'Reduced TT' is 'Corrected time' with source and receiver elevation corrections included and $\Delta/8.0$ sec^{-1} subtracted.

Table 1

REGION Profile	PHASE	Q'	Q'^{-1} (1×10^{-3})	std. error (1×10^{-3})	γ (km^{-1}) (1×10^{-3})	γ_c (sec^{-1}) (1×10^{-3})
BASIN AND RANGE						
Fallon-Eureka*	Pg	471	2.10	0.91	-0.57	-15.
Fallon-S.F.*	Pg	760	1.32	0.36	-0.36	- 9.7
Fallon-Owens V.*	Pg	-446	-2.20	1.16	+	+
Eureka-Fallon*	Pg	972	1.03	0.47	-0.28	- 7.5
Eureka-North†	Pg	-1290	-0.77	0.88	+	+
Mt. City-South†	Pg	403	2.48	3.71	-0.68	-18.
NTS-East‡	Pg	117	8.50	0.87	-2.2	-26.
CALIFORNIA						
S. F.-Fallon*	Pg	3810	0.262	0.076	crit.	crit.
S. F.-S. Monica§	Pg	-1580	-0.63	1.13	+	+
Camp Roberts§	Pg	2860	0.349	0.87	crit.	crit.
S. Monica-L. Mead‖	Pg	230	4.34	2.17	-1.1	-15.

Table 1 (continued)

REGION Profile	PHASE	Q'	Q'^{-1} ($1x10^{-3}$)	std. error ($1x10^{-3}$)	(km^{-1}) ($1x10^{-3}$)	γ_c (sec^{-1}) ($1x10^{-3}$)
San Juan (6.06)¶	Pg	-47	-21.	4.9	+	+
San Juan (6.35)¶	Pg?	54	18.	3.7	-4.7	-20.
COLORADO PLATEAU						
Hanksville**	Pg	1260	0.795	1.02	crit.	crit.
Chinle**	Pg	221	4.53	1.33	-1.3	-16.
MISSOURI						
Hannibal††	Pg	-613	-1.63	0.86	+	+
Swan L.-Hannibal††	Pg	-549	-1.82	0.54	+	+
Swan L.-St. Joseph††	Pg	-1960	-0.511	0.633	+	+
St. Joseph ††	Pg	-475	-2.10	0.63	+	+

Table 1 (continued)

REGION Profile	PHASE	Q'	Q'^{-1} ($1x10^{-3}$)	std. error ($1x10^{-3}$)	γ (km^{-1}) ($1x10^{-3}$)	γ_c (sec^{-1}) ($1x10^{-3}$)
MISSISSIPPI††	P*	-382	-2.62	0.92	+	+
LAKE SUPERIOR§§	P*	31,700	0.0315	0.604	crit.	crit.
SNAKE RIVER PLAIN						
Boise-South†	P*	337	2.97	0.84	-0.80	-4.4

Table 2.

PROFILE	f(Hz)	Q'	Q'^{-1} ($1x10^{-3}$)	std. error. ($1x10^{-3}$)	γ(km^{-1}) ($1x10^{-3}$)	γ_c(sec^{-1}) ($1x10^{-3}$)
NTS -						
Boise*	4.0	-1558	-0.642	0.697	crit.	(-1.2)
Ordway†	3.0	676	1.48	0.370	-0.34	-3.6
BILBY‡	0.75	-458	-2.18	1.94	crit.	(-1.2)
	1.0	-649	-1.54	1.29	crit.	(-1.2)
	1.5	-1038	-0.966	0.92	crit.	(-1.2)
LOGAN BLANCA§	1.0	307	3.25	0.461	-0.80	-6.7
SHOAL -						
East¶	4.0	303	3.29	0.892	-0.81	-6.8
GNOME -						
East¶	4.0	898	1.11	0.884	-0.25	-2.7
West¶	4.0	647	1.54	0.604	-0.37	-3.5

Table 2 (continued)

PROFILE	f(Hz)	Q'	Q'^{-1} ($1x10^{-3}$)	std. error ($1x10^{-3}$)	γ(km^{-1}) ($1x10^{-3}$)	γ_c(sec^{-1}) ($1x10^{-3}$)
EARLY RISE -						
Little Rock**	4.0	-565	-1.77	0.180	+	+
Wichita**	4.0	-451	-2.22	0.204	+	+
Coloradoŧŧ	3.6	-588	-1.70	0.480	+	+
Montanaŧŧ	3.6	-285	-3.50	0.610	+	+
HAWAII -						
Mohole site§§	8.0	-1200	-0.836	1.04	+	+

Table 3

LIST OF STATIONS

N	NAME	LAT	LON	ELEV (KM)
1	T4-1	48.97333	-118.58833	0.890
2	R1-2	48.80516	-118.63632	0.853
3	R5-2	48.78766	-118.64417	0.799
4	T5-3	48.70667	-118.59816	1.112
5	T4-4	48.57933	-118.61366	1.036
6	R1-5	48.44749	-118.74333	0.588
7	R6-5	48.42732	-118.72682	0.573
8	T5-6	48.32683	-118.66116	1.158
9	T5-7	48.22516	-118.66849	0.561
10	R1-8	48.03032	-118.46066	0.439
11	R6-8	48.01033	-118.67017	0.412
12	T4-9	47.95250	-118.71849	0.588
13	R1-10	47.86699	-118.65500	0.813
14	R6-10	47.84467	-118.65517	0.805
15	T5-11	47.74416	-118.67332	0.710
16	T4-12	47.61249	-118.71666	0.640
17	R1-13	47.47949	-118.71950	0.574
18	R6-13	47.45749	-118.71950	0.557
19	T5-14	47.40349	-118.75583	0.500
20	T4-15	47.26166	-118.78133	0.508
21	R1-16	47.15866	-118.76717	0.476
22	R6-16	47.13683	-118.76717	0.497
23	T5-17	47.03465	-118.78932	0.463
24	T4-18	46.92366	-118.80032	0.414
25	R1-19	46.81332	-118.81499	0.335
26	R6-19	46.79332	-118.82500	0.350
27	T5-20	46.67999	-118.79532	0.361
28	T4-218	46.56400	-118.79633	0.354
29	R1-22	46.45799	-118.82433	0.325
30	R6-22	46.43565	-118.82433	0.280
31	T5-23	46.35149	-118.83499	0.302
32	T4-24	46.21149	-118.84532	0.238
33	R1-25	46.09499	-118.75850	0.226
34	R6-25	46.07565	-118.77066	0.158
35	T5-26	45.98965	-118.90199	0.460
36	T4-27	45.86499	-118.85399	0.468
37	R1-28	45.75465	-118.76532	0.496
38	R6-28	45.73299	-118.76532	0.499
39	T5-29	45.62700	-118.93300	0.495
40	T4-30	45.52516	-118.89049	0.546
41	R1-31	45.44350	-119.01700	0.823
42	R6-31	45.42082	-119.01666	0.893
43	T5-32	45.28766	-118.95299	1.326
44	R1-33	45.17899	-118.92032	1.086
45	R6-33	45.15700	-118.92082	1.062
46	T4-34	45.06282	-118.93365	1.210
47	T5-35	44.94666	-118.95349	1.058
48	R1-36	44.79999	-118.85233	1.195
49	R6-36	44.77966	-118.85432	1.073
50	T4-37	44.68765	-118.95166	1.396
51	R1-38	44.61299	-119.19482	1.320
52	R6-38	44.59166	-119.19482	1.326
53	T4-40	44.37233	-118.98082	1.207
54	R1-42	44.09982	-119.00432	1.468
55	R6-42	44.07967	-119.00732	1.605
56	T4-44	43.91832	-118.96516	1.378
57	R1-46	43.67532	-119.07883	1.393
58	R6-46	43.65399	-119.08333	1.323
59	R1-49	43.31667	-118.97766	1.250
60	R5-49	43.29900	-118.97766	1.250
61	R6-49	43.29517	-118.97766	1.252
62	H1	46.23466	-119.31749	0.475
63	H2	46.46500	-119.05832	0.219
64	H3	46.59833	-119.45915	0.330
65	H4	47.30666	-118.74500	0.520
66	H5	46.73999	-119.21666	0.384
67	H6	46.61333	-119.76082	0.372
68	H7	46.86333	-119.61800	0.268
69	BMO	44.84888	-117.30554	1.189

Table 4

SOURCE	RCVR	DELTA		AZIMUTH S-->R	AZIMUTH R-->S	CORRECTED TIME	ELIP CORR	ELEV CORR SRCE	ELEV CORR RCVR	REDUCED TT
		DEG	KM	DEG	DEG	SEC	SEC	SEC	SEC	SEC
EDZ 2	T4-1	1.817	202.0	185.1	4.9	32.31	0.0	-0.14	-0.13	7.06
EDZ 2	R1-2	1.988	221.0	185.6	5.4	35.87	0.0	-0.14	-0.13	8.25
EDZ 2	R1-2	1.988	221.0	185.6	5.4	37.39	0.0	-0.14	-0.13	9.77
EDZ 2	R1-2	1.988	221.0	185.6	5.4	34.81	0.0	-0.14	-0.13	7.19
EDZ 2	R1-2	1.988	221.0	185.6	5.4	36.59	0.0	-0.14	-0.13	8.97
EDZ 2	R5-2	2.006	222.9	185.7	5.5	35.03	0.0	-0.14	-0.12	7.16
EDZ 2	R5-2	2.006	222.9	185.7	5.5	36.14	0.0	-0.14	-0.12	8.27
EDZ 2	R5-2	2.006	222.9	185.7	5.5	37.40	0.0	-0.14	-0.12	9.53
EDZ 2	R5-2	2.006	222.9	185.7	5.5	36.85	0.0	-0.14	-0.12	8.98
EDZ 2	T5-3	2.084	231.6	184.6	4.4	36.03	0.0	-0.14	-0.16	7.08
EDZ 3	T4-4	2.212	245.8	184.6	4.4	38.25	0.0	-0.14	-0.15	7.52
EDZ 3	R1-5	2.351	261.3	186.5	6.2	39.76	0.0	-0.14	-0.09	7.09
EDZ 3	R1-5	2.351	261.3	186.5	6.2	42.59	0.0	-0.14	-0.09	9.92
EDZ 3	R6-5	2.370	263.4	186.2	5.9	39.96	0.0	-0.14	-0.08	7.03
EDZ 3	R6-5	2.370	263.4	186.2	5.9	42.89	0.0	-0.14	-0.08	9.96
EDZ 3	T5-6	2.466	274.1	184.9	4.7	41.25	0.0	-0.14	-0.17	6.98
EDZ 4	T5-7	2.568	285.4	184.9	4.6	44.40	0.0	-0.14	-0.08	8.72
EDZ 4	T5-7	2.568	285.4	184.9	4.6	42.74	0.0	-0.14	-0.08	7.06
EDZ 4	T5-7	2.568	285.4	184.9	4.6	46.05	0.0	-0.14	-0.08	10.37
EDZ 4	T5-7	2.568	285.4	184.9	4.6	46.30	0.0	-0.14	-0.08	10.62
EDZ 4	R1-8	2.762	307.0	184.4	4.2	46.55	0.0	-0.14	-0.06	8.17
EDZ 4	R1-8	2.762	307.0	184.4	4.2	47.80	0.0	-0.14	-0.06	9.42
EDZ 4	R1-8	2.762	307.0	184.4	4.2	50.93	0.0	-0.14	-0.06	12.55
EDZ 4	R1-8	2.762	307.0	184.4	4.2	49.32	0.0	-0.14	-0.06	10.94
EDZ 4	R1-8	2.762	307.0	184.4	4.2	45.13	0.0	-0.14	-0.06	6.75
EDZ 4	R6-8	2.782	309.3	184.5	4.3	45.40	0.0	-0.14	-0.06	6.74
EDZ 4	R6-8	2.782	309.3	184.5	4.3	46.81	0.0	-0.14	-0.06	8.15
EDZ 4	R6-8	2.782	309.3	184.5	4.3	49.81	0.0	-0.14	-0.06	11.15
EDZ 4	R6-8	2.782	309.3	184.5	4.3	48.08	0.0	-0.14	-0.06	9.42
EDZ 4	R6-8	2.782	309.3	184.5	4.3	51.45	0.0	-0.14	-0.06	12.79
EDZ 5	T4-9	2.843	316.0	185.1	4.8	46.29	0.0	-0.14	-0.09	6.79
EDZ 5	T4-9	2.843	316.0	185.1	4.8	51.79	0.0	-0.14	-0.09	12.29
EDZ 5	T4-9	2.843	316.0	185.1	4.8	46.75	0.0	-0.14	-0.09	7.25
EDZ 5	R1-10	2.925	325.1	184.1	3.9	48.84	0.0	-0.14	-0.12	8.20
EDZ 5	R1-10	2.925	325.1	184.1	3.9	49.49	0.0	-0.14	-0.12	8.85
EDZ 5	R1-10	2.925	325.1	184.1	3.9	47.56	0.0	-0.14	-0.12	6.92
EDZ 5	R1-10	2.925	325.1	184.1	3.9	53.70	0.0	-0.14	-0.12	13.06
EDZ 5	R1-10	2.925	325.1	184.1	3.9	52.09	0.0	-0.14	-0.12	11.45
EDZ 5	R6-10	2.947	327.6	184.1	3.8	49.72	0.0	-0.14	-0.12	8.77
EDZ 5	R6-10	2.947	327.6	184.1	3.8	47.80	0.0	-0.14	-0.12	6.85
EDZ 5	R6-10	2.947	327.6	184.1	3.8	49.03	0.0	-0.14	-0.12	8.08
EDZ 5	R6-10	2.947	327.6	184.1	3.8	52.45	0.0	-0.14	-0.12	11.50
EDZ 5	R6-10	2.947	327.6	184.1	3.8	54.10	0.0	-0.14	-0.12	13.15
EDZ 5	T5-11	3.048	338.8	184.2	3.9	58.42	0.0	-0.14	-0.10	16.07
EDZ 5	T5-11	3.048	338.8	184.2	3.9	49.52	0.0	-0.14	-0.10	7.17
EDZ 5	T5-11	3.048	338.8	184.2	3.9	56.38	0.0	-0.14	-0.10	14.03
EDZ 5	T5-11	3.048	338.8	184.2	3.9	55.27	0.0	-0.14	-0.10	12.92
EDZ 5	T5-11	3.048	338.8	184.2	3.9	51.43	0.0	-0.14	-0.10	9.08
EDZ 6	T4-12	3.182	353.7	184.6	4.3	57.37	0.0	-0.14	-0.09	13.17
EDZ 6	T4-12	3.182	353.7	184.6	4.3	50.83	0.0	-0.14	-0.09	6.62

Table 4 (continued)

SOURCE	RCVR	DELTA		AZIMUTH S-->R	AZIMUTH R-->S	CORRECTED TIME	ELIP CORR	ELEV CORR SRCE	ELEV CORR RCVR	REDUCED TT
		DEG	KM	DEG	DEG	SEC	SEC	SEC	SEC	SEC
EDZ 6	T4-12	3.182	353.7	184.6	4.3	56.18	0.0	-0.14	-0.09	11.97
EDZ 6	R1-13	3.315	368.4	184.4	4.1	52.64	0.0	-0.14	-0.08	6.59
EDZ 6	R1-13	3.315	368.4	184.4	4.1	58.80	0.0	-0.14	-0.08	12.75
EDZ 6	R1-13	3.315	368.4	184.4	4.1	54.10	0.0	-0.14	-0.08	8.05
EDZ 6	R1-13	3.315	368.4	184.4	4.1	55.68	0.0	-0.14	-0.08	9.63
EDZ 6	R1-13	3.315	368.4	184.4	4.1	60.93	0.0	-0.14	-0.08	14.88
EDZ 6	R6-13	3.337	370.9	184.4	4.1	59.29	0.0	-0.14	-0.08	12.93
EDZ 6	R6-13	3.337	370.9	184.4	4.1	61.34	0.0	-0.14	-0.08	14.98
EDZ 6	R6-13	3.337	370.9	184.4	4.1	56.04	0.0	-0.14	-0.08	9.68
EDZ 6	R6-13	3.337	370.9	184.4	4.1	54.38	0.0	-0.14	-0.08	8.02
EDZ 6	R6-13	3.337	370.9	184.4	4.1	53.02	0.0	-0.14	-0.08	6.67
EDZ 6	T5-14	3.392	377.1	184.7	4.4	61.70	0.0	-0.14	-0.07	14.57
EDZ 6	T5-14	3.392	377.1	184.7	4.4	58.92	0.0	-0.14	-0.07	11.79
EDZ 6	T5-14	3.392	377.1	184.7	4.4	53.85	0.0	-0.14	-0.07	6.72
EDZ 6	T5-14	3.392	377.1	184.7	4.4	53.85	0.0	-0.14	-0.07	6.72
EDZ14	H4	3.488	387.7	184.5	4.2	55.23	0.0	-0.14	-0.08	6.76
EDZ 7	R1-16	3.637	404.3	184.6	4.2	66.55	0.0	-0.14	-0.07	16.02
EDZ 7	R1-16	3.637	404.3	184.6	4.2	64.14	0.0	-0.14	-0.07	13.61
EDZ 7	R1-16	3.637	404.3	184.6	4.2	61.29	0.0	-0.14	-0.07	10.75
EDZ 7	R1-16	3.637	404.3	184.6	4.2	58.40	0.0	-0.14	-0.07	7.87
EDZ 7	R1-16	3.637	404.3	184.6	4.2	57.13	0.0	-0.14	-0.07	6.60
EDZ 7	R6-16	3.659	406.7	184.5	4.2	66.92	0.0	-0.14	-0.07	16.08
EDZ 7	R6-16	3.659	406.7	184.5	4.2	64.46	0.0	-0.14	-0.07	13.62
EDZ 7	R6-16	3.659	406.7	184.5	4.2	61.55	0.0	-0.14	-0.07	10.71
EDZ 7	R6-16	3.659	406.7	184.5	4.2	58.65	0.0	-0.14	-0.07	7.81
EDZ 7	R6-16	3.659	406.7	184.5	4.2	57.47	0.0	-0.14	-0.07	6.63
EDZ 7	T5-17	3.762	418.2	184.7	4.3	58.80	0.0	-0.14	-0.07	6.53
EDZ 7	T5-17	3.762	418.2	184.7	4.3	66.62	0.0	-0.14	-0.07	14.35
EDZ 7	T5-17	3.762	418.2	184.7	4.3	68.51	0.0	-0.14	-0.07	16.24
EDZ 8	R1-19	3.984	442.8	184.7	4.3	61.48	0.0	-0.14	-0.05	6.12
EDZ 8	R1-19	3.984	442.8	184.7	4.3	74.32	0.0	-0.14	-0.05	18.97
EDZ 8	R1-19	3.984	442.8	184.7	4.3	71.39	0.0	-0.14	-0.05	16.03
EDZ 8	R1-19	3.984	442.8	184.7	4.3	62.80	0.0	-0.14	-0.05	7.44
EDZ 8	R6-19	4.004	445.1	184.7	4.4	74.64	0.0	-0.14	-0.05	19.00
EDZ 8	R6-19	4.004	445.1	184.7	4.4	71.69	0.0	-0.14	-0.05	16.05
EDZ 8	R6-19	4.004	445.1	184.7	4.4	63.09	0.0	-0.14	-0.05	7.45
EDZ 8	R6-19	4.004	445.1	184.7	4.4	61.79	0.0	-0.14	-0.05	6.15
EDZ14	H7	4.011	445.9	192.6	11.7	62.04	0.0	-0.14	-0.04	6.31
EDZ14	H5	4.086	454.2	188.5	7.8	63.39	0.0	-0.14	-0.06	6.61
EDZ10	T4-21B	4.232	470.4	194.2	3.9	76.68	0.0	-0.14	-0.05	17.89
EDZ10	T4-21B	4.232	470.4	184.2	3.9	65.64	0.0	-0.14	-0.05	6.85
EDZ10	T4-21B	4.232	470.4	184.2	3.9	64.89	0.0	-0.14	-0.05	6.10
EDZ10	T4-21B	4.232	470.4	184.2	3.9	78.79	0.0	-0.14	-0.05	19.99
EDZ10	T4-21B	4.232	470.4	184.2	3.9	72.54	0.0	-0.14	-0.05	13.74
EDZ14	H3	4.251	472.6	190.4	9.6	63.98	0.0	-0.14	-0.05	4.91
EDZ14	H6	4.276	475.3	193.2	12.2	65.82	0.0	-0.14	-0.05	6.41
EDZ10	R1-22	4.339	482.3	184.4	4.0	80.49	0.0	-0.14	-0.05	20.20
EDZ10	R1-22	4.339	482.3	184.4	4.0	67.25	0.0	-0.14	-0.05	6.96
EDZ10	R1-22	4.339	482.3	184.4	4.0	65.91	0.0	-0.14	-0.05	5.62
EDZ14	H2	4.346	483.1	186.5	6.0	66.95	0.0	-0.14	-0.03	6.46

Table 4 (continued)

SOURCE	RCVR	DELTA		AZIMUTH S-->R	AZIMUTH R-->S	CORRECTED TIME	ELIP CORR	ELEV CORR SRCE	ELEV CORR RCVR	REDUCED TT
		DEG	KM	DEG	DEG	SEC	SEC	SEC	SEC	SEC
EDZ10	R6-22	4.361	484.8	184.4	4.0	80.87	0.0	-0.14	-0.04	20.27
EDZ10	R6-22	4.361	484.8	184.4	4.0	76.80	0.0	-0.14	-0.04	16.21
EDZ10	R6-22	4.361	484.8	184.4	4.0	76.53	0.0	-0.14	-0.04	15.94
EDZ10	R6-22	4.361	484.8	184.4	4.0	67.41	0.0	-0.14	-0.04	6.82
EDZ10	R6-22	4.361	484.8	184.4	4.0	66.16	0.0	-0.14	-0.04	5.57
EDZ10	T5-23	4.446	494.2	184.4	4.0	82.71	0.0	-0.14	-0.04	20.94
EDZ10	T5-23	4.446	494.2	184.4	4.0	67.81	0.0	-0.14	-0.04	6.04
EDZ10	T5-23	4.446	494.2	184.4	4.0	77.01	0.0	-0.14	-0.04	15.24
EDZ10	T5-23	4.446	494.2	184.4	4.0	88.06	0.0	-0.14	-0.04	26.29
EDZ10	T5-23	4.446	494.2	184.4	4.0	128.46	0.0	-0.14	-0.04	66.69
EDZ12	T4-24	4.586	509.7	184.4	4.0	70.66	0.0	-0.14	-0.04	6.94
EDZ12	T4-24	4.586	509.7	184.4	4.0	69.59	0.0	-0.14	-0.04	5.87
EDZ12	T4-24	4.586	509.7	184.4	4.0	75.69	0.0	-0.14	-0.04	11.97
EDZ12	T4-24	4.586	509.7	184.4	4.0	82.84	0.0	-0.14	-0.04	19.12
EDZ14	H1	4.596	510.9	188.5	7.7	69.46	0.0	-0.14	-0.07	5.59
EDZ12	R1-25	4.699	522.3	183.5	3.2	73.67	0.0	-0.14	-0.03	8.39
EDZ12	R1-25	4.699	522.3	183.5	3.2	70.89	0.0	-0.14	-0.03	5.61
EDZ12	R6-25	4.718	524.5	183.6	3.3	73.94	0.0	-0.14	-0.02	8.39
EDZ12	R6-25	4.718	524.5	183.6	3.3	71.25	0.0	-0.14	-0.02	5.69
EDZ12	T5-26	4.810	534.7	184.6	4.2	69.13	0.0	-0.14	-0.07	2.29
EDZ13	T4-27	4.932	548.2	184.2	3.8	82.48	0.0	-0.14	-0.07	13.95
EDZ13	T4-27	4.932	548.2	184.2	3.8	75.18	0.0	-0.14	-0.07	6.65
EDZ13	T4-27	4.932	548.2	184.2	3.8	74.38	0.0	-0.14	-0.07	5.85
EDZ13	T4-27	4.932	548.2	184.2	3.8	90.79	0.0	-0.14	-0.07	22.27
EDZ13	T4-27	4.932	548.2	184.2	3.8	77.61	0.0	-0.14	-0.07	9.09
EDZ13	T4-27	4.932	548.2	184.2	3.8	78.50	0.0	-0.14	-0.07	9.97
EDZ13	R1-28	5.039	560.1	183.4	3.0	87.18	0.0	-0.14	-0.07	17.18
EDZ13	R1-28	5.039	560.1	183.4	3.0	85.47	0.0	-0.14	-0.07	15.46
EDZ13	R1-28	5.039	560.1	183.4	3.0	84.50	0.0	-0.14	-0.07	14.50
EDZ13	R1-28	5.039	560.1	183.4	3.0	83.36	0.0	-0.14	-0.07	13.35
EDZ13	R1-28	5.039	560.1	183.4	3.0	78.04	0.0	-0.14	-0.07	8.03
EDZ13	R1-28	5.039	560.1	183.4	3.0	76.36	0.0	-0.14	-0.07	6.35
EDZ13	R6-28	5.060	562.5	183.3	3.0	87.54	0.0	-0.14	-0.07	17.23
EDZ13	R6-28	5.060	562.5	183.3	3.0	85.73	0.0	-0.14	-0.07	15.43
EDZ13	R6-28	5.060	562.5	183.3	3.0	84.84	0.0	-0.14	-0.07	14.53
EDZ13	R6-28	5.060	562.5	183.3	3.0	83.64	0.0	-0.14	-0.07	13.34
EDZ13	R6-28	5.060	562.5	183.3	3.0	78.32	0.0	-0.14	-0.07	8.02
EDZ13	R6-28	5.060	562.5	183.3	3.0	76.65	0.0	-0.14	-0.07	6.34
EDZ14	T5-29	5.173	575.0	184.6	4.2	69.77	0.0	-0.14	-0.07	-2.11
EDZ14	T5-29	5.173	575.0	184.6	4.2	80.26	0.0	-0.14	-0.07	8.38
EDZ14	T5-29	5.173	575.0	184.6	4.2	66.48	0.0	-0.14	-0.07	-5.40
EDZ14	T5-29	5.173	575.0	184.6	4.2	61.82	0.0	-0.14	-0.07	-10.06
EDZ14	T5-29	5.173	575.0	184.6	4.2	80.07	0.0	-0.14	-0.07	8.19
EDZ14	R1-31	5.361	595.9	185.1	4.6	90.03	0.0	-0.14	-0.12	15.54
EDZ14	R1-31	5.361	595.9	185.1	4.6	88.01	0.0	-0.14	-0.12	13.52
EDZ14	R1-31	5.361	595.9	185.1	4.6	82.88	0.0	-0.14	-0.12	8.39
EDZ14	R1-31	5.361	595.9	185.1	4.6	80.47	0.0	-0.14	-0.12	5.98
EDZ14	R1-31	5.361	595.9	185.1	4.6	81.92	0.0	-0.14	-0.12	7.43
EDZ14	R6-31	5.384	598.4	185.1	4.6	90.35	0.0	-0.14	-0.13	15.55
EDZ14	R6-31	5.384	598.4	185.1	4.6	88.19	0.0	-0.14	-0.13	13.40

Table 4 (continued)

SOURCE	RCVR	DELTA		AZIMUTH S-->R	AZIMUTH R-->S	CORRECTED TIME	ELIP CORR	ELEV CORR SRCE	ELEV CORR RCVR	REDUCED TT
		DEG	KM	DEG	DEG	SEC	SEC	SEC	SEC	SEC
EDZ14	R6-31	5.384	598.4	185.1	4.6	83.21	0.0	-0.14	-0.13	8.41
EDZ14	R6-31	5.384	598.4	185.1	4.6	80.85	0.0	-0.14	-0.13	6.05
EDZ14	R6-31	5.384	598.4	185.1	4.6	82.87	0.0	-0.14	-0.13	8.07
EDZ15	T5-32	5.513	612.8	184.5	4.0	83.47	0.0	-0.14	-0.20	6.87
EDZ15	T5-32	5.513	612.8	184.5	4.0	102.02	0.0	-0.14	-0.20	25.42
EDZ15	T5-32	5.513	612.8	184.5	4.0	91.32	0.0	-0.14	-0.20	14.72
EDZ15	T5-32	5.513	612.8	184.5	4.0	89.02	0.0	-0.14	-0.20	12.42
EDZ15	T5-32	5.513	612.8	184.5	4.0	84.24	0.0	-0.14	-0.20	7.64
EDZ15	R1-33	5.620	624.6	184.2	3.7	93.49	0.0	-0.14	-0.16	15.41
EDZ15	R1-33	5.620	624.6	184.2	3.7	87.26	0.0	-0.14	-0.16	9.18
EDZ15	R1-33	5.620	624.6	184.2	3.7	86.35	0.0	-0.14	-0.16	8.27
EDZ15	R1-33	5.620	624.6	184.2	3.7	85.06	0.0	-0.14	-0.16	6.98
EDZ15	R6-33	5.642	627.1	184.2	3.7	93.82	0.0	-0.14	-0.16	15.43
EDZ15	R6-33	5.642	627.1	184.2	3.7	87.64	0.0	-0.14	-0.16	9.25
EDZ15	R6-33	5.642	627.1	184.2	3.7	86.95	0.0	-0.14	-0.16	8.56
EDZ15	R6-33	5.642	627.1	184.2	3.7	87.31	0.0	-0.14	-0.16	8.93
EDZ15	T4-34	5.736	637.6	184.2	3.8	87.96	0.0	-0.14	-0.18	8.26
EDZ15	T4-34	5.736	637.6	184.2	3.8	90.81	0.0	-0.14	-0.18	11.11
EDZ16	T5-35	5.853	650.6	184.3	3.8	89.32	0.0	-0.14	-0.16	8.00
EDZ16	T5-35	5.853	650.6	184.3	3.8	99.78	0.0	-0.14	-0.16	18.46
EDZ16	T5-35	5.853	650.6	184.3	3.8	93.83	0.0	-0.14	-0.16	12.51
EDZ16	T5-35	5.853	650.6	184.3	3.8	90.23	0.0	-0.14	-0.16	8.91
EDZ17	BMO	5.978	664.4	172.9	353.6	90.19	0.0	-0.14	-0.18	7.14
EDZ16	R1-36	5.995	666.4	183.5	3.1	91.08	0.0	-0.14	-0.18	7.78
EDZ16	R1-36	5.995	666.4	183.5	3.1	90.16	0.0	-0.14	-0.18	6.86
EDZ16	R1-36	5.995	666.4	183.5	3.1	89.53	0.0	-0.14	-0.18	6.23
EDZ16	R1-36	5.995	666.4	183.5	3.1	100.31	0.0	-0.14	-0.19	17.01
EDZ16	R1-36	5.995	666.4	183.5	3.1	94.46	0.0	-0.14	-0.18	11.16
EDZ16	R6-36	6.016	668.6	183.5	3.1	91.28	0.0	-0.14	-0.16	7.70
EDZ16	R6-36	6.016	668.6	183.5	3.1	90.43	0.0	-0.14	-0.16	6.85
EDZ16	R6-36	6.016	668.6	183.5	3.1	89.78	0.0	-0.14	-0.16	6.20
EDZ16	R6-36	6.016	668.6	183.5	3.1	100.48	0.0	-0.14	-0.16	16.90
EDZ16	R6-36	6.016	668.6	183.5	3.1	98.83	0.0	-0.14	-0.16	15.25
EDZ16	R6-36	6.016	668.6	183.5	3.1	94.71	0.0	-0.14	-0.16	11.13
EDZ17	R1-38	6.199	689.0	185.6	5.0	104.69	0.0	-0.14	-0.19	18.57
EDZ17	R1-38	6.199	689.0	185.6	5.0	100.75	0.0	-0.14	-0.19	14.62
EDZ17	R1-38	6.199	689.0	185.6	5.0	97.53	0.0	-0.14	-0.19	11.41
EDZ17	R1-38	6.199	689.0	185.6	5.0	93.72	0.0	-0.14	-0.19	7.59
EDZ17	R1-38	6.199	689.0	185.6	5.0	92.79	0.0	-0.14	-0.19	6.66
EDZ17	R6-38	6.220	691.4	185.6	5.0	104.94	0.0	-0.14	-0.20	18.52
EDZ17	R6-38	6.220	691.4	185.6	5.0	100.86	0.0	-0.14	-0.20	14.44
EDZ17	R6-38	6.220	691.4	185.6	5.0	97.79	0.0	-0.14	-0.20	11.37
EDZ17	R6-38	6.220	691.4	185.6	5.0	93.94	0.0	-0.14	-0.20	7.52
EDZ17	R6-38	6.220	691.4	185.6	5.0	93.09	0.0	-0.14	-0.20	6.67
EDZ18	R1-42	6.701	744.7	184.1	3.6	108.59	0.0	-0.14	-0.22	15.50
EDZ18	R1-42	6.701	744.7	184.1	3.6	107.50	0.0	-0.14	-0.22	14.41
EDZ18	R1-42	6.701	744.7	184.1	3.6	102.41	0.0	-0.14	-0.22	9.32
EDZ18	R1-42	6.701	744.7	184.1	3.6	100.89	0.0	-0.14	-0.22	7.80
EDZ18	R1-42	6.701	744.7	184.1	3.6	99.75	0.0	-0.14	-0.22	6.66
EDZ18	R6-42	6.721	747.0	184.1	3.6	108.79	0.0	-0.14	-0.24	15.42
EDZ18	R6-42	6.721	747.0	184.1	3.6	107.71	0.0	-0.14	-0.24	14.33
EDZ18	R6-42	6.721	747.0	184.1	3.6	102.68	0.0	-0.14	-0.24	9.31
EDZ18	R6-42	6.721	747.0	184.1	3.6	101.13	0.0	-0.14	-0.24	7.76
EDZ19	R6-42	6.721	747.0	184.1	3.6	100.08	0.0	-0.14	-0.24	6.71
EDZ19	R1-46	7.127	792.2	184.3	3.8	113.74	0.0	-0.14	-0.21	14.72
EDZ19	R1-46	7.127	792.2	184.3	3.8	109.59	0.0	-0.14	-0.21	10.57
EDZ19	R1-46	7.127	792.2	184.3	3.8	108.56	0.0	-0.14	-0.21	9.54
EDZ19	R1-46	7.127	792.2	184.3	3.8	108.29	0.0	-0.14	-0.21	9.27
EDZ19	R6-46	7.149	794.6	184.3	3.8	114.08	0.0	-0.14	-0.20	14.76
EDZ19	R6-46	7.149	794.6	184.3	3.8	110.10	0.0	-0.14	-0.20	10.78
EDZ19	R6-46	7.149	794.6	184.3	3.8	109.05	0.0	-0.14	-0.20	9.73
EDZ19	R6-46	7.149	794.6	184.3	3.8	108.60	0.0	-0.14	-0.20	9.28

Figure Captions

Figure 1. Coordinate system for a spherically symmetric medium with a discontinuous boundary at r = a between a homogeneous region (C_o) and a radially heterogeneous region (C(r)). The point source and receiver are located at r_o and r, respectively.

Figure 2. Integration path for Watson transform in complex ν-plane The heavy line, C, is original contour, and dashed lines, C_1 and C_2, represent alternate positions for deformed contour.

Figure 3a. Coordinate system and parameters for acoustic waves reflected from a plane boundary. The point source is at $+ z_o$, and the receiver is at (z,ρ).

3b. Acoustic velocity, C, as a function of depth. Negative and positive gradient cases are represented by solid and dashed lines, respectively, for $z < 0$.

Figure 4. Locus of turning points (heavy lines) in the lower half-space for positive, null, and negative velocity gradients as a function of the parameter, $p = \sin \theta$. Wavy lines represent traveling waves with arrow indicating direction of propagation; exponential curves represent evanescent waves.

Figure 5a. Modulus of the plane wave reflection coefficient, V_{p-}, for different values of $\varepsilon = (\gamma/k_o)^{1/3}$.

5b. Phase of the reflection coefficient V_{p-}.

Figure 6a. Branch cuts and original contour for Weyl integral in the complex p-plane. (+,-) indicates signs of real and imaginary parts of the radical $\sqrt{1-p^2}$ in each quadrant.

6b. Steepest descents path and head-wave poles in complex p-plane for negative gradient case. P_o is saddle point n_o is index of refraction at boundary.

Figure 7. Steepest descents path and diving wave poles in complex p-plane for positive gradient case.

Figure 8a. Branch cuts and original contour for Weyl integral for generalized ray expansion of reflection coefficient for positive gradient, V_+.

8b. Steepest descents path for nth diving wave. Pn is the saddle point.

Figure 9. Compressional and shear wave velocities as a function of depth for reflection of elastic waves from a plane boundary. Negative and positive gradient cases are represented by solid and dashed lines, respectively.

Figure 10. Coordinate system for computing plane wave reflection coefficient in elastic medium with a plane boundary.

Figure 11. Complex p-plane showing steepest descents path, head-wave poles, and branch cuts for the reflection of elastic P-SV wave from a negative gradient.

Figure 12. Theoretical amplitudes for reflected and refracted waves from a plane boundary and vertically heterogeneous half-space. Both source and receiver are 30 km above the boundary at which $n_o = 0.875$, $m = 1.2$. Dash-dot curves are classical head wave amplitudes ($\gamma = 0$); heavy solid curves are head wave amplitudes for negative gradient ($\gamma = -10^{-3}km^{-1}$); heavy dashed curves are envelope of amplitude curves for positive gradient ($\gamma = 10^{-3}$ km^{-1}); light solid curves are amplitudes of reflected waves. Ray-theoretical amplitudes of direct (0) and once-reflected (1) diving waves are indicated by light dashed lines.

Figure 13. Contours for numerical integration of Weyl integral. X is location of saddle point:

a) Homogeneous case: separate contributions for head wave (H) and reflected wave (R).

b) Homogeneous case: combined contributions for head and reflected waves (HR)

c) Negative gradient case: separate contributions for head wave (H) and reflected wave (R)

d) Positive gradient case: separate contributions for diving waves (0) and reflected wave (R).

Figure 14a. Comparison of exact numerical solutions (solid lines) and asymptotic solutions (dashed lines) for head waves from a spherical boundary with a subcritical velocity gradient in the lower medium. Short and long dashed lines indicate asymptotic solutions for $|\sigma_-| \ll 1$ and $|\sigma_-| \gg 1$, respectively. Exact solution for classical head waves are indicated by dash-dotted curves for reference. Both source and receiver are 30 km above the boundary at which $n_o = 0.80$, $m = 1.2$.

14b. Comparison of exact numerical solutions and asymptotic solutions for diving waves from the same model as in 14a. but with a positive velocity gradient in the lower medium. Solid lines are envelopes for exact diving wave amplitudes; short dashed lines are asymptotic solutions for $|\sigma_+| \ll 1$; long dashed line is ray-theoretical amplitude for direct diving wave.

Figure 15. Schematic representation of effects of curvature and velocity gradients on near-critical waves:

a) Positive gradient case showing two diving waves

b) Homogeneous case showing two diving waves

c) Critical negative gradient case showing classical head wave path.

d) Sub-critical negative gradient case showing inward curving ray and 'diffracted' head wave to surface.

Figure 16. Theoretical amplitude curves for reflected and refracted waves from a spherical M-discontinuity and a homogeneous, 8.0-km/sec mantle; source and receiver are 30 km above the M-discontinuity in a 6.4-km/sec 'crust'. Solid lines are ray-theoretical amplitudes for direct (0) and once reflected (1) diving waves; vertical bars show minimum distance for valid description for wave of indicated frequency. Heavy dashed lines indicate envelopes of interfering diving wave amplitudes. Light dash-dotted lines are classical head wave amplitudes, and heavy dash-dotted line is reflected wave amplitude.

Figure 17. Details of exact numerical solution for diving wave amplitudes in model described in Figure 16. Dash-dotted lines are classical head wave amplitudes.

Figure 18. Spectral amplitudes of diving wave at distances of 1.0 and 3.0 degrees for model described in Figure 16. Dashed lines are classical head wave spectra.

Figure 19. Theoretical amplitude curves for reflected and refracted waves in same model as in Figure 16 but with negative and positive velocity gradients in mantle of $\pm 0.5 \times 10^{-3}$ sec^{-1}. Heavy solid lines are head wave amplitudes

in negative gradient case; code for curves in positive gradient case is the same as in Figure 16.

Figure 20. Theoretical amplitude curves for reflected and refracted waves in same model as in Figures 16 and 19 but with positive and negative velocity gradients in the mantle of $\pm 1 \times 10^{-2}$ sec^{-1}. Code for curves is same as in Figures 16 and 19.

Figure 21. Details of exact numerical solution for diving wave amplitudes for model in Figure 19 with a positive gradient 5×10^{-3} sec^{-1}.

Figure 22. Spectral amplitudes of refracted waves at distances of 1.0 and 3.0 degrees for model in Figure 19. Solid curve is spectrum for interfering diving waves ($\gamma_c = + 5 \times 10^{-3}$ sec^{-1}); dash-dotted curve is spectrum of head wave from negative gradient ($\gamma_c = - 5 \times 10^{-3}$ sec^{-1}); dashed curve is spectrum for classical head wave.

Figure 23. Head wave amplitude vs. distance at 5 Hz for a 3.0 km/sec layer 2 km thick over a 6.0 km/sec horizon. Squares are amplitudes for classical head wave with Q = 10,000. Circles are asymptotic amplitudes for the negative gradient case ($\gamma = 10^{-3}$ km^{-1}) for $|\sigma_-| \ll 1$ and $|\sigma_-| \gg 1$. The dashed line represents the exact

amplitude for the negative gradient case obtained by numerical integration of Weyl integral. $Q = \infty$ for the critical gradient case.

Figure 24. Head wave amplitude vs. distance for same model as in Figure 2 illustrating effects of Q and frequency. Squares, circles, and triangles are amplitudes for classical head wave with Q = 300 at 2, 5, and 10 Hz, respectively. The dashed, dotted, and dash-dot lines are amplitudes from a negative gradient half space with $\gamma = 10^{-3}$ at 2, 5, and 10 Hz obtained by numerical integration of Weyl integral. Note that the 5 Hz negative gradient case is the same as shown in Figure 2.

Figure 25. Amplitude curves illustrating effect of greater-than-critical or positive ($\gamma_c > -V_1/r$), critical ($\gamma_c = -V_1/r$) and sub-critical ($\gamma_c < -V_1/r$) velocity gradients on head wave amplitudes. The reflected wave amplitude which is insensitive to small gradients in the refracting medium, is shown for reference. The arrow at C.D. indicates the ray-theoretical critical point. These curves were generated for 6 Hz waves in a 6.4 km/sec layer 30 km thick over an 8.0 km/sec refractor.

Figure 26. Empirical relation between gradient parameter, γ, (equation (3.12) and Q'. Circles are points determined by fitting equation (7) for Q' through theoretical amplitudes of head waves refracted through media with negative velocity gradients. The theoretical amplitude are for a frequency of 5 Hz and were obtained by numerical integration of Weyl integral. Crosses are points obtained by fitting asymptotic solutions for the negative gradient through observed amplitude data.

Figure 27. Amplitude data for Pg first arrivals in the Basin and Range Province. Solid line is fit of equation (7) through the data points. a) Fallon to Eureka (Eaton), 1963), b) Fallon to San Franciso (Eaton, 1963), c) Fallon to Owens Valley (Eaton, 1963), d) Eureka to Fallon (Eaton, 1963), e) Eureka north (Hill and Pakiser, 1966), f) Mountain City south (Hill and Pakiser, 1966), g) Nevada Test Site east (Ryall and Stuart, 1963). Dashed line shows amplitude decay with Q' = infinity for comparison.

Figure 28. Amplitude data for Pg first arrivals in California. Solid line is fit of equation (7) through the data points. a) San Francisco to Fallon (Eaton, 1963), b) Combination

of Pg data from San Francisco south and Santa Monica north (Healy, 1963), c) Combination of Pg data north and south of Camp Roberts (Healy, 1963), d) Santa Monica to Lake Mead (Roller and Healy, 1963), e) San Juan south - 6.06 km/sec branch (Stewart, 1968), f) San Juan south - 6.35 km/sec branch (Stewart, 1968). Dashed line shows amplitude decay with Q' = infinity for comparison.

Figure 29. Amplitude data for Pg first arrivals in the Colorado Plateau Province. Solid line is fit of equation (7) through the data points. a) Hanksville south (Roller, 1965), b) Chinle north (Roller, 1965). Dashed line shows amplitude decay with Q' = infinity for comparison.

Figure 30. Amplitude data for Pg first arrivals in Missouri. Solid line is fit of equation (7) through the data points. a) Hannibal west (Stewart, 1968), b) Swan Lake to Hannibal (Stewart, 1968), c) Swan Lake to St. Joseph (Stewart, 1968), d) St. Joseph east (Stewart, 1968). Dashed line shows amplitude decay with Q' = infinity for comparison.

Figure 31. Amplitude data for P* first arrivals. Solid line is fit of equation (7) through the data points. a) Combination of P* amplitudes from shot points at Ansley, Raleigh, and Dribble, Mississippi (Warren et al., 1966),

b) Combined P* amplitudes from the Lake Superior experiment (O'Brien, 1968), c) P* amplitudes from Boise south in Snake River Plain (Hill and Pakiser, 1966). Dashed line shows amplitude decay with Q' = infinity for comparison.

Figure 32. Map showing location of crustal profiles and the relation of Q' to heat flow. Number beside each profile is $Q' \times 10^{-2}$. The heavy dashed contour separates the region in which Q' is less than 10^3 from that in which it is either greater than 10^3 or negative. Regional heat flow patterns are from Archambeau et al. (1969).

Figure 33. Same map as in Figure 32 but with regional heat flow patterns from Roy et al. (1970).

Figure 34. Amplitude data for Pn first arrivals from nuclear events at the Nevada Test Site (NTS). Solid line is fit of equation (7) through data points; dashed line shows amplitude decay with Q' = infinity for reference.

a) NTS to Boise, Idaho (Hill and Pakiser, 1966)

b) NTS to Ordway, Colorado (Ryall and Stuart, 1963)

c) Combined data recorded from Bilby event recorded along profiles northeast and southeast from NTS (Archambeau, et al., 1969)

d) Combined data from LOGAN and BLANCA events recorded southeast from NTS (Romny, 1959).

Figure 35. Amplitude data for Pn first arrivals. a) SHOAL (near Fallon, Nevada) recorded along a profile to the east (Roller and Jackson, 1966), b) GNOME (in New Mexico) west (Romny et al., 1962), c) GNOME east (Romny et al., 1962). Solid line is fit of equation (7) through data points; dashed line shows amplitude decay with Q' = infinity for reference.

Figure 36. Amplitude data for Pn first arrivals from EARLY RISE series of chemical explosions in Lake Superior. Solid line is fit of equation (7) through data points; dashed line shows amplitude decay with Q' = infinity for reference:

a) Little Rock, Ark. profile (the data points plotted are seven point moving average of all amplitude data; Green and Hales, 1965)

b) Wichita, Kansas profile (the data points plotted are seven point moving average of all amplitude data; Green and Hales, 1968)

c) Colorado profile (Iyer et al., 1969)

d) Montana profile (Iyer et al., 1969)

Figure 37. Amplitude data for Pn first arrivals at proposed Mohole site (SH31) (Helmberger and Morris, 1969). Solid line is fit of equation (7) through the data points. Dashed line shows amplitude decay with $Q' = \infty$ for comparison.

Figure 38. Map showing location of profiles used for Pn amplitudes. Number associated with each profile is Q'. Dashed 'profiles' indicate general trend stations distributed over a wide area. BILBY profile is combination of northeast (shown) and southeast profiles. Regional heat flow pattern is from Roy et al. (1970). Hashed contours separate region of lower than normal Pn velocities (< 8.0 km/sec) from normal velocities (≥ 8.0 km/sec) according to Pakiser and Steinhart (1964).

Figure 39. Map showing location of recording sites and EDZOE series of explosions for the Columbia Plateau profile. Solid circles are sites occupied by the two CIT trailers; bars are sites occupied by U.S.G.S. 8-channel unit; and open circles are station locations in Hanford array. Major geologic units are indicated by dashed boundaries; heavy dashed lines indicate approximate limits of Blue Mountain uplift.

Figure 40. Reduced travel-time plot of all picked arrivals listed in Table 3.

Figure 41. Record section compiled from seismograms recorded by the 8-channel U.S.G.S. refraction unit. Each trace is chosen from the output of one of six vertical seismometers in a 2.5 km array.

Figure 42. Section showing inferred crustal structure together with reduced travel-time plot of Pn arrivals along profile from Canadian border across the Columbia Plateau to central-east Oregon. Geologic boundaries correspond to those in Figure 39. Open circles are CIT trailer sites, bars are U.S.G.S. 8-channel unit sites, and solid circles are Hanford array stations.

Figure 43. Theoretical travel-times for crustal structure shown in Figure 42 and upper mantle structure for CP1 in Figure 44. Squares are observed arrivals. Lower diagram shows ray paths for this structure.

Figure 44. Upper mantle velocity structures for the Columbia Plateau inferred from later arrivals in Figures 40 and 41. The dashed line is the structure obtained by Julian (1970) from data along a profile north from the Nevada Test Site (NTS).